Technical Physics, Vol. 50, No. 4, 2005, pp. 385–393. Translated from Zhurnal Tekhnicheskoĭ Fiziki, Vol. 75, No. 4, 2005, pp. 1–10.

THEORETICAL AND MATHEMATICAL PHYSICS

Chaotic Synchronization of Unidirectionally Coupled Electron-Wave Media with Interacting Counterpropagating Waves

A. A. Koronovskii, P. V. Popov, and A. E. Hramov

Chernyshevsky State University, Kolledzh State Educational and Scientific Center, Saratov, 410026 Russia
e-mail: alkor@cas.ssu.runnet.ru, aeh@cas.ssu.runnet.ru

Received April 26, 2004

Abstract—Chaotic synchronization of two electron-wave media with interacting counterpropagating waves and cubic phase nonlinearity (transverse-field backward-wave oscillators) is studied. Analysis is based on considering a continuous set of the phases of a chaotic signal. The parameters of chaotic synchronization in a system of unidirectionally coupled backward-wave oscillators are found, and the complex dynamics of establishing the chaotic synchronization conditions in an active medium is investigated. © *2005 Pleiades Publishing, Inc.*

INTRODUCTION

Investigation into chaotic synchronization of self-oscillations is a prominent problem in the modern theory of nonlinear oscillations and waves [1, 2]. This phenomenon is observed in a variety of systems, including physical and biological systems [3–6]. Investigation of this phenomenon is of great importance as applied to data transmission by means of determinate chaotic oscillations [7]. In most cases, chaotic synchronization was studied in systems with a small number of degrees of freedom. In distributed electron-wave systems, such investigations have not been carried out, although this problem seems central to microwave electronics (see, e.g., [8–10]).

Different types of chaotic synchronization are distinguished: phase synchronization, generalized synchronization, lag, and complete synchronization [2]. Phase synchronization, which is described through the phase $\phi(t)$ of a chaotic signal [1, 2, 11, 12], means that the phases of chaotic signals lock in synchronism, while their amplitudes remain unrelated to each other and appear chaotic. Phase lock-in results in coincidence of the frequencies of the signals. The frequency of a chaotic signal is defined as the mean rate of change of phase $\langle\phi(t)\rangle$. However, it does not always happen that the system can be characterized by a single phase especially if the signal has a complex spectral composition [13].

In [14], we suggested a new approach to analysis of chaotic synchronization that is based on considering a continuous set of phases. This set is determined by the continuous wavelet transform [15, 16] of chaotic signal $x(t)$,

$$W(s, t_0) = \int_{-\infty}^{+\infty} x(t)\psi^*_{s, t_0}(t)dt, \quad (1)$$

where $\psi_{s, t_0}(t)$ is a wavelet function derived from generating wavelet $\psi_0(t)$,

$$\psi_{s, t_0}(t) = \frac{1}{\sqrt{s}}\psi_0\left(\frac{t - t_0}{s}\right). \quad (2)$$

Time scale s specifies the width of wavelet $\psi_{s, t_0}(t)$ and t_0, the shift of the wavelet function along the time axis (the asterisk in (1) means the complex conjugate) [16]. Note that, in wavelet analysis, the notion "time scale" is routinely used instead of the notion "frequency," which is generally accepted in conventional Fourier transformation.

As a generating wavelet, we apply Morlet wavelet $\psi_0(\eta) = (1/\sqrt[4]{\pi})\exp(j\omega_0\eta)\exp(-\eta^2/2)$ [16]. Setting wavelet parameter ω_0 equal to 2π ($\omega_0 = 2\pi$) provides the relationship $s = 1/f$, where s is the time scale of wavelet transformation and f is the frequency of Fourier transformation.

Wavelet spectrum

$$W(s, t_0) = |W(s, t_0)|\exp[j\phi_s(t_0)] \quad (3)$$

describes the behavior of the system on each time scale s at any time t_0. The value of $|W(s, t_0)|$ characterizes the presence and significance of corresponding time scale s at time t_0. It is convenient to introduce the integral dis-

1063-7842/05/5004-0385$26.00

tribution of the wavelet energy over the time scales,

$$\langle E(s)\rangle = \int |W(s, t_0)|^2 dt_0. \quad (4)$$

Concurrently, phase $\psi_s(t) = \arg W(s, t)$ becomes definite in a natural way for each of time scales s. In other words, it becomes possible to characterize the behavior of each of time scales s through its associated phase $\psi_s(t)$.

If there exists time scale interval $[s_1, s_2]$ such that the condition of phase lock-in

$$|\psi_{s1}(t) - \psi_{s2}(t)| < \text{const} \quad (5)$$

is met for any time scale $s \in [s_1, s_2]$ and if part of the wavelet spectrum energy falling into this interval is other than zero,

$$E_{\text{sync}} = \int_{s_1}^{s_2} \langle E(s)\rangle ds > 0, \quad (6)$$

time scales $s \in [s_1, s_2]$ are synchronized and the chaotic oscillators are under the condition of time scale synchronization [14]. In (5), $\psi_{s1,2}(t)$, the continuous phases of the first and second oscillators, correspond to synchronized time scales s.

In this work, the above approach is applied to studying chaotic synchronization in a model system of coupled electron-wave media with counterpropagating waves and cubic phase nonlinearity (coupled transverse-field backward-wave oscillators (BWOs)). This is the simplest model of microwave oscillators based on backward-wave tubes, which are in considerable current use [17].

1. MODEL UNDER INVESTIGATION

Consider the basic equations that describe our model of two coupled electron-wave media with counterpropagating waves and cubic phase nonlinearity.

In a linear approximation, interaction between two counterpropagating dispersionless waves can be described by the set of equations

$$\frac{\partial F}{\partial \tau} - \frac{\partial F}{\partial \xi} = -AI, \quad (7)$$

$$\frac{\partial I}{\partial \tau} + \frac{\partial I}{\partial \xi} = -AF, \quad (8)$$

where $F = |F|\exp[j\varphi_F]$ and $I = |I|\exp[j\varphi_I]$ are the amplitudes of the electromagnetic and electron waves, respectively, which slowly (compared with $\exp(j(\hat{\omega}t - \hat{k}\xi))$ vary in time and space; τ and ξ are the dimensionless time and coordinate, respectively; $\hat{\omega}$ and $\hat{k}$ are, respectively, the frequency and wavenumber that correspond to the point of interaction between the dispersion curves for noninteracting electron and electromagnetic waves; and A is a dimensionless control parameter, which can be considered as the dimensionless length of the system or the dimensionless current of the electron beam [18].

A solution to linear equations (7) and (8) predicts the exponential growth of the amplitude of either wave. For oscillations in the system of the interacting waves to become stable, any nonlinear effect in the electron wave should be taken into account. A simple nonlinear effect is nonisochronism of electronic oscillators, which shows up in the dependence of the frequency of an electronic oscillator on its energy [17, 19]. Nonisochronism of electronic oscillators in our system of interacting counterpropagating waves is embodied in the nonlinear variation of phase φ_1 of the electron wave.

Let us assume that the part of phase φ_1 of the electron wave that is proportional to longitudinal coordinate ξ linearly depends on wave energy $W = \alpha I^2$ (α is a proportionality coefficient) in a first approximation. Then, the radiation frequency shifts because of the Doppler effect [19]. In the coordinate system with shifted time, $\tau' = (\tau - \xi)/2$ and $\xi' = \xi$, Eq. (8) can be recast in the form

$$\frac{\partial I}{\partial \xi} + j|I|^2 I = -AF, \quad (9)$$

where the primes at the new variables are omitted.

The set of Eqs. (7) and (9) describes processes occurring in the system of interacting counterpropagating waves with cubic phase nonlinearity (BWOs) [18]. In the regime of self-induced oscillation, Eqs. (7) and (9) should be complemented by standard boundary conditions $F(\xi = 1, \tau) = 0$ and $I(\xi = 0, \tau) = 0$, which reflect the absence of both waves at the system's boundaries. The autonomous nonlinear dynamics of transverse-field BWOs in the case of increasing bifurcation parameter A has been considered in detail elsewhere [18, 20, 21]. At $\pi/2 < A < 1.83$, one-frequency oscillations with stationary spatial distributions $F(\xi)$ and $I(\xi)$ are set up in the system. For $A > 1.83$, the system generates multiple-frequency periodic oscillations (field periodic self-modulation). Note that, when $A > 2.05$, the pattern of input field $F(\tau, \xi = 0)$ consists of pulses with a ripple in between. The ripple appears as a result of complex multiple-hump distributions $F(\xi)$ and $I(\xi)$ occurring in the system. Such distributions arise because of a fast nonlinear variation of the electron wave phase along the coordinate of the pace of interaction. Finally, at $A > 4.1$, chaotic self-oscillations are excited [21].

We will consider a system of two unidirectionally coupled electron-wave media exhibiting chaotic dynamics. The system is described by the set of equations

$$\frac{\partial F_{1,2}}{\partial \tau} - \frac{\partial F_{1,2}}{\partial \xi} = -A_{1,2} I_{1,2}, \quad (10)$$

$$\frac{\partial I_{1,2}}{\partial \xi} + j|I_{1,2}|^2 I_{1,2} = -A_{1,2}F_{1,2}, \quad (11)$$

where subscripts 1 and 2 refer to the "master" and "slave" active media, respectively.

Unidirectional coupling between the self-oscillating media is taken into account through a nonstationary boundary condition for the slowly varying amplitude of field F_2 of the slave active medium. In so doing, the boundary condition for the master medium remains unchanged,

$$I_1(\xi = 0, \tau) = 0, \quad F_1(\xi = 1.0, \tau) = 0, \quad (12)$$

$$\begin{aligned} I_2(\xi = 0, \tau) &= 0, \\ F_2(\xi = 1.0, \tau) &= \rho F_1(\xi = 0.0, \tau), \end{aligned} \quad (13)$$

where $\rho = R\exp[j\theta]$ is the complex coupling coefficient (R and θ are its amplitude and phase, respectively).

Note that coupling thus stated (a control signal acts only at the boundary of a distributed active medium) is natural and physically feasible, unlike the situation where coupling was assumed to be spatially uniform, i.e., a control signal acted (was received) at any point of coupled active media (see [2, 22], where chaotic synchronization of distributed model media was considered).

The values of the control parameters were set equal to $A_1 = 4.2$ (master) and $A_2 = 4.9$ (slave), which meets the condition of field chaotic self-modulation. Phase θ of the coupling coefficient did not influence the processes in the coupled system and was taken to be constant, $\theta = \pi$. Below, we analyze chaotic synchronization of two distributed electron-wave systems that is established under the condition of varying coupling coefficient amplitude R.

2. CHAOTIC SYNCHRONIZATION

Consider the behavior of the coupled system with the master and slave control parameters specified above in the case of increasing coupling coefficient amplitude R. The emphasis will be on oscillations $F_{r1,2} = \mathrm{Re}[F_{1,2}(\xi = 0, \tau)]$ at the exit from either medium.

Figures 1a and 1b show the oscillation power spectra and oscillation phase portraits (reconstructed by the Takens time-delay embedding method [23]) at the exit from the master and slave media, respectively, under the condition of self-excited oscillations ($R = 0$). From Fig. 1a, it follows that output field F_{r1} of the master medium, which is applied to the input of the space of interaction of the slave medium ($\xi = 1$), exhibits the Fourier spectrum of the oscillation power, which corresponds to chaotic oscillations. Two clearly cut peaks at frequencies f_m and f_b (basic frequencies) are observed against the continuous background noise (at a level of roughly –30 dB) in Fig. 1a. Frequency f_b is close to synchronism frequency ω of related noninteracting linear waves. As dimensionless current A_1 in the distributed system decreases, periodic oscillations are set up at a frequency close to microwave frequency f_b. The other frequency, f_m, which lies in the low-frequency part of the spectrum, determines the characteristic frequency of low-frequency modulation of field amplitude F_1. With increasing bifurcation parameter A, the oscillation pattern in the system becomes more tangled, as is clearly seen in Fig. 1b, where the oscillation power spectrum is plotted for $A_2 = 4.9$ and $R = 0$ (self-excited oscillation). In most of the power spectrum, the noise pedestal is rather high (within –5…–10 dB), so that any characteristic oscillation frequencies can no longer be distinguished from the background.

Consider the behavior of the slave system when it interacts with the field of the master system as amplitude R of the coupling coefficient between the distributed self-oscillating systems grows. Note that the power of the external signal acting on the slave system grows as R^2.

When R increases, the oscillation spectrum of the slave system changes, as demonstrated in Figs. 1c and 1d. At small $R < 0.3$ (Fig. 1c), a weak peak (marked by an arrow) corresponding to frequency f_b in the master spectrum (Fig. 1a) appears against an appreciable background. At large $R > 0.3$, the energy of the spectral components that correspond to the basic frequencies in the master spectrum rises in the slave spectrum (Fig. 1d, $R = 0.5$).

It should be noted that the phase portrait of the system (Fig. 1) does not allow us to correctly introduce the phase of the chaotic signal by any of the conventional methods [1, 11–13] because of the complex pattern of the chaotic attractor. Therefore, introduction of a family of phases by means of the wavelet transformation [14] (see also [24]) seems to be the only effective way of studying the chaotic synchronization of coupled electron-wave oscillators.

Figure 2 shows boundaries s_1 and s_2 of the ranges of synchronized time scales on plane (R, s).

A feature of the dynamics of two coupled electron-wave media is that, at a relatively large value of coupling coefficient R, the time scales of chaotic signals from either subsystem become synchronized in the ranges near basic time scales $s_b = 1/f_b$ and $s_m = 1/f_m$, respectively. In Fig. 2, the ranges of the synchronized scales are shown near basic scales s_b (lower part) and s_m (upper part).

From Fig. 2, it follows that, at $R \in (0, 0.029)$, chaotic synchronization is not established. This means that there is no time scale s where the phase dynamics meets chaotic synchronization condition (5). As coupling coefficient amplitude R increases, scale range $\Delta s = s_2 - s_1$ appears where phase lock-in condition (5) is met and the energy corresponding to this range (see (6)) is other than zero. Accordingly, the regime of time scale chaotic

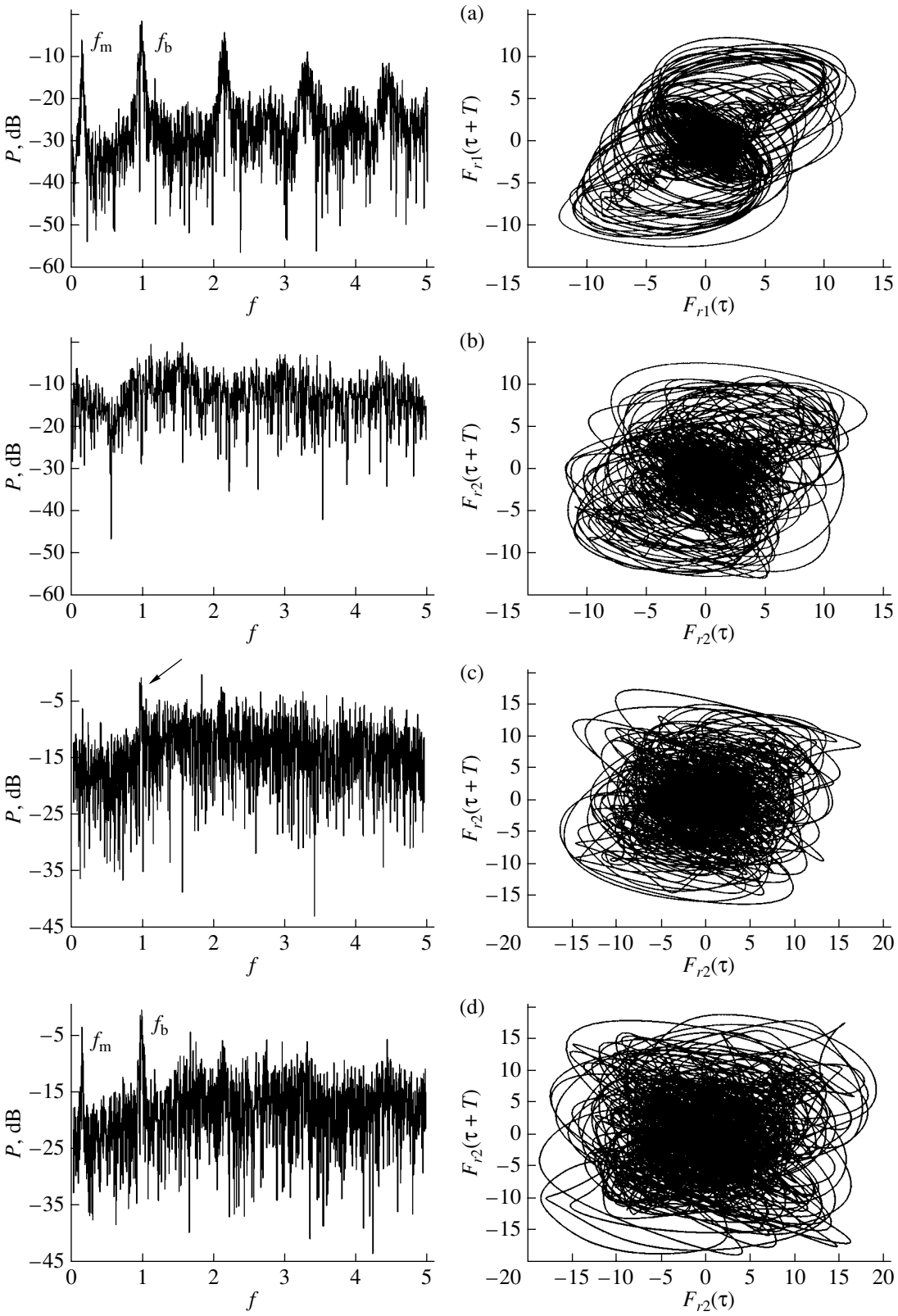

Fig. 1. Power spectra and phase portraits of oscillations in the independent (a) master and (b) slave BWOs and in the dependent slave system at R = (c) 0.2 and (d) 0.5.

synchronization in the coupled active media is established [14].

Note that, as R increases, time scales are first synchronized near basic scale s_b (when $R = R_b$) (see Fig. 2) and then (for $R = R_m > R_b$) the phases of time scales lock in synchronism near basic scale s_m, which corresponds to the modulation frequency of the field at the BWO output.

Consider first the reason for the occurrence of range Δs of synchronized scales (i.e., scales on which synchronism criteria (5) and (6) are fulfilled near basic frequency $f_b = 1/s_b$. To this end, let us turn to wavelet power spectra $\langle E_{1,2}(s)\rangle$, given by (4), for the master and slave media. The wavelet oscillation spectra of the output field for the master (dashed line *1*) and slave (continuous line *2*) BWOs are shown in Fig. 3 for various R. Wavelet spectrum $\langle E_1\rangle$ for the master BWO remains unchanged (for this medium, parameter A_1 is fixed and so the external field does not act on the medium) and is presented for comparison with wavelet power spectra $\langle E_2\rangle$ of the slave BWO.

Figure 3a demonstrates the wavelet oscillation power spectra for the self-excited oscillators. The wavelet spectra of the oscillators are seen to differ substantially. In wavelet spectrum $\langle E_1\rangle$ of the master system, basic time spectra s_b (corresponding to high frequency f_b) and s_m (modulated oscillations with fundamental frequency f_m) indicated in Fig. 3 stand out. In the wavelet spectrum of the slave system, the time scales corresponding to high-frequency spectral components (marked by an arrow in Fig. 3a) are distinctly seen, but the position of the peak in wavelet spectrum $\langle E_2\rangle$ does not correspond to basic time scale s_b of the master subsystem. In other words, the basic frequencies of the subsystems diverge. For large scales (low modulation frequencies), the wavelet spectra are radically different. In the slave subsystem near scale s_m, the spectrum is continuous and uniform; that is, the modulated oscillations exhibit a continuous noiselike spectrum without peaks (time scales) on the background pedestal.

As R increases, only those time scales meet synchronism conditions (5) and (6) for which the oscillation energy in the wavelet spectra of both subsystems is significant. In fact, at $R \approx 0.3$, the synchronism condition is met only for time scales near basic scale $s_b = 1/f_b \approx 1.0$ (see also Fig. 2). As follows from Fig. 3b, it is in this range of time scales that the wavelet oscillation energy is maximal.[1] From Fig. 3b, it is seen that the wavelet spectrum energy falling into scale s_m of the master subsystem also grows. However, at $R \approx 0.3$, this energy is small and the time scales of the field modulated oscillations are out of synchronism.

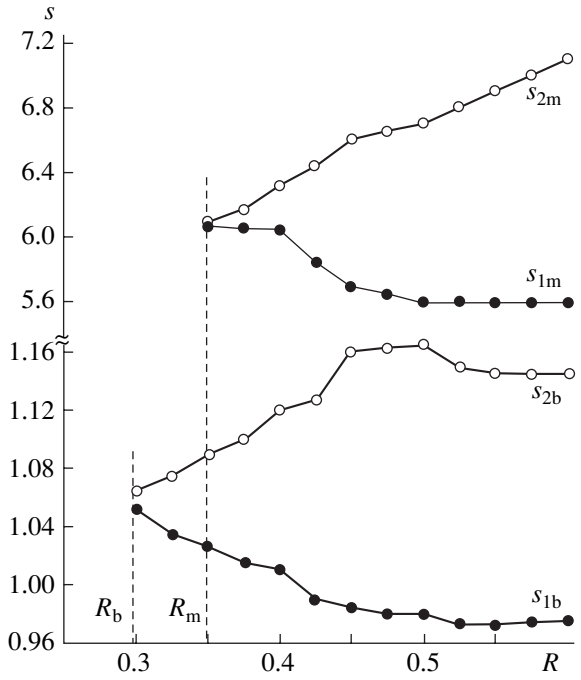

Fig. 2. Boundaries s_1 and s_2 of the synchronized time scale ranges on plane (R, s) for basic scales s_b (lower curves) and s_m (upper curves).

At high $R > 0.35$, the wavelet spectra of field oscillations at the outputs of both subsystems become similar to each other (Fig. 3c). The time scales corresponding to basic frequencies, s_m and s_b, have roughly equal intensities. In this case, synchronization conditions (5) and (6) are met for the most intense (in terms of spectrum energy) time scales in the power spectra and, accordingly, two scale ranges where the phase lock in synchronism appear (Fig. 2, $R > 0.35$).

Thus, those time scales of field chaotic oscillations in the coupled active media are synchronized in the first place on which the energy of the oscillation power spectrum is significant.

With rising coupling coefficient, the range of the time scales for which conditions (5) and (6) are met expands. The scales adjacent to the most intense ones and also providing an appreciable spectrum energy become involved in the synchronous dynamics.

This is illustrated in Fig. 2, from which it is seen that, for both basic scales s_b and s_m, range Δs of scales being synchronized expands with increasing R. At a high coefficient of coupling between the BWOs, range $\Delta s_b = s_{2b} - s_{1b}$ of synchronized scales near basic scale s_b stops expanding; moreover, it even contracts at $R > 0.5$. At the same time, near scale s_m, which describes the output field modulated, range $\Delta s_m = s_{2m} - s_{1m}$ of synchronized scales continues linearly expanding with R

[1] This range is shown by the hatched square and marked by letter s on the scale axis in Fig. 3.

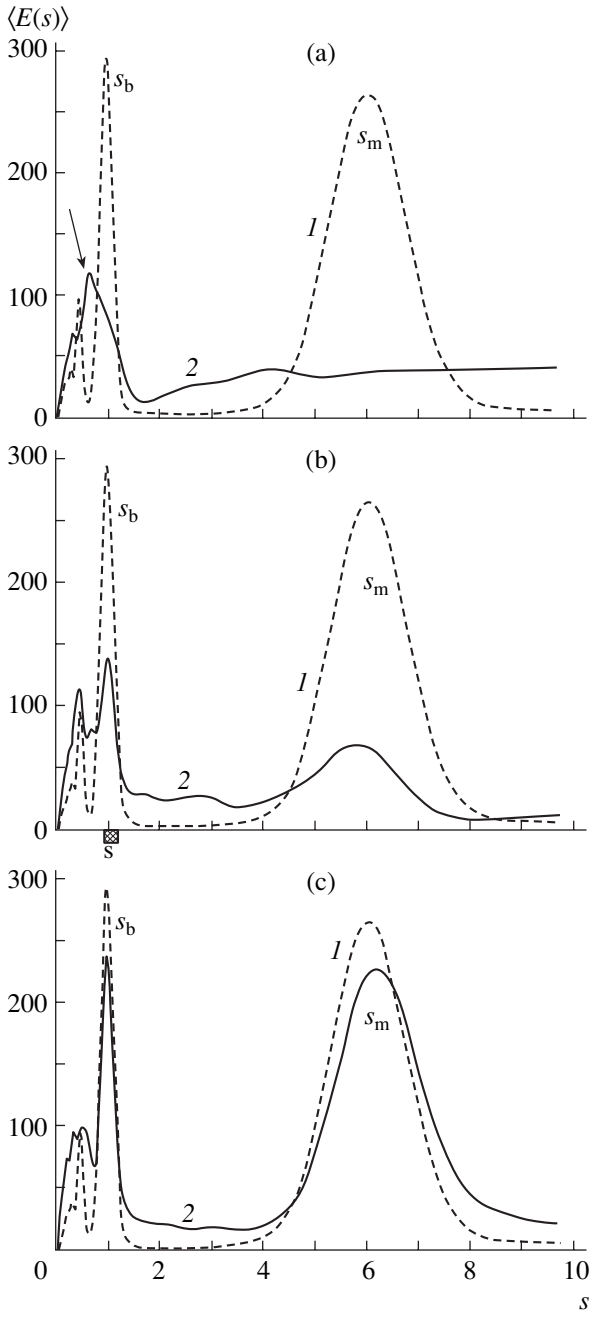

Fig. 3. Wavelet oscillation power spectra for the output field of the master (dashed curve *1*) and slave (continuous curve *2*) BWOs at R = (a) 0, (b) 0.2, and (c) 0.5.

owing to the shift of the upper bound, s_{2m}, of this range. This is associated with the fact that, as R increases, the energy in the wavelet spectrum of the slave subsystem is redistributed in such a way that larger scales ($s > s_m$) become more intense. Accordingly, the most intense time scales turn out to be brought to upper boundary s_{2m} of the range of synchronism and it is these scales that are synchronized first with increasing R.

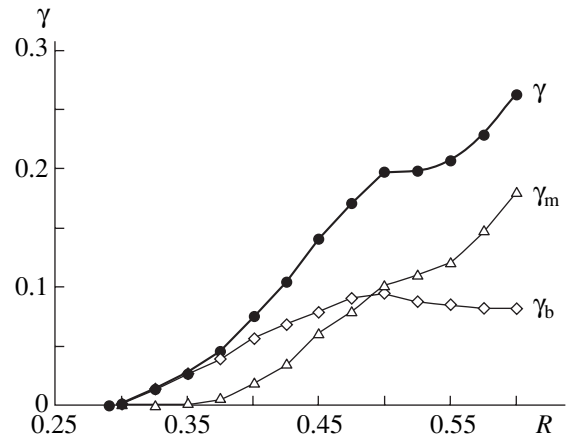

Fig. 4. γ_b, γ_m, and γ vs. coupling R between unidirectionally coupled BWOs.

3. MEASURE OF CHAOTIC SYNCHRONIZATION OF COUPLED ACTIVE ELECTRON-WAVE MEDIA

Introducing the continuous set of time scales s and their associated chaotic signal phases, along with separating range $\Delta s = s_2 - s_1$ of scales synchronized, allows us to consider a quantitative measure of chaotic synchronization of coupled systems. It is defined as the fraction of the wavelet spectrum energy that is due to time scales synchronized [14],

$$\gamma = \int_{s_1}^{s_2} \langle E(s)\rangle ds \Big/ \int_0^\infty \langle E(s)\rangle ds, \qquad (14)$$

where $\langle E(s)\rangle$ is the integral distribution of the wavelet spectrum energy over scales (formula (4)).

If $\gamma = 0$, chaotic synchronization of coupled systems is absent. A nonzero value of γ indicates the presence of synchronization, i.e., the presence of scales for which conditions (5) and (6) are valid. Finally, if $\gamma = 1$, oscillations in the systems are identical or are shifted relative to each other by some time interval T_τ. The latter regime is referred to as the chaotic lag synchronization [2]. The growth of γ from 0 to 1 means the increase in the energy due to time scales of synchronism. In essence, the value of γ shows how much chaotic oscillations in coupled active media are close to each other.

In our case, when synchronism is observed for two basic scales, it is appropriate to introduce measures of synchronization γ_b and γ_m for each of scales s_b and s_m, as well as the integral measure of synchronization, $\gamma = \gamma_b + \gamma_m$, of active distributed systems. The dependence of γ on coupling coefficient R characterizes the degree of chaotic synchronization of oscillations in coupled backward-wave electron-wave media.

Figure 4 demonstrates γ_b, γ_m, and γ versus coefficient R of coupling between the subsystems. For $R <$ 0.4–0.5, a major part of the oscillation energy due to

scales of synchronism falls on basic scale s_b ($\gamma_b > \gamma_m$). In other words, frequencies $f \approx f_b$ (i.e., those that are close to the frequency of synchronism between the electron and electromagnetic waves in the active media) lock in synchronism first. Then, as R grows, frequencies that are close to modulation frequency f_m of the master BWO field lock in synchronism. With R increasing further, more and more scales related to the low-frequency chaotic modulation of the BWO output signal become synchronized. Consequently, fraction γ_m of the synchronized modulated low-frequency oscillation energy grows with R. At $R > 0.5$, the relative energy of synchronized modulated low-frequency oscillations, γ_m, exceeds γ_b, which characterizes the relative energy of synchronized high-frequency oscillations.

The integral fraction of the energy due to time scales of synchronism, γ, grows with the coupling factor amplitude, as follows from Fig. 4. However, even at high R, when the slave system is subjected to a rather intense signal ($R^2 = 0.3$–0.4) from the master, the fraction of the energy due to the scales synchronized does not exceed $\gamma \approx 0.3$.

Thus, when two unidirectionally coupled transverse-field BWOs are chaotically synchronized under the condition of increasing coupling coefficient, those time scales of oscillation are synchronized first that are close to time scale s_b, which is the most intense in the wavelet power spectrum and is close to the frequency of synchronism between the electron and electromagnetic waves. As R grows, so does the energy due to synchronized scales near basic scale s_b. Simultaneously, time scale ranges Δs_m that describe the low-frequency modulated oscillations of field F in the BWOs lock in synchronism. With the coupling factor increasing further, the oscillation energy due to the time scales synchronized grows owing to the expansion of synchronized scale range Δs_m. Such behavior of two coupled BWOs is quantitatively described by the measure of mutual chaotic synchronization, $\gamma = \gamma(R)$.

4. SPATIAL DYNAMICS OF A SLAVE ACTIVE ELECTRON-WAVE MEDIUM

Consider now physical processes taking place when the chaotic synchronization conditions set up in a slave active medium with interacting counterpropagating waves. Emphasis will be on the spatial dynamics of the slave medium during the establishment of chaotic synchronization.

External chaotic signal $F_{ext1}(\tau) = F_1(\tau, \xi = 0)$ generated by the master (first) BWO strikes the slave BWO at point $\xi = L$ and then propagates toward the electron wave, i.e., toward the output, $\xi = 0$. Here, L is the dimensionless length of the active medium ($L = 1.0$ in our normalization). Synchronization in the entire electron-wave system of the two media (i.e., the conditions studied above) means that the time scales of external signal $F_{ext1}(\tau)$ are synchronized with those of signal $F_{out2}(\tau) = F_2(\tau, \xi = 0)$ picked up from the output of the slave (second) medium. We will analyze the space–time dynamics of the slave in terms of synchronization of the time scales for external signal $F_{ext1}(\tau)$ and signals $F_2(\tau, \xi)$ picked up at different points ξ of the slave system.

To be definite, consider the synchronization of time scales near scale s_b, which is the most intense in the wavelet power spectrum of the external chaotic signal. As was noted above, here time scale synchronization occurs at low R (at low energies $P_{ext} = R^2|F_{ext1}|^2$ of the external signal). We will study range Δs_b of time scales synchronized as a function of the spatial coordinate in the active medium. The dependence $\Delta s_b(\xi)$ and the measure of synchronization $\gamma(\xi)$ (see (14)) calculated from this dependence characterize the spatial dynamics of chaotic synchronization in an active medium subjected to an external chaotic signal at one of its ends.

Figure 5a shows the boundaries of the synchronized scale range in different sections of the space of interaction for three values of R. The curves are plotted on the coordinate plane [s, ($\xi - l$)], where s is the time scale and ($\xi - L$) is the coordinate of the space of interaction that is measured from the entrance ($\xi = L$) to the system. The range where synchronization conditions (5) and (6) are met is the widest in the area adjacent to the boundary $\xi = L = 1.0$ to which the control signal from the master BWO is applied (see boundary conditions (13) for field F_2 of the slave BWO). With distance toward the exit from the BWO ($\xi = 0$), range Δs_b of synchronized scales shrinks gradually. Measure of synchronization $\gamma_b(\xi)$ (Fig. 5b) varies over the space of interaction similarly to Δs_b. As coordinate ξ of the space of interaction decreases, the wavelet oscillation spectrum energy due to synchronized scales decreases smoothly.

If R is such that the chaotic synchronization of the coupled BWOs is absent ($R < 0.29$, see Sects. 2 and 3), the synchronized scale range goes down to zero over length of interaction ξ_s, $\xi_s < L$. In other words, the locking of phases corresponding to the time scales of variation of field $F_2(\tau, \xi)$, which occurs over the space of interaction in the dependent (slave) medium under the nonsynchronized chaotic conditions, has complex spatial dynamics. This dynamics is characterized by the following ranges of synchronized time scales (Fig. 5a, $R = 0.2$):

$$\begin{aligned} \Delta s \neq 0 \quad &\text{for} \quad \xi > L - \xi_s, \\ \Delta s = 0 \quad &\text{for} \quad \xi < L - \xi_s. \end{aligned} \tag{15}$$

Then, we may argue that the slave active medium can be subdivided into two specific parts in the nonsynchronized regime. The first has length ξ_s and occupies the interval ($L - \xi_s$, L), i.e., is adjacent to the entrance to the active medium ($\xi = L$). In this part, the oscillations

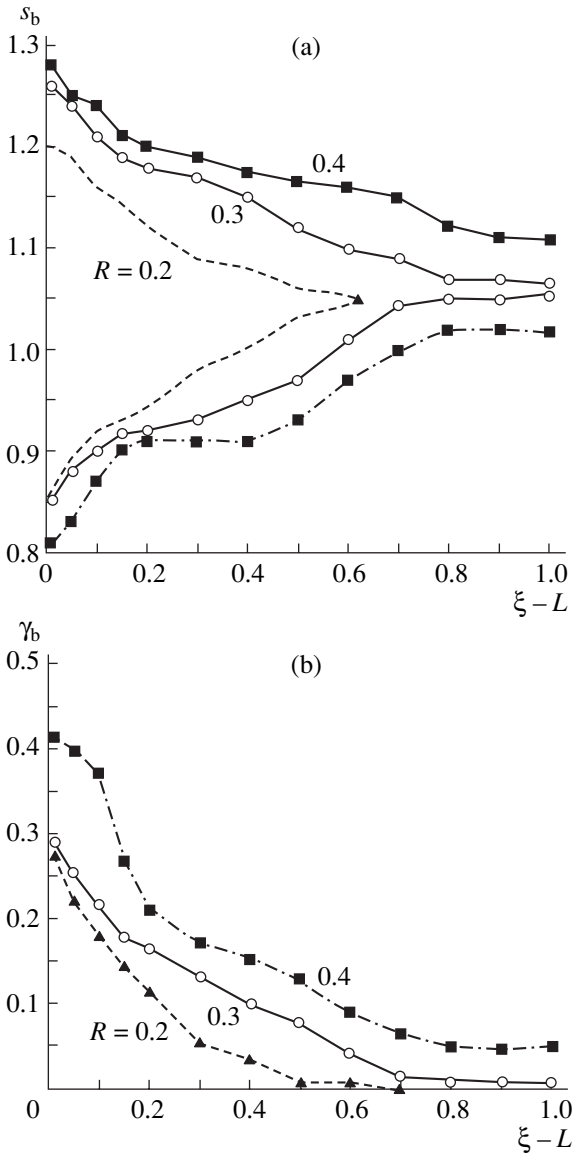

Fig. 5. (a) Boundaries of the synchronized time scale range on plane $[\gamma_b, (\xi - L)]$ (see text) and (b) measure of synchronization $\gamma_b(\xi)$ vs. coordinate $\xi - L$ in the space of interaction for various coupling factor amplitudes R.

of field $F_2(\tau, \xi)$ are chaotically synchronized with those of input signal $F_{ext1}(\tau)$ (hence, the measure of chaotic synchronization is other than zero, $\gamma_b|_{\xi > L - \xi_s} \neq 0$) on time scales in some range Δs. This part it is natural to call the region of synchronous oscillations; its length ξ_s, the length of synchronization. The other part, $\xi \in (0, L - \xi_s)$, is the region where chaotic synchronization breaks and where, accordingly, the range of synchronized time scales given by (15) and, hence, degree of synchronization γ_b vanish.

Length of synchronization ξ_s grows with the coupling coefficient and eventually becomes equal to the length of space of interaction, $\xi_s \equiv L$, at some $R = R_b$ (Fig. 2). This means that the chaotic synchronization conditions are set up throughout the active electron-wave medium; that is, we may speak of the chaotic synchronization of the BWO as a whole. It is such conditions that were studied in the previous sections where the dynamics of time scales and their associated output ($\xi = 0$) chaotic signal of the slave were concerned.

The case of chaotic synchronization throughout the active medium is illustrated in Fig. 5a for $R = 0.3 \approx R_b$. Here, range Δs of synchronized time scales is nonzero in all the sections of the medium; i.e., the process of chaotic synchronization covers the medium as a whole. As the coupling factor grows, range $\Delta s(\xi)$ of synchronized scales expands (Fig. 5a, $R = 0.4$), which is consistent with the previous results. In this case, the relative energy of the wavelet oscillation spectrum that falls on the synchronized time scales near the entrance ($\xi = L$) amounts to 30–40% at $\xi = 0.99L$. As the signal propagates over the space, γ_b decreases, reaching 1–5% at the exit ($\xi = 0$).

It should be noted that similar results were obtained in our earlier work [9] for another distributed system subjected to a harmonic action. It was shown that an external harmonic signal interacting with chaotic oscillation in a traveling-wave gyrotron may establish both synchronization and asynchronous conditions, depending on its parameters. In the former case, the basic (most intense) spectral component in the power chaotic spectrum is locked in. In [9], the locking of the basic oscillation frequency was observed (as in this work) only over length $\Delta\xi < L$ in the space of interaction (L is the length of the space of interaction in the gyrotron). The external harmonic action considered in [9] made it possible to analyze the locking of the single basic frequency in the chaotic oscillation spectrum but did not allow us to carefully study the process of establishing induced chaotic synchronization over the active medium.

Note in conclusion that the dependences shown in Fig. 5 are plotted on basic scale s_b. Similar dependences were obtained when the dynamics of synchronized scales near modulation scale s_m was analyzed. The only difference is that, for s_m, the length of synchronization becomes equal to the length of the active medium at coupling factor amplitudes higher than for s_b, which is consistent with the results reported in the previous sections of this work.

CONCLUSIONS

In this work, we used a new method [14] of analyzing chaotic synchronization that is based on introducing a set of time scales and their associated phases of a chaotic signal. The application of such an approach (instead of the conventional methods dealing with the chaotic signal phase) to chaotic oscillations in two unidirectionally coupled transverse-field BWOs allowed

us to study chaotic synchronization in coupled electron-wave oscillators with complex dynamics (the conventional methods fail in studying chaotic signals with a complex topology of the attractor). In addition, the approach suggested made it possible to separate out the chaotic synchronization of low-frequency modulated oscillations of the field amplitude and the synchronization of high-frequency spectral components in the BWO oscillation spectrum. This would also have been impossible with the conventional methods of chaotic synchronization analysis.

It was shown that chaotic synchronization occurs with increasing coupling between microwave oscillators and shows up in a phase relation between the time scales of field chaotic oscillations in the master and slave systems. As the coupling factor grows, the phases of the power spectrum high-frequency components lock in synchronism first (their phases correspond to the synchronism frequencies of the electron and electromagnetic waves). The synchronization of the low-frequency modulated oscillations is observed at higher values of the coupling factor. In the asynchronous regime of chaotic oscillations, the space of the active medium can be subdivided into two regions. In one adjacent to the entrance to the system ($\xi = L$), chaotic synchronization of the field oscillation time scales is set up. Synchronization length (the length of synchronous oscillation region) ξ_s grows with coupling coefficient. The chaotic synchronization regime throughout the space of two coupled oscillators is established when the synchronization length of the slave becomes equal to the length of the active medium, $\xi_s = L$.

ACKNOWLEDGMENTS

The authors thank D.I. Trubetskov for valuable discussions and comments.

This work was supported by the CRDF (grant no. REC-006), the program “Universities of Russia” (grant no. UR.01.01.051), the Dynasty Foundation, and the International Center of Fundamental Physics.

REFERENCES

1. M. G. Rosenblum, A. S. Pikovsky, and J. Kurths, Phys. Rev. Lett. **76**, 1804 (1996).
2. A. Pikovsky, M. Rosenblum, and J. Kurths, *Synchronization: Universal Concept in Nonlinear Sciences* (Cambridge Univ. Press, Cambridge, 2001).
3. C. M. Ticos, E. Rosa, W. B. Pardo, *et al.*, Phys. Rev. Lett. **85**, 2929 (2000).
4. V. A. Anishenko, A. G. Balanov, N. B. Janson, *et al.*, Int. J. Bifurcation Chaos Appl. Sci. Eng. **10**, 2339 (2000).
5. P. A. Tass *et al.*, Phys. Rev. Lett. **90**, 088101 (2003).
6. M. D. Prokhorov *et al.*, Phys. Rev. E **68**, 041913 (2003).
7. A. S. Dmitriev and A. I. Panas, *Dynamic Chaos: Advanced Data Carries for Communications* (Fizmatlit, Moscow, 2002) [in Russian].
8. A. A. Koronovskii, D. I. Trubetskov, and A. E. Hramov, Izv. Vyssh. Uchebn. Zaved. Radiofiz. **45**, 773 (2002).
9. D. I. Trubetskov and A. E. Hramov, Radiotekh. Élektron. (Moscow) **48**, 116 (2003).
10. N. M. Ryskin and V. N. Titov, Zh. Tekh. Fiz. **73** (9), 90 (2003) [Tech. Phys. **48**, 1170 (2003)].
11. V. S. Anishchenko and T. E. Vadivasova, Radiotekh. Élektron. (Moscow) **47**, 133 (2002).
12. A. Pikovsky, M. Rosenblum, and J. Kurths, Int. J. Bifurcation Chaos Appl. Sci. Eng. **10**, 2291 (2000).
13. V. S. Anishchenko and T. E. Vadivasova, Radiotekh. Élektron. (Moscow) **49**, 123 (2004).
14. A. A. Koronovskii and A. E. Hramov, Pis’ma Zh. Éksp. Teor. Fiz. **79**, 391 (2004) [JETP Lett. **79**, 316 (2004)].
15. *Wavelets in Physics*, Ed. by J. C. van den Berg (Cambridge Univ. Press, Cambridge, 1998).
16. A. A. Koronovskii and A. E. Hramov, *Continuous Wavelet Analysis and Its Applications* (Fizmatlit, Moscow, 2003) [in Russian].
17. D. I. Trubetskov and A. E. Hramov, *Lectures on Microwave Electronics for Physicists* (Fizmatlit, Moscow, 2003), Vol. 1 [in Russian].
18. A. P. Chetverikov, Izv. Akad. Nauk, Ser. Fiz. **58**, 171 (1994).
19. A. V. Gaponov, M. I. Petelin, and V. K. Yulpatov, Izv. Vyssh. Uchebn. Zaved. Radiofiz. **10**, 1415 (1967).
20. S. P. Kuznetsov and A. P. Chetverikov, Izv. Vyssh. Uchebn. Zaved. Radiofiz. **24**, 109 (1981).
21. A. P. Chetverikov, Vyssh. Uchebn. Zaved. Prikl. Nelin. Din. **2** (5), 46 (1994).
22. J. Kurths and A. S. Pikovsky, Chaos, Solitons and Fractals **5**, 1893 (1995).
23. F. Takens, *Lectures Notes in Mathematics*, Ed. by D. Rand and L.-S. Young (Springer, New York, 1981).
24. A. A. Koronovskii, D. I. Trubetskov, and A. E. Hramov, Dokl. Akad. Nauk **395**, 143 (2004) [Dokl. Phys. **49**, 143 (2004)].

Translated by V. Isaakyan

Technical Physics, Vol. 50, No. 4, 2005, pp. 394–401. Translated from Zhurnal Tekhnicheskoĭ Fiziki, Vol. 75, No. 4, 2005, pp. 11–18.

THEORETICAL AND MATHEMATICAL PHYSICS

Principles of Invariant Embedding in the Problem of Self-Sputtering of Solids

V. V. Manukhin

Moscow Power Engineering Institute (Technical University), ul. Krasnokazarmennaya 14, Moscow, 111250 Russia

e-mail: ManukhinVV@mpei.ru

Received May 20, 2004; in final form, September 8, 2004

Abstract—Principles of invariant embedding are applied to investigation into the phenomenon of self-sputtering of solids. Integral equations describing the flux of the sputtered atoms with regard for the boundary conditions are obtained. Approximate solutions to the integral equation for a function that describes the energy and angular spectra of the atoms escaping from the material surface in the case of self-sputtering are found. © *2005 Pleiades Publishing, Inc.*

Principles of invariant embedding were first suggested by Ambartsumyan [1] for the solution of the problem of light scattering by turbid medium. Equations obtained with the use of this approach contain boundary conditions, which is the main advantage of this method. Moreover, such equations describe variables that are directly measurable by an experiment.

Applied to investigating the transmission and reflection of light and charged particles from layers of various materials [1–3], principles of invariant embedding allowed a considerable advance in the theory of scattering of charged particles by solids.

When using principles of invariant embedding in sputtering, similar to the case of describing the characteristics of scattering of charged particles by solids (transmission and reflection), allowance should be made for the condition that, during the analysis period, the considered fluences of the bombarding ions cause no significant change in the material surface.

Let a parallel monochromatic beam of particles with energy E_0 be incident on a plane-parallel target of thickness z_0 in direction $\Omega_0 = \{\mu_0, \varphi_0\}$ (the normal is directed into the material). The total flux of particles is N_0^a. As soon as the phenomenon of self-sputtering is under consideration, i.e., target bombardment by particles of the same kind as the atoms the target consists of, the scattered and sputtered particles are theoretically indistinguishable.

Denote the differential density of the ascending component of the atom flux on the target surface by $N_{\text{out}}^a(z = 0, E_0, \mu_0, \varphi_0; E, \mu, \varphi)$ and the differential density of the descending component of the atom flux at depth z_0 by $N_{\text{in}}^a(z_0, E_0, \mu_0, \varphi_0; E, \mu, \varphi)$. Introduce auxiliary functions of self-sputtering $G(z_0, E_0, \mu_0, \varphi_0; E, \mu, \varphi)$ and transmission $T_a(z_0, E_0, \mu_0, \varphi_0; E, \mu, \varphi)$ describing the energy and angular spectra of atoms on the target surface and related to the differential density of the atom flux as follows [4, 5]:

$$G(z_0, E_0, \mu_0, \varphi_0; E, \mu, \varphi) = \frac{\mu}{N_0^a} N_{\text{out}}^a(z = 0, E_0, \mu_0, \varphi_0; E, \mu, \varphi), \quad (1)$$

$$T_a(z_0, E_0, \mu_0, \varphi_0; E, \mu, \varphi) = \frac{\mu}{N_0^a} N_{\text{in}}^a(z_0, E_0, \mu_0, \varphi_0; E, \mu, \varphi). \quad (2)$$

Here, $\mu_0 = \cos(\theta_0)$, $\mu = \cos(\theta)$; θ_0 and θ are polar angles; and φ_0 and φ are lateral angles. The processes that cause the target atom sputtering are described on the basis of the following principles [4].

(1) The ascending atom flux density at level z is a result of sputtering (and scattering) of the $(z_0 - z)$-thick layer of atoms beneath z by the descending atom flux,

$$N_{\text{out}}^a(z, E_0, \mu_0, \varphi_0; E, \mu, \varphi) = \frac{1}{4\pi\mu} \int_0^1 \int_0^{2\pi} \int_E^{E_0} N_{\text{in}}^a(z, E_0, \mu_0, \varphi_0; E_1, \mu_1, \varphi_1) \times G(z_0 - z, E_1, \mu_1, \varphi_1; E, \mu, \varphi) d\mu_1 d\varphi_1 dE_1. \quad (3)$$

(2) The descending atom flux density at level z is a result of sputtering (and scattering) of the z-thick layer of atoms above z by the ascending atom flux and transmission of atoms by the z-thick layer above z,

$$N_{\text{in}}^a(z, E_0, \mu_0, \varphi_0; E, \mu, \varphi) = \frac{N_0^a}{4\mu} T_a(z, E_0, \mu_0, \varphi_0; E, \mu, \varphi)$$

1063-7842/05/5004-0394$26.00

$$+\frac{1}{4\pi\mu}\int_0^{1}\int_0^{2\pi}\int_E^{E_0} N^a_{\text{out}}(z, E_0, \mu_0, \varphi_0; E_1, \mu_1, \varphi_1) \quad (4)$$

$$\times G(z, E_1, \mu_1\varphi_1; E, \mu, \varphi)d\mu_1 d\varphi_1 dE_1.$$

(3) The ascending atom flux density on the target surface is a result of transmission (with due regard for atom knocking-out) of the atoms that approach the surface z from below by the z-thick layer

$$N^a_{\text{out}}(z = 0, E_0, \mu_0, \varphi_0; E, \mu, \varphi)$$

$$= \frac{1}{4\pi\mu}\int_0^{1}\int_0^{2\pi}\int_E^{E_0} N^a_{\text{in}}(z, E_0, \mu_0, \varphi_0; E_1, \mu_1, \varphi_1) \quad (5)$$

$$\times T_a(z, E_1, \mu_1\varphi_1; E, \mu, \varphi)d\mu_1 d\varphi_1 dE_1.$$

The above principles are graphically illustrated in Fig. 1.

It has already been demonstrated [6, 7] that sputtering is a surface phenomenon; hence, an exact and proper consideration should be given to the boundary conditions. Assume that a plane potential barrier is present on the material surface. Since the laws describing the motion of an atom in a solid differ from those in the neighborhood of the potential barrier, the sputtering target is convenient to be represented as consisting of two layers (Fig. 1). Then, in accordance with principle 3, the outgoing atom flux may be considered as a result of transmission, by the potential barrier layer, of the atoms that approach this layer from below. With this principle being put in mathematical form, the self-sputtering function may be determined as follows:

$$S(z, E_0, \mu_0, \varphi_0; E, \mu, \varphi)$$

$$= \mu\int_0^{1}\int_0^{2\pi}\int_E^{E_0} G(z, E_0, \mu_0, \varphi_0; E_1, \mu_1, \varphi_0) \quad (6)$$

$$\times P(E_1, \mu_1, \varphi_1; E, \mu, \varphi)dE_1\frac{d\mu_1}{\mu_1}d\varphi_1.$$

Here, function $P(E_1, \mu_1, \varphi_1; E, \mu, \varphi)$ expresses the probability that an atom having energy E_1 on the surface and moving in direction $\Omega = \{\mu_1, \varphi_1\}$ away from the surface will surmount the barrier and escape from the surface in direction $\Omega = \{\mu, \varphi\}$ with energy E [6]

$$P(E_1, \Omega_1; E, \Omega) = \delta(E + U - E_1)\delta(\varphi - \varphi_1)$$

$$\times\delta\left(\cos\theta - \left[\left(1 + \frac{U}{E}\right)\cos^2\theta_1 - \frac{U}{E}\right]^{1/2}\right), \quad (7)$$

where $\delta()$ is the Dirac delta and U is the surface atom binding energy.

Since function $G(z_0, E_0, \mu_0, \varphi_0; E, \mu, \varphi)$ describes the energy and angular spectra of atoms that have not yet surmounted the potential barrier, while function $S(z_0, E_0, \mu_0, \varphi_0; E, \mu, \varphi)$ characterizes the really measured energy and angular spectra of the sputtered atoms, below, $S(z_0, E_0, \mu_0, \varphi_0; E, \mu, \varphi)$ is referred to as the self-sputtering function, while $G(z_0, E_0, \mu_0, \varphi_0; E, \mu, \varphi)$ is the auxiliary function of self-sputtering.

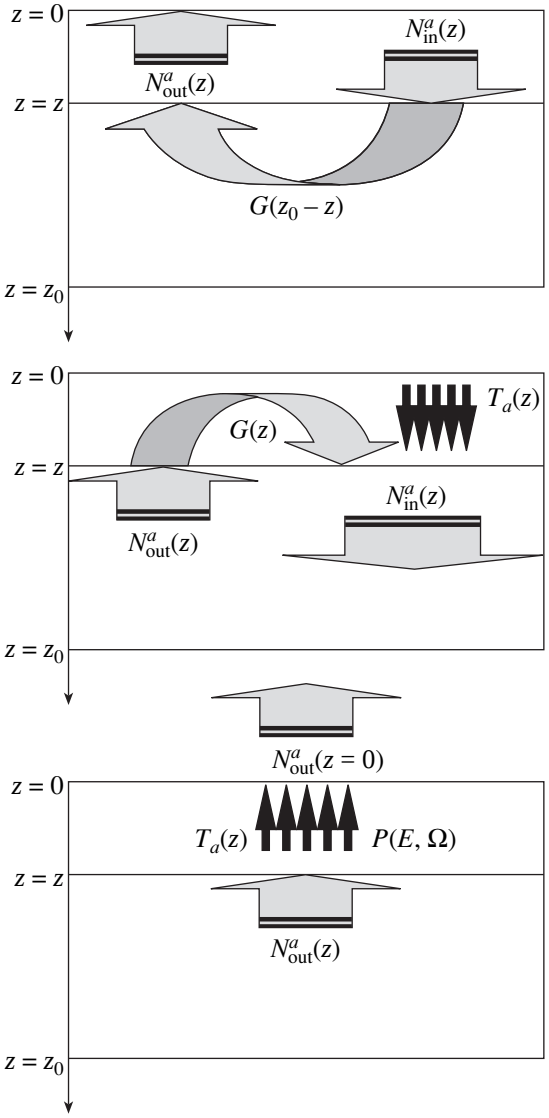

Fig. 1. Graphical interpretation of the principles of invariant embedding.

In [4], analytical procedures for determining the unknown function $G(z_0, E_0, \mu_0, \varphi_0; E, \mu, \varphi)$ from the transfer equation with the use of the invariance principles are presented. In this case, we apply the method suggested by Ambartsumyan [1] for the problem of light scattering and elaborated upon by Afanas'ev [3] for the problems of scattering of charged particles. This phenomenological method is applied for the reason that it is more demonstrative and provides the same results as the method in [4].

Let us thicken the layer of the bombarded target by attaching (from above) a layer of thickness dz such that,

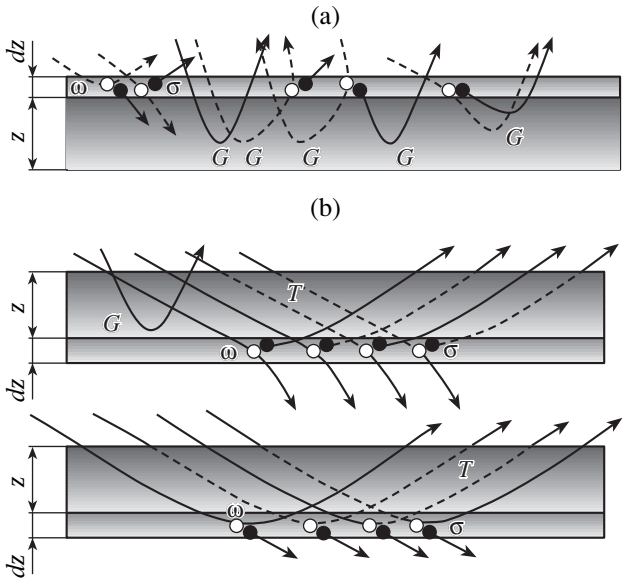

Fig. 2. Schematic representation of the processes that bring about the variation of the self-sputtering function when attaching a *dz*-thick layer from above (a) and from below (b).

within this layer, a moving particle collides with at most one atom at rest (we assume that only binary collisions occur and that moving particles do not interact). Then, the auxiliary function of self-sputtering $G(\ldots)$ is changed by the value determined by the processes presented in Fig. 2, where the white circle and symbol ω correspond to particle scattering and the black circle and symbol σ correspond to atom knocking-out.

Assume that the change $G(z + dz, E_0, \mu_0, \varphi_0; E, \mu, \varphi) - G(z, E_0, \mu_0, \varphi_0; E, \mu, \varphi)$ of the auxiliary function of self-sputtering is proportional to *dz*. Then, this function may be represented by the (symbolic) mathematical expression that describes the processes shown in Fig. 2a,

$$\frac{G(z+dz)-G(z)}{ndz} = -\left(\frac{\Sigma(E_0)}{\mu_0}+\frac{\Sigma(E)}{\mu}\right)G + \omega^b + \mathbf{G}\cdot\boldsymbol{\omega} + \boldsymbol{\omega}\cdot\mathbf{G} + \mathbf{G}\cdot\boldsymbol{\omega}^{\mathbf{b}}\cdot\mathbf{G}. \quad (8)$$

In these formulas, the following notation is used: *z* is the target thickness, *n* is the concentration of atoms in the target, $\Sigma(E)$ is the total cross section of atom-by-atom elastic and inelastic scattering; $\omega(E_0, \mu_0, \varphi_0; E, \mu, \varphi)$ is the total differential cross section of elastic scattering, inelastic scattering, and atom knocking-out; and $\omega^b(E_0, \mu_0, \varphi_0; E, \mu, \varphi)$ is the total differential cross section of backward elastic scattering and backward atom knocking-out. The boldface symbols denote integral operators, e.g.,

$$\boldsymbol{\omega}\mathbf{G} = \int_E^{E_0} dE_1 \int_0^1 \frac{d\mu_1}{\mu_1} \int_0^{2\pi} d\varphi_1 \omega(E_0, \mu_0, \varphi_0; E_1, \mu_1, \varphi_1) \times G(z, E_1, \mu_1, \varphi_1; E, \mu, \varphi),$$

$$\mathbf{G}\boldsymbol{\omega}^{\mathbf{b}}\mathbf{G} = \int_E^{E_0} dE_1 \int_0^1 \frac{d\mu_1}{\mu_1} \int_0^{2\pi} d\varphi_1 \int_E^{E_0} dE_2 \quad (9)$$

$$\times \int_0^1 \frac{d\mu_2}{\mu_2} \int_0^{2\pi} d\varphi_2 G(z, E_0, \mu_0, \varphi_0; E_1, \mu_1, \varphi_1) \times \omega^b(E_1, \mu_1, \varphi_1; E_2, \mu_2, \varphi_2) G(z, E_2, \mu_2, \varphi_2; E, \mu, \varphi).$$

If the target is thickened by attaching a layer *dz* from below, then the change of the auxiliary function of self-sputtering is determined by the processes illustrated in Fig. 2b. Mathematically, this change can be written as follows:

$$\frac{G(z+dz)-G(z)}{ndz} = \exp\left(-\frac{z\Sigma(E_0)n}{\mu_0}\right)\left[\omega^b \exp\left(-\frac{z\Sigma(E)n}{\mu}\right) + \boldsymbol{\omega}^{\mathbf{b}}\mathbf{T}_{\mathbf{a}}\right] + \mathbf{T}_{\mathbf{a}}\boldsymbol{\omega}^{\mathbf{b}}\exp\left(-\frac{z\Sigma(E)n}{\mu}\right) + \mathbf{T}_{\mathbf{a}}\boldsymbol{\omega}^{\mathbf{b}}\mathbf{T}_{\mathbf{a}}. \quad (10)$$

In both cases, the target is thickened by the same value. Hence, the auxiliary function of self-sputtering is changed in an equivalent way. From these considerations, the following expression may be deduced:

$$G(z, E_0, \mu_0, \varphi_0; E, \mu, \varphi)\left(\frac{\Sigma(E_0)}{\mu_0}+\frac{\Sigma(E)}{\mu}\right) = \boldsymbol{\omega}\mathbf{G} + \mathbf{G}\boldsymbol{\omega} - \mathbf{T}_{\mathbf{a}}\boldsymbol{\omega}^{\mathbf{b}}\exp\left(-nz\frac{\Sigma(E)}{\mu}\right) + \omega^b(E_0, \mu_0, \varphi_0; E, \mu, \varphi) \times \left[1 - \exp\left(-nz\left(\frac{\Sigma(E_0)}{\mu_0}+\frac{\Sigma(E)}{\mu}\right)\right)\right] - \boldsymbol{\omega}^{\mathbf{b}}\mathbf{T}_{\mathbf{a}}\exp\left(-nz\frac{\Sigma(E_0)}{\mu_0}\right) + \mathbf{G}\boldsymbol{\omega}^{\mathbf{b}}\mathbf{G} - \mathbf{T}_{\mathbf{a}}\boldsymbol{\omega}^{\mathbf{b}}\mathbf{T}_{\mathbf{a}}. \quad (11)$$

In this equation, similar to (4), the boldface symbols denote integral operators.

Transmission function $T_a(z, E_0, \mu_0, \varphi_0; E, \mu, \varphi)$ present in Eq. (11) also requires an equation for it to be written. However, there is no need to do it here, because below, semiinfinite targets ($z \longrightarrow \infty$) are considered, for which $T_a(z \longrightarrow \infty, E_0, \mu_0, \varphi_0; E, \mu, \varphi) = 0$.

In the case of sputtering (self-sputtering) of a semiinfinite target ($z \longrightarrow \infty$), the spectra of the backward sputtered atoms are described by the following equa-

tion (within the plane geometry approximation):

$$G(E_0, \mu_0; E, \mu)\left(\frac{\Sigma(E_0)}{\mu_0} + \frac{\Sigma(E)}{\mu}\right) = \omega(E_0, \mu_0; E, \mu)$$
$$+ \int_E^{E_0} dE_1 \int_0^1 \frac{d\mu_1}{\mu_1} \omega(E_0, \mu_0; E_1, \mu_1) G(E_1, \mu_1; E, \mu)$$
$$+ \frac{1}{\mu_0} \int_E^{E_0} dE_1 \omega_{in}(E_0; E_1) G(E_1, \mu_1; E, \mu)$$
$$+ \int_E^{E_0} dE_1 \int_0^1 \frac{d\mu_1}{\mu_1} G(E_0, \mu_0; E_1, \mu_1) \omega(E_1, \mu_1; E, \mu) \quad (12)$$
$$+ \frac{1}{\mu} \int_E^{E_0} dE_1 G(E_0, \mu_0; E_1, \mu) \omega_{in}(E_1; E)$$
$$+ \int_E^{E_0} dE_1 \int_0^1 \frac{d\mu_1}{\mu_1} \int_E^{E_0} dE_2 \int_0^1 \frac{d\mu_2}{\mu_2} G(E_0, \mu_0; E_1, \mu_1)$$
$$\times \omega(E_1, \mu_1; E_2, \mu_2) G(E_2, \mu_2; E, \mu).$$

From here on, notation $G(E_0, \mu_0; E, \mu)$ is used for function $G(z \longrightarrow \infty, E_0, \mu_0, \varphi_0; E, \mu, \varphi)$ and $S(E_0, \mu_0; E, \mu)$, for function $S(z \longrightarrow \infty, E_0, \mu_0, \varphi_0; E, \mu, \varphi)$ (within the plane geometry approximation, argument φ vanishes).

In this equation, it is assumed that interaction goes on via two independent channels, namely, an elastic one and an inelastic channel described by elastic, ω, and inelastic, ω_{in}, interaction cross sections, respectively. The total differential cross section of elastic scattering and atom knocking-out (the elastic component $\boldsymbol{\omega}$) and the total differential cross section of backward elastic scattering and backward atom knocking-out $\boldsymbol{\omega}^{\mathbf{b}}$ are determined by the same elastic interaction cross section $\omega(E_0, \mu_0; E, \mu)$.

Since the elastic interaction cross section includes elastic scattering cross section ω_{sc} and cross section ω_r of atom elastic knocking-out, it can be written in the form

$$\omega(E_0, \mu_0; E, \mu) = [\omega_{sc}(E_0, \mu_0; E, \mu) + \omega_r(E_0, \mu_0; E, \mu)] \times \delta\left(\cos(\theta - \theta_0) - \sqrt{\frac{E}{E_0}}\right). \quad (13)$$

It should be noted that, up to notation, equations describing the auxiliary function of self-sputtering $G(\ldots)$ coincide with those describing the spectra of the particles reflected from and passed through the material layers [8]. Therefore, the earlier developed [9] methods for solving such equations may be used.

So far, there seems to be no way of solving Eq. (12) in the general form. However, in some approximations, solutions may be obtained that adequately describe the mechanism of self-sputtering.

It is known from sputtering experiments [10] that most of the knocked out atoms escape from the target surface with low energies. Taking due account of this fact and restricting our consideration to the low-energy region, we seek solutions to Eq. (12) through the scattering cross section of hard spheres for describing the atom elastic interaction. In this case, the elastic scattering cross section and cross section of atom elastic knocking-out are described by the same expression,

$$\omega_{sc}(E_0, \mu_0; E, \mu) = \omega_r(E_0, \mu_0; E, \mu) = \frac{d\sigma}{dE} = \frac{\Sigma_{el}}{E_0}. \quad (14)$$

Herein, the total cross section Σ_{el} of the elastic scattering is independent of energy. The inelastic interaction cross section is also assumed to be independent of the initial energy and may be represented in the form

$$\omega_{in}(E_0, E) = \Sigma_{in} \omega_{in}(E_0 - E). \quad (15)$$

With due regard for the foregoing, Eq. (12) can be simplified as follows:

$$G(E_0, \mu_0; E, \mu)\left(\frac{1}{\mu_0} + \frac{1}{\mu}\right)(\Sigma_{el} + \Sigma_{in})$$
$$= \frac{2\Sigma_{el}}{E_0} \delta\left(\cos(\theta - \theta_0) - \sqrt{\frac{E}{E_0}}\right) + \int_E^{E_0} dE_1 \int_0^1 \frac{d\mu_1}{\mu_1} \frac{2\Sigma_{el}}{E_0}$$
$$\times \delta\left(\cos(\theta_1 - \theta_0) - \sqrt{\frac{E_1}{E_0}}\right) G(E_1, \mu_1; E, \mu) + \int_E^{E_0} dE_1$$
$$\times \int_0^1 \frac{d\mu_1}{\mu_1} G(E_0, \mu_0; E_1, \mu_1) \frac{2\Sigma_{el}}{E_1} \delta\left(\cos(\theta - \theta_1) - \sqrt{\frac{E}{E_1}}\right) \quad (16)$$
$$+ \frac{\Sigma_{in}}{\mu_0} \int_E^{E_0} dE_1 \omega_{in}(E_0 - E_1) G(E_1, \mu_0; E, \mu)$$
$$+ \frac{\Sigma_{in}}{\mu} \int_E^{E_0} dE_1 G(E_0, \mu_0; E_1, \mu) \omega_{in}(E_1 - E)$$
$$+ \int_E^{E_0} dE_1 \int_0^1 \frac{d\mu_1}{\mu_1} \int_E^{E_0} dE_2 \int_0^1 \frac{d\mu_2}{\mu_2} G(E_0, \mu_0; E_1, \mu_1)$$
$$\times \frac{2\Sigma_{el}}{E_1} \delta\left(\cos(\theta_2 - \theta_1) - \sqrt{\frac{E_2}{E_1}}\right) G(E_2, \mu_2; E, \mu).$$

We seek the auxiliary function of self-sputtering in the form

$$E_0 G(E_0, \mu_0; E, \mu) = \frac{\mu_0 \mu}{\mu_0 + \mu} G_u(u, \mu_0, \mu), \qquad (17)$$

where a new variable $u = \ln(E_0/E)$ is introduced. Then, the equation for function G_u takes the form

$$\begin{aligned} G_u(u, \mu_0, \mu)(1+\lambda) &= 2\delta\left(\cos(\theta-\theta_0) - \exp\left(-\frac{u}{2}\right)\right) \\ &+ 2\mu\int_0^u du_1 \int_0^1 \frac{d\mu_1}{\mu_1+\mu}\delta\left(\cos(\theta_1-\theta_0) - \exp\left(-\frac{u_1}{2}\right)\right) \\ &\times G_u(u-u_1, \mu_1, \mu) + 2\mu_0\int_0^u du_1 \int_0^1 \frac{d\mu_1}{\mu_1+\mu_0} \\ &\times G_u(u_1, \mu_0, \mu_1)\delta\left(\cos(\theta-\theta_1) - \exp\left(-\frac{u-u_1}{2}\right)\right) \\ &+ \frac{\lambda\mu}{\mu_0+\mu}\int_0^u du_1 \omega_{\text{in}}(u_1) G_u(u-u_1, \mu_0, \mu) \\ &+ \frac{\lambda\mu_0}{\mu_0+\mu}\int_0^u du_1 G_u(u_1, \mu_0, \mu)\omega_{\text{in}}(u-u_1) \\ &+ 2\mu_0\mu\int_0^u du_1 \int_0^1 \frac{d\mu_1}{\mu_1+\mu_0}\int_0^u du_2 \int_0^1 \frac{d\mu_2}{\mu_2+\mu} G_u(u_1, \mu_0, \mu_1) \\ &\times \delta\left(\cos(\theta_2-\theta_1) - \exp\left(-\frac{u_2-u_1}{2}\right)\right) G_u(u-u_2, \mu_2, \mu), \end{aligned} \qquad (18)$$

where $\lambda = \Sigma_{\text{in}}/\Sigma_{\text{el}}$ and $\omega_{\text{in}}(u) = E_0\omega_{\text{in}}(E_0 - E)$.

Now, take into account that, when particles with equal masses collide (under consideration is the phenomenon of self-sputtering), the scattering angles of both the knocked out particle and the sputtered one cannot exceed $\pi/2$, and that the self-sputtering function is defined within the angle range $0 \le \mu_0 \le 1$, $0 \le |\mu| \le 1$. Expand the functions in Jacobi polynomials $\psi_n(x)$ [11] orthogonal on the interval (0, 1),

$$G_u(u, \mu_0, \mu) = \sum_{n=0}^{\infty} g_u(u)\psi_n(\mu_0)\psi_n(\mu), \qquad (19)$$

$$\begin{aligned} &\delta\left(\cos(\theta-\theta_0) - \exp\left(-\frac{u}{2}\right)\right) \\ &= \sum_{n=0}^{\infty}(2n+1)\psi_n\left(\exp\left(-\frac{u}{2}\right)\right)\psi_n(\mu_0)\psi_n(\mu). \end{aligned} \qquad (20)$$

Such expansions are possible, since Jacobi polynomials are a particular case of matrix elements in representations of the group of second-order unitary matrices [12]. Substitute these expansions into Eq. (18). Within the "multiple change of the normal" approximation [9],

$$\frac{1}{\mu+\mu_1} \approx \frac{1}{2\mu}, \qquad (21)$$

integration with respect to variable μ_1 is easily performed with due regard for the orthogonality of the Jacobi polynomials,

$$\int_0^1 \psi_n(x)\psi_m(x)dx = \delta_{n,m}\frac{1}{2n+1} \qquad (22)$$

(here, $\delta_{n,m}$ is the Kronecker delta).

As a result, the equation for the coefficients of the expansion in the polynomials can be written as

$$\begin{aligned} g_n(u)(1+\lambda) &= 2(2n+1)\psi_n\left(\exp\left(-\frac{u}{2}\right)\right) \\ &+ 2\int_0^u du_1 g_n(u_1)\psi_n\left(\exp\left(-\frac{u-u_1}{2}\right)\right) \\ &+ \lambda\int_0^u du_1 \omega_{\text{in}}(u_1) g_n(u-u_1) + \frac{1}{2(2n+1)} \\ &\times \int_0^u\int_0^u du_1 du_2 g_n(u_1)\psi_n\left(\exp\left(-\frac{u_2-u_1}{2}\right)\right) g_n(u-u_2). \end{aligned} \qquad (23)$$

In this equation, it is taken into account that the convolution of two functions satisfies the relation

$$\int_0^x f_1(x-t) f_2(t)dt \equiv \int_0^x f_2(x-t) f_1(t)dt. \qquad (24)$$

Applying the Laplace transform with respect to variable u defined as

$$g_n(p) = \int_0^{\infty} g_n(u)\exp(-pu)du \qquad (25)$$

to integral equation (23), we obtain the following algebraic equation for the images of the expansion coefficients:

$$\begin{aligned} g_n(p)(1+\lambda W(p)) &= 2(2n+1)\psi_n(p) \\ &+ 2g_n(p)\psi_n(p) + \frac{1}{2(2n+1)} g_n(p)\psi_n(p)g_n(p). \end{aligned} \qquad (26)$$

Here, $\psi_n(x)$ and $W(p)$ are the images defined by the formulas

$$\psi_n(p) = \int_0^\infty \psi_n\left(\exp\left(-\frac{u}{2}\right)\right)\exp(-pu)du, \quad (27)$$

$$W(p) = \int_0^\infty \omega_{in}(u)(1-\exp(-pu))du. \quad (28)$$

The concrete form of image $W(p)$ depends on the form of function $\omega_{in}(u)$. Function $\psi_n(x)$ can be defined as follows:

$$\begin{aligned}\psi_0(p) &= \frac{1}{p},\\ \psi_1(p) &= \frac{1}{p}-\frac{4}{2p+1},\\ \psi_{n+1}(p) &= \frac{1+2n}{1+n}(\psi_n(p)-2\psi_n(p+1/2))\\ &\quad -\frac{n}{1+n}\psi_{n-1}(p), \quad n>1.\end{aligned} \quad (29)$$

Quadratic equation (26) has only one meaningful root,

$$g_n(p) = (2n+1)\left\{\left[\frac{1+\lambda W(p)}{\psi_n(p)}-2\right] - \sqrt{\left[\frac{1+\lambda W(p)}{\psi_n(p)}-2\right]^2-4}\right\}. \quad (30)$$

The original for the expansion coefficients can be found by the Efros theorem [13],

$$g_n(u) = \int_0^\infty \frac{2}{x} I_1(2x)\exp(2x) f_n(u,x)dx. \quad (31)$$

Here, $I_1(x)$ is the modified first-order Bessel function [14] and $f_n(u, x)$ is the original for the image

$$F_n(p) = \exp\left(-x\frac{1+\lambda W(p)}{\psi_n(p)}\right). \quad (32)$$

In view of this solution, the desired function $G(E_0, \mu_0; E, \mu)$ can be written in the form

$$G(E_0,\mu_0;E,\mu) = \frac{1}{E_0}\frac{\mu\mu_0}{\mu_0+\mu}\sum_{n=0}^\infty (2n+1)\psi_n(\mu_0)\psi_n(\mu) \times \int_0^\infty \frac{2}{x} I_1(2x)\exp(2x) f_n\left(\ln\left(\frac{E_0}{E}\right), x\right)dx. \quad (33)$$

By definition (6) of the self-sputtering function, which describes the energy and angular spectra of the sputtered atoms that have surmounted the surface barrier, we obtain

$$S(E_0,\mu_0;E,\mu) = \frac{E}{E_0}\frac{\mu\mu_0}{\mu_0+\mu^*}\frac{\mu}{\sqrt{(\mu^2E+U)(E+U)}} \times \sum_{n=0}^\infty (2n+1)\psi_n(\mu_0)\psi_n(\mu^*) \times \int_0^\infty \frac{2}{x} I_1(2x)\exp(2x) f_n\left(\ln\left(\frac{E_0}{E+U}\right), x\right)dx, \quad (34)$$

$$\mu^* = \sqrt{\frac{\mu^2E+U}{E+U}}.$$

At the present time, the original for image (32) in the general form has not been found. In the case of no inelastic energy losses $\lambda \longrightarrow 0$, the approximate solution for the energy spectrum has the form

$$S(E_0,\mu_0;E) \approx \frac{\mu_0}{\mu_0+c}\frac{E_0EI_1\left(2\ln\left(\frac{E_0}{E+U}\right)\right)}{(E+U)^3\ln\left(\frac{E_0}{E+U}\right)}. \quad (35)$$

Here, c is an approximating constant, which has been taken to be equal to $c = E/(E + U)$ in the calculations. Based on Eq. (12) and assuming that the sputtered and knocked-out atoms can move only within the semisphere around the direction of motion of the primary particle, we can suppose that the contribution of the last term is negligible. Throwing away the last term in Eq. (12), we reduce the nonlinear integral equation to a linear equation. It is demonstrated in papers [3, 15] that such a linearization yields reasonably good results.

Solving linearized equation (12), we obtain the following expression for expansion coefficients $g_n(p)$:

$$g_n(p) = 2(2n+1)\left[\frac{1+\lambda W(p)}{\psi_n(p)}-2\right]^{-1}. \quad (36)$$

By the Efros theorem, the solution for the auxiliary function of self-sputtering $G(E_0, \mu_0; E, \mu)$ can be presented in the form

$$G(E_0,\mu_0;E,\mu) = \frac{2}{E_0}\frac{\mu\mu_0}{\mu_0+\mu}\sum_{n=0}^\infty (2n+1)\psi_n(\mu_0)\psi_n(\mu) \times \int_0^\infty \exp(2x) f_n\left(\ln\left(\frac{E_0}{E}\right), x\right)dx, \quad (37)$$

where $f_n(u, x)$ is the original for image (32).

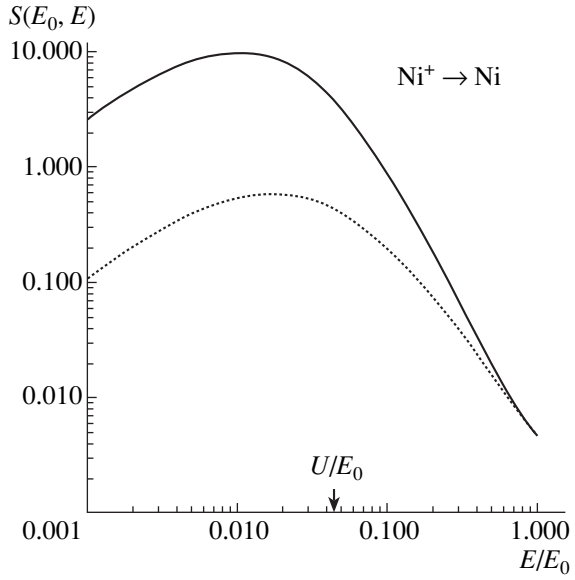

Fig. 3. Dependence of the energy spectrum of sputtered atoms of nickel bombarded by nickel ions with energy 100 eV (normal incidence). Calculation by formula (35) (the solid line) and by formula (39) (the dotted line).

Herein, the energy and angular spectra of the atom sputtering are determined by the expression

$$S(E_0, \mu_0; E, \mu) = \frac{E}{E_0}\frac{\mu\mu_0}{\mu_0 + \mu^*}\frac{\mu}{\sqrt{(\mu^2 E + U)(E + U)}} \times \sum_{n=0}^{\infty}(2n+1)\psi_n(\mu_0)\psi_n(\mu^*) \times \int_0^{\infty}\exp(2x) f_n\left(\ln\left(\frac{E_0}{E+U}\right), x\right)dx, \quad (38)$$

where μ^* is the same as in formula (34).

From analysis of expressions (34) and (38), conclusion can be drawn that the angular spectra of the sputtered atoms are basically nonisotropic. However, under certain conditions, the angular spectrum of the sputtered atoms is little different from the isotropic spectrum.

Neglecting the inelastic energy losses, we find a solution for the energy spectrum similar to those obtained from the transfer equation,

$$S(E_0, \mu_0; E) \approx \frac{\mu_0}{\mu_0 + c}\left(\frac{E_0 E}{(E+U)^3} - \frac{0.047 E\psi_1(\mu_0)}{E_0^2}\left(\frac{E_0}{E+U}\right)^{1.35}\right). \quad (39)$$

Calculations by formulas (35) and (39) are given in Fig. 3. When comparing the calculation results, several facts should be noted: (1) energy spectra have a maximum; (2) the spectra coincide in the high-energy region; and (3) in the low-energy region, the spectrum calculated by formula (35) is above the spectrum calculated by formula (39) and has a maximum at lower energies.

The differences in the spectra are explained by the fact that solution (35) accounts for the atoms that are redirected (change the normal) several times. Since the angles of sputtering and knocking-out cannot exceed 90°, only a small fraction of atoms can change their normal. But herewith, they lose almost all their energy. Inclusion of such atoms in spectrum (35) is responsible for shifting the distribution maximum and increasing it in the low-energy region.

The approximate solutions given above ignore the inelastic energy losses by particles which, being considered, would result both in decreasing the flux of the sputtered atoms and in changing the spectrum shape [16]. However, as soon as low-energy heavy particles are considered, the inelastic energy losses are negligible [17] and may be disregarded.

Solutions (33) and (37) look rather simple, though, when calculating by these formulas, computation of the inverse Laplace transform of function $F_n(p)$ presents some difficulties. With the use of expansion of $g_n(p)$ in powers of $1/(1 + \lambda W(p))$, function $G(E_0, \mu_0; E, \mu)$ can be written in another form, which is computationally easier [8]; namely,

$$G(E_0, \mu_0; E, \mu) = \frac{1}{E_0}\frac{\mu\mu_0}{\mu_0 + \mu}\int_0^{\infty}\int_0^{u} T_{\text{in}}(x, u-\varepsilon)A(x, \varepsilon, \mu_0, \mu)dx d\varepsilon. \quad (40)$$

Here, $T_{in}(x, u)$ is the inelastic atom transmission function defined as

$$T_{\text{in}}(x, u) = \frac{1}{2\pi i}\int_{-i\infty}^{+i\infty}\exp(-x\lambda W(p))\exp(pu)dp, \quad (41)$$

and $A(x, u, \mu_0, \mu)$ is the distribution of atoms over elastic paths x, which is the original for the image

$$A(x, p, \mu_0, \mu) = \exp(-x)\sum_{n=0}^{\infty}\sum_{k=1}^{\infty}\rho_{n,k}(p)\frac{x^{k-1}}{(k-1)!}\psi_n(\mu_0)\psi_n(\mu). \quad (42)$$

Coefficients in the nonlinear equation are determined iteratively:

$$\rho_{n,1}(p) = 2(2n+1)\psi_n(p), \quad \rho_{n,2}(p) = 2\rho_{n,1}(p)\psi_n(p), \quad \rho_{n,k}(p) = 2\rho_{n,k-1}(p)\psi_n(p) \quad (43)$$

$$+\frac{\psi_n(p)}{2(2n+1)}\sum_{i=1}^{k-2}\rho_{n,i}\rho_{n,k-1-i},\quad k\geq 3.$$

For the linearized equation, these coefficients can be found in a simpler way:

$$\rho_{n,1}(p) = 2(2n+1)\psi_n(p),$$

$$\rho_{n,k}(p) = 2\rho_{n,k-1}(p)\psi_n(p) = (2n+1)2^k\psi_n(p)^k, \quad k\geq 2. \tag{44}$$

Note that solution (40) results from the additivity of the cross sections of particle elastic and inelastic interactions.

CONCLUSIONS

A rough approximation notwithstanding, the shape of the energy spectrum of the sputtered atoms that agrees well with the physical meaning of the phenomenon is found. Moreover, the energy spectrum of the sputtered atoms is demonstrated to be essentially different from E^{-2} in the low-energy region (of the order of the surface atom binding energy). More accurate solutions to the obtained equations require computing machinery and are certainly not as demonstrative as the pure analytical solution.

The results of this paper demonstrate that the principles of invariant embedding may be applied to describing the phenomenon of sputtering. New interesting results can be obtained along this line.

REFERENCES

1. V. A. Ambartsumyan, Zh. Éksp. Teor. Fiz. **13**, 323 (1943).
2. R. V. Dashen, Phys. Rev. A **134**, 1025 (1964).
3. V. P. Afanas'ev and A. V. Lubenchenko, Poverkhnost, No. 9, 12 (1997).
4. S. Chandrasekar, *Radiative Transfer* (Oxford Univ. Press, Oxford, 1950; Inostrannaya Literatura, Moscow, 1956).
5. V. S. Remizovich and V. V. Marinyuk, in *Proceedings of the 14th International Conference on Ion–Surface Interaction, Moscow, 1999*, Vol. 1, p. 384.
6. G. Falcone, Radiat. Eff. **1**, 147 (1987).
7. R. Kelly, Nucl. Instrum. Methods **18**, 388 (1987).
8. V. P. Afanas'ev and A. V. Lubenchenko, Surf. Invest. **14**, 821 (1999).
9. A. V. Lubenchenko, Poverkhnost, No. 4, 22 (2003).
10. *Sputtering by Particle Bombardment*, Ed. by R. Behrisch (Springer-Verlag, New York, 1981; Mir, Moscow, 1984).
11. G. A. Korn and T. M. Korn, *Mathematical Handbook for Scientists and Engineers* (McGraw-Hill, New York, 1968; Nauka, Moscow, 1984).
12. N. Ya. Vilenkin, *Special Functions and the Theory of Group Representation* (Nauka, Moscow, 1965; American Mathematical Society, Providence, 1968).
13. M. A. Lavrent'ev and B. V. Shabat, *Methods of the Theory of Functions of Complex Variable* (Nauka, Moscow, 1965) [in Russian].
14. A. F. Nikiforov and V. B. Uvarov, *Special Functions of Mathematical Physics: A Unified Introduction with Applications* (Nauka, Moscow, 1978; Birkhauser, Basel, 1987).
15. V. P. Afanas'ev and D. Naueks, Z. Phys. B: Condens. Matter **83**, 65 (1991).
16. V. V. Marinyuk and V. S. Remizovich, Zh. Tekh. Fiz. **71** (10), 29 (2001) [Tech. Phys. **46**, 1235 (2001)].
17. M. A. Kumakhov and F. F. Komarov, *Energy Losses and Ion Ranges in Solids* (Belorus. Gos. Univ., Minsk, 1978) [in Russian].

Translated by A. Pankrat'ev

Technical Physics, Vol. 50, No. 4, 2005, pp. 402–407. Translated from Zhurnal Tekhnicheskoĭ Fiziki, Vol. 75, No. 4, 2005, pp. 19–24.

ATOMS, SPECTRA, RADIATION

Ionization of Nitrogen, Oxygen, Water, and Carbon Dioxide Molecules by Near-Threshold Electron Impact

A. N. Zavilopulo, F. F. Chipev, and O. B. Shpenik

Institute of Electron Physics, National Academy of Sciences of Ukraine, Uzhgorod, 88017 Ukraine

e-mail: an@zvl.iep.uzhgorod.ua

Received March 31, 2004

Abstract—An experimental technique for measuring the cross sections of direct and dissociative ionization of N_2, O_2, H_2O, and CO_2 molecules by electron impact in the near-threshold energy range is described. The setup used in the experiments allows mass separation of ions with a monopole mass spectrometer. It is shown that such a setup can be used to advantage in separation experiments. For incident electron energies between 7 and 35 eV, the energy dependences of the cross sections of generation of parent ions and ion fragments due to parent molecule dissociation are obtained. © *2005 Pleiades Publishing, Inc.*

INTRODUCTION

Experimental investigation of dissociation products due to single ionization of molecules by electron impact in the near-threshold energy range is an undeniably topical problem. It suffices to note that the NIST standard atomic and molecular constant database [1] gives more than 20 values of the direct ionization potential for the parent CO_2 molecule and the energy of appearance (E_{ap}) of ion fragments. The dissociation process is of great significance, since the resulting ionic and neutral fragments possess an appreciable kinetic energy [2]. Dissociative ionization may contribute significantly to the plasma energy balance, which should be taken into account in relevant simulation.

Study of near-threshold single and dissociative ionization of polyatomic molecules helps to uncover the role of initial energy dissipation in electron–molecule interaction. It is in the near-threshold range that many features of molecular and atomic structures are highlighted and their influence on the energy dependence of the process becomes obvious. In our laboratory, investigation of electron-impact single and dissociative ionization of complex organic [3] and halogen-containing [4] molecules, deuterated molecules [5], and molecules of atmospheric gases [6, 7], as well as the energy threshold of appearing ionization products, is under way.

In this work, we for the first time study the single and dissociative ionization cross sections versus the incident electron energy for N_2, O_2, H_2O, and CO_2 molecules by means of a commercial monopole mass spectrometer. The emphasis was on measuring and carefully analyzing the dissociative ionization thresholds for parent molecules and daughter ion fragments.

EXPERIMENTAL

In the experiments, residual gases were removed using oil-free pumping. As an analytical instrument, we used an MX-7304A monopole mass spectrometer [8] (a single-pole version of the quadrupole mass spectrometer), which refers to the class of dynamic instruments and is, in essence, a band-pass mass filter. Ions passed through the mass filter are detected by the measuring system. The instrument is also configured with a system for digital indication of the mass number and intensity. The manual, cyclic, and software-programmable modes of mass spectra sweeping are provided. The sensitivity can be controlled by switching the mass range, varying the electron emission current, or gradually varying the supply voltage of the secondary electron multiplier (SEM). At high currents, the valid signal is picked up from the collector (a Faraday cup). In this case, SEM-induced discrimination in mass is excluded. Weak signals were detected in the computer-controlled counting mode. The basic parameters of the instrument are given in [8]: the resolution at a level of 10% of the spectrum line height is 1 M or higher; the threshold sensitivity in argon, 7.5×10^{-12} Pa; and the limiting rms deviation of the mass value detected in the range 1–200, 2%.

Owing to the parameters listed, as well as computer control, the instrument makes it possible to reliably detect both mass spectra and electron-impact-induced atom and molecule ionization cross sections in the energy range from the ionization threshold to 100 eV. The parameters of the mass spectrometer were computer-adjusted by means of the interface card using a special application program. Finally, the instrument may operate independently under the control of the built-in one-chip microcomputer.

Consider now the experimental technique in greater detail. The molecular beams under study were gener-

1063-7842/05/5004-0402$26.00

ated by a multichannel effusion-type source that provides a molecule concentration in the region of interaction with the electron beam on the order of 10^{10}–10^{11} cm^{-3}. The material (or a mixture of materials) to be studied enters the source through the doser of a specially tailored gas-supply system. This system consists of a tank with independent evacuation facilities, an SNA-2 precision two-channel gas-supply unit, and strain and reference vacuum gages. The gas pressure in the source can be intelligently maintained at a desired level via feedback from the output of the direct current amplifier of the mass spectrometer or from the gage.

The molecules under study are ionized in the ion source by electron bombardment. In the electron current stabilization mode, the source generates controlled-energy electron beams with energies of 5–90 eV and currents of 0.5–1.5 mA. The nonuniformity in energy (FWHM) is ΔE = 500 meV. The ions extracted from the space of interaction between the electron and neutral beams are applied to the input of the ion–optical system (mass filter). The ions are analyzed in real time and detected by the recording system, which operates in the analog and ion-count modes. The ion current can be measured at both the input and output of the mass spectrometer, which makes it possible to determine the "productivity" of the mass filter for each type of the ions.

The performance of the mass spectrometer is qualitatively evaluated in the way illustrated in Fig. 1. The CO_2 mass spectrum presented here results after automatically subtracting the background due to residual gases. As is seen from Fig. 1, the beam contains the parent ion CO_2^+ along with fragments (daughter ions) due to dissociative ionization, such as C^+, O^+, and CO^+. Other background ions with masses M = 22, 29, 45, and 46 are of low intensity (no higher than 1% of the basic CO_2^+ ion intensity), which indicates the high purity of the gas. Note that, at such an electron energy, the molecular ion O_2^+ is absent in the spectrum (Fig. 1), as well as in the NIST database [1].

Since our primary goal was to determine the threshold behavior of the ionization functions, as well as to exactly measure the energy of appearance of the daughter ions (see Fig. 1), calibration of the electron energy scale was given special attention. This procedure remains a biggest bugaboo in both present-day mass spectroscopy and the physics of electron–electron collisions. It should be noted that ambiguity in the ionizing electron energy is due to the contact potential difference between the electron gun and ion extraction and focusing system, superposition of the electrostatic fields, and other instrument-related effects. Thus, the accuracy of determining the potentials of ionization and potentials of appearance of fragments depends on the accuracy with which the primary electron energy is reduced to the absolute energy scale. We solved this problem by relating the initial portions of the measured energy dependences of the ion yield (ionization functions) to the ionization potentials that are known with a high reliability [1]. We took argon and krypton as calibration gases and measured the early portions of the electron-impact ionization function. The validity of such a technique can be judged from the control experiment on taking the initial portion of the energy dependence of the krypton atom ionization cross section (this experiment was similar to that performed in [6]) and from good agreement with the results obtained in [9]. The electron energy resolution was high, ΔE = 0.05 eV. The experiments on taking the initial portions of the energy dependences of the argon and krypton atom ionization cross sections allowed us to calibrate the electron energy scale with an accuracy of ±0.25 eV. The calibration procedure was repeated several-fold (four to five times) during each measurement cycle. Eventually, the energy scale was determined with an accuracy comparable to the FWHM of the electron energy distribution in the beam. As was noted above, the total mass spectrum was taken for each of the gases under study, which made it possible to evaluate the relative yield of ions of different mass and to judge the grade of the material.

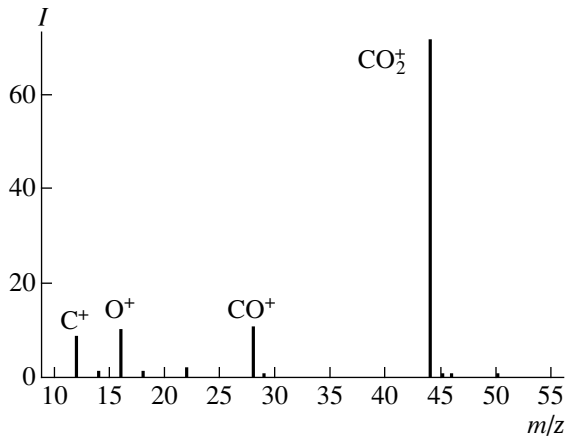

Fig. 1. Carbon dioxide molecule mass spectrum for ionizing electron energy E = 70 eV.

Another challenge in the experiments on dissociative ionization was to estimate the efficiency of extraction (collection) of the ions from the region of interaction. This is especially true for absolute measurements. For the efficiency to be measured correctly, it is necessary that the source design provide the equipotentiality of the region of electron–molecule interaction, the analyzer be equally "transparent" for ions with different mass numbers, and ion discrimination at ion-to-electron conversion in the SEM be minimized (i.e., a high-voltage converter or special SEMs be used).

These requirements deserve special consideration, which is beyond the scope of this work.

RESULTS AND DISCUSSION

The threshold behavior of the atom ionization effective cross section was first found in a work by Wannier [10] for the hydrogen atom. Wannier considered three radial ranges: the first one covers small particle spacings (to ~a_0), where the interaction should be analyzed in terms of quantum mechanics; the second refers to particle spacings on the order of $100a_0$, where Coulomb forces come into play; and the third range, where the interaction is virtually absent. Considering in this way, Wannier put forward two important postulates. First, scattered, e_s, and removed (ejected), e_{ej}, electrons (see (2) below) move oppositely to each other and the moment of momentum of the system equals zero. Second, both electrons take away equal parts of the energy. It turned out that the energy dependence of the ionization cross section near the threshold is an exponential function (the Wannier threshold law). In [11], modified coefficients for calculating the exponent of this function were derived. These coefficients take into account the mass and charge of a target particle. The threshold behavior of molecule ionization by electron impact was discussed in [9, 12, 13]. It was shown that the exponent may vary between 1.127 (the lower bound for atoms) and 4 (for polyatomic molecules) and that the threshold behavior of the molecule ionization cross section is a superposition of several exponentials.

Two factors may shade the true threshold behavior of the ionization cross section: a dependence of the effective cross section on the energy (velocity) of interacting particles when they approach each other and the energy spread of ionizing electrons. The value of the signal measured and its near-threshold variation at electron–atom (molecule) collision has the form [12]

$$S(E) = k\int_0^\infty \sigma(E - E')f(E')dE', \qquad (1)$$

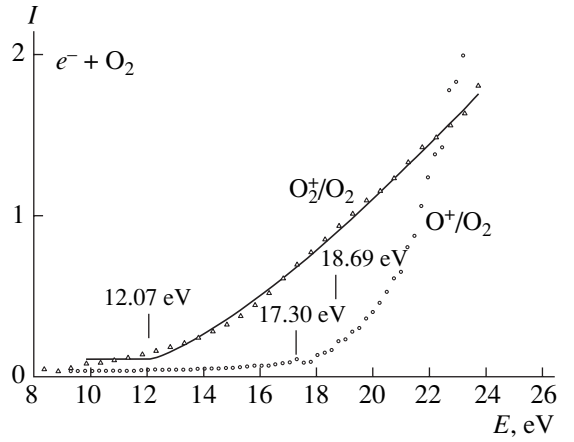

Fig. 2. Threshold portions of the cross sections of oxygen molecule direct ionization and atomic ion generation by electron-impact-induced dissociative ionization.

where k is the detection constant, E is the accelerating-electrode-specified energy of bombarding electrons, E' is the electron energy in the beam, σ is the cross section of the process, and $f(E)$ is the electron energy distribution function (which is usually the Gauss distribution). As applied to the ionization process, it is just function $f(E)$ that is largely responsible for the error in the value of the cross section and its energy dependence at near-threshold electron energies.

As the energy of ionizing electrons increases, various new processes come into play, which may variously influence the near-threshold cross section depending on their efficiency. In the case of diatomic molecules, these processes may be the following:

$$\begin{aligned}
&\text{single ionization: } M + e \longrightarrow M^+ + e_s + e_{ej};\\
&\text{dissociative ionization: } A^+ + B + e_s + e_{ej};\\
&\text{ionization with excitation: } M^{+*} + e_s + e_{ej};\\
&\text{auto-ionization: } M^{**} + e_s \longrightarrow M^+ + e_s + e_{ej}.
\end{aligned} \qquad (2)$$

Here, M is a diatomic target molecule, e is the incident (ionizing) electron, e_s is the electron scattered, and e_{ej} is the electron ejected. For the nitrogen molecule studied by us in [6], the threshold portion of the energy dependence of the ionization cross section deviates markedly from the monotonic growth in the energy interval 16.7–19.5 eV. A reason for such a deviation seems to be the auto-ionization of the vibrational levels of the molecular ion N_2^+, most probably, the levels $A^2\Pi_u$ (E = 16.70 eV) and $B^2\Sigma_u^+$ (E = 18.75 eV) of the N_2^+ ion [14].

Figures 2–4 show the initial portions of the single ionization cross sections for the molecules that are the most abundant in the terrestrial atmosphere and of the cross sections of their fragmentation due to electron-impact-induced dissociative ionization (the symbols are data points; continuous lines, calculation by formulas (3) given below). The threshold behavior of the ion fragment production cross section is seen to depend on the bonding energy and type in the parent molecule (see table). The number of atoms in the molecule has the most significant effect on the threshold behavior: for the diatomic molecule (Fig. 2), the post-threshold increase is sharp (see table); for the three-atomic molecules (Figs. 3, 4), the increase is smooth.

To exactly determine the ionization potentials for molecules (atoms) and the fragmentation potentials (the potentials of fragment appearance due to dissociative ionization), we used the method elaborated by Märk *et al.* [9, 13].

According to this method, the experimental dependence of ionization cross section σ on ionizing electron energy E is fitted to some functional dependence $F(E)$

that has the form

$$F(E) = \begin{cases} b & \text{for} \quad E < E_{ap} \\ b + c(E - E_{ap})^p & \text{for} \quad E > E_{ap}. \end{cases} \tag{3}$$

It is seen from Fig. 3 that the fitting involves four parameters: background signal b (the absence of ions at the output of the mass spectrometer); the energy of appearance of an ion fragment, E_{ap}; proportionality coefficient c; and exponent p in the Wannier threshold law [10] for single ionization of atoms. The fitting algorithm is implemented with a special computer program that makes it possible to obtain the four parameters with a large number of iterations with regard for their standard deviations.

In the calculations, the instrument electron energy distribution function was taken to be a free parameter that can be approximated (see (1)) by the Gaussian distribution that is centered at desired point E_{ap} and has a FWHM of ΔE. Then, fitted function $F(E)$ is a convolution with electron energy distribution, i.e., has the form

$$P(E) = \int_{-\infty}^{+\infty} e^{-\frac{(E - E_{ap})^2}{2\Delta E}} [b + c(E - E_{ap})^p] dE. \tag{4}$$

This procedure also gives information about the real electron energy spread.

The table lists the threshold values of ionization potentials that were determined with the fitting algorithm mentioned above versus data published earlier [1, 9, 15]. Let us analyze the data presented in the table and Figs. 2–4 more carefully. The difference in the threshold behavior of the cross section of fragmentation due to dissociative ionization (see (2)) is noteworthy. In the case of a diatomic oxygen molecule (Fig. 2), the cross section of O^+ ion yield increases more rapidly than the ionization cross section for the O_2 parent molecule. Possibly, such behavior is explained by the fact that the other fragment may be either a neutral atom or a negatively charged ion,

$$\begin{aligned} e + O_2 \longrightarrow\ & O^+ + O + 2e \quad (E_{ap} = 18.69 \text{ eV}), \\ & O^+ + O^- + e \quad (E_{ap} = 17.25 \text{ eV}). \end{aligned} \tag{5}$$

Hereafter (see also (6) and (7)), the parenthesized quantity is the energy of appearance of dissociative ionization fragments [1] that was determined with a highest accuracy. The energy dependence of the O^+ ion generation cross section (Fig. 2) becomes nonmonotonic in the interval E = 17.25–18.69 eV, which suggests that dissociative ionization is a complex process. An increase in the extent of monochromatism of electrons would shed more light on the threshold behavior.

The energy dependence of the cross section of fragmentation due to dissociative ionization was also measured for water and carbon dioxide molecules (Figs. 3, 4). The associated curves are seen to behave in a radically different manner. A possible reason for such a difference is various channels involved in the dissociation process:

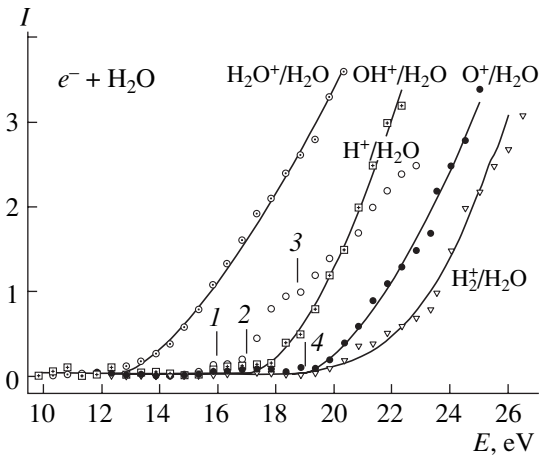

Fig. 3. Threshold portions of the relative cross sections of water molecule direct ionization and ion generation by electron-impact-induced dissociative ionization: (*1*) H^+, E_{ap} = 16.00 eV; (*2*) H^+, E_{ap} = 16.95 eV; (*3*) H^+, E_{ap} = 18.70 eV; and (*4*) O^+, E_{ap} = 19.00 eV.

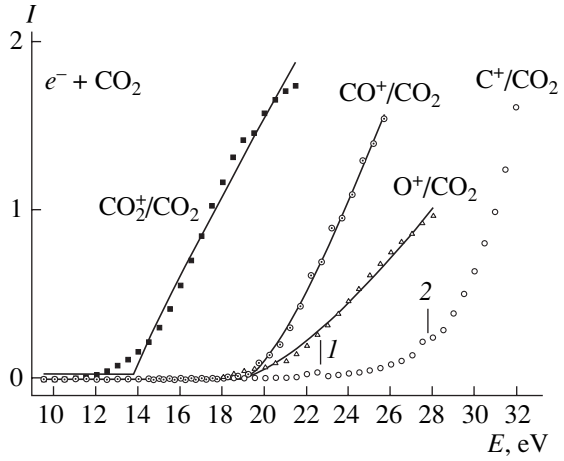

Fig. 4. Threshold portions of the relative cross sections of carbon dioxide molecule direct ionization and ion generation by electron-impact-induced dissociative ionization: (*1*) C^+, E_{ap} = 22.70 eV and (*2*) C^+, E_{ap} = 27.80 eV.

$$\begin{aligned} e + H_2O \longrightarrow\ & H^+ + OH + 2e \quad (E_{ap} = 16.95 \text{ eV}), \\ & H^+ + OH^- + e \quad (E_{ap} = 16.00 \text{ eV}), \\ & H^+ + OH(X_2P) + 2e \quad (E_{ap} = 18.70 \text{ eV}), \\ & H_2^+ + O + 2e \quad (E_{ap} = 20.70 \text{ eV}), \\ & HO^+ + H + 2e \quad (E_{ap} = 18.11 \text{ eV}), \\ & O^+ + H_2 + 2e \quad (E_{ap} = 19.00 \text{ eV}), \\ & O^+ + 2H + 2e \quad (E_{ap} = 26.80 \text{ eV}). \end{aligned} \tag{6}$$

Table

Ion/primary ion or molecule	Bond	Data from [15]			Data from [13]	NIST database [1] (generally accepted data)		Our data	
		bond rupture energy E_r, eV	energy of dissociation E_d, eV	ionization potential E_i, eV	ionization potential E_i, eV	ionization potential E_i, eV	energy of fragment appearance $E_{ap} = E_i + E_d$, eV	ionization potential E_i, eV	energy of fragment appearance $E_{ap} = E_i + E_d$, eV
Ar^+/Ar	–	–	–	15.76 (Ar)	15.7 ± 0.05	15.759 ± 0.001 (Ar)	–	15.75 ± 0.25	–
Kr^+/Kr	–	–	–	13.996 (Kr)	13.99 ± 0.02	13.99961 ± 0.00001 (Kr)		14.00 ± 0.25	
O_2^+/O_2		–	5.12	12.077 (O_2)	12.07 ± 0.02	12.0697 ± 0.0002 (O_2)	–	12.07 ± 0.25	–
O^+/O_2	O–O	–		13.618 (O)	–	13.6181 (O)	18.69 ± 0.04	–	18.45 ± 0.25
N_2^+/N_2		–	9.76	15.580 (N_2)	15.52 ± 0.05	15.581 ± 0.008 (N_2)	–	15.54 ± 0.25	–
N^+/N_2	N–N	–		14.534 (N)	–	14.5341 (N)	24.32 ± 0.03		24.21 ± 0.25
H_2O^+/H_2O		5.12	–	12.614 (H_2O)	–	12.621 ± 0.002 (H_2O)	–	12.58 ± 0.25	–
H^+/H_2O	H–OH	6.11	–	13.5985 (H)	–	13.5984 (H)	16.95 ± 0.05	–	16.51 ± 0.25
$OH^+/H_2/H_2O$	OH–H	6.31	–	13.18 (OH)	–	13.017 ± 0.0002 (OH)	18.115 ± 0.008	–	18.32 ± 0.25
O^+/H_2O	$O–H_2$	5.00	–	13.618 (O)	–	13.6181 (O)	19.00 ± 0.2	–	18.78 ± 0.25
H_2^+/H_2O	$H_2–O$	5.00	–	15.4261 (H_2)	–	15.42593 ± 0.00005 (H_2)	20.7 ± 0.4	–	21.05 ± 0.25
CO_2^+/CO_2		5.45	–	13.79 (CO_2)	–	13.777 ± 0.001 (CO_2)	–	13.79 ± 0.25	–
C^+/CO_2	$C–O_2$	10.9*	–	11.26 (C)	–	11.2603 (C)	22.7 ± 0.2	–	23.8 ± 0.25
CO^+/CO_2	CO–O	5.45	–	14.014 (CO)	–	14.014 ± 0.0003 (CO)	19.42 ± 0.075	–	19.38 ± 0.25
O^+/CO_2	O–CO	5.45	–	13.618 (O)	–	13.6181 (O)	19.05 ± 0.05	–	19.05 ± 0.25

* Our data.

As is seen, H^+ ions may form via three channels depending on E_{ap}; O^+ ions, via two channels; and H_2^+ and HO^+ ions, via one channel (one threshold energy). The signs of a threshold in the energy dependence of the cross section of oxygen ion generation at dissociative ionization of oxygen and water molecules deserve attention (Figs. 2, 3): the cross section increases very slowly with ionizing electron energy.

The results for the carbon dioxide molecule (Fig. 4) are generally similar to those for the water molecule. However, in the former case, carbon ions alone are generated via two channels ((see also two last processes in (6)),

$$\begin{aligned} e + CO_2 &\longrightarrow C^+ + O_2 + 2e \quad (E_{ap} = 22.70 \text{ eV}), \\ &\quad C^+ + 2O + 2e \quad (E_{ap} = 27.80 \text{ eV}). \end{aligned} \tag{7}$$

These channels specify the run of the energy dependence of the cross section: a smooth increase as in the same dependence for the oxygen ion (O^+/O_2 and O^+/H_2O, Figs. 2 and 3).

An important parameter influencing the threshold behavior of molecule fragmentation into ions is the bond rupture energy of the molecule. The effect of this parameter is most distinctly seen in the case of the carbon dioxide molecule. It is for reaction (7) of dissociative ionization that the rupture energy is the highest (10.9 eV), as follows from the table.

Our findings for the relative cross sections of positive ion yield at direct ionization of a parent molecule and for those of fragmentation at dissociative ionization provide a qualitative description of the processes. As was mentioned earlier, the absolute values of the cross sections can be obtained from the number of molecules participating in collisions combined with the angular distribution of ion fragments. The kinematics of collisions in the process of dissociative ionization is rather difficult to analyze: the difference in kinematic energy gained by daughter ions may considerably change their angular distributions and, hence, their trajectories. This problem is of great significance in mass-spectrometric studies, where many factors must be taken into account (see Experimental). Therefore, the absolute values of ionization cross sections can be obtained from special experiments (like those performed in [16]).

CONCLUSIONS

(1) A high-sensitivity MX7304A mass spectrometer is used for the first time for determining the cross section of molecule direct and dissociative ionization in the near-threshold energy range.

(2) From the threshold dependences measured, the energies of fragmentation of a parent molecule into daughter ions are calculated.

(3) The nonmonotonic behavior of the fragmentation cross section in a wide energy range is to some extent associated with a variety of dissociative ionization routes.

ACKNOWLEDGMENTS

The authors are indebted to E.Yu. Remeta and E.É. Kontrosh for fruitful discussions. Special thanks to A. Surkov, a senior designer at SELMI Co. (Sumy, Ukraine), for valuable consultations and advice.

This work was partially supported by the CRDF, grant no. UP2-2118.

REFERENCES

1. G. Mallard and P. J. Linstrom, http://www.webbook.nist.gov.
2. G. N. Polyakova, B. M. Fizgeer, and V. F. Erko, Khim. Vys. Énerg. **11**, 214 (1977).
3. A. N. Zavilopulo, A. V. Snegursky, E. É. Kontrosh, *et al.*, Pis'ma Zh. Tekh. Fiz. **22** (1), 3 (1996) [Tech. Phys. Lett. **22**, 6 (1996)].
4. A. V. Snegursky, A. N. Zavilopulo, F. F. Chipev, *et al.*, Radiat. Phys. Chem. **68**, 291 (2003).
5. A. N. Zavilopulo and A. V. Snegursky, in *Proceedings of the International Symposium on Vacuum Technology and Equipment, Kharkov, 2002*, Ed. by V. I. Lapshin and V. M. Shulaev, pp. 16–19.
6. A. N. Zavilopulo and A. V. Snegursky, Pis'ma Zh. Tekh. Fiz. **28**, 68 (2002) [Tech. Phys. Lett. **28**, 913 (2002)].
7. A. N. Zavilopulo, F. F. Chipev, and O. B. Shpenik, in *Proceedings of the EMS Conference, Prague, 2003*, pp. 200–201.
8. *MX-7304A Monopole Mass Spectrometer: Description and Manual* (SELMI, Sumy, 2002) [in Russian].
9. T. Fiegele, G. Hanel, I. Torres, *et al.*, J. Phys. B **33**, 4263 (2000).
10. G. H. Wannier, Phys. Rev. **90**, 817 (1953).
11. H. Z. Klar, Z. Phys. A **307**, 75 (1982).
12. T. D. Märk, in *Electron Molecule Interactions and Their Applications*, Ed. by L. G. Christophorou (Academic, Orlando, 1984).
13. G. Hanel, B. Gstir, T. Fiegele, *et al.*, J. Chem. Phys. **116**, 2456 (2002).
14. A. Lofihus and P. M. Krupenie, J. Phys. Chem. Ref. Data **6**, 113 (1977).
15. A. A. Radtsig and B. M. Smirnov, *Reference Data on Atoms, Molecules, and Ions* (Énergoatomizdat, Moscow, 1986; Springer-Verlag, Berlin, 1985).
16. A. I. Zhukov, A. N. Zavilopulo, O. B. Shpenik, *et al.*, J. Phys. B **23**, S2373 (1990).

Translated by V. Isaakyan

Technical Physics, Vol. 50, No. 4, 2005, pp. 408–414. Translated from Zhurnal Tekhnicheskoĭ Fiziki, Vol. 75, No. 4, 2005, pp. 25–30.

GASES AND LIQUIDS

Impact of the External Energy Supply to the Shock Layer Region on the Shock Wave Parameters

V. Yu. Golyatin,[1] V. V. Kuchinskii,[2] and V. S. Sukhomlinov[1]

[1] *Research Institute of Physics, St. Petersburg State University, ul. Ul'yanovskaya 1, Petrodvorets, St. Petersburg, 198903 Russia*
e-mail: SUKHOMLINOV@POBOX.RU

[2] *Research Institute of Hypersonic Systems, Leninets Holding Company, St. Petersburg, 196066 Russia*
e-mail: AJAX@COMSET.NET

Received May 28, 2004

Abstract—A system of equations describing supersonic gas flow in the presence of a heat source near the shock front is obtained. Relations between the gas parameters in disturbed and undisturbed regions, which generalize the classical Hugoniot–Rankine relations, are derived. Formulas for calculation of the flow parameters in the presence of an energy supply to the shock layer region are presented. It is demonstrated that there exists a critical intensity of energy supply at which the system of equations of the conservation laws for the gas parameters on both sides of the shock layer possesses no stationary solution. © *2005 Pleiades Publishing, Inc.*

INTRODUCTION

The impact of the external energy supply ahead of the shock front on the aerodynamic characteristics of various bodies moving at super- and hypersonic velocities has been studied earlier by several authors [1–3]. At the same time, the shock wave intensity (hence, the drag of the streamlined body) may be varied by creating domains of energy release behind the shock front. For instance, as for a normal shock wave in a gas, the shock wave intensity is uniquely determined by the laws of conservation of mass, momentum, and energy when passing through the shock layer. An additional energy release behind the shock front will at least alter the energy exchange between the regions adjacent to the shock layer, and, through this, affect the relationship between the main parameters responsible for transfer of energy, momentum, and mass through the shock wave, i.e., change the shock wave intensity.

Of undeniable interest is the study of the effect produced by energy release in the region adjacent to the shock layer behind the shock front at a transonic speed, i.e., in the case of weak shock waves. Energy supply to the region behind the shock front, as well as directly to the expectable shock layer region, may change the dynamics of formation of the shock layer itself. These processes need to be investigated for the purpose of solving burning applied problems such as breaking the sound barrier, promotion of the appropriate safety of the breaking, and reduction of aircraft dynamic load.

The exact physical statement of the problem and its mathematical algorithmic presentation are as follows. In the gas parameter region where the gas flow can be described with the use of the hydrodynamic approach, the complete system of Navier–Stokes equations is written and the gas macroparameters are specified at infinity upstream (i.e., in the undisturbed region). A gas density nonuniformity moving at some constant speed with respect to the fixed system of reference is stated to exist. The system of flow equations accounts for an external heat source moving at the same speed as the density disturbance.

The results obtained in this paper relate only to the behavior of the gas macroparameters in the shock wave region; i.e., they are integral relations. Such an approach reveals some fundamental peculiar features of the impact of the external power supply on the shock wave parameters.

MAIN EQUATIONS

Consider the laws of conservation of the collision integral in the Boltzmann kinetic equation as applied to the isolated gas volume $V = V(t)$ bounded by surface $\Sigma_d(t)$ (Fig. 1), where t is time.

The law of conservation of the gas mass and the Euler equation are described by the following expressions [4]:

$$\frac{\partial \rho}{\partial t} + \mathrm{div}\rho\mathbf{U} = 0, \tag{1}$$

$$\frac{\partial \mathbf{U}}{\partial t} + \mathrm{grad}\frac{|\mathbf{U}|^2}{2} - [\mathbf{U} \times \mathrm{curl}\mathbf{U}] = -\frac{1}{\rho}\mathrm{grad}\, p. \tag{2}$$

Here, ρ is the density, $\mathbf{U}$ is the mass flow rate at the volume boundary, and the law of conservation of energy

has the form

$$\frac{dE}{dt} = \frac{d}{dt}\int\limits_{V(t)} \rho\left(\varepsilon + \frac{1}{2}U^2\right)dV = Q_m, \qquad (3)$$

where quantity $Q_m = \int_{V(t)} q\,dV$ accounts for the energy released by a source of power q in the volume, ε is the internal energy of a gas mass unit, and the internal friction is neglected.

Formula (3) takes the form

$$\int\limits_{V(t)} \frac{\partial}{\partial t}\left\{\rho\left(\varepsilon + \frac{1}{2}U^2\right)\right\}dV + \int\limits_{\Sigma(t)} \left[\rho\left(\varepsilon + \frac{1}{2}U^2\right)\right]\mathbf{U}\,d\mathbf{\Sigma} \qquad (4)$$

$$= -\int\limits_{\Sigma(t)} p(\mathbf{U}d\mathbf{\Sigma}) + \int\limits_{V(t)} q dV.$$

By the Gauss theorem, this implies

$$\frac{\partial}{\partial t}\left\{\rho\left(\varepsilon + \frac{1}{2}U^2\right)\right\} + \mathrm{div}\left[\rho\mathbf{U}\left(\varepsilon + \frac{1}{2}U^2 + \frac{p}{\rho}\right)\right] = q. \quad (5)$$

GENERALIZED HUGONIOT–RANKINE RELATIONS

Suppose that, in the gas flow, there occur conditions that the flow parameters $\mathbf{U}$, ρ, p, and T (T is the gas temperature and p is the pressure) sharply change within the range of several lengths of the gas molecule mean free path with respect to elastic collisions. The high-gradient zone of the flow parameters is replaced by a discontinuity surface and it is assumed that, when passing through this surface, the flow parameters change abruptly, i.e., have a discontinuity. This discontinuity is conventionally called the shock (wave) front.

Surface Σ_d (Fig. 1) cuts the gas flow from left to right. On the left of the surface, the gas flow parameters are $\mathbf{V}_1$, ρ_1, p_1, and T_1; on the right, $\mathbf{V}_2$, ρ_2, p_2, and T_2. The surface moves at velocity $\mathbf{U}$ with respect to the fixed system of reference. In the surface-referenced coordinate system, the flow parameters on the left / right of the surface are $\mathbf{U}_1 = \mathbf{V}_1 - \mathbf{U}$; ρ_1, p_1, T_1 and $\mathbf{U}_2 = \mathbf{V}_2 = \mathbf{U}$; ρ_1, p_1, T_2, respectively. Distinguish an arbitrary volume $V(t)$ of the gas limited by a surface S and containing a part of the discontinuity surface Σ_d. The maximal distance from S to Σ_d on the left of the discontinuity surface is l_1; on the right, l_2. Using the laws of conservation of mass, momentum, and energy in the form obtained above and passing to the limit as l_1, $l_2 \longrightarrow \Delta x/2$, where Δx is the shock layer thickness (of order of several lengths of the mean free path λ), one can obtain the following relations between the flow parameters on the left and on the right of the discontinuity surface:

$$\rho_1 U_{n1} = \rho_2 U_{n2}, \quad \rho_1 U_{n1}^2 + p_1 = \rho_2 U_{n2}^2 + p_2,$$

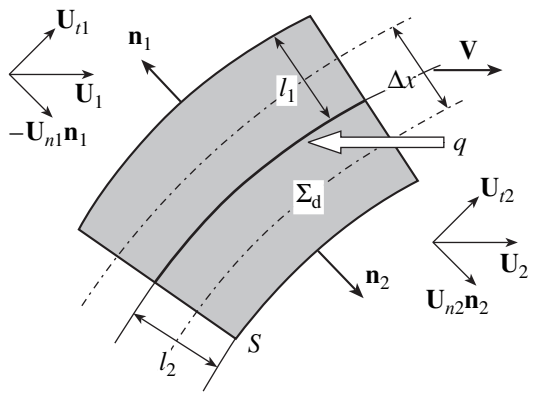

Fig. 1. Deduction of the conservation laws for a gas flow passing through discontinuity surface Σ_d.

$$U_{t1} = U_{t2}, \quad U_{k1} = U_{k2}, \qquad (6)$$

$$\left(\frac{1}{2}U_{n1}^2 + i_1\right)\rho_1 U_{n1} = \left(\frac{1}{2}U_{n2}^2 + i_2 - W\right)\rho_2 U_{n2}.$$

Here, $W = q\Delta x/\rho_2 U_{n2}$, q is the volume power of the heat source in the shock layer, $i = \varepsilon + p/\rho$ is the gas enthalpy; U_n is the normal component; and U_t, U_k are the tangential components of velocity $\mathbf{U}$ with respect to the discontinuity surface.

For further transformations, the gas law is used. For perfect gas, we have

$$\varepsilon = \frac{p}{\rho}\frac{1}{\gamma - 1},$$

$c^2 = \gamma p/\rho$ (the velocity of sound in the gas),

$$i = \frac{c^2}{\gamma - 1}, \quad \gamma = \frac{C_p}{C_V}.$$

Here, C_p and C_V denote the specific heat of the gas at constant pressure and volume, respectively.

With the use of these equalities and formulas (6), the ratio between the pressure p_2 behind the shock front and pressure p_1 ahead of the shock front can be written in the form

$$\frac{p_2}{p_1} = 1 + \frac{2\gamma(M_1^2 - 1)}{\gamma + 1} - \frac{2\gamma M_1(\gamma - 1)}{(\gamma + 1)}\frac{q\Delta x}{(p_2 - p_1)c_1} \qquad (7)$$

$$= 1 + \chi_0 - \frac{2\gamma M_1(\gamma - 1)}{(\gamma + 1)}\frac{q\Delta x}{(p_2 - p_1)c_1},$$

where $M_1 = U_{n1}/c_1$ is the Mach number ahead of the shock front.

In the case $q = 0$, the above formula and the corresponding expression for ρ_2/ρ_1 are reduced to the well-known Hugoniot relations which relate the perfect gas

flow parameters before and after the shock,

$$\frac{p_2}{p_1} = 1 + \frac{2\gamma(M_1^2 - 1)}{\gamma + 1} = 1 + \chi_0,$$

$$\frac{\rho_2}{\rho_1} = 1 + \frac{2(M_1^2 - 1)}{2 + M_1^2(\gamma - 1)} = \left(1 - \frac{\chi_0}{\gamma M_1^2}\right)^{-1}, \qquad (8)$$

$$\chi_0 = \frac{2\gamma(M_1^2 - 1)}{\gamma + 1}.$$

Here, quantity χ_0 is the shock wave intensity in the absence of the energy supply.

In particular, formulas (8) imply the well-known fact [5] that, as $M_1 \longrightarrow \infty$, we have $p_2/p_1 \longrightarrow \infty$ and $\rho_2/\rho_1 \longrightarrow (\gamma + 1)/(\gamma - 1)$.

Let us present another formula which directly follows from the first two equalities in (6) and relates the density ratio ρ_2/ρ_1 to the pressure ratio p_2/p_1:

$$\frac{\rho_2}{\rho_1} = \left[1 - \frac{\frac{p_2}{p_1} - 1}{M_1^2\gamma}\right]^{-1}. \qquad (9)$$

The shock layer thickness Δx is uniquely determined by Mach number M_1 or, which is the same thing, by the shock wave intensity $\chi = (p_2/p_1) - 1$, for χ is a single-valued function of M_1: $\chi = \chi(M_1)$. Introduce the function $\Delta x = \Delta x(\chi)$ and derive from formula (7) the main relation determining the ratio p_2/p_1:

$$\frac{p_2}{p_1} = 1 + \chi_0 - \frac{2\gamma M_1}{(\gamma + 1)\left(\frac{p_2}{p_1} - 1\right)}\frac{1}{c_1\varepsilon_1\rho_1}q\Delta x$$
$$= 1 + \chi_0 - \frac{\beta M_1}{\left(\frac{p_2}{p_1} - 1\right)}. \qquad (10)$$

Here, we introduced the main characteristic of energy deposition employed in the further consideration, namely, the dimensionless parameter β of energy deposition,

$$\beta = \frac{2\gamma}{\gamma + 1}\left(\frac{q\Delta x(\chi)}{c_1}\right)\frac{1}{\rho_1\varepsilon_1}. \qquad (11)$$

As is clear from formulas (7), (10), and (11), the variation of the shock wave parameters is related to the ratio between the supplied (to a volume unit) energy $q\Delta x(\chi)/c_1$ and energy $\varepsilon_1\rho_1$ carried by the incident air flow. Therefore, parameter β is the one that determines the evolving physical situation when energy is supplied to the shock layer region. As for the required energy density q, it cannot be determined until intensity $\chi = (p_2/p_1) - 1$ is found by means of solving Eq. (10) for a specified β:

$$\frac{p_2}{p_1} = 1 + \frac{\chi_0}{2}\left(1 + \sqrt{1 - \frac{4M_1}{\chi_0^2}\beta}\right). \qquad (12)$$

Herein, the value of q is determined by the concrete pressure dependence of the shock layer thickness on the pressure,

$$q = \frac{(\gamma + 1)p_1c_1}{2\gamma(\gamma - 1)\Delta x(\chi)}\beta. \qquad (13)$$

For $\beta = 0$, expression (12) reduces to the well-known formula (8) for the ratio p_2/p_1 (recall that χ_0 determines the shock wave intensity in the absence of the energy supply). Since $\beta > 0$ and $\chi_0 \geq 0$, formula (12) implies that the double inequality $1 \leq p_2/p_1 \leq 1 + \chi_0$ is always valid, i.e., in the presence of the energy supply, the shock wave intensity is always lower than that in the case of no energy supply.

The ratio of densities may be calculated by the expression

$$\frac{\rho_2}{\rho_1} = \frac{(\gamma + 1)\frac{p_2}{p_1} + \gamma - 1}{(\gamma - 1)\frac{p_2}{p_1} + \gamma + 1 + \frac{\beta}{\gamma M_1}} = \left[1 - \frac{\frac{p_2}{p_1} - 1}{M_1^2\gamma}\right]^{-1} \qquad (14)$$

derived from formulas (7), (9), and (11) (the ratio p_2/p_1 is everywhere determined by formula (12)). From the law of conservation of mass, we obtain the following formula for the ratio of velocities:

$$\frac{U_{n2}}{U_{n1}} = \frac{(\gamma - 1)\frac{p_2}{p_1} + \gamma + 1 + \frac{\beta}{\gamma M_1}}{(\gamma + 1)\frac{p_2}{p_1} + \gamma - 1} = 1 - \frac{\frac{p_2}{p_1} - 1}{M_1^2\gamma}. \qquad (15)$$

The ratio of temperatures T_2 behind the shock front and T_1 ahead of it and the ratio between the corresponding Mach numbers are

$$\frac{T_2}{T_1} = \frac{(\gamma - 1)\frac{p_2}{p_1} + \gamma + 1 + \frac{\beta}{\gamma M_1}}{(\gamma + 1)\frac{p_2}{p_1} + \gamma - 1}\frac{p_2}{p_1},$$
$$\frac{M_2}{M_1} = \sqrt{\left(1 - \frac{\frac{p_2}{p_1} - 1}{M_1^2\gamma}\right)\left(\frac{p_2}{p_1}\right)^{-1}}. \qquad (16)$$

ANALYSIS OF THE RELATIONS OBTAINED

When energy is supplied to a subsonic flow, the flow accelerates. By virtue of the law of conservation of

mass, this results in decreasing density. The drop of pressure p_2 with increasing β may be explained with the help of the second equation in system (6), which expresses the law of conservation of momentum. One can easily see that the value $\rho_2 U_{n2}^2$ in the right-hand side of this equation increases, because $\rho_2 U_{n2} = \rho_1 U_{n1} =$ const and U_{n2} grows with β. Accordingly, pressure p_2 should decrease, in so far as the left-hand side of this equation is independent of parameter β.

Consider another interesting fact that follows from formulas (12), (14), and (16). It is clear from formula (12) that there exists a limiting parameter value $\beta_{\min}$ such that, given Mach number M_1, for any $\beta > \beta_{\min}$, the ratio p_2/p_1 (and, consequently, the ratios ρ_2/ρ_1 and U_{n2}/U_{n1} as well) becomes complex, which is physically meaningless. Thus, the conservation laws cannot be satisfied under the assumption that a discontinuity surface (the shock wave) is present, just as these equations cannot be satisfied in the case $\beta = 0$ when $M_1^2 < (\gamma - 1)/(2\gamma)$ (because then, the first formula in (8) implies that $p_2/p_1 < 0$, which is also physically meaningless). In actual fact, when $\beta = 0$, the conservation laws cannot be satisfied even for $M_1 < 1$, because, in this case, it follows from (8) that $p_2/p_1 < 1$, which means that a depression-type shock wave propagates. However, it is demonstrated in [1] that this is impossible. The above result can be reformulated as follows. For any $\beta \neq 0$, there is a minimal value $M_{1\,\min} > 1$ of Mach number M_1 such that, for $M_1 < M_{1\,\min}$, the shock wave does not exist. More exactly, these inequalities being satisfied, there exists no stationary solution to the system of equations of the conservation laws in the form of a discontinuity of the gas parameters. From the physical standpoint, this means that the flow rearranges and becomes smoother or the gas parameters are varied in the upstream direction. Such a phenomenon is known to be observed in pipe flows when the supplied external energy exceeds a certain critical value [6]. This fact is of great practical consequence: there is a theoretical possibility of moving at a supersonic ($M_1 > 1$) speed in a flow with a subsonic structure. According to formula (12), the shock wave intensity can be weakened at most by half for $\beta = \beta_{\min}$.

Let us find an expression for the minimal value of energy supply $\beta_{\min}$ such that, given Mach number M_1, the existence condition for the shock wave is still not fulfilled. Since the radicand in formula (12) is equal to zero, we have

$$\beta_{\min} = \frac{\chi_0^2}{4M_1} = \frac{\gamma^2(M_1^2-1)^2}{(\gamma+1)^2 M_1}. \tag{17}$$

When $\beta = \beta_{\min}$, formula (16) implies $M_1 = 1$. Thus, for the critical value of energy supply, the flow at infinity upstream asymptotically tends to the sonic flow.

Let us analyze some quantitative results that are implied by formulas (12), (14), and (15). It is seen from formula (17) that value $\beta_{\min}$ is proportional to the square of value $M_1 - 1$ at near-sonic velocities and to the cube of value M_1 at hypersonic velocities. This goes to show that such a method of weakening the shock wave is energetically more efficient in the case $M_1 - 1 \ll 1$ rather than for $M_1 \gg 1$, since pressure p_2 is proportional to M_1^2 and the energy deposition is proportional to Q, which, in turn, is proportional to M_1^3 for $M_1 \gg 1$.

For the dependence of the minimal Mach number on parameter $\beta_{\min}$, which is the function inverse to (17), we have

$$\gamma^2(M_1^2-1)^2 = \beta_{\min} M_1(\gamma+1)^2. \tag{18}$$

The exact solution to this equation (which determines the minimal value $M_{1\,\min}$) has the form

$$M_{1\,\min} = \frac{\gamma+1}{2\gamma}\sqrt{\frac{\beta}{\varphi(\beta)}} + \sqrt{\frac{(\gamma+1)\sqrt{\beta\varphi(\beta)}}{2\gamma} - \left(\frac{\varphi(\beta)}{2}\right)^2}, \tag{19}$$

where

$$\varphi(\beta) = \frac{4}{\sqrt{3}}\sinh\left[\frac{1}{3}\operatorname{arcsinh}\left(\frac{3\sqrt{3}(\gamma+1)^2\beta_{\min}}{16\gamma^2}\right)\right]. \tag{20}$$

In most cases, $M_{1\,\min}$ can be determined (up to 5%) by the asymptotically correct approximate formula

$$M_{1\,\min} \approx \begin{cases} 1 + \dfrac{(\gamma+1)\sqrt{\beta}}{2\gamma} & \text{for} \quad \beta < \beta_{Q0} \\ \dfrac{\dfrac{\beta}{\beta_{Q0}} - 1}{\left(\dfrac{\beta}{\beta_{Q0}}\right)^{\frac{2}{3}} - 1} & \text{for} \quad \beta \geq \beta_{Q0}, \quad \beta_{Q0} = \dfrac{\gamma^2}{(\gamma+1)^2} \end{cases} \tag{21}$$

or by the approximation

$$M_{1\,\min} \approx 1 + \frac{(\gamma+1)\sqrt{\beta}}{2\gamma}\left(1 - \frac{(\gamma+1)^2\beta}{32\gamma^2}\left(1 - \frac{(\gamma+1)\sqrt{\beta}}{2\gamma}\right)\right) \approx 1 + \frac{(\gamma+1)\sqrt{\beta}}{2\gamma} \tag{22}$$

which is valid for small $\beta \ll 1$.

Figure 2 shows the dependence of the minimal Mach number $M_{1\,\min}$ at which the shock wave cannot exist on parameter β characterizing the energy deposition. For $M_1 = M_{1\,\min}$, the main parameter ratios (p_2/p_1,

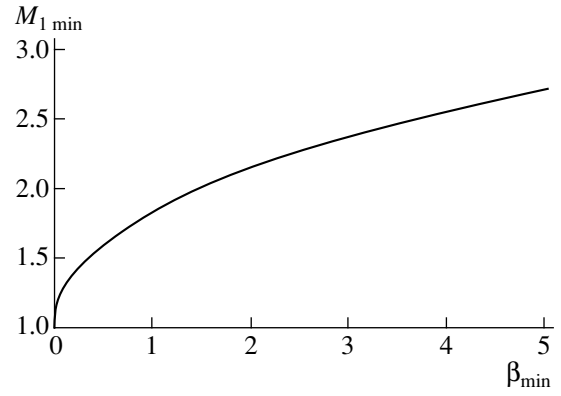

Fig. 2. Dependence of the minimal Mach number $M_{1\,\min}$ at which the shock wave does not exist on parameter $\beta_{\min}$ characterizing the energy deposition.

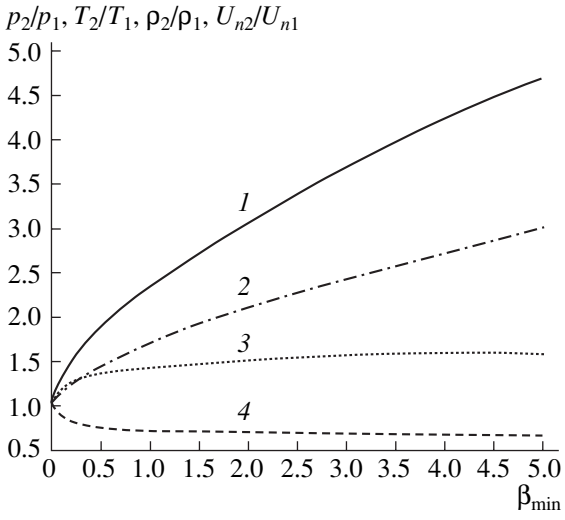

Fig. 3. $\beta_{\min}$-dependence of the ratios of pressure (*1*), temperature (*2*), density (*3*), and velocity (*4*) behind and ahead of the shock front. The calculation is performed for the minimal (for a given $\beta_{\min}$) Mach number $M_{1\,\min}(\beta_{\min})$ at which the shock wave does not exist (Fig. 2).

ρ_2/ρ_1, U_{n2}/U_{n1}, T_2/T_1) are calculated in accordance with (12), (14)–(16) by the formulas

$$\left.\frac{p_2}{p_1}\right|_{M_1 = M_{1\,\min}} = 1 + \frac{\gamma(M_1^2 - 1)}{\gamma + 1},$$

$$\left.\frac{\rho_2}{\rho_1}\right|_{M_1 = M_{1\,\min}} = 1 + \frac{M_1^2 - 1}{\gamma M_1^2 + 1},$$

$$\left.\frac{U_{n2}}{U_{n1}}\right|_{M_1 = M_{1\,\min}} = 1 - \frac{M_1^2 - 1}{(\gamma + 1)M_1^2}, \qquad (23)$$

$$\left.\frac{T_2}{T_1}\right|_{M_1 = M_{1\,\min}} = 1 + \frac{(\gamma^2 M_1^2 - 1)(M_1^2 - 1)}{(\gamma + 1)^2 M_1^2}.$$

In these expressions, the value of $M_{1\,\min}$ is calculated by one of formulas (19)–(22) (depending on the required accuracy). When $\beta \ll 1$, a single term in (22) would suffice.

An important characteristic of the process is the weakening of the shock wave intensity and variation of the temperature and normal velocity for $M_1 = M_{1\,\min}$ in the cases when a heat source is present or absent. To find this characteristic, supplement formulas (8) with the known relations

$$\left.\frac{U_{n2}}{U_{n1}}\right|_{\beta = 0} = 1 - \frac{2(M_1^2 - 1)}{M_1^2(\gamma + 1)} = 1 - \frac{\chi_0}{M_1^2\gamma},$$

$$\left.\frac{T_2}{T_1}\right|_{\beta = 0} = 1 + \frac{2(M_1^2 - 1)(\gamma - 1)(\gamma M_1^2 + 1)}{M_1^2(\gamma + 1)^2}. \qquad (24)$$

Dividing formulas (23) by expressions (8) and (24) and taking into account that all parameters ahead of the shock front (subscripted with 1) are independent of the energy deposition, we obtain the relations

$$\frac{p_2}{p_2|_{\beta = 0}} = 1 - \frac{\gamma(M_1^2 - 1)}{2\gamma M_1^2 - \gamma + 1}, \quad \frac{\rho_2}{\rho_2|_{\beta = 0}} = 1 - \frac{M_1^2 - 1}{\gamma M_1^2 + 1},$$

$$\frac{U_{n2}}{U_{n2}|_{\beta = 0}} = 1 + \frac{M_1^2 - 1}{2 + M_1^2(\gamma - 1)}, \qquad (25)$$

$$\frac{T_2}{T_2|_{\beta = 0}} = 1 + \frac{(M_1^2 - 1)[1 - \gamma^2 M_1^2 + 2\gamma(M_1^2 - 1)]}{(2\gamma M_1^2 - \gamma + 1)(2 + M_1^2(\gamma - 1))}.$$

Expressions (25) are calculated for $M_1 = M_{1\,\min}$, which is a function of parameter β. This allows us to find the corresponding dependences of the shock wave characteristics as functions of the energy deposition.

The above conclusions are of a general nature and depend neither on the model of the shock layer nor on the mode of heat supply, i.e., the dependences $\Delta x(\chi)$ and $q(\chi)$. Formula (10) implies that, for $q\Delta x(\chi) > 0$ and $p_2/p_1 > 1$, inequality $p_2/p_1 < 1 + \chi_0 = p_2/p_1|_{\beta = 0}$ is always valid (here, $p_2/p_1|_{\beta = 0}$ is the pressure drop with no energy supply), whence follows the above assertion.

It is noteworthy that, though Eq. (10) seems to imply the relation $\chi - \chi_0 \approx \beta + o(\beta^2)$ for $M_1 \geq 1$, what actually happens is $\chi - \chi_0 \approx \sqrt{\beta} + o(\beta)$. There is no contradiction here, because, as $M_1 \longrightarrow 1 + 0$, we have $p_2/p_1 \longrightarrow 1 + 0$ and the last term in formula (10) starts increasing without limit. This is just what causes, for $\beta \ll 1$, the real correction to be proportional to $\sqrt{\beta} > \beta$.

Figure 3 shows the $\beta_{\min}$-dependences of the ratios between the parameter values ahead of and behind the shock front constructed by formulas (23) with the Mach number $M_{\min}$ calculated for a given $\beta_{\min}$. Figure 4 is constructed in a similar way by formulas (25) in order to estimate the impact of energy deposition on the

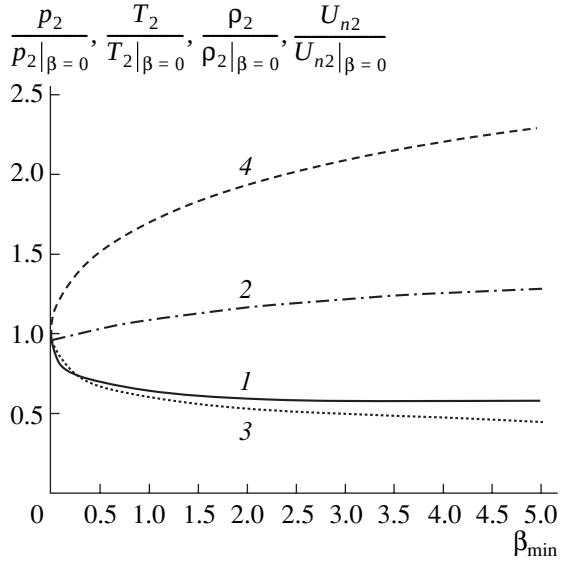

Fig. 4. β_{min}-dependence of the ratios of pressure (*1*), temperature (*2*), density (*3*), and velocity (*4*) behind the shock front in the cases of presence and absence of energy deposition. The calculation is performed for the minimal (for a given β_{min}) Mach number $M_{1\,min}(\beta_{min})$ at which the shock wave does not exist (Fig. 2).

parameters behind the shock front. In Fig. 5, the pressure ratio and temperature ratio (calculated for the same Mach number M_{min}) in the cases of presence (curves *1* and *3*) and absence ($\beta = 0$, curves *2* and *4*) of energy deposition are depicted. It can be seen in Fig. 5 that, at small values of energy deposition ($\beta < 0.5$), the presence of an energy supply significantly lowers the shock wave intensity, while it scarcely increases the temperature behind the shock front.

Let us present formulas for estimating all the above considered ratios at small values of parameter $\beta_{min} \le 0.1$. For the ratios between the shock wave parameters behind and ahead of the shock front, we have

$$\left.\frac{p_2}{p_1}\right|_{M_1 = M_{1\,min}} = 1 + \sqrt{\beta},$$

$$\left.\frac{\rho_2}{\rho_1}\right|_{M_1 = M_{1\,min}} = 1 + \frac{\sqrt{\beta}}{\gamma(\sqrt{\beta}+1)},$$

$$\left.\frac{U_{n2}}{U_{n1}}\right|_{M_1 = M_{1\,min}} = 1 - \frac{\sqrt{\beta}}{(\gamma+1)\sqrt{\beta}+\gamma}, \qquad (26)$$

$$\left.\frac{T_2}{T_1}\right|_{M_1 = M_{1\,min}} = 1 + \sqrt{\beta}\left[1 - \frac{1+\sqrt{\beta}}{(\gamma+1)\sqrt{\beta}+\gamma}\right]$$

(subscript "min" at β_{min} is omitted for brevity). In the disturbed region (behind the shock front), the ratios between the parameters in the cases of presence and absence of energy deposition are

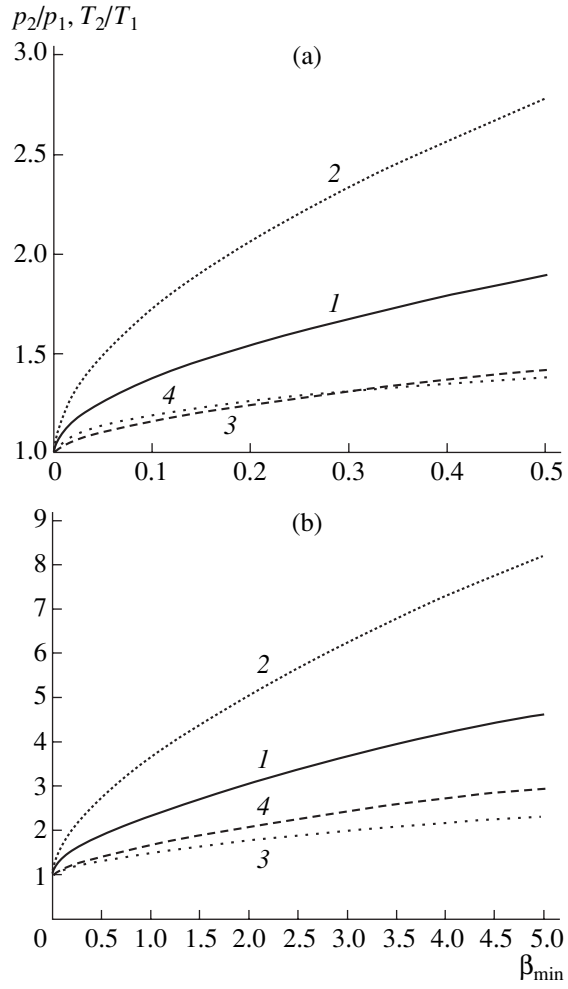

Fig. 5. β_{min}-dependence of the ratios of pressure (*1*) and temperature (*3*) behind and ahead of the shock front. The calculation is performed for the minimal (for a given β_{min}) Mach number $M_{1\,min}(\beta_{min})$ at which the shock wave does not exist (Fig. 2). Curves *2* and *4* show the pressure ratio $p_2/p_1|_{\beta=0}$ and temperature ratio $T_2/T_1|_{\beta=0}$ calculated for the same Mach number $M_{1\,min}$ and zero energy deposition (formulas (8) and (24)). Case (a) corresponds to $\beta_{min} \le 0.5$, case (b), to $\beta_{min} \le 5$.

$$\frac{p_2}{p_2|_{\beta=0}} = 1 - \frac{\sqrt{\beta}}{1+\sqrt{\beta}}, \quad \frac{\rho_2}{\rho_2|_{\beta=0}} = 1 - \frac{\sqrt{\beta}}{\gamma(\sqrt{\beta}+1)},$$

$$\frac{U_{n2}}{U_{n2}|_{\beta=0}} = 1 + \frac{\sqrt{\beta}}{\gamma+\sqrt{\beta}(\gamma-1)}, \qquad (27)$$

$$\frac{T_2}{T_2|_{\beta=0}} = 1 - \frac{(\gamma-1)\sqrt{\beta}}{(1+\sqrt{\beta})[(\gamma-1)\sqrt{\beta}+\gamma]}.$$

The limiting values of parameter β at which approximate formulas (26)–(27) provide a calculation error within 5% are the following. In formulas (26): $\beta \le 0.19$

for the pressure ratio, $\beta \le 5$ for the density ratio, $\beta \le 5$ for the velocity ratio, and $\beta \le 0.33$ for the temperature ratio. In formulas (27): $\beta \le 0.13$ for the pressure ratio, $\beta \le 0.35$ for the density ratio, $\beta \le 0.38$ for the velocity ratio, and $\beta \le 0.13$ for the temperature ratio.

CONCLUSIONS

The results of the paper allow one to estimate the change in the parameters of weak shock waves due to the impact of energy deposition into the shock front region. To study the exposure of the shock wave to heating for $M > 2$ in more detail, one needs to solve the kinetic equation. The value of the supplied power can be estimated by formula (13). For a flight at altitude 30 000 m, Mach number 1.2, and area of local plasma influence 10^{-3} m^2, the supplied power is about 400 W. Since the region filled with plasma is much wider than the shock front, the shock wave expected always falls within the plasma layer. This ensures the smooth variation of the shock wave parameters. When solving concrete flow-around problems, it is advisable to use the aforementioned relations in the required gas-dynamic calculation.

REFERENCES

1. I. A. Belov, *Interaction of Nonuniform Flows with Obstacles* (Mashinostroenie, Leningrad, 1983) [in Russian].
2. P. Yu. Georgievskiĭ and V. A. Levin, Pis'ma Zh. Tekh. Fiz. **14**, 684 (1988) [Sov. Tech. Phys. Lett. **14**, 303 (1988)].
3. V. Yu. Borzov, I. V. Rybka, and A. S. Yur'ev, Inzh.-Fiz. Zh. **62**, 243 (1994).
4. A. L. Velikovich and M. A. Liberman, *Physics of Shock Waves in Gases and Plasmas* (Springer-Verlag, Berlin, 1985; Nauka, Moscow, 1987).
5. *High-Speed Physics*, Ed. by K. Vollrath and G. Thomer (Springer, Vienna, 1967; Mir, Moscow, 1971), Vol. 3.
6. L. A. Vulis, *Thermodynamics of Gas Flows* (Gosénergoizdat, Leningrad, 1950) [in Russian].

Translated by A. Pankrat'ev

Technical Physics, Vol. 50, No. 4, 2005, pp. 415–420. Translated from Zhurnal Tekhnicheskoĭ Fiziki, Vol. 75, No. 4, 2005, pp. 31–36.

GASES AND LIQUIDS

Computer-Aided Processing of Optical Measurements in Aeroballistic Experiment

V. A. Sakharov and E. A. Tropp

Ioffe Physicotechnical Institute, Russian Academy of Sciences, Politekhnicheskaya ul. 26, St. Petersburg, 194021 Russia

e-mail: v.sakharov@mail.ioffe.ru

Received June 30, 2004

Abstract—The idea of semiautomatic computer-aided processing of photos as applied to the problem of external ballistics, namely, determination of aerodynamic characteristics of flying objects from trajectory data, is put forward. The impetus to write this article is the development of an original software product that was used to advantage in processing data of full-scale experiments with the aim of creating a photo database of ballistic experiments performed at the Ioffe Physicotechnical Institute. This software is integrated into the Arkhimed information–retrieval system used to control this database. The advantages of the semiautomatic approach over "manual" measurements and the fully automatic version are indicated. © *2005 Pleiades Publishing, Inc.*

INTRODUCTION

Determination of the flight properties, i.e., the aerodynamic characteristics (ADCs), of objects remains to a challenging problem of aerodynamics. The ADCs can be measured experimentally in various aerodynamic tunnels, where inverse modeling of motion (a gas flows about an immovable model) is accomplished, or can be determined from experimental data obtained in ballistic ranges (direct modeling).

Determining the ADCs of freely flying objects can be subdivided into two subproblems: measuring the object's trajectory parameters (the so-called problem of identification of motion [1]) and computing the ADCs themselves from the trajectory parameters measured. The solution methods for the second subproblem have been touched upon elsewhere (see, for example, [2, 3]) and are not considered here.

The tracking of a flying object in an aeroballistic experiment is usually accomplished either by telemetry means (this issue goes beyond the scope of this article) or by successively photographing the object together with bench marks in the unique coordinate system of a ballistic range and timing marks. In the latter case, the trajectory data in the form of tables summarizing the space–time coordinates of the object (in the laboratory coordinate system) are obtained from measurements made directly on the photos taken in the course of the ballistic experiment. For each recording time, it is necessary to know (measure) longitudinal coordinate X of the object in the direction of shooting, transverse coordinates Y (vertical displacement) and Z (lateral displacement), and the angles specifying the spatial orientation of the object's axis (or the characteristic line of the object) and the rotation (roll) of the object (projectile) about its axis. Consequently, two projections of the object must be at hand at each recording time. The number of pairs of such projections depends on the capabilities of the experimental setup and on the object under study. However, even if the ADCs are determined in the linear approximation (i.e., under the assumption that vibration amplitudes are small), one needs more than two records (observations) per vibration half-period; moreover, when the vibration damping is measured, observations must cover more than one period. The number of recording stations that is optimal in terms of completeness and accuracy of the final results can be found by numerical simulation [4] with the desired parameters appropriately approximated. Thus, the number of photos to be processed after each experiment may be as large as several tens. Thus, the need for computer-aided processing of measurements made on ballistic object images is obvious.

Digitization of negative images (when a photographic film is used as a record medium) is certainly a labor-consuming task. However, digitized data are much easier to handle than measurements taken using measuring optical microscopes, densitometers, and other instruments, and their further processing provides exact and correct final results. In addition, one should bear in mind the recent tendency toward CCD (nonphotographic) imaging (see, for example, [5]; a ballistic range entirely equipped with CCD cameras was designed in [6]). It seems likely that photos will soon be digitized immediately during photographing. Even today, it seems reasonable to digitize photo archives concerning experimental aerodynamics and create a unified database (this work is now under way at the Ioffe Physicotechnical Institute [7]).

1063-7842/05/5004-0415$26.00

PRINCIPLE OF PARTIAL AUTOMATION

When measurements are taken with optico-mechanical devices (like a UIM-23 measuring microscope), all operations (from film positioning to coordinate recording) are made "manually"; then, after measurements on photos taken in each experiment have been completed, the results are tediously recalculated to relate them to the unique coordinate system. Errors inevitably arising in the course of recalculation usually come to light too late, and numerous time-consuming operations are repeated. Measurement automation is primarily aimed at combining all stages of measurement and computing into a unified information procedure that can be interrupted, reset, or continued without loss of data acquired earlier (or with a minimal loss if an error is detected). In addition, data formats for the interface must be compatible with trajectory data processing codes intended for extracting the ADCs of the object [8]. Necessary experience in developing such computational was gained in interferogram processing [9]. The continuity of the new software with the previous approach will be discussed below. However, the new formulation of the problem and an object under study other than that considered in [9] have required that the issue of automation be tackled on a radically different basis.

Many people hold the viewpoint that measurement must be fully computerized. It is anticipated that, by mathematically processing the grayscale value of a digital image, an application code will reveal the contour of the object's image, find the position of its center of mass, trace reference coordinate lines, calculate the center-of-mass coordinates of the object relative to the reference lines, and relate these coordinates to the unique (laboratory) coordinate system. Indeed, a code performing such functions can be devised. However, the practical implementation of this code is associated with appreciable difficulties. Photos taken in experiments are always very noisy (foreign illumination, defects of the film, stationary and moving foreign objects in the field of vision of the optical system, etc.). These gremlins attack most severely the images of fine reference lines or strokes. To separate the object's image from the reference lines when they partially overlap is basically possible, since their characteristic sizes differ considerably. However, in the automated regime, it often becomes impossible to distinguish between the images of the reference lines and those of shock waves and avoid detection of false objects. In addition, the shape of a flying object on the photo is often distorted compared with its geometrical projection because of light refraction in areas where the gradient of the density of a gas flowing about the object is high, let alone the fact that the geometrical projection may be skew-angular. Even at moderate velocities, the projection of the nose of the body turns out to be distorted because of light refraction in the shock layer and, probably, screening of light rays deflected by the holders of optical elements (in the case of imaging in transmitted light). At hypersonic velocities, additional distortions result from a visible plasma radiation in the flow. Since the distortions mentioned above are of complicated character (they depend on the flow velocity and other factors), it seems impossible to refine (correct) the coordinates of the object's center of mass that are calculated from the coordinates of the projections of the center of mass measured on the photo. These difficulties (which are evident even from general considerations) were faced by Yates [10], who made a serious effort to introduce a fully computerized system. Eventually, she was forced to conclude that wide application of her design is problematic.

The authors of this paper think that the operator must keep track of the object throughout the measuring process. Implementation of such an idea in software was outlined in work [9], which deals with interferogram processing. The key point here is provision of interaction between the operator and a software environment via the interface of a graphics editor into which the images are successively loaded. The operator "manually" assigns functional meanings to the features visible in the image according to his own comprehension of the pattern, while the measurement of the coordinates on the image and their subsequent conversion are intelligently executed in accordance with a given algorithm. Thus, the operator must (i) input (in advance) the necessary parameters of a ballistic range and initial conditions of an experiment (including the geometrical characteristics of the object), (ii) load files containing photos pertaining to the experiment (prescanning the images if necessary), and (iii) mark the positions of the reference lines (that is, the coordinate axes) and the body on each of the photos. It is clear that the primary processing of the trajectory data is aimed at determining the coordinates of the body's center of mass together with the angular orientation of the body (model). However, because of the difficulties mentioned above, direct determination of the center-of-mass coordinates from the images often lacks a desired accuracy. For this reason, the decision was made to locate the so-called characteristic point (i.e., a point on the body or in space that is uniquely related to the body), which can be identified with a desired accuracy on all the projections, and then to convert its coordinates to those of the center of mass. As such a point for a sphere, one may take the rear stagnation point, when measuring the longitudinal (along the flight path) coordinate, or the midpoint of the apparent "transverse" diameter of the sphere, when measuring its lateral deflection. For a blunted cone, this may be the point of intersection of the extensions of the cone generatrix. The characteristic point is selected at the stage of preliminary analysis of the whole body of photos related to the object under study.

A special issue in scanning of negatives is the resolution. As was shown in [9], when setting this parameter, one should take into account the properties of the optics and the specific features of the object. If imaging

consists in projecting the object onto a film without resort to lenses and other optical components (as in the ballistic range at the Ioffe Physicotechnical Institute), the resolution of the negative depends largely on the properties of the film. A 320-mm-wide isopanchromatic aerophotographic film offers a resolution on the order of 100 lines/mm. Measurements with the desired accuracy, which is as high as 0.01 mm and far exceeds the adjustment accuracy of the photographic systems used in ballistic ranges, are meaningless. Roughly estimating the standard error of coordinate measurements as 0.1 mm, we recommend setting a resolution of about 500 dpi.

The scale of electronic images can be determined by measuring that distance on the image the true length of which is known. To this end, it is most convenient to apply the image of a scale on a transparent carrier on the image of the object. One can also simultaneously scan the photo and a transparent ruler beneath it. Scanning should be accomplished on an original negative (not on a print or a copy) in order to minimize distortions (caused by optical aberrations introduced by a copier, nonuniform shrinkage of the film or paper, etc.).

To avoid losses in accuracy upon scanning, the image files are not archived and are saved in the *.bmp format. Subsequent operations are fulfilled intelligently.

SOFTWARE OF THE BALLISTIC OBJECT IMAGE METER

In terms of [9], one can speak of designing an intelligent workstation for a researcher engaged in processing of ballistic experiment data. The hardware of the work station comprises a PC (a low-end PC with a 32-Mbit RAM suffices to process data of a normal experiment), and a two-axis scanner (necessary when the images are recorded on a film). The software of the station is the Windows-32-based Pascal-written BalMeasure program package. The object-oriented principle of programming allowed us to take advantage of the previous developments [9] for the organization of the user interface, which helps an operator who is familiar with work [9] to master the new product.

Figure 1 shows the flowchart of the program for processing trajectory photos taken in the course of the flight, i.e., the results of a ballistic experiment. The dashed frame combines the program-controlled operations.

To start the program, it is necessary to have an installation file (Fig. 1, Software Installation Parameters) that describes a given ballistic range. It relates the bench marks of the recording stations to the unique coordinate system (referencing data) and contains the parameters of the photographic optics. This file includes coordinates x_i, δy, and δz of the points of intersection between two reference lines on the images (coordinate system $x'y'z'$) relative to the terrestrial coordinate system (XYZ). Included in this file are also the photofilm–light source distances (L) and photofilm–ballistic range axis distances (a) for each of the recording stations. These parameters are necessary for processing photos taken in divergent light beams (see the horizontal projection in Fig. 2, where OX is the longitudinal axis of the ballistic range and S is the light source). To avoid operator errors in generating this file, the software package contains a file-generation supervisor.

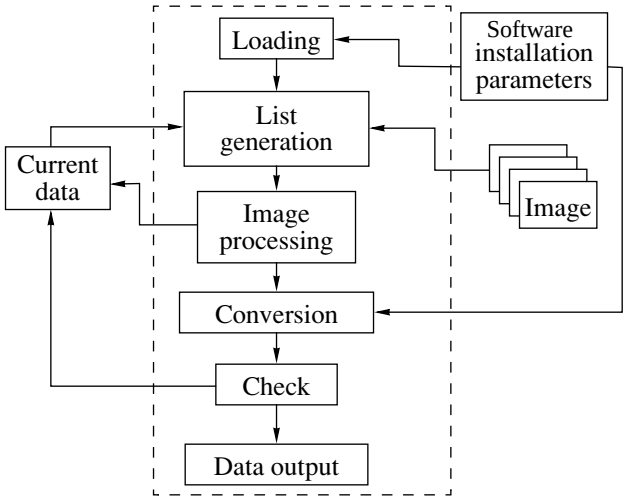

Fig. 1. Flowchart of the program for processing trajectory photos.

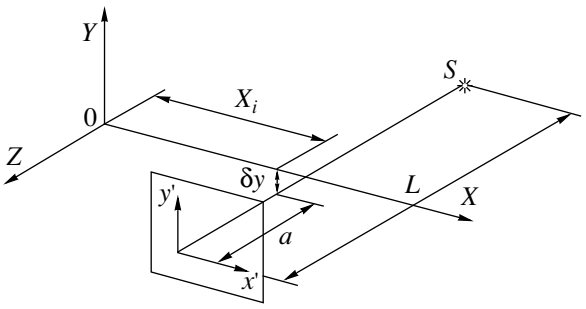

Fig. 2. Coordinate systems of the photo and ballistic range (horizontal projection).

At the first stage (Loading), the operator may either launch a new session or continue the preceding one. In the former case, it is necessary to select a ballistic range (to enter the installation file name) and enter the distances (along two axes) between the center of mass of a model and the characteristic point.

In the latter case, the referencing data and the distances mentioned above are automatically loaded from the current data file, which is generated and stored during the session (Current Data). In addition, this file contains data for the coordinates of the characteristic point in the planes of images processed, angles on inclination of the model axis, the numbers of recording stations,

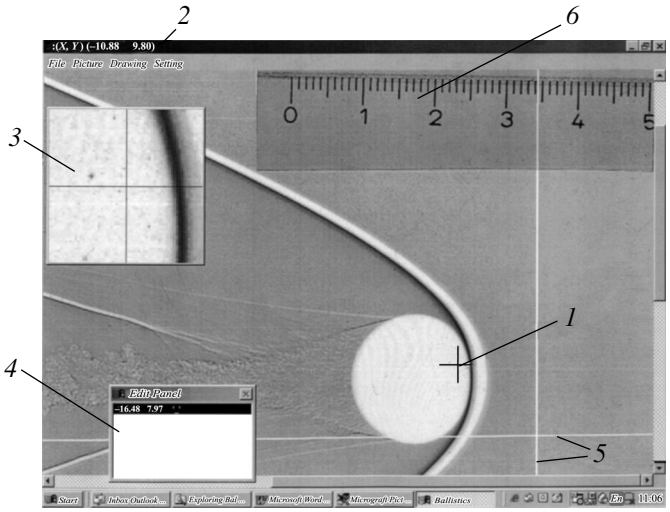

Fig. 3. Basic viewport of the BalMeasure program.

the orientation of projection planes (horizontal and vertical), and the filenames of the images on which the measurements were taken.

At the second stage (List Generation), a list of filenames for images to be processed is generated. The operator types the filenames, which are then entered into the list after the checking procedure, excluding duplicated files or files of already processed images (as was mentioned above, the information on the images processed is stored in the current data file).

The third stage consists in processing an image. At this stage, measurements are taken on the image of the model and the coordinates of the characteristic point and the angular orientation of the body axis are written into the current data file.[1] This file is refreshed after entering each new measurement; therefore, the operator can interrupt the measuring process without loss of previous results. This stage will be described in detail below.

After the list of files has been generated (though it can be augmented at any stage), the coordinates of the projections of the characteristic point (measured of the photo) are converted to the coordinates of the center of mass of the model in the ballistic range coordinate system (Conversion). At this stage, the data from the installation file, as well as the distance between the characteristic point and the center of mass, are involved.

After determination of the coordinates of the center of mass, the operator may look through the results obtained (Check), which are represented as plots of variation of the linear and angular coordinates along the axis of the ballistic range. If errors are detected, it is necessary to delete associated entries in the current data file and process the images again.

At the final stage (Data Output), each of the recording stations participating in the experiment (i.e., in photographing) is assigned its corresponding photographing time. Thus, a summary table listing the space (including angular) coordinates of a flying body and the times (the nodal points in the design of experiment) at which the measurements were taken is generated. These data are stored in a file available for further processing by the program intended for aerodynamic coefficient identification. Extracting the ADCs from free-flight trajectory data is beyond the scope of this work (see Refs. to [8]).

Among the stages listed above, the third one, image processing with a graphics editor, is generally the most labor-intensive. Let us consider how this editor may facilitate the chore of the operator.

Figure 3 shows the basic viewport of the program displaying the image of a freely flying supersonic spherical body. The editor allows one to record the coordinates (in pixels) of a current point of measurement marked by crosslike cursor *1*. The cross can be moved over the screen using a mouse or dedicated keys. The current coordinates of the cross are displayed in headline *2* of the viewport.

To observe the image in detail, its fragment near the point of measurement can be displayed in zoom window *3* with a desired magnification. If necessary, one can use text editor window *4*. The operator can move both auxiliary windows over the screen or hide any of them. The text editor accomplishes online checking of entries and sends them into the current data file.

Menu options makes it possible to observe the whole image on the screen, as well as rotate it through 90° or 180° about the horizontal and vertical axes (if the film was misoriented upon scanning).

[1] In this version of the program, roll measurements are not provided. To do this requires specific expedients to be called on in photographing that are infeasible in ballistic experiments carried out at the Ioffe Physicotechnical Institute.

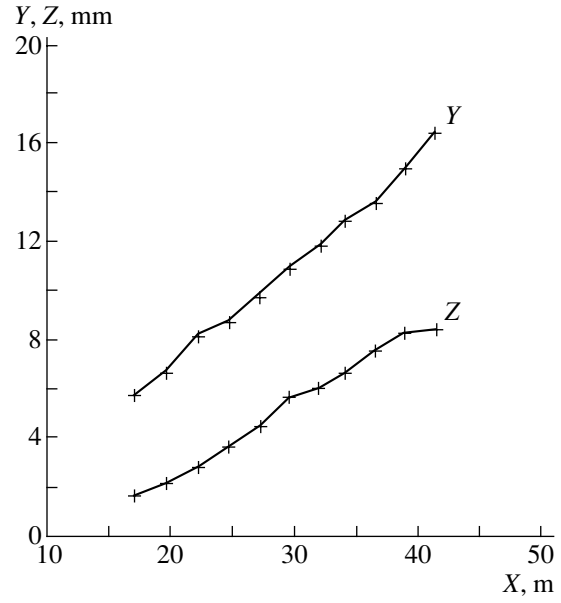

Fig. 4. Example of using the BalMeasure program: transverse coordinates *Y* and *Z* of the steel spherical body vs. flight path *X*.

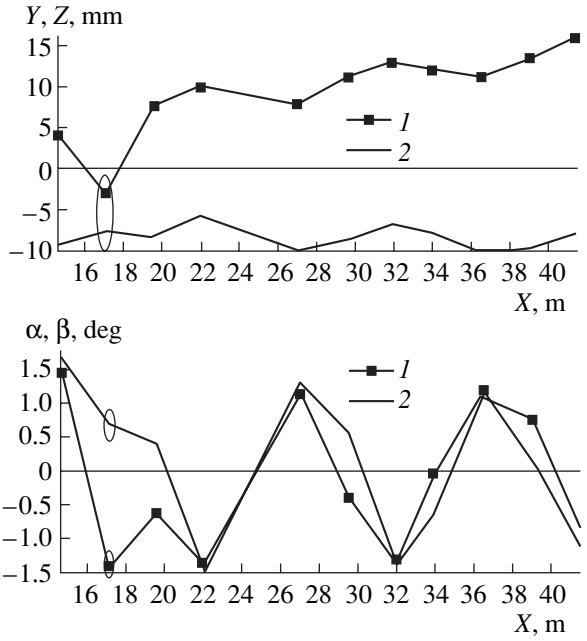

Fig. 5. Validity check provided in the BalMeasure program as applied to the intricate body trajectory. The upper plot, the transverse coordinates of the body on the (*1*) vertical and (*2*) horizontal photographic projections; the lower plot, the angular coordinates. The oval marks measurement errors (in photos taken in the recording station near $x = 17$ m).

Measurements are preceded by setting the coordinate axes. To do this, it is necessary to bring the central point of the cross into coincidence with the point of intersection of reference lines *5* on the image and fix the origin with a dedicated key. Then, the cross is placed on the horizontal reference line away from the origin and the abscissa direction is specified by another dedicated key (the "right" vertical axis is automatically issued from the origin). When imposed on the image, ruler *6* allows the operator to determine the coefficient with which the current pixel coordinates of a point of measurement is converted to the natural scale.

The graphics editor has simple means to draw straight lines and circles, dot, and measure lengths and angles, thereby allowing for elementary geometrical manipulations on the image. They may help in finding the position of the characteristic point. These means also serve to measure the slope angle of the axis of the model.

In the frame of reference of the photo, the coordinates of a point of measurement are automatically recorded by pressing the "Enter" key. In doing so, the coordinates of the point are written into the list of the text editor, each row of which is related to its corresponding point on the image: with the mouse on the row, double click carries the cursor to that point on the image whose coordinates are written in the row. In addition, the text editor allows for row handling ("insert" and "delete" operations) and makes it possible to put down short remarks at the end of the line. Taken together, all these factors appreciably facilitate geometrical constructions on the image, which are aimed at determining the coordinates of the characteristic point.

Once the characteristic point has been found and its coordinates have been written into the text editor, the slope angle of the axis of the model is measured with the two dedicated keys mentioned above. The coordinates of the characteristic point and the slope angle of the axis are then entered into the current data file (see Fig. 1) by doing the corresponding writing in the list of the text editor and pressing the "Recording" button. As this takes place, dialoguing is activated for entering the number of the recording station, type of projection (vertical or horizontal), and the sign of the slope angle (the precaution taken in the case of close-to-zero angles).

After recording the coordinates of the characteristic point, the image file next in the list of image files is automatically loaded and the same sequence of actions is repeated.

TESTING OF THE IMAGE METER

The approach implemented in the BalMeasure program package was tested in full-scale experiments with flying bodies of simple and intricate shape.

Figure 4 demonstrates the BalMeasure-assisted measurements of the transverse coordinates of a steel ball 16 mm in diameter launched with an initial velocity of 1300 m/s. Vertical coordinate *Y* of the center of mass exhibits irregular deviations from the ballistic curve, and horizontal coordinate *Z* deviates from a straight line (the rms deviations amount to 0.46 and 0.26 mm,

respectively). Since the exact equations of motion of a spherical body in air are known (approximation errors are absent), the deviations are measurement errors. They cover random errors associated with the BalMeasure meter (a human-factor inaccuracy in positioning the cross) and systematic errors resulting from misadjustment of the reference marks of the ballistic range. Joint mathematical processing of such data acquired from several launchings makes it possible to detect misadjusted recording stations and evaluate the corresponding systematic errors.

When the trajectory of an intricate body is processed for which the parameters of the equation of motion are not known in advance, the BalMeasure meter provides only monitoring of the operator's actions. For example, Fig. 5 shows the screen at the stage of checking the results of processing of all photos taken of an intricate body. The run of the curves near the third recording station is seen to be highly irregular. It turned out after checking that the negative taken in this station was scanned improperly (in the inverted position).

CONCLUSIONS

Thus, employing the intelligent meter intended for processing photos taken in the ballistic ranges at the Ioffe Physicotechnical Institute and other organizations considerably cuts the labor inputs and reduces the error rate. The adopted concept of partial automation in the interactive regime seems to be promising. The software developed has been integrated into the Arkhimed system [11], supporting a database being generated for gasdynamic phenomenon visualization [7].

ACKNOWLEDGMENTS

This work was supported by the Russian Foundation for Basic Research, grant no. 03-07-90203.

REFERENCES

1. V. A. Viktorov and G. D. Sadchikov, in *Proceedings of the 3rd Scientific Conference "Advanced Methods in Designing and Testing Rocket and Artillery Weapons," Sarov, 2003* (RFYaTs-VNIIÉF, Sarov, 2003), p. 58.
2. N. P. Mende, in *Gas Dynamics*, Ed. by Yu. I. Koptev (Nova Science, New York, 1992), pp. 325–356.
3. A. B. Podlaskin, Zh. Tekh. Fiz. **68** (6), 32 (1998) [Tech. Phys. **43**, 644 (1998)].
4. E. R. Kronberg, N. P. Mende, A. B. Samsonov, and A. I. Sedel'nikov, Preprint No. 1465, FTI (Ioffe Physicotechnical Institute, USSR Academy of Sciences, Leningrad, 1990) [in Russian].
5. *Proceedings of the 7th International Scientific and Technical Conference on Optical Methods in Flow Diagnostics, Moscow, 2003.*
6. M. I. Krutik, V. P. Maĭorov, V. V. Popov, and M. S. Semin, in *Proceedings of the 3rd Scientific Conference "Advanced Methods in Designing and Testing Rocket and Artillery Weapons," Sarov, 2003* (RFYaTs-VNIIÉF, Sarov, 2003), pp. 180–181.
7. Yu. G. Morozov, A. B. Podlaskin, and É. A. Tropp, in *Proceedings of the 7th International Scientific- and Technical Conference on Optical Methods in Flow Diagnostics, Moscow, 2003*, pp. 210–213.
8. N. P. Mende, Preprint No. 1326, FTI (Ioffe Physicotechnical Institute, USSR Academy of Sciences, Leningrad, 1989).
9. N. P. Mende, A. B. Podlaskin, and V. A. Sakharov, Zh. Tekh. Fiz. **70** (2), 110 (2000) [Tech. Phys. **45**, 251 (2000)].
10. L. A. Yates, J. Spacecr. Rockets **30**, 248 (1995).
11. Yu. G. Morozov, Candidate's Dissertation (Ioffe Physicotechnical Institute, Russian Academy of Sciences, St. Petersburg, 1996).

Translated by N. Mende

Technical Physics, Vol. 50, No. 4, 2005, pp. 421–426. Translated from Zhurnal Tekhnicheskoĭ Fiziki, Vol. 75, No. 4, 2005, pp. 37–41.

GAS DISCHARGES, PLASMA

Saturation Current Densities at the Critical Point of a Spherical Probe in a Moving Collisional Plasma with Negative Ions or Dust Grains

A. V. Kashevarov

Zhukovsky Central Institute of Aerohydrodynamics, Zhukovsky, Moscow oblast, 140180 Russia
e-mail: kash@dept.aerocentr.msk.su

Received February 18, 2004

Abstract—The problem is considered of the probe diagnostics of a moving, weakly ionized, collision-dominated plasma containing singly charged negative ions or dust grains (heavy multicharged ions). Based on an asymptotic analysis, expressions are obtained that describe the saturation current densities of the electrons and of the charged particles of other species at the point where the plasma flowing around a spherical probe in the laminar boundary layer regime stagnates. *© 2005 Pleiades Publishing, Inc.*

INTRODUCTION

Electric probes are widely utilized to diagnose various plasmas, in particular, a dense plasma containing negative ions [1, 2] or charged dust grains [3]. One of the problems in such a diagnostics is that of interpreting probe measurement data. The operation of a probe in a flow of a collision-dominated plasma is described by a set of partial differential equations [4]. The solution to these equations, which provides the basis for determining the relationship between the probe current and the charged particle density, can generally be obtained only numerically. Numerical investigations are, in turn, complicated by the fact that the problem involves small and large parameters that describe the formation of boundary layers and account for essentially different scales on which the electric and hydrodynamic quantities vary. This is why the saturation currents are usually calculated as certain limiting currents to the probe under the assumption that its potential is high.

When the plasma also contains negatively charged ions (in addition to electrons and positive ions), the problem becomes even more complicated. The only case in which its analysis is relatively easy is that of a spherical probe in a chemically inactive immobile plasma. In [4], it was shown that, when singly charged negative ions are present in a plasma, they have no effect on the processes whereby the probe collects charged particles of other species, i.e., they do not change the dimensionless currents of the electrons and positive ions to the probe surface (see also [5]).

The effect of negative ions on the current–voltage (*I–V*) characteristic of a probe in a chemically inactive moving plasma was investigated in [6, 7] by asymptotic and numerical methods. In those two papers, a study was made of an incompressible plasma flowing parallel to the surface of a probe in the form of a planar wall in the boundary layer regime. It was found that, while negative ions exert their primary effect on the electron current, they only insignificantly increase the current of positive ions. Similar results were obtained by Benilov *et al.* [1] in calculating the saturation current of positive ions to a spherical and a cylindrical probe in a moving plasma with several species of negative ions that result from chemical reactions occurring in the products of combustion of a carbon-based fuel with an easily ionizable additive. Papers [1, 6, 7], however, do not contain diagnostic formulas accounting for the presence of negative ions.

Such a formula that describes the ratio between the currents of negative and positive ions to the probe surface as a function of the ratio between the densities of negative ions and electrons was obtained by Vlasov *et al.* [2] based on the results of calculating the *I–V* characteristic of a cylindrical probe in a chemically active immobile plasma. This formula, however, seems to be of somewhat doubtful validity because, in this case, the question of the solvability of the boundary-value problem for the basic set of equations [8] arises (in [2] this question was not analyzed).

In recent years, a great deal of attention has been devoted to a so-called dusty plasma (an ionized gas containing a dust component), in which the dust grains can acquire large electric charges and thereby can form spatially ordered structures [3, 9, 10]. The theory of a probe in a dusty plasma began to be developed in my recent paper [5] for a simple case of a spherical probe in an immobile plasma. The dust grains were treated as an additional plasma component consisting of very heavy ions that carry a large negative charge. In the present work, this assumption is used to investigate how the dusty plasma motion affects the saturation current densities at the critical point of a spherical probe.

1063-7842/05/5004-0421$26.00

The plasma with singly charged negative ions is considered here as a limiting case. In what follows, a formula that is similar to the formula obtained in [2] and describes the ratio between the saturation current densities of negatively and positively charged particles will be derived analytically for certain limiting values of the parameters of the problem.

FORMULATION OF THE PROBLEM

We consider a steady-state laminar incompressible flow of a chemically inactive, thermally equilibrium, weakly ionized, collisional plasma around a spherical probe. We assume that the plasma consists of neutral particles, electrons, singly charged positive ions, and negatively charged dust grains with a fixed charge number Z. We also assume that the temperature of the probe surface is the same as the plasma temperature (the uncooled probe model), so the plasma transport properties remain unchanged. The coefficients of diffusion and mobility of charged particles are related by the Einstein relationship. Under these conditions, the set of dimensionless probe equations has the form

$$ReSc_i(\mathbf{u}\nabla)n_i - \nabla(\nabla n_i - n_i\nabla\psi) = 0, \quad (1)$$

$$\beta_d ReSc_i(\mathbf{u}\nabla)n_d - \nabla(\nabla n_d + Zn_d\nabla\psi) = 0, \quad (2)$$

$$\beta_e ReSc_i(\mathbf{u}\nabla)n_e - \nabla(\nabla n_e + n_e\nabla\psi) = 0, \quad (3)$$

$$\alpha^2\nabla^2\psi = n_i - \gamma n_e - (1-\gamma)n_d. \quad (4)$$

Here, the number densities of the positive ions, dust grains, and electrons, n_i n_d, and n_e, are normalized to their values N_i, N_d, and N_e at infinity; the dimensionless electric potential ψ is related to the dimensional potential φ by the formula $\psi = -e\varphi/kT$ (where e is an elementary charge, k is Boltzmann's constant, and T is the plasma temperature); and $\mathbf{u}$ is the field of the flow velocity normalized to its value U_∞ at infinity. The spatial variables are expressed in units of a characteristic dimension, whose role is played by the probe radius R.

The problem involves the following parameters: the hydrodynamic Reynolds number $Re = U_\infty R/\nu$ (where ν is the kinematic viscosity coefficient); the ion Schmidt number $Sc_i = \nu/D_i$ (where D_i is the diffusion coefficient of the positive ions); the ratios of the diffusion coefficients, $\beta_d = D_i/D_d$ and $\beta_e = D_i/D_e$; the ratio of the densities of electrons and positive ions at infinity, $\gamma = N_e/N_i$; and the ratio of the Debye radius to the probe radius, $\alpha = \lambda_D/R$. The Debye radius is defined by $\lambda_D = \sqrt{\varepsilon_0 kT/N_i e^2}$, where ε_0 is the dielectric constant of empty space. Equation (4) is written using the quasineutrality condition at infinity, $N_i = N_e + ZN_d$.

The boundary conditions for Eqs. (1)–(4) at the surface $r = 1$ of a spherical probe with the potential ψ_p have the form

$$n_i = n_d = n_e = 0, \quad \psi = \psi_p, \quad (5)$$

the conditions at infinity ($r \longrightarrow \infty$) being

$$n_i \longrightarrow 1, \ n_d \longrightarrow 1, \ n_e \longrightarrow 1, \ \psi \longrightarrow 0. \quad (6)$$

Under ordinary circumstances, the ion Schmidt number is about unity, $Sc_i \cong 1$, and the ratio of the diffusion coefficients of the ions and electrons is $\beta_e \ll 1$. For singly charged negative ions, the ratio of the diffusion coefficients of the ions and dust grains is $\beta_d \cong 1$ and, for grains with a charge number of $Z \gg 1$, this parameter is $\beta_d \gg 1$.

We assume that the Reynolds number of the plasma flow around the probe is much higher than unity, $Re \gg 1$, and that the Debye radius is small in comparison to the probe radius, $\alpha \ll 1$. We also require that the relative fraction of electrons in the plasma flow incident on the probe be small, $\gamma \ll 1$, or, more precisely, $\gamma \longrightarrow 0$. It is instructive to consider this limiting case for the following two reasons. First, the electron contribution to the total current of negatively charged particles to the probe is proportional to γ/β_e, and, accordingly, it can be important because the parameter β_e is small (under the additional assumption that $\beta_e \longrightarrow 0$). Second, in studying this case, one can determine the greatest possible effect of negative ions on the current of positive ions. Note that, in a plasma with negatively charged dust, the electron density is indeed substantially reduced.

Let us find the saturation current densities of the charged particles of different species at the point where the plasma flow stagnates. Formally, the currents saturate in the limiting case such that $|\psi_p| \longrightarrow \infty$ and $\alpha \longrightarrow 0$.

ION (DUST GRAIN) SATURATION CURRENT DENSITY

The requirement $\gamma \longrightarrow 0$ allows us to ignore the term γn_e in Eq. (4), so the first stage in solving the problem is to exclude Eq. (3) from consideration. The problem can thus be analyzed in essentially the same way as was done in my earlier paper [11] for a plasma without negative ions.

For $\alpha \ll 1$, Eq. (4) implies that the plasma is quasineutral, $n_i \cong n_d = n$, over almost the entire space, except for a thin space-charge sheath near the probe. In the field of a flow such that $Re \gg 1$, we can distinguish between an inviscid region and a viscous boundary sheath.

For the inviscid region, the solution to Eqs. (1), (2), and (4) that satisfies boundary conditions (6) is given by the relationships

$$n_i = 1, \quad n_d = 1, \quad \psi = B/r, \quad (7)$$

where B is a constant to be determined and r is the radial coordinate. In the viscous boundary layer, the variations in the densities n_i and n_d along the stagnation lines are described by the ordinary differential equations

$$ReSc_i v(y)\frac{dn_i}{dy} - \frac{d}{dy}\left(\frac{dn_i}{dy} - n_i\frac{d\psi}{dy}\right) = 0, \quad (8)$$

$$\beta_d ReSc_i v(y)\frac{dn_d}{dy} - \frac{d}{dy}\left(\frac{dn_d}{dy} + Zn_d\frac{d\psi}{dy}\right) = 0. \quad (9)$$

These equations are derived from Eqs. (1) and (2) by taking the limit $Re \longrightarrow \infty$ and $y \longrightarrow 0$ in such a way that the product $yRe^{1/2}$ is finite and then by making the replacement $r = 1 + y$.

According to the boundary sheath theory [12], the distribution of the transverse velocity component $v(y)$ about the critical velocity of a plasma flow around a sphere has the form

$$v(y) = -3^{-1/2}Re^{-1/2}f_1(\eta), \quad \eta = 3^{1/2}Re^{1/2}y, \quad (10)$$

where $f_1(\eta)$ is a known function—the coefficient in the first term in the Blasius series.

We assume that the space-charge sheath is much thinner than the viscous boundary layer, so the plasma is quasineutral over most of the volume of the latter. With allowance for distribution (10), we obtain from Eqs. (8) and (9) the following equation for the plasma density distribution in the boundary layer:

$$Scf_1(\eta)\frac{dn}{d\eta} + \frac{d^2n}{d\eta^2} = 0,$$

where $Sc = (\beta_d + Z)Sc_i/(1 + Z)$ is the ambipolar Schmidt number.

The solution to this equation that passes over to solution (7) in the limit $\eta \longrightarrow \infty$ is given by the relationships

$$n = 1 - cI(Sc) + c\int_0^\eta \exp\{-ScF_1(\eta)\}d\eta,$$
$$I(Sc) = \int_0^\infty \exp\{-ScF_1(\eta)\}d\eta, \quad F_1(\eta) = \int_0^\eta f_1(\eta)d\eta, \quad (11)$$

where c is a constant of integration.

For $\eta \ll 1$, we again switch to the variable y in order to write solution (11) in the following approximate form:

$$n \cong 1 - cI(Sc) + c3^{1/2}Re^{1/2}y. \quad (12)$$

On the other hand, near the probe, we have $v(y) \longrightarrow 0$ as $y \longrightarrow 0$. Consequently, ignoring the first term in each of Eqs. (8) and (9) and integrating them, we find

$$\frac{dn_i}{dy} - n_i\frac{d\psi}{dy} = j_i, \quad (13)$$

$$\frac{dn_d}{dy} + Zn_d\frac{d\psi}{dy} = j_d, \quad (14)$$

where j_i and j_d are the dimensionless current densities of the positively charged ions and negatively charged dust grains (very heavy ions) at the flow stagnation point.

We multiply Eq. (13) by Z, sum it up with Eq. (14), and integrate the resulting equation to obtain the following expression for the densities of the charged particles of a quasineutral plasma near the probe:

$$n = A + \frac{Zj_i + j_d}{1 + Z}y = \frac{Zj_i + j_d}{1 + Z}(y - y_s), \quad (15)$$

where A is a constant of integration and $y_s = (1 + Z)A/(Zj_i + j_d)$ is the conditional coordinate of the boundary of the space-charge sheath. Comparing expressions (16) and (12) yields

$$c = 3^{-1/2}Re^{-1/2}(Zj_i + j_d)/(1 + Z), \quad A = 1 - cI(Sc).$$

The saturation current densities are obtained from expression (15) by satisfying the boundary condition $n \longrightarrow 0$ at $y \longrightarrow 0$. We then have $A \longrightarrow 0$; this implies that $y_s \longrightarrow 0$, i.e., that the space-charge sheath degenerates, which corresponds to $\alpha \longrightarrow 0$. Taking the limit $j_i \longrightarrow 0$ or $j_d \longrightarrow 0$, which corresponds to infinitely large absolute values of the probe potential, $|\psi_p| \longrightarrow \infty$, we arrive at the following expressions for the saturation current densities j_1^* and j_d^*:

$$j_i^* = (1 + Z^{-1})3^{1/2}Re^{1/2}/I(Sc), \quad j_d^* = Zj_i^*. \quad (16)$$

For negative ions, and for $Z = 1$ and $\beta_d \cong 1$, the ambipolar Schmidt number is $Sc \cong 1$. For $Sc \leq 1$, the dependence $I(Sc)$ is approximated by the formula [11]

$$I(Sc) = (\pi/2)^{1/2}Sc^{-1/2}(1 + 0.405Sc^{0.427}). \quad (17)$$

Expression (16) with $Z = 1$ also describes the saturation current density of the positive ions in a plasma containing no negative ions. In this case, we have $Sc \cong 0.5$. From formula (17), we obtain $I(1) \approx 1.76$ and $I(0.5) \approx 2.31$. We thus see from formulas (16) and (17) that, in a plasma containing negative ions, the saturation current density of positive ions is higher than that in the absence of negative ions by at most 31%.

For dust grains, we have $Z \gg 1$ and $\beta_d \gg 1$. For instance, under conditions of probe experiments in a flame plasma, the diffusion coefficient of the positive ions is about $D_i \sim 5$ cm^2/s, while the coefficient of diffusion of dust grains of radius 1 μm is about $D_d \sim 2 \times$

10^{-7} cm^2/s [5], which gives $\beta_d \sim 2.5 \times 10^7$. The charge number Z of the grains ranges between 10^2 and 10^5 [3], so the ambipolar Schmidt number for a dusty plasma is $Sc \cong \beta_d/Z \gg 1$.

For $Sc \gg 1$, the integrand in the integral $I(Sc)$ decreases abruptly and the value of the integral is determined by the behavior of the integrand in the vicinity of zero. We expand the function $F_1(\eta)$ from relationships (11) in a Taylor series in this vicinity and take into account the fact that $f_1(0) = f_1'(0) = 0$ to obtain the expression

$$I(Sc) = \int_0^\infty \exp[-Sc\, f_1''(0)\eta^3/6]d\eta = \frac{2^{1/3}}{3^{2/3}[f_1''(0)]^{1/3}Sc^{1/3}}\Gamma\left(\frac{1}{3}\right) \approx 2.35Sc^{-1/3}, \quad (18)$$

in which we used the value of the gamma function $\Gamma(1/3) \approx 2.68$ and the approximate equality $f_1''(0) \approx 0.332$ [12].

For $Z = 10^3$, expression (18) yields $I(2500) \approx 0.08$. In this case, we find from expressions (16) that, in the presence of dust grains, the saturation current density of positive ions can be 14.4 times higher than that in the absence of dust. It is of interest to note that, for an immobile dusty plasma, this current density is predicted not to increase but to decrease by a factor of up to two [5].

The dimensional density J_i^* of the ion saturation current is related to its dimensionless density by the relationship $J_i^* = eN_iD_i j_i^*/R$.

ELECTRON SATURATION CURRENT DENSITY

In order to determine the electron saturation current, it is necessary to investigate the behavior of the electric potential. Combining Eqs. (8) and (9) so as to eliminate the convective terms and integrating the resulting equation yields the following expression, which is valid over the entire quasineutral region of the viscous boundary layer:

$$\psi = \frac{\beta_d - 1}{\beta_d + Z}\ln n + b_1\int\frac{dy}{n} + b_2, \quad (19)$$

where b_1 and b_2 are constants of integration.

At the boundary of the viscous layer, we have $n \longrightarrow 1$ as $y \longrightarrow \infty$, so dimensionless electric potential (19) behaves as

$$\psi \longrightarrow b_1 y + b_2. \quad (20)$$

This indicates that the electric field does not vanish at the boundary of the viscous layer and penetrates into the external inviscid flow. In expressions (7) for the potential in the inviscid region, we switch from the variable r to the variable y in order to represent the potential in the viscous boundary layer as

$$\psi = B(1 - y).$$

Comparing this representation with formula (20), we find that $b_2 = -b_1 = B$.

Equations (13) and (14) immediately yield the expression for the electric potential in the quasineutral region near the probe:

$$\psi = -\lambda\ln\left[\frac{Zj_i + j_d}{1 + Z}(y - y_s)\right] - b_1, \qquad \lambda = \frac{j_i - j_d}{Zj_i + j_d}. \quad (21)$$

The constant b_1 can be found by substituting expression (16) for n into solution (19) and then by comparing expression (21) with the resulting solution:

$$b_1 = (j_d - \beta_d j_i)/(Z + \beta_d). \quad (22)$$

After we have determined the behavior of the electric potential in the three zones of the quasineutral region, namely, in the near and far zones of the viscous boundary layer and in the external inviscid flow, we can turn to an analysis of the remaining equation (3) for the electron density.

For $\beta_e \longrightarrow 0$, we integrate Eq. (3) along the stagnation line and obtain

$$dn_e/dr + n_e d\psi/dr = j_e/r^2, \quad (23)$$

where j_e is the dimensionless electron current density at the critical point.

For an external inviscid flow, in which $\psi = -b_1/r$, we find the following solution that satisfies boundary conditions (6):

$$n_e = j_e/b_1 + (1 - j_e/b_1)\exp(b_1/r).$$

Switching to the boundary layer variable y and taking the limit $y \ll 1$, we arrive at the following representation for the external solution in the boundary layer region:

$$n_e = j_e/b_1 + (1 - j_e/b_1)\exp(b_1)\exp(-b_1 y). \quad (24)$$

On the other hand, in the viscous boundary layer region, we have, instead of Eq. (23), the equation

$$dn_e/dy + n_e d\psi/dy = j_e,$$

which has the general solution

$$n_e = e^{-\psi}(C + j_e\int e^{\psi}dy), \quad (25)$$

where C is a constant of integration.

Inserting formula (20) for ψ into Eq. (25), we determine how the electron density behaves at the boundary of the viscous layer as $y \longrightarrow \infty$:

$$n_e \longrightarrow j_e/b_1 + C\exp(b_1)\exp(-b_1 y).$$

Comparing this behavior with that described by formula (21), we find the constant of integration:

$$C = 1 - j_e/b_1.$$

Substituting expression (21) for ψ into solution (25), we obtain the distribution of the electron density n_e in the quasineutral region near the probe:

$$n_e = C\exp(b_1)\left(\frac{Zj_i + j_d}{1+Z}\right)^{\lambda}(y-y_s)^{\lambda} + \frac{j_e}{1-\lambda}(y-y_s). \quad (26)$$

The electron saturation current can be deduced from the condition $n_e = 0$ at $y = 0$ by taking into account the relationships $j_i = 0$, $j_d = j_d^*$, and also $y_s = 0$. In this case, expression (21) gives $\lambda = -1$. In order to avoid a singularity in distribution (26), we must set $C = 0$. As a result, with allowance for expressions (22) and (16), we arrive at the relationship

$$j_e^* = j_d^*/(Z+\beta_d) = Zj_i^*/(Z+\beta_d).$$

The dimensionless density J_e^* of the electron saturation current is defined by $J_e^* = eN_eD_ej_e^*/R = e\gamma N_iD_ej_e^*/R$, and the dimensionless density J_d^* of the saturation current of negatively charged ions or dust grains, by $J_d^* = eZN_dD_dj_d^*/R = e(1-\gamma)N_iD_dj_d^*/R$ (in [5], the formula relating the dimensionless saturation current of the dust grains to their dimensional saturation current was given somewhat inaccurately, with the result that the contribution from the dust to the total dimensional saturation current of negatively charged particles was overestimated by a factor of Z).

We introduce the ratio $\Im = (J_e^* + J_d^*)/J_i^*$ through the relationship

$$\Im = \frac{\gamma}{\beta_e(1+\beta_d/Z)} + \frac{1-\gamma}{\beta_d/Z}, \quad (27)$$

in which the first term accounts for the electron contribution to the total current of negatively charged particles.

In a particular case of negative ions, $\beta_d/Z \cong 1$, we ignore the density ratio γ in comparison with unity to reduce relationship (27) to

$$\Im \approx \gamma/2\beta_e + 1.$$

Setting $\gamma = 0.05$ and assuming that the parameter β_e is equal to $\beta_e = 1.7 \times 10^{-3}$ [5], we obtain the estimate $\Im \approx 15.7$, in which the electron contribution to the total current is 14.7 times greater than the contribution of negative ions, even though the relative fraction of electrons in the plasma is low. It is known that, for a plasma containing no negative ions, the ratio just introduced is equal to $\Im = 1/\beta_e$ (regardless of the shape of the probe); i.e., for the adopted parameter values, we have $\Im = 588$. Measurements by, e.g., a cylindrical probe in a plasma with a sodium additive [13] showed that the electron saturation current is only seven times higher than the ion saturation current; this provides evidence of production of a large amount of negative ions near the colder part of the probe surface.

For a dust plasma component such that $\beta_d/Z \gg 1$, we obtain

$$\Im \approx (Z/\beta_d)(\gamma/\beta_d + 1).$$

This indicates that the electron contribution to the total current of negatively charged particles is two times higher than that in the case of negative ions. However, the saturation current of positive ions substantially exceeds the total saturation current of negatively charged particles. Thus, for $Z = 10^3$ and $\beta_d = 2.5 \times 10^7$ and for the above values of γ and β_e, we have $\Im \approx 1.2 \times 10^{-3}$, so the saturation current of positive ions is 800 times higher than that of negatively charged particles.

In order to make the description more complete, we also present the value of the parameter $\Im$ for a spherical probe in an immobile dusty plasma [5]:

$$\Im \approx 2\gamma/\beta_e + Z/\beta_d.$$

We see that, in this case, negatively charged dust grains make a negligibly low contribution to the total current. For the parameter values adopted for estimates, we have $\Im \approx 60$.

CONCLUSIONS

The results of the above theoretical investigation show that, in a moving high-density plasma containing negatively charged dust grains, the saturation current density of positive ions at the critical point of a spherical probe should be significantly higher than that in the absence of dust. In a plasma with singly charged negative ions, the saturation current density of positive ions only slightly exceed that in a plasma containing no negative ions. The value of the ratio between the saturation current densities of negatively and positively charged particles can help to judge whether or not negatively charged ions or dust grains are present in the plasma.

ACKNOWLEDGMENTS

This work was supported in part by INTAS, grant no. 1817.

REFERENCES

1. M. S. Benilov, V. F. Kosov, B. V. Rogov, and V. A. Sinel'shchikov, Teplofiz. Vys. Temp. **25**, 573 (1987).
2. P. A. Vlasov, Yu. K. Karasevich, I. L. Pankrat'eva, and V. A. Polyanskiĭ, Teplofiz. Vys. Temp. **26**, 1047 (1988).
3. A. P. Nefedov, O. K. Petrov, and V. E. Fortov, Usp. Fiz. Nauk **167**, 1215 (1997) [Phys. Usp. **40**, 1163 (1997)].
4. P. M. Chung, L. Talbot, and K. J. Touryan, *Electric Probes in Stationary and Flowing Plasmas* (Springer-Verlag, New York, 1975; Mir, Moscow, 1978).
5. A. V. Kashevarov, Teplofiz. Vys. Temp. **40**, 702 (2002).
6. K. J. Touryan and P. M. Chung, AIAA J. **9**, 365 (1971).
7. P. B. Bailey and K. J. Touryan, AIAA J. **11**, 1225 (1973).
8. A. V. Kashevarov, Uch. Zap. TsAGI **34** (3–4), 59 (2003).
9. V. N. Tsytovich, Usp. Fiz. Nauk **167**, 57 (1997) [Phys. Usp. **40**, 53 (1997)].
10. A. M. Ignatov, Usp. Fiz. Nauk **171**, 213 (2001) [Phys. Usp. **44**, 199 (2001)].
11. A. V. Kashevarov, Teplofiz. Vys. Temp. **39**, 381 (2001).
12. H. Schlichting, *Boundary Layer Theory*, 6th ed. (McGraw-Hill, New York, 1968; Nauka, Moscow, 1974).
13. Z. M. Egorova and A. V. Kashevarov, Prikl. Mekh. Tekh. Fiz. **34** (2), 3 (1993).

Translated by O. Khadin

Technical Physics, Vol. 50, No. 4, 2005, pp. 427–433. Translated from Zhurnal Tekhnicheskoĭ Fiziki, Vol. 75, No. 4, 2005, pp. 42–47.

GAS DISCHARGES, PLASMA

Ion Emission from a Hollow-Cathode Discharge with the Plasma Penetrating into the High-Voltage Acceleration Gap

A. P. Semenov

Buryat Scientific Center, Siberian Division, Russian Academy of Sciences, Ulan-Ude, 670047 Russia
e-mail: semenov@pres.bsc.buryatia.ru

Received March 9, 2004

Abstract—The general features of ion emission from a gas-discharge plasma are considered under conditions such that the plasma penetrates into the acceleration gap. It is found that the wall sheath limiting the open plasma surface substantially affects the stability of the penetrating plasma. It is shown that there are two plasma states with different positions of the plasma boundary. The stable state corresponds to the inequality $r/R > 0.54$, where r is the plasma radius in the accelerating electrode and R is the radius of the aperture of the accelerating electrode. It is shown that the plasma–sheath system within the aperture of the accelerating electrode can exist only if the voltage drop across the sheath does not exceed a certain limiting voltage, which depends on the plasma parameters. *© 2005 Pleiades Publishing, Inc.*

INTRODUCTION

According to the Bohm condition, the ion emission current is defined by the formula

$$I_i = 0.4en_i(2kT_eM_i^{-1})^{1/2}S, \quad (1)$$

where n_i is the plasma density, T_e is the electron temperature, k is the Boltzmann constant, M_i is the ion mass, e is the electron charge, and S is the area of the emitting plasma surface; i.e., the emission current depends on the plasma density and electron temperature.

The ion emission current also depends on the distributions of the electric and magnetic fields within the discharge gap and the emission channel, as well as on the channel dimensions [1]. At a given discharge current, the ion emission current can naturally be increased by enlarging the area of the emitting plasma at a fixed plasma density. However, an attempt to enlarge this area by increasing the channel radius under the conditions such that $r_1 \gg l_1$ holds (where r_1 is the channel radius and l_1 is the length of the cathode fall region) leads to the break of the ion sheath in front of the emission channel. As a result, the plasma freely flows out of the discharge gap and expands into the equipotential space [2] and a discharge regime is established in which the plasma fills the acceleration gap [3]. In such a situation, the extraction of ions can be achieved by "contracting" the plasma, i.e., by creating conditions under which no stable plasma–sheath system can exist within the wide aperture of the accelerating electrode [4]. Instability of the plasma penetrating into the acceleration gap makes it possible to stably extract ions through a wide aperture in the cathode without stabilizing the emitting plasma surface by a grid. This allows one to create wide-aperture ion sources without fine-mesh emitting electrodes. Under these conditions, charged particles can be extracted from the discharge plasma through an aperture in the accelerating electrode, the aperture diameter being at least no less than the transverse dimensions of the emission channel. In this case, the length of the acceleration gap turns out to be much shorter than the aperture diameter. Below, we will consider the extraction of charged particles (ions) from the plasma penetrating into the acceleration gap under conditions such that there is no stable plasma–sheath system within the aperture of the accelerating electrode.

EXPERIMENTAL TECHNIQUES

Figure 1 shows the schematic of the electrode system that allows one to produce a plasma penetrating into the acceleration gap. A low-pressure hollow-cathode discharge was excited between hollow (*1*) and annular (*2*) cathodes and a cylindrical anode (*3*). The magnetic field at the axis of the cylindrical anode was ~0.1 T, the discharge current was 50–100 mA, and the discharge voltage was ~350 V. The working gas was argon. The gas pressure in the acceleration gap between cathode *2* and accelerating electrode *4* was $\sim 7.3 \times 10^{-2}$ Pa. The plasma density was $n_l \sim 5.2 \times 10^{16}$ m^{-3}, and the electron temperature was $T_e \sim 3.5 \times 10^4$ K (the temperature was estimated from the electron and ion saturation currents of a single cylindrical probe placed within the aperture of the accelerating electrode). The emission channel was a cavity whose diameter coincided with the anode diameter (20 mm). The channel height was 4 mm. The dimensions and shape of the channel were chosen such that we could create conditions under which the 26-mm-diameter aperture in the accelerating electrode contained both the plasma

1063-7842/05/5004-0427$26.00 © 2005 Pleiades Publishing, Inc.

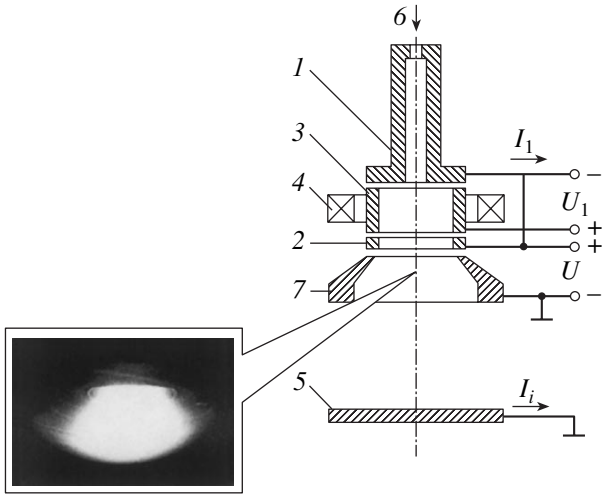

Fig. 1. Schematic of the electrode system and the glow of the plasma penetrating into a vacuum through the accelerating electrode: (*1*) hollow cathode, (*2*) annular cathode, (*3*) cylindrical anode, (*4*) permanent annular magnet, (*5*) collector, (*6*) channel for gas admission, and (*7*) accelerating electrode.

and the space charge sheath separating the plasma from the cavity wall. The length of the acceleration gap was 3 mm. Ion collector *5* was located a distance of 100 mm from the cathode. When measuring the ion current at the collector, we took into account the current produced by the secondary electrons. In addition to direct measurements of the ion current, optical radiation of the penetrating plasma was output through a special window and was recorded by a Digital Stil Camera. Rectifiers with output voltages that could be varied in the ranges 0–1.5 and 0–10 kV were used as power supplies.

EXPERIMENTAL RESULTS

Figure 2 shows a typical current–voltage (*I–V*) characteristic indicating the existence of two types of discharges in the electrode system shown in Fig. 1: a high-voltage low-current discharge (reflex discharge) and a low-voltage high-current discharge (hollow-cathode discharge). Our experiments have shown that a high-voltage discharge changes to a low-voltage one (the glow inside the cylindrical anode changes to the glow inside the hollow cathode) by a jump at low pressures and with no jump at high pressures (>2.6 Pa). In the latter case, it is difficult to distinguish these two types of discharge, because even a slow increase in the voltage immediately initiates a hollow-cathode discharge. The effect of the hollow cathode depends on the ratio between the area of the emitting inner surface of the cavity and the area of the aperture that determines the electron and ion losses [5]. At low pressures, when the voltage was decreased to the level corresponding to the disruption of the discharge in the cathode cavity, the discharge glow disappeared not only in the cathode cavity but also in the cylindrical anode, i.e., the quenching of the discharge in the cathode cavity was accompanied by the quenching of the discharge in the cylindrical anode. Attempts to achieve a continuous transition from a low-voltage to a high-voltage discharge by decreasing the voltage did not meet with success. Obviously, at low pressures, a transition is only possible from a high-voltage to a low-voltage discharge.

The high-voltage and low-voltage discharges have different current distributions between the cathodes. In a high-voltage discharge, the current is distributed in equal shares between the annular cathode and the end of the hollow cathode. When a high-voltage discharge transforms into a low-voltage one, the distribution of the discharge current changes significantly (Fig. 3). Our experiments have shown that the fraction of the discharge current I_1 flowing through the anode–hollow cathode circuit reaches ~0.9. For low-voltage discharges, the ratio between the cathode currents is constant and equal to ~8.5 over the entire current range under study.

Figure 4 shows the ignition voltage of the hollow-cathode discharge as a function of the pressure. It can be seen that the ignition voltage decreases rapidly with increasing pressure. At a pressure of $\sim 6 \times 10^{-1}$ Pa, the decrease becomes more gentle and, at pressures of $p > 6 \times 10^{-1}$ Pa, the ignition voltage decreases only slightly. Thus, there are high- and low-pressure ranges within which the pressure dependences of the ignition voltage are weak and strong, respectively. In the low-pressure range ($p < 6 \times 10^{-1}$ Pa), the ignition voltage of a hollow-cathode discharge is fairly high; in particular, at pressures of $p < 3.6 \times 10^{-1}$ Pa, it is higher than 1 kV. In the high-pressure range ($p \geq 6 \times 10^{-1}$ Pa), the ignition voltage is lower than 0.5 kV.

The pressure dependence of the hollow-cathode discharge current (see Fig. 5) shows that the current gradually decreases with decreasing pressure to a level of $\sim 3.6 \times 10^{-1}$ Pa. A further decrease in the pressure results in the disruption of the discharge. In this case, the discharge glow disappears not only in the cathode cavity but also in the cylindrical anode. As the pressure is decreased at a fixed current, the discharge voltage varies only slightly and increases only as p approaches the level at which the discharge is quenched.

Figure 6 shows the ion current at the collector as a function of the accelerating voltage at a discharge voltage of ~350 V and discharge current of 0.1 A. There are three characteristic regions corresponding to the high-voltage glow discharge (segment *AB*), the extraction of an ion beam (segment *CE*), and the fast transition from the ion current of the penetrating plasma to the ion emission current and back (segments *BC* and *DA*, respectively). Let us consider the dependence of the collector current on the accelerating voltage, $I_1(U)$, in more detail (Fig. 6). At $U = 0$, the ion current at the collector is 2 mA. The presence of a nonzero current indicates that the ion sheath in front of the emission aper-

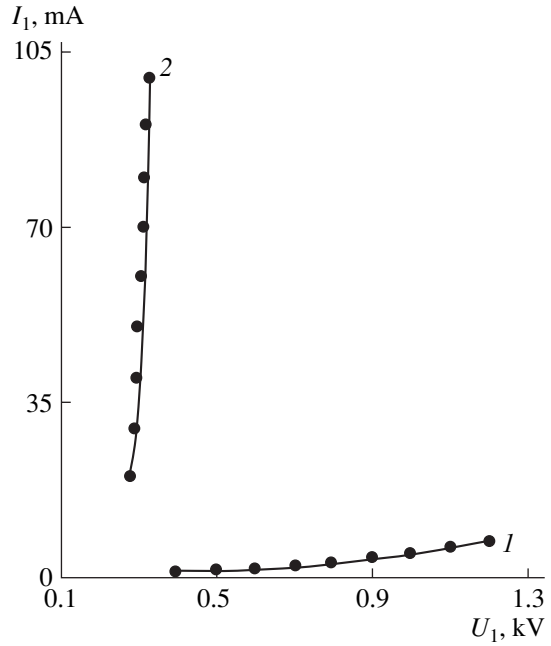

Fig. 2. *I–V* characteristics of the discharge for gas pressures of $p = 3.6 \times 10^{-1}$–8 Pa: (*1*) reflex discharge and (*2*) hollow-cathode discharge.

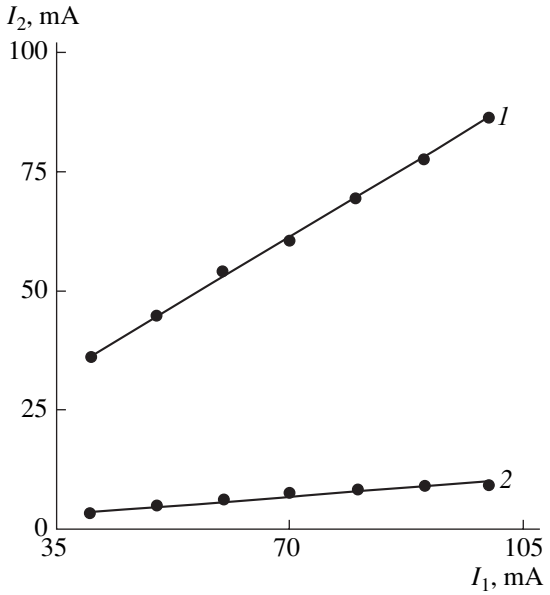

Fig. 3. Currents through the (*1*) hollow and (*2*) annular cathodes as functions of the hollow-cathode discharge current at $p = 7.3 \times 10^{-2}$ Pa.

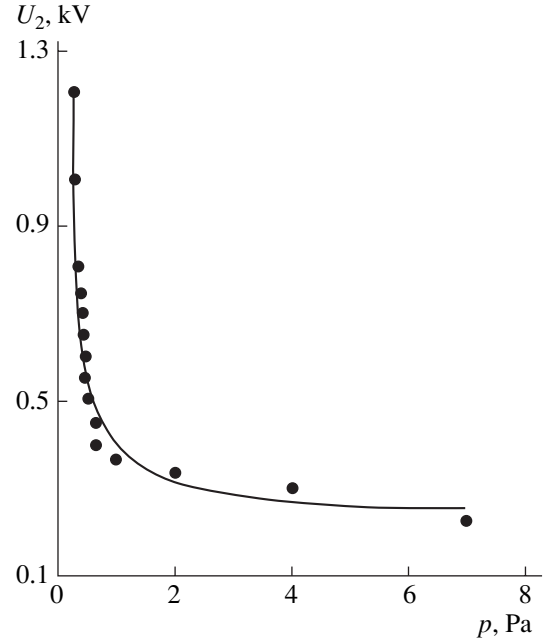

Fig. 4. Pressure dependence of the ignition voltage of a hollow-cathode discharge.

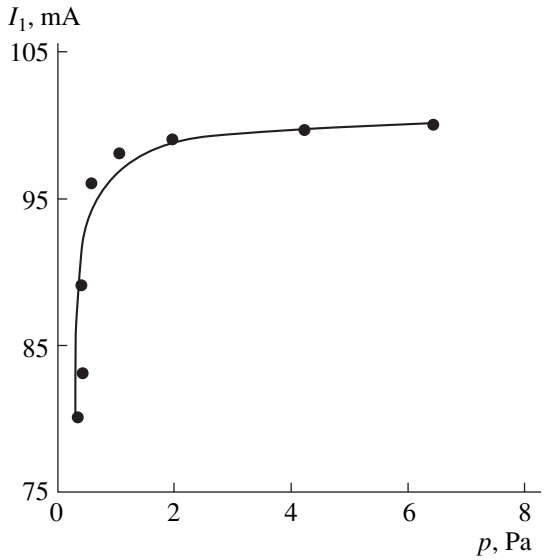

Fig. 5. Pressure dependence of the hollow-cathode discharge current.

ture is broken and a wide plasma flow penetrates into the space between the extraction electrode and the collector (see the plasma-glow photograph corresponding to point *A* on the dependence of the ion current on the accelerating voltage in Fig. 6). On applying the accelerating voltage, the ion current first rapidly increases. As the accelerating voltage increases further, the plasma at the outlet of the accelerating electrode contracts in the radial direction to form a neck (see the plasma-glow photograph corresponding to point *B* on the dependence of the ion current on the accelerating voltage in Fig. 6). At $U \sim 880$ V, the plasma in the neck

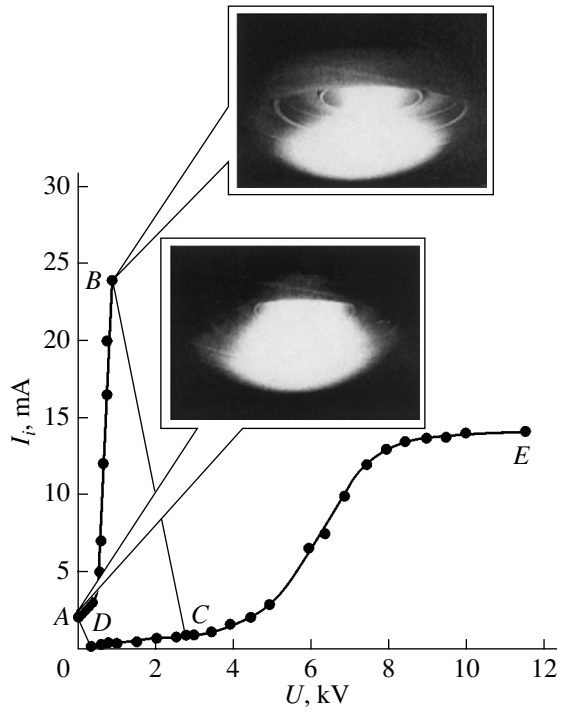

Fig. 6. Ion current through the collector as a function of the accelerating voltage and photographs of the plasma glow for $I_1 = 0.1$ A, $U_1 = 350$ V, and $p = 1.2 \times 10^{-1}$ Pa.

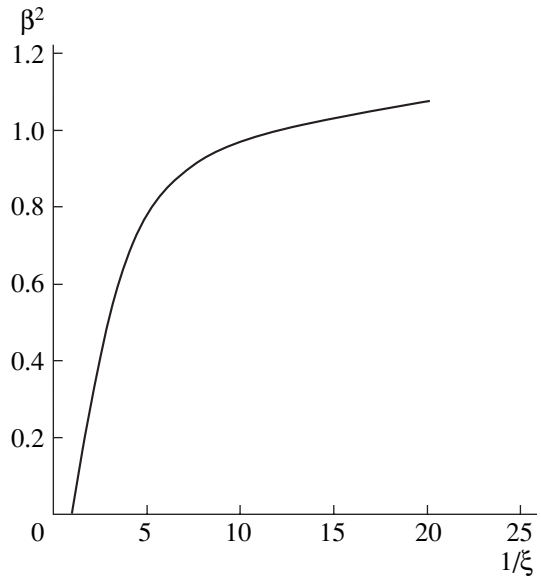

Fig. 7. Plot of the function $\beta^2(1/\xi)$.

decays and the current sharply decreases from 24 to 0.8 mA (segment *BC*), while the voltage increases to 2.7 kV. In this case, an ion beam current is detected at the collector. As the voltage increases to values $U >$ 2.7 kV, the plasma does not go out of the emission channel (this indicates a reduction in the loss of the extracted ion current at the accelerating electrode; see Fig. 9, curve *2*), the ion losses decrease, and the extracted ion current increases (Fig. 6). The increase in the current is most pronounced at $U > 5$ kV. As U increases further, the ion current saturates [6]. As the accelerating voltage then decreases to <2.7 kV, the ion-beam current slowly decreases. However, the ion current cannot be reduced to zero, because there is a critical accelerating voltage (~450 V) below which the plasma is no longer confined within the emission channel. As the voltage becomes lower than this critical value, the plasma escapes from the channel, the current increases abruptly from 0.2 to 2 mA, and the voltage drops to ~80 V (segment *DA*).

DISCUSSION OF RESULTS

Let us consider the plasma within the aperture of the accelerating electrode, whose negative potential is lower than the potential of the annular electrode. The length of the cathode fall can be written as

$$l_1 = R - r, \tag{2}$$

where R is the radius of the aperture in the accelerating electrode and r is the radius of the plasma boundary.

We rewrite expression (2) in the form

$$l_1 R^{-1} = 1 - \xi, \tag{3}$$

where $\xi = rR^{-1}$.

We ignore the electron space charge and assume the ion motion to be collisionless (at a pressure of 7.3×10^{-2} Pa, the mean free path of argon ions is $\lambda \sim 10^{-1}$ m). We also assume that the surface of the emitting plasma is cylindrical and that the transmission capacity of the gap corresponds to the emissive ability of the plasma. Then, ignoring the longitudinal plasma gradient inside the aperture of the accelerating electrode and using the 3/2 low, we obtain the following expression for the ion current density of a vacuum cylindrical diode:

$$j_i = 0.444\varepsilon_0 (2eM_i^{-1})^{1/2} U^{3/2} R^{-2} (f(\xi))^{-1}, \tag{4}$$

where $f(\xi) = \xi\beta^2(1/\xi)$, $\beta^2(1/\xi)$ is a tabulated transcendental function (Fig. 7).

The 3/2 law can be represented in the form

$$\xi = 0.444\varepsilon_0 (2eM_i^{-1})^{1/2} U^{3/2} j_i^{-1} R^{-2} (\beta^2(1/\xi))^{-1}, \tag{5}$$

where j_i is defined by the Bohm formula (1).

In view of Eq. (5), expression (4) can be reduced to the form

$$\xi = 1.1\varepsilon_0 U^{3/2} n_i^{-1} R^{-2} (ekT_e)^{-1/2} (\beta^2(1/\xi))^{-1}. \tag{6}$$

Let us calculate the value of $\xi\beta^2(1/\xi)$ at which the plasma within the aperture of the accelerating electrode decays and the emitting plasma surface does not go out of the emission channel. Substituting $R = 1.3 \times 10^{-2}$ m, $\varepsilon_0 = 8.85 \times 10^{-12}$ F/m, $n_i = 5.2 \times 10^{16}$ m^{-3}, $T_e = 3.5 \times$

10^4 K, $e = 1.6 \times 10^{-19}$ C, $k = 1.38 \times 10^{-23}$ J/K, and $U =$ 880 V into expression (6), we find

$$\xi\beta^2(1/\xi) = 0.11. \quad (7)$$

Since the dependence $f(\xi)$ is nonmonotonic (see Fig. 8), there are two values of the argument ($\xi = 0.54$ and 0.12) for the same value $f(\xi) = 0.11$. These two values of ξ correspond to two plasma states with different radii: $r \sim 7 \times 10^{-3}$ and $\sim 1.5 \times 10^{-3}$ m. The value $\xi = 0.12 < \xi_m = 0.31$ corresponds to the left branch of the dependence, i.e., to an unstable state of the plasma–sheath system (here, ξ_m is the lower boundary of the stability region). The value $\xi = 0.54$ corresponds to the right branch of the dependence $f(\xi)$, i.e., to a stable plasma state. Note that $\xi = 0.54$ exceeds the calculated minimal value $\xi = 0.31$ [6, 7]. A discrepancy between the measured and calculated values of ξ at which the plasma loses its stability may be explained by a rather gentle slope of $f(\xi)$ within the interval $0.31 \le \xi \le 0.54$. Photographs taken under conditions such that even a very small perturbation causes a fast plasma decay show that the minimal plasma cross is $r \sim 7.2 \times 10^{-3}$ mm ($\xi = 0.54$), which coincides with the calculated value. This indicates that, for the electrode configuration used in our experiments, a stable plasma–sheath system can exist not for any ξ value on the ascending branch of the function $f(\xi)$, but only for $\xi \ge 0.54$. In this case, the voltage drop across the sheath does not exceed a certain limiting value, which depends on the plasma parameters [6]:

$$U^* < 8.79 \times 10^{-8} n_i^{2/3} T e^{1/3} R^{4/3}, \quad (8)$$

and the plasma density cannot be lower than a certain critical density [7].

The use of an emitter cathode with a wide channel not only predetermines the annular shape of the cathode, appreciably changes the magnetic field structure, and creates high-vacuum conditions (which are untypical of discharge systems with a small aperture in the emitter cathode), but also makes it necessary to satisfy conditions under which the plasma penetrating into the channel of the accelerating electrode rapidly decays. In this case, the regime with an ion current produced by the penetrating plasma is rapidly switched to the regime of the ion emission current.

The ion current can be additionally increased by minimizing the loss of the extracted ions at the wall of the accelerating electrode, i.e., by optimizing its design. Clearly, such an increase is possible in principle, because, for an open discharge, the loss of the ion current at the accelerating electrode may comprise a large fraction of the total extracted ion current. Let us consider the dependences of the ion currents through the accelerating electrode and the collector on the accelerating voltage U and analyze the possibility of additionally lowering the cost of ion extraction, $C_1 \sim I_1 U_1 / I_i$ (the ratio of the discharge power to the ion emission current). It can be seen in Fig. 9 that the extracted current is distributed between the accelerating electrode and the collector. The ascending and descending segments in the dependence of the current through the accelerating electrode (curve *2*) correspond to the slow and rapid

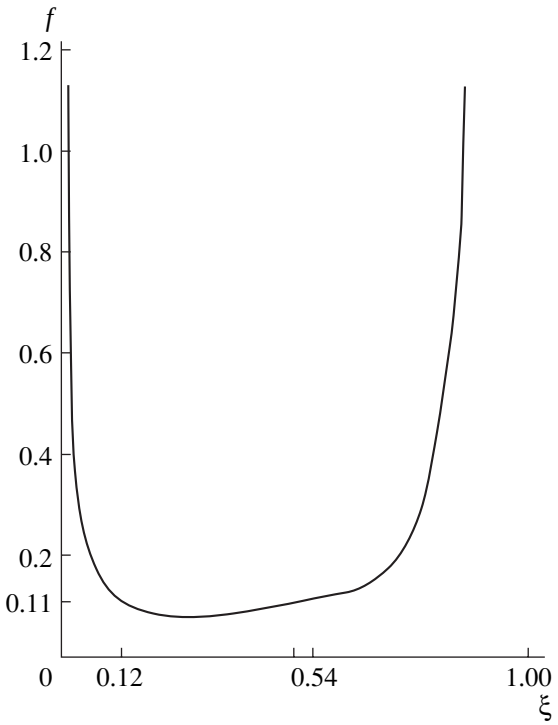

Fig. 8. Plot of the function $f(\xi) = \xi\beta^2$.

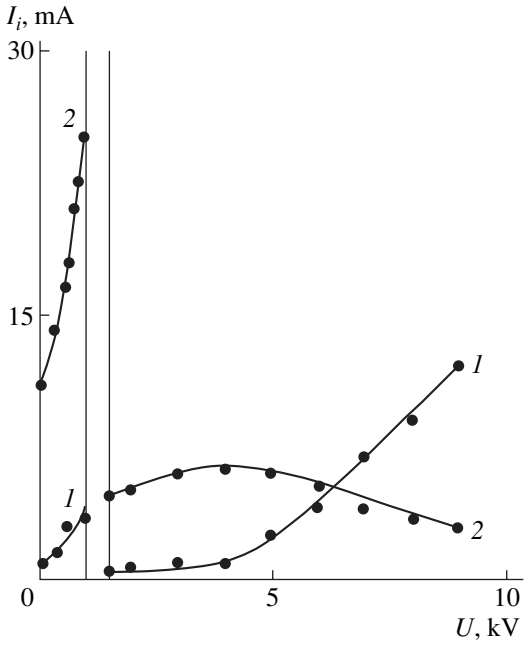

Fig. 9. Ion currents through the (*1*) collector and (*2*) accelerating electrode as functions of the accelerating voltage for $I_1 = 70$ mA, $U_1 = 350$ V, and $p = 1.2 \times 10^{-1}$ Pa.

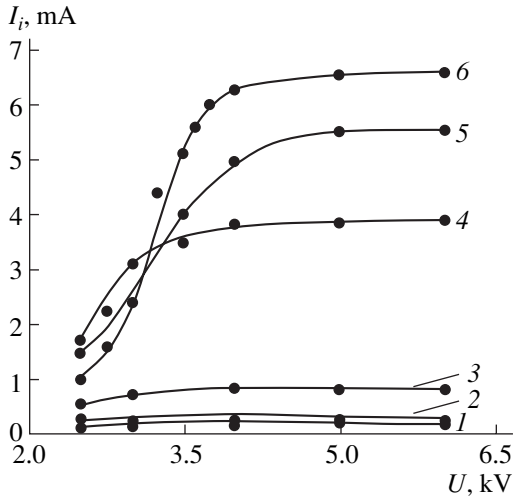

Fig. 10. Ion extraction current vs. accelerating voltage for emission-channel diameters d of (*1–3*) 3 and (*4–6*) 18 mm; discharge currents I_1 of (*1*, *4*) 50, (*2*, *5*) 80, and (*3*, *6*) 100 mA, and pressures in the acceleration gap of (*1–3*) 4×10^{-2} and (*4–6*) 4×10^{-1} Pa.

increase in the ion current through the collector (curve *1*), respectively. At accelerating voltages below 5 kV, the plasma goes out of the emission channel and the emitting plasma surface at the exit of the channel is convex. A substantial fraction of the ion current is lost at the accelerating electrode, and the collector current is lower than the current through the accelerating electrode. As the voltage increases, the emitting plasma surface flattens; the fraction of the ion current that is lost at the accelerating electrode decreases (the descending segment in curve *2*); and the current through the collector sharply increases, which indicates an increase in the transmission capacity of the accelerating electrode. The fraction of the ions arriving at the collector is larger than the fraction of the ions intercepted by the accelerating electrode. For the given geometry of the acceleration gap, the loss of the ion current decreases with increasing accelerating voltage; however, it still remains substantial and amounts to 0.4–0.5 of the ion current through the collector. Therefore, one of the ways of increasing the ion current at the outlet of the wide-aperture accelerating electrode is to optimize the geometry of the accelerating electrode. It may be expected that the nonproductive loss of the ion current can be reduced to an acceptable level of 0.90–0.95 by properly choosing the shape and dimensions of the accelerating electrode.

The dependences of the extracted ion current on the accelerating voltage (see Fig. 10) indicate that the plasma is best utilized in the electrode configuration with a wide emission channel. In this case, a sevenfold increase in the extracted ion current without increasing the discharge current was achieved by widening the diameter of the emission channel from 3 to 18 mm. The maximal ion current was obtained for the maximal diameter of the aperture in the annular cathode (the aperture diameter was limited by the diameter of the anode cavity).

CONCLUSIONS

An analysis of the discharge properties and the conditions of ion extraction in the regime of plasma penetration into the acceleration gap has shown the following:

The discharge with a broken ion sheath in front of the emission channel is excited and stably operates in the regime with an evacuated cathode cavity at a gas pressure in the cylindrical anode of 4×10^{-2} Pa.

A stable plasma–sheath system within the aperture of the accelerating electrode exists only at $\xi \geq 0.54$.

As the cross-sectional area of the emission channel in the cathode is increased to the area of the window in the cylindrical anode, the cost of ion extraction decreases from 10 to 1–1.5 W/mA.

An external factor affecting the plasma decay within the aperture of the accelerating electrode is the voltage between the annular cathode and the accelerating electrode. Therefore, the high accelerating voltage $U > U^*$ should be applied before the penetration of the plasma into the accelerating gap; moreover, this should be done in the following way: it is first necessary to produce an electric field penetrating into the emission channel, and only then the discharge should be ignited. When the conditions preventing the penetration of the plasma into the aperture of the accelerating electrode are satisfied, the ions can be stably extracted through the wide aperture in the cathode in the absence of a grid stabilizing the emitting plasma surface. This allows one to create wide-aperture ion sources without using fine-mesh emitting electrodes.

To increase the efficiency of ion extraction, it is necessary to optimize the shape and dimensions of the accelerating electrodes.

The limiting conditions for the excitation and stable operation of a hollow-cathode discharge in an electrode system with an annular emitter cathode have been determined, and the possibility of extracting charged particles (ions) in the absence of a pressure gradient in the acceleration gap has been demonstrated. It has been shown that a substantial increase in the extracted ion current can be achieved by enlarging the emitting plasma surface.

ACKNOWLEDGMENTS

This work was supported in part by INTAS (project no. 2001-2399) and the “Complex Integration Project

no. 7" of the Siberian Division of the Russian Academy of Sciences.

REFERENCES

1. A. P. Semenov, in *Sputtering Ion Beams: Generation and Application*, Ed. by G. A. Mesyats (Izd. BNTs SO RAN, Ulan-Ude, 1999) [in Russian].
2. A. P. Semenov and B.-Sh. Ch. Batuev, Zh. Tekh. Fiz. **60** (10), 171 (1990) [Sov. Phys. Tech. Phys. **35**, 1216 (1990)].
3. A. P. Semenov, Teplofiz. Vys. Temp. **30**, 36 (1992).
4. A. P. Semenov and B.-Sh. Ch. Batuev, Zh. Tekh. Fiz. **61** (5), 120 (1991) [Sov. Phys. Tech. Phys. **36**, 570 (1991)].
5. V. N. Glazunov and A. S. Metel', Fiz. Plazmy **8**, 1099 (1982) [Sov. J. Plasma Phys. **8**, 625 (1982)].
6. Yu. E. Kreĭndel' and S. P. Nikulin, Zh. Tekh. Fiz. **58** (6), 1208 (1988) [Sov. Phys. Tech. Phys. **33**, 714 (1988)].
7. S. P. Nikulin, Doctoral Dissertation (Yekaterinburg, 1999).

Translated by N. Larionova

Technical Physics, Vol. 50, No. 4, 2005, pp. 434–438. Translated from Zhurnal Tekhnicheskoĭ Fiziki, Vol. 75, No. 4, 2005, pp. 48–52.

GAS DISCHARGES, PLASMA

Hollow-Cathode Magnetron Discharge as a Generator of Charged Particles

A. P. Semenov and I. A. Semenova

Buryat Scientific Center, Siberian Division, Russian Academy of Sciences, Ulan-Ude, 670047 Russia

e-mail: semenov@pres.bsc.buryatia.ru

Received April 6, 2004

Abstract—A magnetron discharge with a cold hollow cathode and an uncooled rod cathode is studied. It is shown that such a discharge can be efficiently used to generate a plasma emitting charged particles. For a discharge current of 2 A and an accelerating voltage of 10 kV, ion and electron emission currents of 0.1–0.15 and 1 A, respectively, are achieved. The energy cost of ion extraction is 1–2 W/mA, which is two to five times less than for typical ion sources, and the energy efficiency is 15 mA/W, which is a factor of five or six higher than for electron emitters based on a hollow-cathode reflex discharge. © *2005 Pleiades Publishing, Inc.*

INTRODUCTION

In gas discharges with a cold cathode, the ion component of the emission current can be characterized by the energy cost of ion extraction, which is defined as the ratio of discharge power to the ion emission current: $C_i \sim IU/I_i$, where I and U are the discharge current and discharge voltage, respectively, and I_i is the ion beam current. The electron emission is characterized by the energy efficiency $W_e \sim I_e/IU$, where I_e is the electron beam current. In low-pressure reflex discharges with a cold hollow cathode [1] at discharge voltages of $U \sim$ 400–450 V, C_i is rather high (~10 W/mA), whereas W_e is low (~2.5 mA/W). The reason for the high energy cost of ion extraction and the low energy efficiency is the high value of the discharge voltage. The high discharge voltage leads to the rapid erosion of the wall of the emission channel and an unwanted heating of the cathode. In present-day plasma sources of electrons and ions [2–7], a significant fraction of the discharge power is released at the electrodes and carried away by a cooling system. Besides the high operating voltage, a characteristic feature of hollow-cathode reflex discharges is that the charge density in the output aperture of the cavity and the reflex cathode is redistributed due to a change in the radial motion of charged particles [2]; as a result, the slope of the dependence of the plasma density on the discharge current decreases for discharge currents of $I > 0.6$ A. In this study, we consider some properties of a magnetron discharge with the purpose of achieving the most efficient regime of discharge operation and high emission characteristics of the discharge plasma. The heat erosion of the end of the rod cathode is investigated experimentally.

EXPERIMENTAL SETUP, RESULTS, AND DISCUSSION

Figure 1 shows a schematic of the electrode system of a hollow-cathode magnetron discharge [8]. In the course of a discharge, the cathode is heated up to temperatures at which thermionic emission comes into play. Cylindrical copper anode *1* with a diameter of 8 mm and length of 12 mm coaxially encloses movable rod cathode *2* with a diameter of d = 1.5–4.0 mm. The rod cathode is mounted on the axis of cathode cavity *3* coaxially with its output aperture so that there be a gap between the rod and the aperture in reflex cathode *6*. An axial magnetic field of 0.1 T in the anode cylinder is produced by ring magnet *5*. The aperture in reflex cathode *6* is used to pump out the working gas. It can also serve as an emission channel when the discharge system is used as a generator of a plasma emitting electrons and ions or an ejector nozzle through which, e.g., an atomic hydrogen beam is output. The temperature of the rod cathode was measured directly by a tungsten–rhenium thermoelectric gauge. The plasma-forming

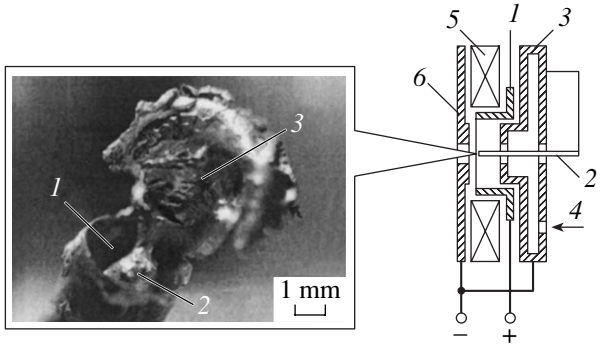

Fig. 1. Schematic of the electrode system and a photograph of the thermal erosion of the end of the brass rod cathode: (*1*) anode, (*2*) rod cathode, (*3*) hollow cathode, (*4*) gas input, (*5*) permanent magnet, and (*6*) reflex cathode.

1063-7842/05/5004-0434$26.00 © 2005 Pleiades Publishing, Inc.

gas (air) was delivered at a rate of 0.8–1.2 mPa m^3/s through hole *4* at the periphery of the cavity. To measure the plasma parameters, a cylindrical tungsten probe with a diameter of 0.05 mm was inserted through the aperture in cathode *6*. Its working surface was 1 mm in length, and the remaining (inactive) part of the probe was covered with an alundum coating. To extract charged particles from the cathode plasma, an accelerating electrode [6] was installed coaxially with cathode *6*.

The properties of the hollow-cathode magnetron discharge (Fig. 1) are determined to a great extent by the thermionic properties of the rod cathode [9] heated by the power released in the discharge [10–12]. To measure the temperature T_c of the rod tungsten cathode, a tungsten–rhenium junction was formed at the rod end; this junction was used as a sensitive element of a VR-5/20 thermoelectric tungsten–rhenium calibration gauge. The heating of this junction to the temperature T_c did not affect the structure and operating regime of the discharge. The thermoelectromotive force (with allowance for plasma radiation) was monitored with a S8-11 storage oscilloscope. The temperature T_c was measured after the rapid termination of the discharge with a plasma decay time of $\sim 10^{-5}$ s. If we assume the decay rate of the cathode temperature to be $\sim 10^6$ K/s [13], then, over a time of $\sim 10^{-5}$ s, the measured temperature of the cathode will decrease by ~10 K as compared to the its true value. Figure 2 shows the waveform of the thermoelectromotive force after the rapid (over a time of 5×10^{-6} s) termination of the discharge. Plasma decay is accompanied by a sharp decrease in the thermoelectromotive force to the value corresponding to the true temperature T_c (point *A*) because, during the discharge, the thermoelectric gauge gives a substantially overestimated value of the thermoelectromotive force due to the presence of the discharge plasma. The part of the waveform below point *A* shows the cooling of the rod cathode from the maximal temperature to a certain temperature that is established a few seconds after the plasma has decayed. The thermoelectromotive force at point *A* corresponds to a cathode temperature of $\sim 2.6 \times 10^3$ K, which coincides with the temperature measured by a pyrometer [14].

Figure 3 shows the waveform of the anode current for an amplitude of the ignition voltage pulse of $U_1 = 10^3$ V. A steady regime of discharge operation was reached in a few intermediate stages (see Fig. 4). The time τ_f of the discharge development was a function of the amplitude of the ignition voltage pulse: as U_1 increased from 0.7 to 1.2 kV, τ_f decreased from 0.35 to 0.15 s. When a new voltage pulse U_1 was again applied in a time less than 0.1 s after the termination of the previous discharge, no intermediate stages were observed. For $U_1 < 0.7$ kV, a low-current magnetron discharge occurred. The descending part of the discharge current–voltage characteristic (Fig. 4) is related to the change in the mechanism of the rod cathode emission when the

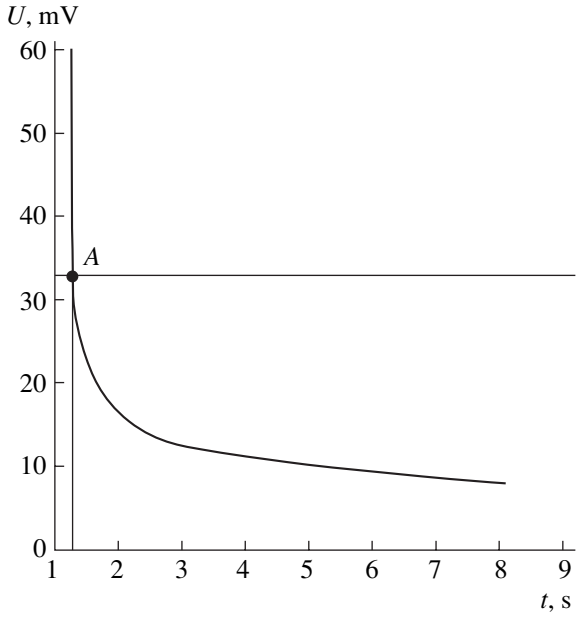

Fig. 2. Waveform of the thermoelectromotive force after the termination of a discharge with a 1.5-mm-diameter tungsten rod cathode at a discharge current of $I = 0.66$ A.

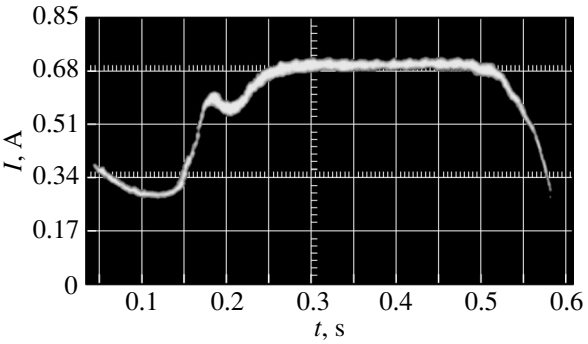

Fig. 3. Waveform of the anode current for $\tau_f = 0.225$ s and $I = 0.715$ A.

contribution of thermionic emission to the ionization processes in the cathode region becomes significant. The rod cathode temperature reaches 2500–2700 K, which enables a thermoemission current density of 0.3–1.6 A/cm^2. Such current densities were obtained when measuring the current–voltage characteristics of discharges with cathode rods made of different materials [9]. The lowest discharge voltage was obtained with a rod cathode made of LaB_6, whose thermoemission ability is the highest. It can be seen from the waveform of the discharge current *I* (see Fig. 3) that a steady regime of discharge operation is established 0.225 s after applying the ignition voltage pulse. The delay in the discharge development is caused by the heating of the cathode rod.

Figure 5 (curve *2*) shows the axial plasma density as a function of the discharge current. The plasma density

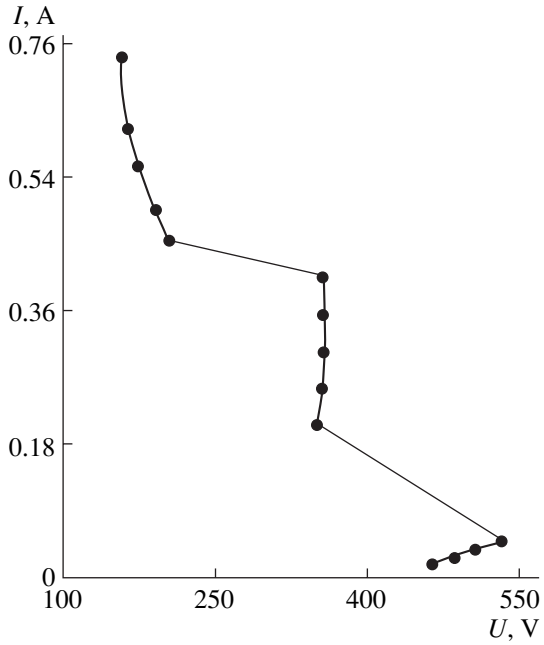

Fig. 4. Current–voltage characteristic of a discharge with $d = 1.5$ mm.

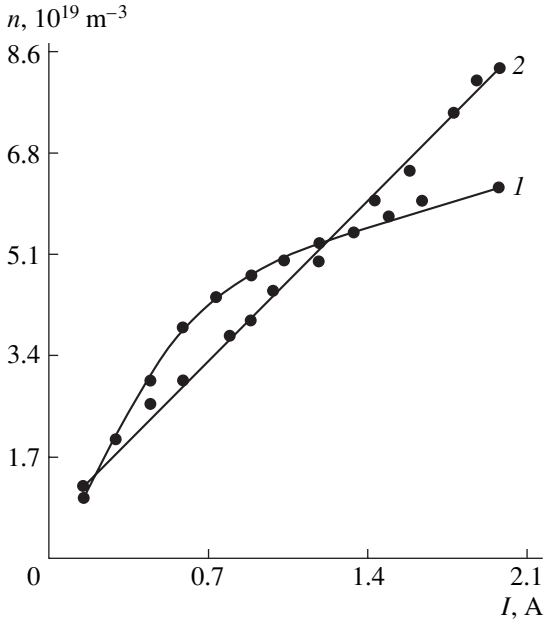

Fig. 5. Plasma density vs. discharge current for (*1*) a hollow-cathode reflex discharge [2] and (*2*) a hollow-cathode magnetron discharge.

was determined from the ion saturation current to a probe placed in the aperture of cathode *6*. The plasma density was measured under the conditions of electron emission from the white-hot tungsten rod heated by the plasma ions accelerated in the cathode fall region. Figure 5 also shows the plasma density in the aperture of cathode *6* as a function of the current of a hollow-cathode reflex discharge (curve *1*) [12]. A comparison between these dependences shows that the effect of the limitation of the space charge density does not manifest itself in a hollow-cathode magnetron discharge, in which dissipation of the discharge energy at the uncooled cathode can heat it to temperatures that are high enough to enable electron emission. This allows one to significantly decrease the operating voltage of a high-current discharge, to obtain a linearly increasing dependence of the plasma density on the discharge current at currents of >0.6 A, and to provide conditions for the gradual conversion of an anomalous glow discharge into a diffuse (without cathode spots) arc discharge.

Under our experimental conditions, a significant contribution to ionization is made by thermoelectrons. The higher the rod temperature and the larger its emission surface, the lower the discharge voltage. The combined effect of these two factors is especially pronounced for a certain distance between the rod end and the reflex cathode at which U is minimal. It was found experimentally that the discharge voltage varied nonmotonically as the rod cathode was inserted into the discharge gap (see Fig. 6). In our experiments, the rod was displaced with the help of a micrometer screw along the axis of the electrode system during a steadily operating discharge. Initially, the cathode rod end was set flush with the base plane of the cathode cavity. As the rod was inserted to a depth of ~9 mm (the cavity inner depth), the discharge voltage decreased from 390 to ~375 V (at a discharge current of 0.5 A). As the rod was further shifted by the output aperture depth (~2 mm), the discharge voltage U decreased to 360 V. As the rod was moved within the gap between the cathode cavity aperture and the reflex cathode, the voltage sharply decreased from 360 to 145 V when the distance between the rod end and the cathode cavity aperture was 8.5 mm; the decrease in the discharge voltage was accompanied by an appreciable increase in the current through the rod. As the rod end approached the reflex cathode, the current through the rod increased at a lower rate and the discharge voltage somewhat increased. The point where the discharge voltage U is minimal determines the optimal gap length d_{opt} between the end of the rod cathode and the wall of the reflex cathode. Generally, $d_{opt} \sim \lambda_0$, where λ_0 is the mean free path of the atoms of the plasma-forming gas. In our case, this corresponds to an optimal gap length of ~1.5 mm.

Over a relatively short time of $<10^{-1}$ s after a steady hollow-cathode discharge had been established, we observed the erosion of the ends of the 4-mm-diameter cylindrical rods. The character of erosion depends on the rod material: stainless steel, aluminum, or brass. For stainless-steel rods, the rod end was partially melted and took a hemispherical shape. For aluminum rods, the rod end softened, extended, took a pearlike shape (the gravitation was directed along the rod axis), and

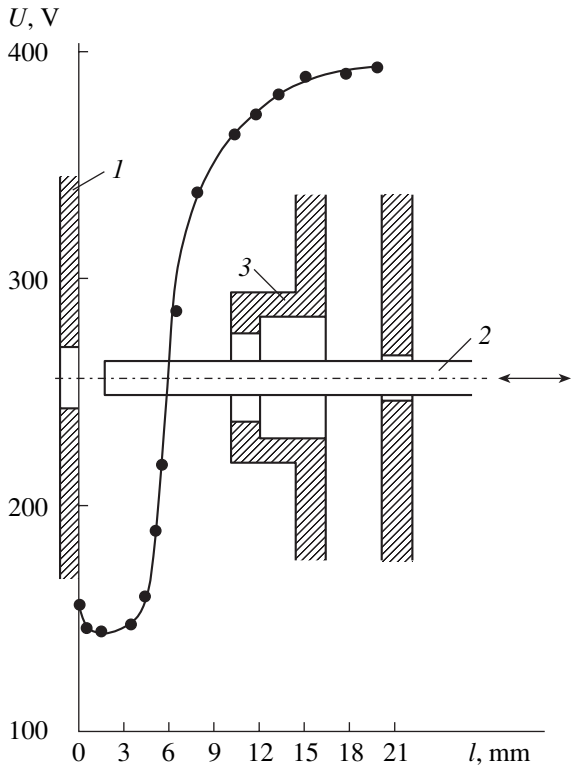

Fig. 6. Discharge voltage vs. distance between the rod cathode end and the reflex cathode for $d = 1.5$ mm and $I = 0.5$ A: (*1*) reflex cathode, (*2*) rod cathode, and (*3*) hollow cathode.

then (after touching the cold surface of the reflex cathode) solidified. For brass rods, the erosion picture was the most complicated. It can be seen in Figs. 1 and 7 that liquid metal *3* is expelled through the rod end and then (after touching the cold surface of the reflex cathode) solidifies. At the place from which the liquid metal has been expelled, 4-mm-deep crater *1* forms. Due to the explosive expulsion of the liquid metal, cone *2* arises inside the crater, the cone apex being in contact with the body of the expelled metal. An analysis of the longitudinal cross section of the end part of the rod cathode (Fig. 7) shows that, when the melted metal is expelled from the rod volume, a thin cylindrical surface layer remains cool and does not undergo melting, although the melting border is at a depth of only 0.1 mm from the rod surface (i.e., the thickness of the wall bordering the crater is 0.1 mm). The explosive expulsion of the metal through the rod end and the formation of a crater like those shown in Figs. 1 and 7 are seemingly related to resonance processes in the gap between the end of the rod cathode and the reflex cathode. This gap acts as an equivalent capacitance of a toroidal cavity, whose equivalent inductance is formed by the cavity of the anode cylinder [15]. Estimates show that the resonance frequency of this cavity is ~1 GHz, which coincides with the frequency of plasma oscillations., In order to gain a deeper insight into the physical nature of this phenomenon, it is necessary to perform

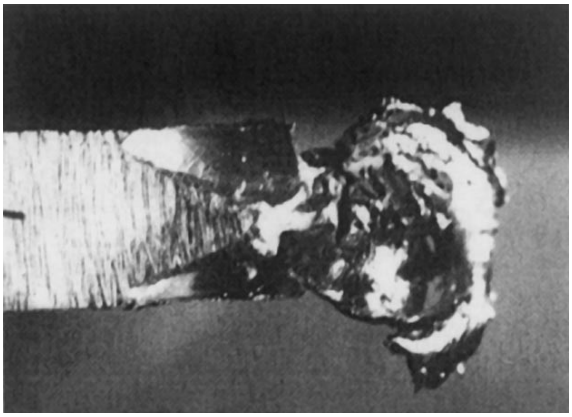

Fig. 7. Longitudinal cross section of the eroded end of the rod cathode (see Fig. 1).

additional experiments, which are worthy of separate consideration.

For a discharge current of 2 A and an accelerating voltage of 10 kV, the ion and electron emission currents at the output aperture of the reflex cathode were 0.1–0.15 and 1 A, respectively.

CONCLUSIONS

It has been shown that hollow-cathode magnetron discharge (whose characteristics, including the parameters of the cathode plasma and conditions for its formation, were first considered in [10, 11, 16–18]) can be used as a generator of high-current ion beams with a low energy cost of ion extraction and of electron beams with a high energy efficiency. The single-valued dependence of the plasma density on the discharge current (see Fig. 5, curve *2*) and the descending current–voltage characteristic make it possible to operate at a relatively low discharge voltages and to achieve an efficient extraction of ions and electrons along the axis of the magnetron rod cathode. In this case, the energy cost of ion extraction reduces to ~1 W/mA and the energy efficiency increases to ~15 mA/W. The study of a magnetron discharge with a cold hollow cathode provides only a qualitative idea of its consumer properties. The rather complicated interplay of the physical processes occurring in the discharge and determining its efficiency is even more complicated when the specifics of different plasma processes and their effect on the emission of ions and electrons are taken into account. The observed decrease in the discharge voltage with increasing discharge current is related to the thermionic emission from the strongly heated magnetron rod cathode. Varying the gap length between the rod cathode end and the reflex cathode also affects the discharge voltage.

The above properties of the hollow-cathode magnetron discharge have already been used to sharpen tungsten points (needles) by ion sputtering, to efficiently

generate atomic hydrogen by the high-temperature activation of molecular hydrogen (which is of especial importance for growing diamond films and treating semiconductor surfaces [19]), and to deposit refractory-metal coatings on the walls of tubular cavities [20]. They are also used to produce high-density plasma through thermionic emission, which allows one to gradually transform the discharge into a high-current arc without generating cathode spots. In such a regime, there are no limitations related to the arc instability at low currents, the instability and nonsteady behavior of the cathode spots, and the emission from cathode spots of particles that contaminate both the discharge plasma and the particle flow injected through the emission channel. New, efficient sources of ions and electrons are being presently developed based on a hollow-cathode magnetron discharge with an uncooled rod cathode [8].

ACKNOWLEDGMENTS

This study was supported in part by the Complex Integration Project no. 7 of the Siberian Division of the Russian Academy of Sciences, INTAS (grant no. 2001–2399), and Lavrent'ev's Competition of Young Scientists of the Siberian Division of the Russian Academy of Sciences (project no. 37).

REFERENCES

1. Yu. E. Kreĭndel', *Plasma Sources of Electrons* (Atomizdat, Moscow, 1977) [in Russian].
2. V. A. Gruzdev, Yu. E. Kreĭndel', and O. E. Troyan, *Electron Sources with Plasma Emitter* (Nauka, Novosibirsk, 1983), pp. 5–14 [in Russian].
3. A. P. Semenov, Prib. Tekh. Éksp., No. 5, 23 (1984).
4. A. A. Glazov, M. Kuzmyak, D. L. Novikov, *et al.*, Prib. Tekh. Éksp., No. 1, 34 (1964).
5. A. P. Semenov, Prib. Tekh. Éksp., No. 4, 3 (1996).
6. M. A. Zav'yalov, Yu. E. Kreĭndel', A. A. Novikov, and L. P. Shanturin, *Plasma Processes in Electron Guns* (Énergoatomizdat, Moscow, 1989) [in Russian].
7. A. P. Semenov, Prib. Tekh. Éksp., No. 5, 128 (1993).
8. A. P. Semenov and I. A. Semyonova, Zh. Tekh. Fiz. **74** (4), 102 (2004) [Tech. Phys. **49**, 479 (2004)].
9. A. P. Semenov and I. A. Semenova, in *Proceedings of the 5th International Conference on Vacuum Technology and Equipment, Khar'kov, 2002*, pp. 227–235.
10. V. A. Gruzdev and A. P. Semenov, in *Proceedings of the 5th Symposium on Field-Emission Cathodes, Tomsk, 1985*, pp. 159–161.
11. A. P. Semenov and M. V. Mokhosoev, Dokl. Akad. Nauk SSSR **82**, 888 (1985) [Sov. Phys. Dokl. **30**, 516 (1982)].
12. V. A. Gruzdev, Yu. E. Kreĭndel', and A. P. Semenov, Teplofiz. Vys. Temp. **26**, 1005 (1988).
13. M. F. Zhukov, N. P. Kozlov, A. V. Pustogarov, *et al.*, *Near-Electrode Processes in Arc Discharges* (Nauka, Novosibirsk, 1982) [in Russian].
14. A. P. Semenov, *Sputtering Ion Beams: Generation and Application*, Ed. by G. A. Mesyats (Izd. BNTs SO RAN, Ulan-Ude, 1999) [in Russian].
15. V. F. Kovalenko, *Introduction to Microwave Electronics* (Sov. Radio, Moscow, 1955) [in Russian].
16. A. P. Semenov and M. V. Mokhosoev, Prib. Tekh. Éksp., No. 2, 138 (1987).
17. A. P. Semenov, USSR Inventor's Certificate No. 1375024 (1985).
18. A. P. Semenov and M. V. Mokhosoev, Zh. Tekh. Fiz. **54**, 2276 (1984) [Sov. Phys. Tech. Phys. **29**, 1337 (1984)].
19. A. P. Semenov and I. A. Semenova, Izv. Vyssh. Uchebn. Zaved. Fiz., No. 9, 69 (2001).
20. A. P. Semenov and A. F. Belyanin, USSR Inventor's Certificate No. 1565289 (1987).

Translated by N. Ustinovskiĭ

Technical Physics, Vol. 50, No. 4, 2005, pp. 439–446. Translated from Zhurnal Tekhnicheskoĭ Fiziki, Vol. 75, No. 4, 2005, pp. 53–59.

GAS DISCHARGES, PLASMA

Formation of Compression Shocks in a Nonequilibrium Plasma Flow in a Magnetic Field

A. V. Erofeev, R. V. Vasil'eva, T. A. Lapushkina, and S. A. Ponyaev

Ioffe Physicotechnical Institute, Russian Academy of Sciences, Politekhnicheskaya ul. 26, St. Petersburg, 194021 Russia

e-mail: alex.erofeev@mail.ioffe.ru

Received March 16, 2004

Abstract—Plasma flow in a linearly widening, ideally sectioned, short-circuited magnetohydrodynamic (MHD) channel is studied. MHD flows are classified into two types: continuous flows and flows with a compressional MHD shock in plasmas that are stable and unstable against the onset of ionization instability. Specific features in the evolution of a stationary compression MHD shock are investigated, and its position as a function of the Stewart number is determined. It is found that, in a plasma flow in which ionization instability develops, a compression MHD shock arises at lower values of the MHD interaction parameter than in a stable plasma flow. An unidentified type of instability of MHD discontinuities is revealed. © *2005 Pleiades Publishing, Inc*.

INTRODUCTION

When a supersonic flow is decelerated by the Lorentz force under conditions of strong magnetohydrodynamic (MHD) interaction, a gas-dynamic shock arises at which the supersonic flow transforms into a subsonic one. Situations in which the decelerated flow remains continuous refer to the case of weak MHD interaction.

Compression MHD shocks were first studied in [1]; in more detail, they were investigated in [2, 3] and, later, in [4, 5]. A comprehensive study of MHD flows with compression shocks was performed in [6] using an analogy between MHD and gas-dynamic flows. All of the above experiments were carried out with homogeneous plasma flows. Inhomogeneities of a nonequilibrium plasma flow may arise due to the onset of various instabilities [7], first of all, ionization instability, which develops faster than other instabilities. In this study, we assume that the reason why the plasma is nonequilibrium is that the electron temperature is higher than the temperature of the heavy component and the degree of ionization differs from its equilibrium value corresponding to the electron temperature. The formation of compression MHD shocks under conditions such that MHD interaction is accompanied by the generation of plasma inhomogeneities should possess specific features [8]. The aim of this study is to outline the conditions under which the formation of gas-dynamic shocks in the course of MHD interaction has already been comprehensively studied both experimentally and theoretically and to reveal special features of shock formation in flows in which plasma inhomogeneities may arise due to MHD interactions.

CLASSIFICATION OF MHD INTERACTIONS

MHD flows may be classified as follows: First, the gas-dynamic flow may be continuous or there may be an MHD shock induced by the Lorentz force. Second, the plasma in the flow may be homogeneous or there may be plasma inhomogeneities that arise from small initial variations in the plasma parameters due to the onset of plasma instabilities. The type of interaction is determined by the Stewart number *St*, which characterizes the ratio of the work produced by the Lorentz force to the gas kinetic energy, and the Hall parameter β, which is the ratio of the electron cyclotron frequency to the effective frequency of momentum transfer.

Let us consider a linearly widening MHD channel. A specific case of a linearly widening MHD channel is a channel in the form of a constant-height disk. Figure 1 shows a schematic of the MHD channel and the directions of the main vectors: the flow velocity **u**, the magnetic induction **B**, and the induced current density **j**. Here, x_0 and x_e are the distances from the vertex of the channel to the beginning and the end of the MHD inter-

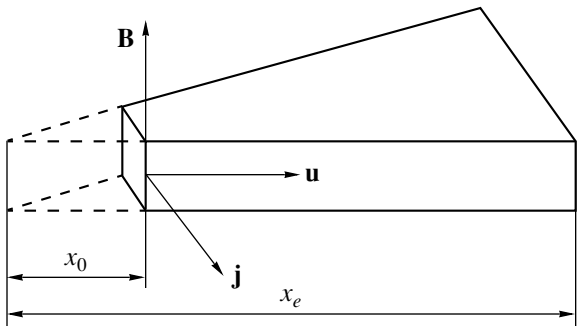

Fig. 1. Scheme of a linearly widening channel.

1063-7842/05/5004-0439$26.00 © 2005 Pleiades Publishing, Inc.

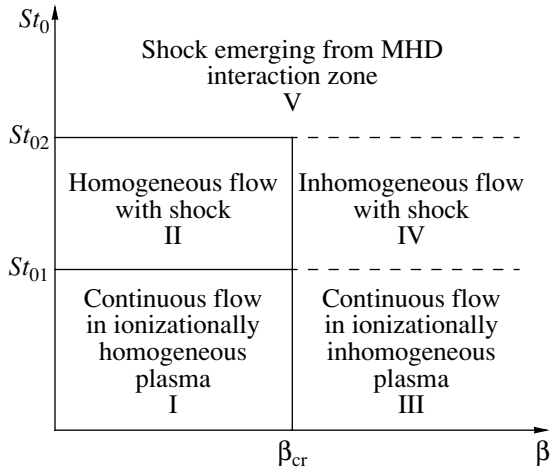

Fig. 2. Classification of the types of MHD interaction. Here, $St_0 = \sigma B^2 x_0/\rho_0 u_0$ and $\beta = \omega/\nu$.

action space, respectively. According to [4], the similarity criterion for a short-circuited Faraday channel with ideally sectioned electrodes is the Stewart number at the entrance to the channel:

$$St_0 = \sigma B^2 x_0/\rho_0 u_0. \quad (1)$$

Here, x_0 is taken as a characteristic length, ρ is the gas density, σ is the plasma conductivity, and the subscript 0 refers to the parameter values at $x = x_0$.

In principle, one can find the critical value of the Stewart number St_0 below which the flow is a continuous supersonic flow over the entire MHD interaction region (weak MHD interaction) and above which a compressional MHD shock arises in the channel (strong MHD interaction).

The regimes in which plasma flows are stable and unstable against the onset of ionization instability are separated by the critical value of the Hall parameter. The Hall parameter is defined as

$$\beta = eB/m_e\nu, \quad \nu = n_a c_e Q_{ea} + n_i c_e Q_{ei}, \quad (2)$$

where ν is the frequency of momentum transfer in collisions of electrons with atoms and ions; n_a and n_i are the atom and ion densities, respectively; c_e is the mean electron velocity; and Q_{ea} and Q_{ei} are the cross sections for momentum transfer in collisions of electrons with atoms and ions, respectively (both averaged over the Maxwellian electron distribution function).

The classification of the possible types of interaction is illustrated in Fig. 2. The (St, β) plane is divided into the following domains corresponding to different types of MHD interaction: type I is weak interaction in a homogeneous plasma, type II is strong interaction in a homogeneous plasma, type III is weak interaction in a plasma that is unstable against the onset of ionization instability, type IV is strong interaction in a plasma that is unstable against the onset of ionization instability, and type V is superstrong interaction corresponding to the case where the shock comes out from the MHD channel towards the flow (this case is beyond the scope of the present study).

The critical value of the Stewart number that separates the regimes with weak and strong MHD interaction in homogeneous plasmas (domains I and II) can be estimated using the results of the previous theoretical and experimental studies [4, 5]. It was shown that the position x_{sh} of a stationary compressional MHD shock in a linearly widening short-circuited channel can be described over a wide range of the Mach numbers ($1 < M < 5$) by the following simple formula

$$x_{sh}/x_0 = (\gamma St_0)^{-0.5}, \quad (3)$$

where γ is the adiabatic index.

As the MHD interaction parameter increases, a continuous MHD flow transforms into a flow with a compressional shock. The shock first arises at the end of the channel: $x_{sh} = x_e$. The corresponding value of the Stewart number St_{01} at which the shock arises defines the upper boundary of domain I:

$$St_{01} = (x_e/x_0)^{-2}\gamma^{-1}. \quad (4)$$

As the Stewart number increases, the shock shifts closer to the entrance of the channel and, at

$$St_{02} = 1/\gamma, \quad (5)$$

it reaches the ultimate position $x_{sh} = x_0$, which corresponds to the upper boundary of domain II. At $St_0 > St_{02}$, the shock comes out from the channel toward the flow.

In the parameter range corresponding to an ionizationally inhomogeneous plasma (domains III, IV), no distinct boundary can be drawn between the regimes with weak and strong interaction. This is because the critical value of the Hall parameter at which ionization instability develops and plasma inhomogeneities arise depends on the sort of gas and on the degree to which the flow is far from the ionizational equilibrium. In the case of the full ionizational equilibrium, the critical value of the Hall parameter β_{cr} can easily be estimated [6, 7]: $\beta_{cr} = 1$–2. At $\beta > \beta_{cr}$, ionization instability inevitably develops in the MHD channel because its growth time is much shorter than the flight time of the flow through the channel. In the absence of ionization equilibrium, the growth time of instability is determined by the characteristic ionization time. For pure noble gases, this time may be comparable to the flight time [9]. In this case, the critical conditions depend on both the Hall parameter and the ratio between the growth time of instability and the flight time. Hence, for each specific MHD channel, there is its own critical value of the Hall parameter. This is why the boundary between the regimes in which the flow is stable and unstable against the onset of ionization instability is drawn arbitrarily.

EXPERIMENTAL

We performed experiments with a disk MHD channel. A detailed description of the experimental setup and diagnostic technique can be found in [5]. An ionized gas flow was produced in a 5-cm-diameter cylindrical shock tube. It was then turned in the radial direction, expanded between Plexiglass disks, and entered the dump chamber. The gap between disks was 1 cm, and the disk diameter was 28 cm. The disks were positioned between the poles of an electromagnet, which produced a magnetic field with an induction of up to 1.6 T. The radial motion of the plasma flow in the axial magnetic field induces the ring Faraday current $j = \sigma uB$. As a result, the radial Hall field $E_x = \beta uB$ is generated and the retarding Lorentz force $F = j \times B$ arises. The disk MHD channel can be treated as a short-circuited Faraday channel with ideally sectioned electrodes. In our experiments, we measured the propagation velocity of the shock, the gas pressure, the flow velocity, the current density, the plasma conductivity, the Hall field, and the electron density and temperature [10]. We also took frame-by-frame photographs of the glowing inhomogeneities. Since the poles of the electromagnet overlapped the field of view, 45° turning mirrors were placed between the external disk and the pole (see Fig. 3a). Mirrors *1–3* directed the radiation from the disk channel to the focal plane of a fast framing camera (FFC). Mirror *4* directed the radiation from the vertical slit to a triggered streak camera to obtain (x, t) images of the plasma glow (in this case, mirror *3* was absent). Figure 3a also shows the test pattern of concentric circles on the disk surface. The resulting image of this pattern in the FFC focal plane is shown in Fig. 3b.

The stationary distribution of the plasma parameters in the disk MHD channel was computed in the approximation of a two-temperature plasma with nonequilibrium ionization [5]. The point $r_0 = 2$ cm was taken as the beginning of the MHD interaction space. The initial values of the parameters were chosen such that the plasma flow parameters measured within the observational region ($4 < r < 12$ cm) at low values of the magnetic field were close to the calculated ones.

The working gas was xenon. The experiments were performed for several gas-dynamic modes, which were specified by the pressures of the driven and driver gases in the shock tube and were characterized by the Mach number M_1 of the shock front in the shock tube and the gas pressure p_1 in the low-pressure chamber. In each of the gas-dynamic modes, the flow in the disk channel was studied at several different values of the magnetic field.

PARAMETERS OF THE GAS-DYNAMIC MODES

The values of M_1 and p_1 for some of the gas-dynamic modes and the calculated parameters of the disk channel at the entrance to the interaction space (at $r_0 = 2$ cm) are presented in the table.

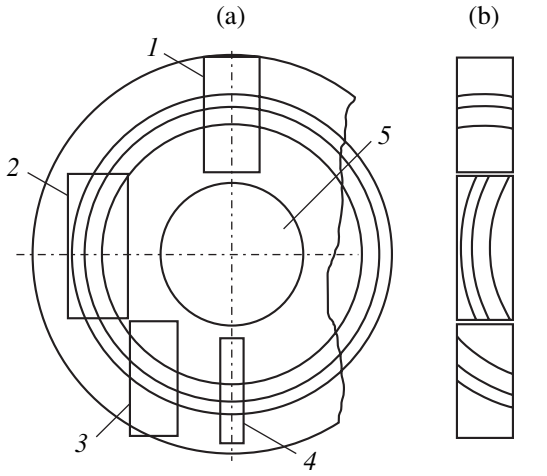

Fig. 3. (a) The arrangement of the turning mirrors on the disk surface (*1–4*), and the position of the end of the shock tube (*5*) (the concentric circles show the test pattern). (b) The test pattern image produced by the turning mirrors in the FFC focal plane.

Varying the magnetic field from 0 to 1.6 T in these modes allows one to analyze all the above four types of MHD interaction. These modes primarily differ in the degrees of gas ionization α, which largely governs the plasma state. The critical value of the degree of ionization is $\alpha = Q_{ea}/Q_{ei} \sim 10^{-3}$. At lower degrees of ionization, the frequency of momentum transfer is mainly determined by electron–atom collisions (ν_{ea}). At higher degrees of ionization, it is equal to the electron–ion collision frequency (ν_{ei}) and, therefore, is higher than in the previous case. Under our experimental conditions and at low degrees of ionization, the Hall parameter and the degree to which the temperatures of the light and heavy plasma components differ from one another are fairly high; this leads to the onset of ionization instability. In contrast, at high degrees of ionization (when Coulomb collisions prevails), both the Hall parameter and the degree to which the temperatures of the light and heavy plasma components differ from one another are much lower; as a result, the plasma is more stable. Results of experiments on studying critical conditions for the onset of ionization instability [5, 9, 10] allow one to find the parameter regions corresponding to flows that are stable and unstable against the onset of ionization instability. The boundary between these regions is determined by the ratio of the frequencies of electron–ion and electron–atom collisions at the entrance to the channel, $\nu_{ei0} = n_{e0}c_{e0}Q_{ei0}$ and $\nu_{ea0} = n_{a0}c_{e0}Q_{ea0}$, and by the ratio between the magnetic induction and the density of atoms at the entrance to the channel, B/n_{a0}. Under our experimental conditions, the flow is stable at $\nu_{ei0}/\nu_{ea0} \le 1$ and at $B/n_{a0} \times 10^{24}$ (T m^3) < 0.1. When $B/n_{a0} \times 10^{24} > 0.1$, the plasma is unstable.

Table

Shock-tube modes			Parameters of the disk channel at the entrance to the MHD interaction region at $r_0 = 2$ cm				
mode number	M_1	p_1, torr	M_0	$T_{0h} = T_{0e}$, K	n_{a0}, 10^{25} m^{-3}	α_0	σ_0, S/m
1	6.4	26	1.15	5500	0.54	10^{-4}	110
2	6.9	26	1.21	5900	0.625	0.3×10^{-3}	270
3	8.4	26	1.19	6700	0.85	1.1×10^{-3}	340
4	9.4	13	1.25	7300	0.5	0.4×10^{-2}	1300
5	9.7	13	1.3	8040	0.68	0.92×10^{-2}	1800
6	10.5	13	1.2	8600	0.845	1.54×10^{-2}	2500

A relative increase in the frequency of Coulomb collisions leads to plasma stabilization. For example, at $\nu_{ei0}/\nu_{ea0} > 2$, the plasma is stable over the entire range of B and n_{a0} under study. Thus, when studying the formation of compressional MHD shocks in homogeneous plasma flows, we used modes with higher Mach numbers (which correspond to higher degrees of ionization). The modes with lower degrees of ionization (which occur at lower Mach numbers) were employed to study the formation of compressional MHD shocks in plasma flows that are unstable against the onset of ionization instability.

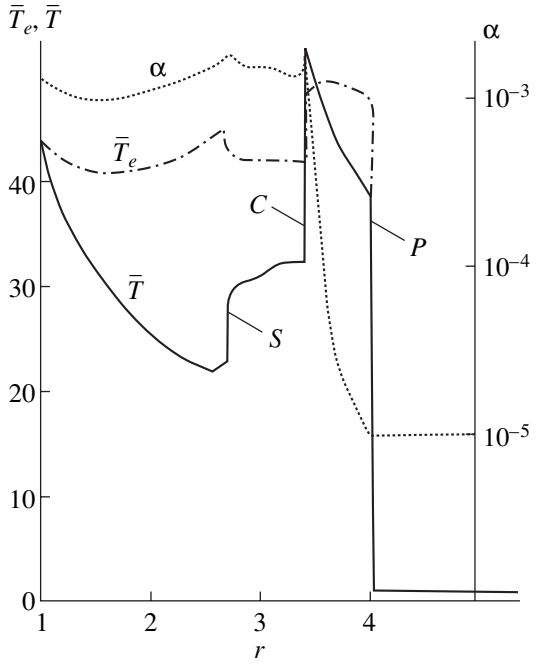

Fig. 4. Calculated profiles of the temperatures of the heavy ($\bar{T}$) and electron ($\bar{T}_e$) plasma components and the degree of ionization α in an unsteady homogeneous plasma flow under conditions of strong MHD interaction: (*P*) primary shock wave, (*C*) contact surface, and (*S*) secondary shock wave.

COMPARISON BETWEEN COMPRESSIONAL MHD SHOCKS IN PLASMA FLOWS THAT ARE STABLE AND UNSTABLE AGAINST THE ONSET OF IONIZATION INSTABILITY

The type of MHD interaction under study has been investigated rather comprehensively. Here, we present the main results concerning this type of interaction and will compare them to experimental results related to the other types of MHD interaction. Under our experimental conditions, the MHD shock develops as follows (see [4, 5]): The shock wave *P* emitted from the shock tube (the primary shock wave) propagates through the stationary gas filling the widening disk channel. The primary shock wave gives rise to a reversed (secondary) shock wave *S*, which is directed backward but is carried downstream by the flow. The gas portions compressed by the secondary and primary shock waves are separated by the contact surface *C*. These are the main gas-dynamic discontinuities. Due to MHD interaction, the secondary shock wave slows down and transforms into a stationary compressional MHD shock. Note that the existence of a stationary flow implies that the conditions of flow trapping are satisfied at the end of the MHD interaction space; i.e., $M = 1$ at $x = x_e$. The system of nonstationary equations describing the behavior of the gas and the electron plasma component in a disk channel was solved in [5]. Figure 4 shows the calculated distributions of the parameters at the instant $t = 35$ μs after the primary shock wave has entered the disk MHD channel. The main gas-dynamic discontinuities and the different behavior of the heavy and the electron plasma components are clearly seen. Specifically, the temperature of the heavy component exhibits consider-

able and sharp changes: it decreases appreciably as the gas expands from the channel entrance to the secondary shock wave, undergoes an abrupt jump at the secondary shock front, sharply increases at the contact surface, and drops abruptly at the front of the incident wave. In contrast, the electron temperature and the degree of ionization in the region between the channel entrance and the contact surface vary insignificantly. It should be noted that the gas in this region was previously heated and ionized in the shock tube. The gas that was initially cold and unionized and that was then heated by the incident shock wave (the region between *P* and *C*) is ionized at a comparatively low rate. When calculating the degree of ionization in this region, it was assumed that the degree of ionization in front of the primary shock was 10^{-5}.

The plasma glow recorded in our experiments is mainly related to the recombination continuum, whose intensity depends on the plasma parameters as $n_e^2 T_e^{-0.5}$. The electron density at the gas-dynamic discontinuities changes by approximately the same value as the temperature of the heavy component; i.e., sharp changes in the glow intensity correspond to sharp changes in the gas density. This allows one to determine the positions of the secondary shock front and the contact surface by measuring the glow gradient. As regards to the position of the first shock wave, it was established experimentally that a glow peak is always present at the front of the incident shock wave. To detect the arrival of the primary shock wave, a gas-filled cylinder was also placed at the end of the disk channel. The arrival of the shock wave was indicated by a sharp increase in the glow of the gas from which the shock wave was reflected. Figure 5 shows a series of photographs of the glowing disk channel for mode 5 at $B = 1.2$ T. These are fragments of the glow that were obtained with the help of the turning mirrors arranged as is shown in Fig. 3a. At the front of the primary shock wave *P*, a glow peak is clearly seen, which is then followed by a dark stripe. The subsequent sharp change in the glow intensity indicates the position of the contact surface *C*. Finally, the rapid drop in the glow intensity corresponds to the boundary of the secondary shock wave *S*.

The first three photographs (t_1, t_2, and t_3), which were taken with a 12-μs interval, demonstrate the nonstationary flow stage. The last photograph (t_4) shows the stationary flow pattern recorded 100 μs after the shock wave has entered the disk channel. The same process is illustrated in Fig. 6a, which presents an (*x*, *t*) streak image of the glow recorded through two vertical slits in the upper and lower parts of the disk. The contact surface (the leading front of the glow) and the secondary shock wave are clearly seen. The plasma density and, hence, the glow intensity behind the secondary shock wave are much higher than those in front of the shock. It can be seen that the secondary wave slows down and then comes to a stop; therefore, the stationary MHD shock is, in essence, identical to the stopped secondary shock wave. We compared the recorded (*x*, *t*) streak image to the results calculated in [4]. Figure 6b presents the data on the propagation of the primary shock wave, the contact surface, and the secondary shock wave. It can be seen that the experimental and theoretical results are in good agreement. Figure 7a shows the positions of the MHD discontinuities

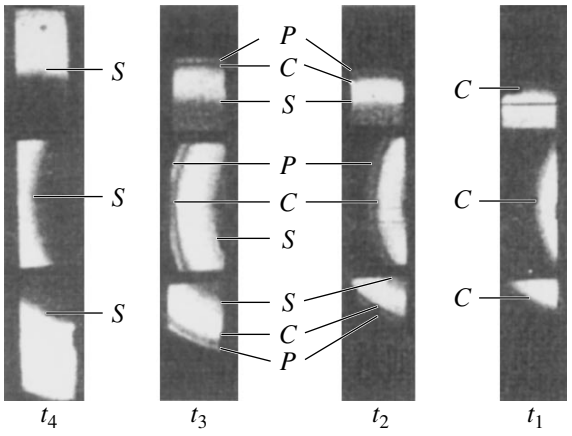

Fig. 5. Photographs of shock-wave configurations at different instants ($t_1 < t_2 < t_3 < t_4$): (*P*) primary shock wave, (*C*) contact surface, and (*S*) secondary shock wave.

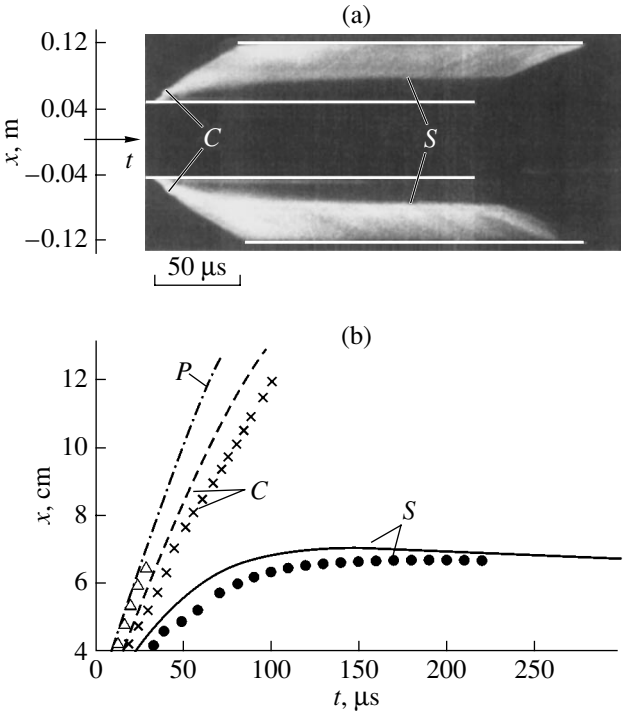

Fig. 6. (a) Streak images of the plasma glow recorded through two vertical slits: (*C*) contact surface and (*S*) secondary shock wave. (b) Positions of the primary shock wave (*P*), the contact surface (*C*), and the secondary shock wave (*S*) in the (*x*, *t*) plane. Symbols and curves show the experimental and calculated results, respectively.

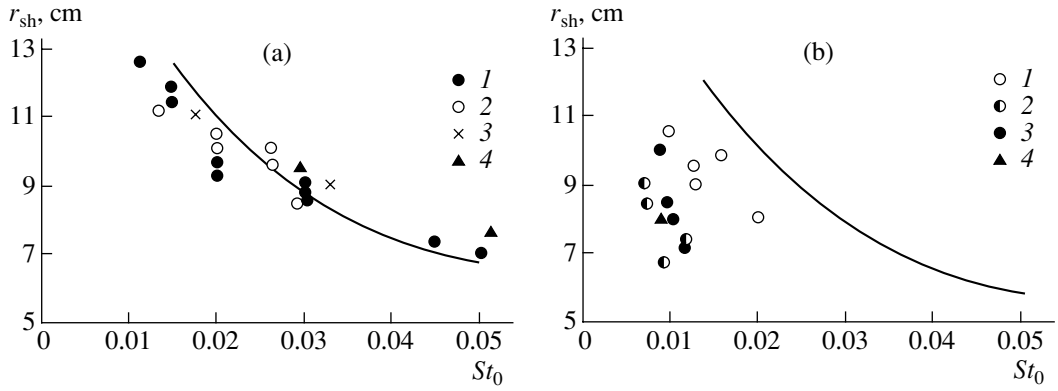

Fig. 7. Position of a compressional MHD shock in plasma flows that are (a) stable and (b) unstable against the onset of ionization instability as a function of the initial Stewart number for different gas-dynamic modes: (a) M_1 = (*1*) 9.7, (*2*) 9.4, (*3*) 10.5 (13 torr), and (*4*) 9.2 (26 torr); (b) M_1 = (*1*) 8.7, (*2*) 7.5 (13 torr), (*3*) 6.5, and (*4*) 6.9 (26 torr).

obtained in different MHD modes for different values of the magnetic field in homogeneous plasma flows. The experimental data are compared to the calculated results and to estimates by simplified formula (3). An analysis of the results presented in Fig. 6b allows us to conclude that formula (3) adequately describes the position of the shock in the channel. We recall once again that, in a stationary state, the secondary shock wave *S* is identical to the MHD shock.

Inhomogeneities in an MHD channel arise due to the onset of ionization (electrothermal) instability of a two-temperature plasma [6, 7]. It is conventionally assumed that a gas-dynamic flow is not perturbed by ionization instability. Ionization instability can be regarded as a thermal instability of the electron component in the presence of the Hall effect. However, as the plasma inhomogeneities grow, they may also cause gas-dynamic inhomogeneities; in this case, we are dealing with ionization–acoustic instability [5, 6]. As applied to our working substance (pure noble gases), plasma inhomogeneities arising in the absence of ionization equilibrium were studied in detail in [10, 11]. Plasma inhomogeneities were detected by the plasma glow. They appear at a certain distance from the entrance to MHD interaction space. Regions with enhanced luminosity are referred to as striations and are shown [10] to have an enhanced conductivity. The striations are shaped as spokes inclined by approximately 20° to the average direction of the current. From four to six spokes can be located on one radius. On average, two spokes simultaneously exist over the channel length. The velocity of plasma inhomogeneities is close to the flow velocity. It was shown in [11] that the plasma conductivity in striations increases with magnetic induction and grows as the striations propagate through the channel. As the degree to which the magnetic field exceeds its critical value increases, the gas conductivity in striations may reach fairly high values, so the interaction of these conducting layers with the magnetic field may change the gas-dynamic parameters of the flow and lead to the formation of a shock [12]. Figure 7b shows the measured position of the shock in different gas-dynamic modes at different values of the magnetic field. Similarly to the case of a homogeneous plasma, the plot presents the dimensionless shock coordinate versus the Stewart number at the entrance to the MHD interaction space. Figure 8 shows the structure of a shock formed in a flow with plasma inhomogeneities. It can be seen that the striations are refracted at the shock wave front and considerably slows down. Once formed, the shock only slightly migrates in the channel, so one can find the

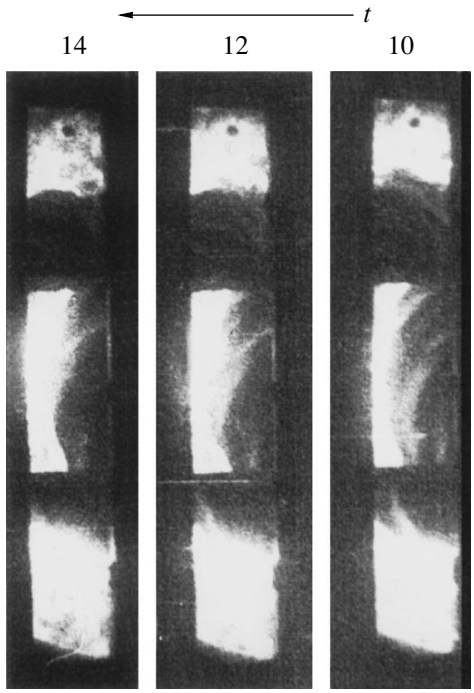

Fig. 8. Shock structure in an inhomogeneous plasma flow. Numerals above the photographs show the numbers of frames. The time interval between the frames is 2 μs.

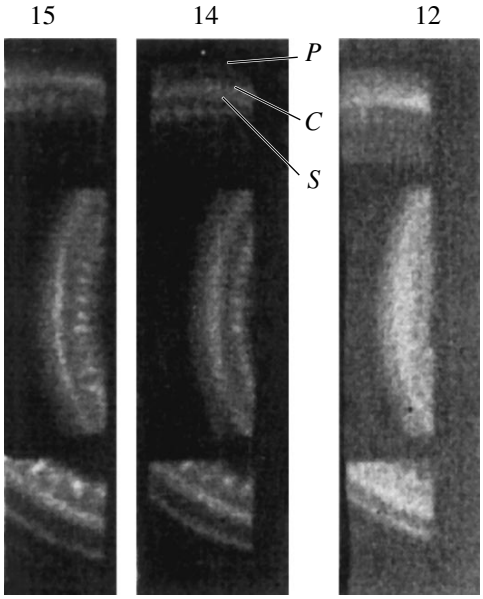

Fig. 9. Photographs illustrating instability of gas-dynamic discontinuities that arise due to MHD interaction: (*P*) primary shock wave, (*C*) contact surface, and (*S*) secondary shock wave. Numerals above the photographs show the numbers of frames.

quasi-steady position of the shock in a plasma that is unstable against the onset of ionization instability. A comparison of Figs. 7a and 7b shows that, in such plasmas, the MHD shock forms at appreciably lower initial Stewart numbers than in stable plasmas. This may be explained as follows: In striations, the conductivity and, hence, the Stewart number are higher than in the surrounding plasma. Therefore, in striations, the flow is decelerated and the kinetic energy is converted into thermal energy more efficiently than in the main body of the flow. As a result, the gas conductivity, the Stewart number, and the deceleration rate increase further. However, the deceleration of striations is hindered by the dynamic pressure of the surrounding gas. Thus, not only the kinetic energy of the striation but also the energy of the rest of the flow is partially converted into the thermal energy of the gas within the striation. For this reason, the local parameter of MHD interaction in the striation increases, the striation comes to a stop, and the incoming gas flow gives rise to a shock wave. Shock waves that appear near different striations interact with one another to form a quasi-steady MHD shock.

ON ONE TYPE OF INSTABILITY OF MHD DISCONTINUITIES

In experimental regime 5, an unusual behavior of the gas-dynamic fronts of the initial shock-wave configuration (the primary shock wave, the contact surface, and the secondary shock wave) propagating in a magnetic field was revealed [13]. Figure 9 shows photographs of the plasma glow recorded at different instants with a time interval between the frames of 2 μs. Frame 12 shows the front of the primary shock wave (*P*), the contact surface (*C*), and the secondary shock wave (*S*) 36 μs after the shock wave has entered the MHD interaction region. It can be seen that, at this instant, the glow region between the contact surface and the secondary shock wave is uniform and the gas-dynamic discontinuities have sharp boundaries. The subsequent frames reveal the formation of a complicated regular structure: in the *C*–*S* region, bright rings arise, whereas near the secondary wave front, small-scale drop- or cog-like formations oriented toward the flow appear. Some later, similar cogs also appear near the contact surface and, then, the glow pattern becomes irregular. The instability has a pronounced threshold character: it starts at $B = 0.7$ T and is suppressed as the magnetic field increases further. It is known [7] that the gravitational or electrodynamical Rayleigh–Taylor instability may take place in regions with high gradients of the plasma parameters; however, the growth rates of these instabilities are several orders of magnitude lower than that observed in our experiments. In [13], we made an attempt to explain the appearance of such perturbations in terms of ionization instability in the presence of high electron-pressure gradients; however, this hypothesis failed to explain the structure of the formation observed. Thus, the nature of this instability still remains unclear.

CONCLUSIONS

A comparative study has been performed of the formation of a compressional MHD shock in plasma flows that are stable and unstable against the onset of ionization instability. It is found that, in the later case, compressional MHD shocks form at considerably lower values of the MHD interaction parameter. An unidentified type of shock instability caused by MHD interaction is revealed.

REFERENCES

1. R. M. Patrick and T. R. Brogan, J. Fluid Mech. **5**, 289 (1959).
2. S. G. Zaytsev, E. I. Chebotareva, E. V. Lasareva, *et al.*, in *Proceedings of the 7th International Shock Tube Symposium, Toronto, 1969*, pp. 538–549.
3. S. G. Zaytsev, I. K. Favorskaya, and Yu. M. Chistyakova, Izv. Akad. Nauk SSSR, Mekh. Zhidk. Gaza, No. 5, 112 (1977).
4. R. V. Vasil'eva, A. V. Erofeev, A. D. Zuev, *et al.*, Zh. Tekh. Fiz. **57** (2), 251 (1987) [Sov. Phys. Tech. Phys. **32**, 150 (1987)].
5. R. V. Vasil'eva, A. L. Genkin, V. L. Goryachev, *et al.*, *Low-Temperature Nonequilibriumly Ionized Plasma of Inert Gases and MHD Generators* (FTI im. A. F. Ioffe, St. Petersburg, 1991) [in Russian].
6. L. A. Vulis, A. L. Genkin, and V. A. Fomenko, *Analysis of Magnetohydrodynamic Streams through Channels* (Atomizdat, Moscow, 1971) [in Russian].

7. A. V. Nedospasov and V. D. Khait, *Principles of Physical Processes in Low-Temperature Plasma Devices* (Énergoatomizdat, Moscow, 1991) [in Russian].
8. R. V. Vasil'eva, A. V. Erofeev, T. A. Lapushkina, *et al.*, AIAA Pap., No. 2000-2671 (2000).
9. R. V. Vasil'eva and A. V. Erofeev, Zh. Tekh. Fiz. **61** (4), 47 (1991) [Sov. Phys. Tech. Phys. **36**, 398 (1991)].
10. R. V. Vasil'eva, A. V. Erofeev, T. A. Lapushkina, *et al.*, Phys. Rev. E **63**, 03642-1 (2001).
11. R. V. Vasil'eva, A. V. Erofeev, D. N. Mirshanov, and T. A. Alekseeva, Zh. Tekh. Fiz. **59** (7), 27 (1989) [Sov. Phys. Tech. Phys. **34**, 728 (1989)].
12. R. V. Vasil'eva, A. V. Erofeev, A. D. Zuev, *et al.*, Zh. Tekh. Fiz. **56**, 1125 (1986) [Sov. Phys. Tech. Phys. **31**, 658 (1986)].
13. R. V. Vasil'eva, A. V. Erofeev, A. D. Zuev, *et al.*, Pis'ma Zh. Tekh. Fiz. **10**, 1390 (1984) [Sov. Tech. Phys. Lett. **10**, 587 (1984)].

Translated by A. Sidorova

Technical Physics, Vol. 50, No. 4, 2005, pp. 447–454. Translated from Zhurnal Tekhnicheskoĭ Fiziki, Vol. 75, No. 4, 2005, pp. 60–66.

GAS DISCHARGES, PLASMA

Townsend Coefficient and Efficiency of the Formation of Runaway Electrons in Neon

A. N. Tkachev, A. A. Fedenev, and S. I. Yakovlenko

General Physics Institute, Russian Academy of Sciences, ul. Vavilova 3, Moscow, 119991 Russia

Received April 14, 2004

Abstract—Basic ionization and drift properties are simulated for neon by the method of multiparticle dynamics. This calculation revealed that, in neon—in just the same way as in other gases that were studied previously—the Townsend ionization regime is realized even in strong fields if the distance between electrodes is rather large. The dependences of basic ionization and drift properties on the reduced electric-field strength are obtained. The results agree with available experimental data. The escape curve separating the region of efficient electron multiplication from the region in which electrons leave the discharge gap without undergoing multiplication is found for neon. The efficiency of the formation of a runaway-electron beam in helium and neon is simulated. © *2005 Pleiades Publishing, Inc.*

INTRODUCTION

Over the past year, considerable advances were made in understanding the phenomenon of electron runaway in gases [1–7]. On the basis of a simulation by the method of multiparticle dynamics and with the aid of simple analytic models, it was shown that the Townsend electron-multiplication mechanism is realized even in strong fields such that the ionization friction of electrons against a gas can be disregarded. Previously, it was assumed (see, for example, [8–10]) that, in such strong fields, electrons move in the continuous-acceleration regime (whistling), as in fully ionized plasma (see, for example, [11]).

The understanding of this fact led to several important conclusions. First, it was revealed that, despite the nonmonotonic dependence of the Townsend multiplication coefficient on the electric-field strength (in high fields, the Townsend coefficient decreases with increasing field strength, this being due to a decrease in the ionization cross section at high electron energies), the very concept of the Townsend coefficient does not lose meaning if the distance between the electrodes is rather large. This statement is based on the fact that, even in very strong fields, there is an exponential growth of the number of electrons with increasing distance from the cathode, their mean speed and energy remaining invariable.

The second point of importance is that, since there can be no runaway of electrons even in the case where one can disregard the ionization friction of electrons against a gas, a nonlocal criterion that differs from the local criterion adopted previously [8–10] was proposed in [1, 3] for electron runaway in gases. Specifically, the equality of the inverse Townsend coefficient and the distance between the electrodes was taken to be a criterion for the runaway of the bulk of the electrons in a gas.

Third, the nonmonotonic dependence of the Townsend coefficient on the field strength and the nonlocal character of the electron-runaway criterion resulted in revealing, for the curve separating the region of efficient electron multiplication from the region where the electrons escape from the discharge gap without undergoing multiplication, a two-valued dependence of the voltage on the product of pressure and the distance between the electrodes, this dependence being universal for a given gas. Curves that are analogs of Paschen curves and which have, in contrast to conventional Paschen curves, an additional upper branch, were constructed on the basis of the aforementioned dependence.

An analysis of the mechanism of runaway-electron formation in a gas is especially important at the present time in connection with obtaining electron beams of subnanosecond duration and a record amplitude of the current (about 70 A in air and about 200 A in helium [6, 7]) at atmospheric pressure. Indeed, a series of experiments was performed in 2002 and 2003 that aimed at obtaining runaway electrons in air, helium, and nitrogen at atmospheric pressure [6, 7, 11–16]. Beams of subnanosecond duration and high amplitude of the current that were recorded in those experiments were obtained at electric-field-strength values that were less than the value required in accordance with the local criterion [8–10] but satisfied the new, nonlocal, criterion as the plasma moves from the cathode to the anode [1–7].

1063-7842/05/5004-0447$26.00

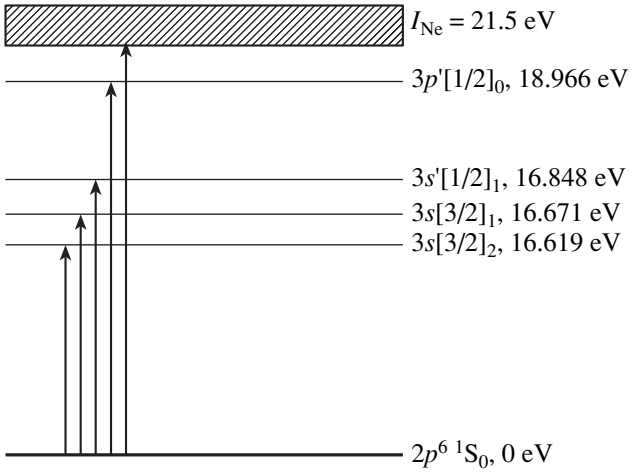

Fig. 1. Transitions in the neon atom that are considered in the model used. The quantum numbers of a state and its excitation energy are indicated on the right.

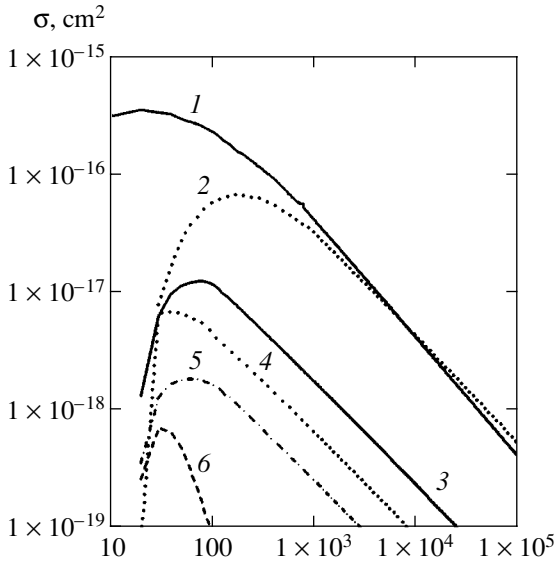

Fig. 2. Cross sections for electron collisions with a neon atom vs. energy: (*1*) elastic-collision cross section $\sigma_{el}(\varepsilon)$, (*2*) ionization cross section $\sigma_i(\varepsilon)$, (*3*) cross section for the excitation of the $3s'[1/2]_1$ level, (*4*) cross section for the excitation of the $3p'[1/2]_0$ level, (*5*) cross section for the excitation of the $3s[3/2]_1$ level, and (*6*) cross section for the excitation of the $3s[3/2]_2$ (according to data from [23–25]).

It should also be noted that the results obtained in [1–7] were used in constructing a streamer model [17–19] that makes it possible to explain the motion of its head both to the anode and to the cathode without invoking the well-known photon hypothesis.

Previously, a numerical simulation of electron multiplication and the tabulation of ionization and drift properties were performed for helium [1, 2, 4, 5], xenon [2, 4, 5], nitrogen [5], and sulfur hexafluoride [3]. Below, we present the result of similar calculations for neon.

MULTIPLICATION OF ELECTRONS

Description of the model used. In order to find ionization and drift properties, we used the same model of multiparticle dynamics as in [1–7]. It was described in detail elsewhere [20]. In this model, electrons are produced at the cathode with a chaotically directed velocities and initial energies obeying the Poisson distribution at a mean value of $\varepsilon_0 = 0.2$ eV. At small time steps, we solved the equations of motion for all electrons and simulated elastic and inelastic collisions with probabilities determined by cross sections for elementary processes. The motion of the electrons was assumed to be nonrelativistic (for the inclusion of relativistic effects, the interested reader is referred to [21]). Below, we present our results for the case of flat electrodes separated by a distance *d*, denoting the voltage applied between them by *U*. The method for treating the case of coaxial cylinders is described in [20]. The shape of avalanches is not considered here (for information about this issue, see [22]).

We took into account elementary events schematically represented in Fig. 1. We considered events of elastic electron scattering on neon atoms and events involving the electron-induced ionization of neon atoms and the excitation of the $3s'[1/2]_1$, $3p'[1/2]_0$, $3s[3/2]_2$, and $3s[3/2]_1$ neon-atom levels, but we disregarded multiple and stepwise ionization. The cross sections used here for elementary events are based on data reported in [23–27] and are displayed in Fig. 2.

Townsend regime of ionization. Our calculations reveal that, for neon—as well as for all gases considered previously [1–5]—the Townsend regime of ionization is indeed realized for all values of the ratio of the field strength to pressure in the range E/p = 5–5000 V/(cm Torr), which is considered here, if the distance *d* between the electrodes is rather large, runaway electrons being virtually absent in this case (see Fig. 3).

The Townsend character of the ionization regime is confirmed by the fact that, as the distance *x* from the cathode increases, the number of excitation and electron-production events always begins to grow exponentially from some value of *x*. Concurrently, the mean electron energy ε* and the mean electron-velocity projection onto the *x* axis become independent of *x* at rather large distances from the cathode. The distribution of electrons that reached the anode has a maximum in the region of low energies ($\varepsilon^* \ll eU$). As was indicated above, these signatures of the Townsend regime are observed at all values of the ratio E/p that were considered here. It is only necessary that the distance *d* be rather large.

The slope of the logarithm of the number of ionization events and of the current determine the Townsend multiplication coefficient α_i (Fig. 4). The calculations reveal that, as is usually assumed, the multiplication coefficient α_i is proportional to the gas density (pressure) and can be represented in the form $\alpha_i(E, p) = p\xi(E/p)$, where $\xi(E/p)$ is a function that is characteristic for a given gas.

For neon, there exists the approximation [9]

$$\xi_i = A\left(\frac{E}{p}\right)^{s - b\ln(E/p)}, \quad (1)$$

where $A = 1.584 \times 10^{-4}$ (cm Torr)$^{-1}$, $s = 3.052$, and $b = 0.23$.

However, the calculations show that this approximation is correct only for $E/p < 300$ V/(cm Torr). At larger values of the ratio E/p, the coefficient α_i begins to decrease. This decrease with increasing E/p is due to a decrease in the number of ionization events—that is, to a decrease in the ionization cross section for $\varepsilon > 170$ eV, the mean electron energy being close to this value at $E/p = 300$ V/(cm Torr). From Fig. 4b, one can see that, for $E/p < 1$ keV, the velocity component u_x along the field is much less than the velocity component $u_\perp$ orthogonal to the field. At small values of the ratio E/p, the velocity component u_x is a nearly linear function of the field strength.

The mean electron energy can be approximated as

$$\varepsilon^* = 7.0\exp(E/75p). \quad (2)$$

The reduced Townsend coefficient α_i/p for helium and neon is shown in Fig. 5 as a function of E/p. One can see that the maximum value of α_i/p is greater in neon than in helium and is attained at a higher value of the reduced electric-field strength E/p. For inert gases, the function $\xi(E/p)$, which describes the decrease in the Townsend coefficient with increasing electric-field strength, can be represented in the form [1, 2]

$$\xi(E/p) = A\exp\left[-B\left(\frac{p}{E}\right)^{\frac{1}{2}} - C\frac{E}{p}\right]. \quad (3)$$

On the basis of our simulation, we obtained the following values for neon: $A = 7.2$ [V/(cm Torr)]$^{-1}$, $B = 16.1$ [V/(cm Torr)]$^{1/2}$, and $C = 7 \times 10^{-3}$ (cm Torr/V). As can be seen from Fig. 5, the approximation in (3) describes well the results of our calculations.

In a number of applications, the relative efficiencies of various inelastic events in a given external electric field are of interest. We define them as $\delta_i = n_i/n_\Sigma$, $\delta_{s2} = n_{s2}/n_\Sigma$, $\delta_{s1} = n_{s1}/n_\Sigma$, $\delta_{ss2} = n_{ss2}/n_\Sigma$, and $\delta_{pp1} = n_{pp1}/n_\Sigma$, where n_i is the number of ionization events; n_{s2}, n_{s1}, n_{ss1}, and n_{pp0} are the numbers of events involving the excitation of the $3s[3/2]_2$, $3s[3/2]_1$, $3s'[1/2]_1$, and $3p'[1/2]_0$ states, respectively; and $n_\Sigma = n_i + n_{s2} + n_{s1} + n_{ss1} + n_{pp0}$ is the total number of inelastic events.

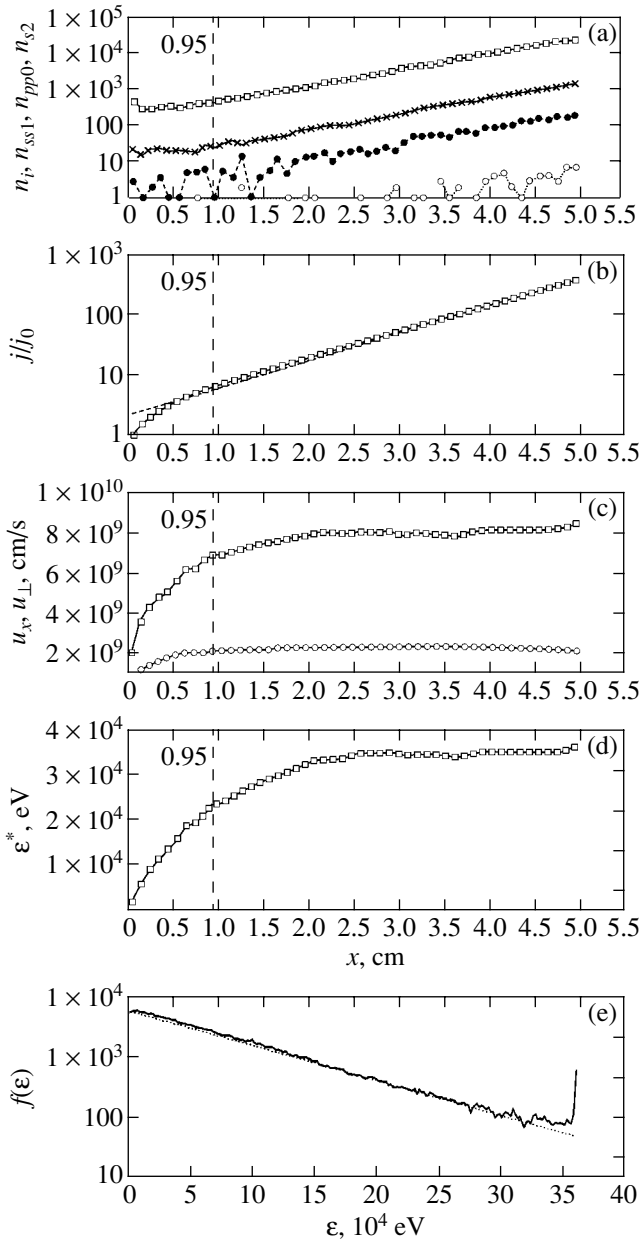

Fig. 3. Features of electron multiplication in the Townsend regime vs. the distance x from the cathode at $N_{Ne} = 3.219 \times 10^{17}$ cm^{-3} ($p = 10$ Torr), $U = 360$ kV, $d = 50$ mm, and $E = 72$ kV/cm [$E/p = 7200$ V/(cm Torr)]: (a) number n_i of product ions (boxes) and numbers n_{s2}, n_{s1}, n_{ss1}, and n_{pp0} of events involving the excitation of, respectively, the (circles) $3s[3/2]_2$, $3s[3/2]_1$, (crosses) $3s'[1/2]_1$, and (diamonds) $3p'[1/2]_0$ states (under these conditions, $\alpha_i = 1.05$ cm^{-1} and $\alpha_i d \approx 5$); (b) ratio of the electron flux at a given point, $j(x)$, to the flux of electrons emitted from the cathode, j_0, the dashed line representing the dependence $2.2\exp(1.05x)$; (c) electron-velocity projection u_x onto the x axis aligned with the electric field (boxes) and absolute value of the velocity component $u_\perp$ in the plane orthogonal to the x axis (circles); (d) mean electron energy; and (e) calculated energy (eV) distribution (in arbitrary units) of electrons that reached the anode (solid curve), along with the dependence $5.4 \times 10^3 \exp(-\varepsilon/75$ keV) (dotted curve).

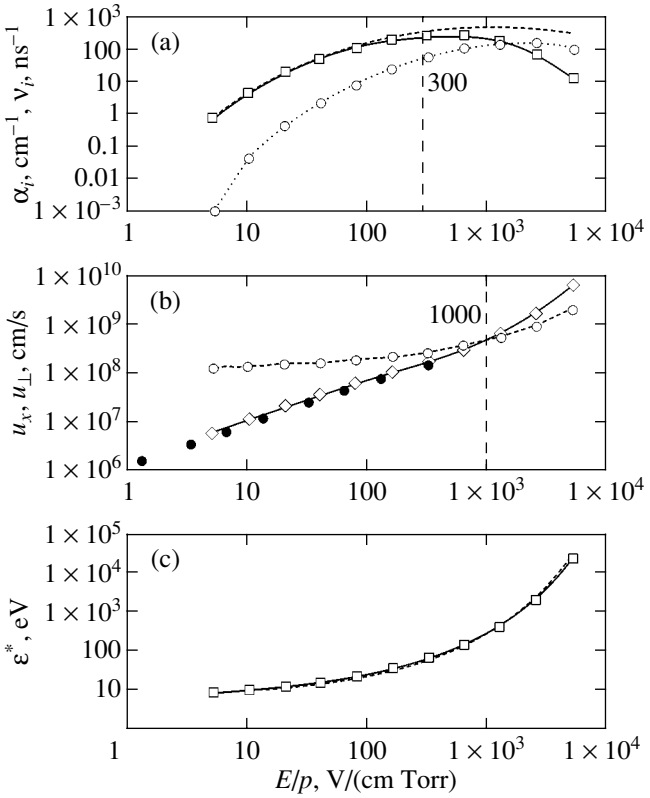

Fig. 4. Ionization and drift features vs. the reduced electric-field strength E/p [values represented by the symbols in the figure were obtained for various electric-field strengths at a neon pressure of p = 100 Torr ($N_{Ne} = 3.219 \times 10^{18}$ cm^{-3})]: (a) Townsend ionization coefficient α_i (boxes), ionization frequency ν_i (circles), and approximation in form (1) for neon [9] (dashed line); (b) mean velocity projection u_x on the x axis aligned with the electric field (diamonds), mean modulus of the velocity component $u_\perp$ in the plane orthogonal to the x axis (open circles), and experimental points borrowed from [26] (closed circles); and (c) mean value of the electron energy at various electric-field strengths at a neon pressure of p = 100 Torr (circles).

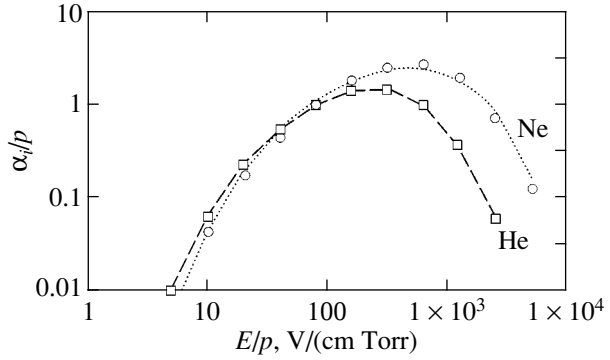

Fig. 5. Reduced Townsend coefficient α_i/p for (circles) neon and (boxes) helium. The dotted curve represents the approximation in form (3) for neon [9].

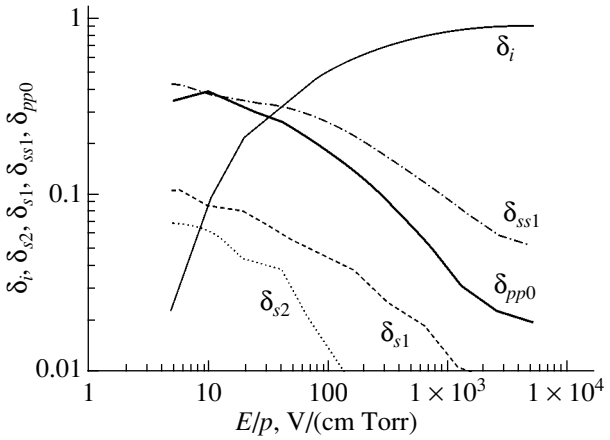

Fig. 6. Efficiencies of various inelastic processes vs. the reduced electric-field strength.

The quantities n_Σ, n_i, n_{s1}, n_{ss1}, and n_{pp0} depend on the distance from the cathode (see Fig. 3); however, their ratios (in particular, the relative efficiencies δ) are independent of the distance from the cathode in the Townsend multiplication regime (see Fig. 6).

NONLOCAL CRITERION

Critical voltage. The Townsend regime of ionization sets in at some distance from the cathode, $x \sim \alpha_i^{-1}$, this distance corresponding to the characteristic multiplication length. But if the distance between the electrodes is small, $d < \alpha_i^{-1}$, the electron-multiplication pattern differs drastically from that in the Townsend regime (see [1] for details). A significant part of the electrons are continuously accelerated: both the projection u_x of the electron velocity onto the electric-field direction and the mean electron energy ε^* increase with increasing distance x from the cathode, the peak of the energy distribution of electrons that reach the anode corresponding to the maximum energy $eU = eEd$ acquired by an electron as it travels from the cathode to the anode.

In contrast to the conventional approach employed in [8–10], it was proposed in [1–7] to assume that runaway electrons appear to be dominant in the case where the distance d between the electrodes becomes commensurate with the characteristic multiplication length—that is, with the inverse Townsend coefficient α_i^{-1}. For $\alpha_i d < 1$, runaway electrons also dominate the spectrum of electrons that reached the anode. Accordingly, the criterion that determines the boundary value

of the electric-field strength, E_{cr}, takes the form

$$\alpha_i(E_{cr}, p)d = 1.$$

In the Townsend coefficient, we further factor out pressure and/or gas density and consider that the remaining factor depends only on the reduced field strength E/p: $\alpha_i(E, p) = p\xi(E/p)$. For flat electrodes $E = U/d$; accordingly, $E_{cr} = U_{cr}/d$. The criterion for the escape of electrons from the gap between flat electrodes assumes the form

$$pd\xi(E_{cr}/p) = 1 \quad \text{or} \quad pd\xi(U_{cr}/pd) = 1. \qquad (4)$$

The last formula in (4) gives an implicit dependence of the critical voltage $U_{cr}(pd)$ (see Fig. 7) on the product of the distance between the electrodes and pressure, pd. The curve representing the dependence $U_{cr}(pd)$ separates the region of efficient electron multiplication from the region in which the electrons leave the discharge gap without undergoing multiplication. This curve is universal for a given gas. Following [1–5], we refer to it as the escape curve for electrons.

Lower and upper branches of the escape curve. Since the dependence $\xi(E/p)$ features a maximum, the curve $U_{cr}(pd)$ is horseshoe-shaped for various gases. The results of our calculations for neon are displayed in Fig. 7. The electron-escape curve features a lower and an upper branch. For the boundary point between them, we take the turning point—that is, the point at which the product pd takes the minimum value $(pd)_{min}$. We will now show that this point corresponds to the maximum of the function $\xi(x)$.

Let us consider the product pd as a function of U_{cr}. Under the condition $d(pd)/dU_{cr} = 0$, which corresponds to the minimum of pd as a function U_{cr}, we find from (4) that $\xi'(x) = 0$, which corresponds to the maximum of the function $\xi(x)$. Thus, we see that, at the boundary point defined as the minimum value of the product pd on the curve $U_{cr}(pd)$, the reduced electric-field strength takes precisely the value $E/p = (E/p)_{max}$ at which the reduced Townsend coefficient $\alpha_i/p = \xi(E/p)$ has a maximum.

The existence of the upper branch of the escape curve $U_{cr}(pd)$ is due to a decrease in the Townsend coefficient with increasing E/p. In turn, the decrease in the Townsend coefficient is caused by a decrease in the ionization cross section with increasing incident-electron energy and by the growth of multiplied-electron energy with increasing E/p. The region above the upper branch of the escape curve corresponds to the situation where, acquiring a high energy over the mean free path, the electrons leave the discharge gap without having time to be efficiently multiplied because of the smallness of the ionization cross sections at high energies. In view of this, it is natural to refer to this region as the region of electron runaway (whistling); accordingly, the upper branch of the curve is referred to as the escape curve.

The lower part of the escape curve corresponds to the ascending branch of the dependence of the reduced

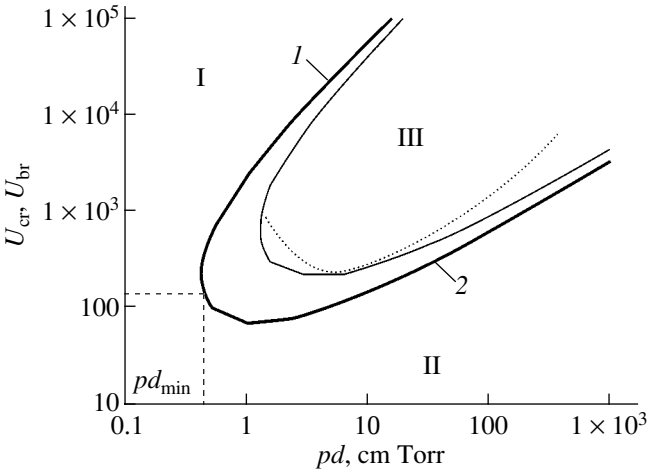

Fig. 7. Curve $U_{cr}(pd)$ separating the regions of electron escape and electron multiplication in neon (thick solid curve) and curve $U_{br}(pd)$ characterizing the discharge-ignition criterion at $L = 3$ and $\gamma = 0.05$ (thin solid curve) along with experimental data from [10] (dotted curve). The following notation is used here: (*1*) runaway curve; (*2*) drift curve; (I) runaway region; (II) drift region; and (III) electron multiplication, self-sustaining discharge.

Townsend coefficient α_i/p on E/p. In this region, the electrons acquire a moderately small energy over the mean free path, and this energy corresponds to the ascending branch of the dependence of the ionization cross section on the electron energy. In the region below the lower branch of the curve $U_{cr}(pd)$, one has a situation where the electrons drift from the cathode to the anode without acquiring energy sufficient for an efficient multiplication. Therefore, it is natural to refer to the region below the lower branch of the escape curve as the region of electron drift and to the lower branch of the curve as the drift curve.

ON THE CRITERION OF IGNITION OF A SELF-SUSTAINING DISCHARGE

Upper branch of the curve of ignition of a self-sustaining discharge. The curve that determines the criterion for the ignition of a self-sustaining discharge is usually found from the condition that each electron must generate ions whose number is sufficient for the production of yet another electron at the cathode via secondary electron emission. Accordingly, the breakdown voltage $U_{br}(pd)$ is determined from the condition (see, for example, [10])

$$\alpha_i(E, p)d = \ln(1 + 1/\gamma), \quad \text{or} \quad pd\xi(U_{br}/pd) = L, \quad \text{where} \quad L \equiv \ln(1 + 1/\gamma). \qquad (5)$$

Here, γ is the coefficient of secondary electron emission. Comparing the discharge-ignition criterion in (5) with the electron-runaway criterion in (4), we find the

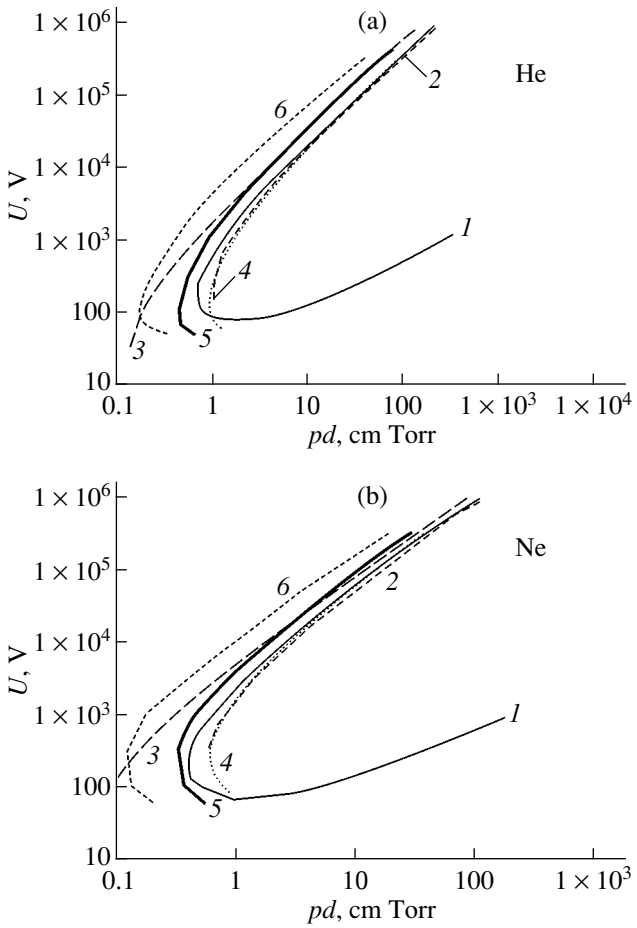

Fig. 8. Equal-efficiency curves and escape curves in (a) helium and (b) neon: (*1*) escape curves at $\alpha_i d = 1$, (*2*) runaway curves at $\alpha_i d = 1.5$, (*3*) runaway curves at $\alpha_i d = 0.2$, (*4*) efficiency curves at $\eta = 20\%$, (*5*) efficiency curves at $\eta = 50\%$, and (*6*) efficiency curves at $\eta = 80\%$.

relationship between the escape and ignition curves, $U_{br}(pd) = LU_{cr}(pd/L)$.

The resulting dependence $U_{br}(pd)$ contains radically new information in relation to the well-known Paschen ignition curve. Paschen curves are known to feature the right and the left branch going from the minimum of $U_{br}(pd)$ to the regions of, respectively, high and low values of the product pd. According to [1–7], however, the curve of ignition of a self-sustaining discharge must also involve an upper branch that is associated with the decrease in α_i with increasing E/p. The presence of the minimum value $(pd)_{min}$ at which the ignition of a self-sustaining discharge is still possible owing to electron multiplication via gas ionization in the gas-discharge gap (see Fig. 7) is yet another important corollary of the above analysis.

The fact that the burning of a discharge can be quenched at high voltages was indicated in [26].

Comparison with experimental data at low pressure. We note, however, that the character of the ignition curve $U_{br}(pd)$ is less general than the character of the escape curve $U_{cr}(pd)$: the latter is a universal feature of a given gas, while the former depends on the choice of discharge-ignition model—in particular, on the properties of the electrodes.

As was shown by Penning as far back as 1932 [28], the Paschen curve for helium has a loop with a turning point at $pd \approx 1.5$ cm Torr. The position of this turning point is in good agreement with the results of the calculations performed in [1–5]. Penning put forth the correct assumption that this loop is due to the presence of a maximum in the electron-energy dependence of the ionization cross section. However, this point of view did not receive general support from the physics community. In all probability, this was because (see, for example, [29]) no other inert gas displayed such a loop, despite the fact that the ionization cross sections for all elements had a maximum. Apart from helium, such a loop was observed only for mercury [30].

The point is that the part of the Paschen curve to the left of the point $(pd)_{min}$ reflects a different discharge-ignition mechanism that is weakly related to electron multiplication in a gas. This is suggested by the fact that, in this region, Paschen curves depend not only on the properties of a cathode material but also on the properties of an anode material [29]. The mechanism describing the left branch of Paschen curves for helium was studied in [31], where it was found that the three-valued character of the curve $U_{br}(pd)$ in the region around $pd \sim (pd)_{min}$ is due to the competition between different electron-production mechanisms in the volume and at the electrodes: Townsend ionization, secondary electron emission from the cathode under the effect of fast ions and atoms produced in ion charge-exchange processes, and electron scattering on the anode.

The results of experiments with gases at atmospheric pressure are reported in [6, 7, 12–16]. The state-of-the-art nanosecond technique made it possible to pass the lower branch of Paschen curves before the gas-discharge plasma shortens the interelectrode gap completely and to approach the runaway curve.

Curves describing the efficiency of electron-beam formation. From the definition of the runaway curve, it is clear that this curve characterizes qualitatively the fraction of runaway electrons. In general, there is some arbitrariness in the expression on the right-hand side of (4). The right-hand sides in (4) can be set to π or $1/\pi$, for example, instead of unity. It is obvious, however, that the choice of constant on the right-hand sides here is not of crucial importance. Setting $\alpha_i d = A = \text{const}$, for example, we find that there arises a new quantity U'_{cr} that satisfies the equation $pd\xi(U'_{cr}/pd) = A$, whence it follows that $U_{cr}(pd) = U'_{cr}(pd/A)/A$. If use is made of logarithmic scales, the

curve $U'_{cr}(pd)$ is obtained from the curve $U_{cr}(pd)$ by means of shifts along the axes.

Although the escape curve characterizes qualitatively the boundary between electron multiplication and electron runaway, it does not determine directly the fraction of runaway electrons. In order to reveal relevant quantitative features, we directly calculated the fractions $\eta \le 20\%$ of runaway electrons as functions of U and pd. The results of the calculations for helium on the basis of the model proposed in [1] and the respective results for neon that are based on the model outlined above are represented in the form of equal-efficiency curves in the plane spanned by the variables U and pd.

The calculations revealed (Fig. 8) that, at not very high values of efficiency ($\eta \le 20\%$), the escape curves are virtually coincident with the equal-efficiency curves. At higher values of the efficiencies, the escape curves agree with equal-efficiency curves only at large values of U and pd.

CONCLUSIONS

The ionization and drift properties of neon have been simulated by the method of multiparticle dynamics along the same lines as in [1–5], and the general results of those studies have been confirmed. Our numerical calculations have revealed that, at rather high fields, the Townsend ionization regime is also realized in the case of neon if the condition $\alpha_i d \gg 1$ holds. The dependences of basic ionization and drift properties on the reduced electric-field strength E/p have been obtained. The results agree with available experimental data. For neon, we have obtained the dependence of the critical voltage on the product of pressure and the distance between the electrodes—that is, the escape curve, which separates the region of efficient electron multiplication from the region in which the electrons leave the discharge gap without undergoing multiplication. We have also calculated the efficiency of electron-beam formation as a function of the voltage between flat electrodes and the product of pressure and the distance between the electrodes. It has been shown that the equal-efficiency curves are consistent with the escape curves previously introduced in [1–5].

The importance of considering runaway curves (upper branches of escape curves) and equal-efficiency curves is associated, in particular, with the fact that the present-day nanosecond technology makes it possible to obtain intense beams in a dense gas when the required discharge parameters in the vicinity of the escape curve are rapidly approached [6, 7, 11–16]. Possibly, this method for obtaining subnanosecond electron beams will prove to be competitive with the traditional approach [31, 32].

ACKNOWLEDGMENTS

We are grateful to V.F. Tarasenko for encouraging discussions.

This work was supported by the International Science and Technology Center, grant no. 2706.

REFERENCES

1. A. N. Tkachev and S. I. Yakovlenko, Pis'ma Zh. Éksp. Teor. Fiz. **77**, 254 (2003) [JETP Lett. **77**, 221 (2003)].
2. A. N. Tkachev and S. I. Yakovlenko, Pis'ma Zh. Tekh. Fiz. **29** (16), 54 (2003) [Tech. Phys. Lett. **29**, 683 (2003)].
3. A. M. Boĭchenko, A. N. Tkachev, and S. I. Yakovlenko, Pis'ma Zh. Éksp. Teor. Fiz. **78**, 1223 (2003) [JETP Lett. **78**, 709 (2003)].
4. A. N. Tkachev and S. I. Yakovlenko, Pis'ma Zh. Tekh. Fiz. **30** (7), 14 (2004) [Tech. Phys. Lett. **30**, 265 (2004)].
5. S. I. Yakovlenko and A. N. Tkachev, in *Proceedings of the 5th International Conference on Atomic and Molecular Pulsed Lasers, Tomsk, 2003*, Ed. by V. F. Tarasenko, G. V. Mayer, and G. G. Petrash; Proc. SPIE **5483**, 161–173 (2003).
6. V. F. Tarasenko, S. I. Yakovlenko, V. M. Orlovskiĭ, and A. N. Tkachev, Kratk. Soobshch. Fiz., No. 4, 8 (2003).
7. V. F. Tarasenko, S. I. Yakovlenko, V. M. Orlovskiĭ, *et al.*, Pis'ma Zh. Éksp. Teor. Fiz. **77**, 737 (2003) [JETP Lett. **77**, 611 (2003)].
8. L. P. Babich, T. V. Loĭko, and V. A. Tsukerman, Usp. Fiz. Nauk **160** (7), 49 (1990) [Sov. Phys. Usp. **33**, 521 (2003)].
9. Yu. D. Korolev and G. A. Mesyats, *Physics of Impulse Breakdown in Gases* (Nauka, Moscow, 1991).
10. Yu. P. Raizer, *Gas Discharge Physics* (Nauka, Moscow, 1992; Springer-Verlag, Berlin, 1991) [in Russian].
11. D. V. Sivukhin, in *Reviews of Plasma Physics*, Ed. by M. A. Leontovich (Gosatomizdat, Moscow, 1964; Consultants Bureau, New York, 1968), Vol. 4, pp. 81–187.
12. S. B. Alekseev, V. M. Orlovskiĭ, and V. F. Tarasenko, Pis'ma Zh. Tekh. Fiz. **29** (10), 29 (2003) [Tech. Phys. Lett. **29**, 411 (2003)].
13. S. B. Alekseev, V. M. Orlovskiĭ, V. F. Tarasenko, *et al.*, Pis'ma Zh. Tekh. Fiz. **29** (16), 45 (2003) [Tech. Phys. Lett. **29**, 679 (2003)].
14. S. B. Alekseev, V. P. Gubanov, V. M. Orlovskiĭ, *et al.*, Prib. Tekh. Éksp., No. 4, 81 (2003).
15. V. F. Tarasenko, V. M. Orlovskiĭ, and S. A. Shunaĭlov, Izv. Vyssh. Uchebn. Zaved. Fiz., No. 3, 94 (2003).
16. V. F. Tarasenko, V. G. Shpak, S. A. Shunaĭlov, *et al.*, Pis'ma Zh. Tekh. Fiz. **29** (21), 1 (2003) [Tech. Phys. Lett. **29**, 879 (2003)].
17. S. I. Yakovlenko, http://zhurnal.ape.relarn.ru/articles/2004/009/pdf.
18. S. I. Yakovlenko, Kratk. Soobshch. Fiz., No. 10, 27 (2003).
19. S. I. Yakovlenko, Pis'ma Zh. Tekh. Fiz. **30** (9), 12 (2004) [Tech. Phys. Lett. **30**, 354 (2004)].
20. A. N. Tkachev and S. I. Yakovlenko, Laser Phys. **12**, 1022 (2002).

21. A. N. Tkachev and S. I. Yakovlenko, Kratk. Soobshch. Fiz., (2004).
22. A. N. Tkachev and S. I. Yakovlenko, Zh. Tekh. Fiz. **74** (3), 91 (2004) [Tech. Phys. **49**, 371 (2004)].
23. D. F. Register and S. Trajmar, Phys. Rev. A **29**, 1785 (1984).
24. G. D. Meneses, R. E. H. Clark, J. Abdallah, and G. Csanak, Jr., J. Phys. B **35**, 3119 (2002).
25. F. A. Sharpton, R. M. St. John, C. C. Lin, and F. E. Fajen, Phys. Rev. A **2**, 1305 (1970).
26. A. V. Eletskiĭ and B. M. Smirnov, *Physical Processes in Gas Lasers* (Énergoatomizdat, Moscow, 1985) [in Russian].
27. G. V. Kolbychev, Zh. Tekh. Fiz. **52**, 511 (1982) [Sov. Phys. Tech. Phys. **27**, 326 (1982)].
28. F. M. Penning, Physica (Amsterdam) **12** (4), 65 (1932).
29. A. N. Dikidzhi and B. N. Klyarfel'd, Zh. Tekh. Fiz. **25**, 1038 (1955).
30. L. G. Guseva and B. N. Klyarfel'd, Zh. Tekh. Fiz. **24**, 1169 (1955).
31. K. N. Ul'yanov and V. V. Chulkov, Zh. Tekh. Fiz. **58**, 328 (1988) [Sov. Phys. Tech. Phys. **33**, 201 (1988)].
32. K. A. Zheltov, *High-Current Picosecond Electron Accelerators* (Énergoatomizdat, Moscow, 1991) [in Russian].

Translated by A. Isaakyan

Technical Physics, Vol. 50, No. 4, 2005, pp. 455–461. Translated from Zhurnal Tekhnicheskoĭ Fiziki, Vol. 75, No. 4, 2005, pp. 67–73.

GAS DISCHARGES, PLASMA

Microwave Discharge on the Surface of a Dielectric Antenna

V. M. Shibkov, A. P. Ershov, V. A. Chernikov, and L. V. Shibkova

Moscow State University, Vorob'evy Gory, Moscow, 119992 Russia

e-mail: shibkov@ph-elec.phys.msu.ru

Received June 22, 2004

Abstract—A microwave discharge initiated by a surface wave on a dielectric body placed in a supersonic air flow is studied. The discharge is shown to represent a thin plasma layer that uniformly covers the antenna surface. In experiments, the discharge propagation velocity may be as high as 100 km/s, which is several orders of magnitude higher than the velocity of sound in air. The peak pulse power necessary to excite the discharge in a wide range of air pressures (from 10^{-3} to 10^3 Torr) is no higher than 100 kW. It is shown that the gas temperature may rise to 1000–2000 K, rapidly increasing (with a rate of ≈50 K/μs) at the early stage of discharge evolution. The discharge of this type may find applications in super- and hypersonic plasma aerodynamics (such as control of the flow near the surface of a body moving in a dense atmosphere, reduction of surface friction, optimization of ignition and combustion conditions for supersonic flows of gaseous fuel, etc.). It may also be used to advantage in development of new-generation plasma sources for micro- and nanoelectronics purposes (plasma treatment of surfaces, etching, and film deposition). © *2005 Pleiades Publishing, Inc.*

INTRODUCTION

Advances in aviation technology call for R&D aimed at creating new efficient means for controlling the gas flow parameters near an aircraft's surface, heat and mass transfer in the boundary layer, and flow separation; reducing the surface friction; and suppressing the laminar–turbulent transition; as well as for cutting the ignition time and controlling the combustion of supersonic fuel flows in a ramjet engine. A new solution to these problems is application of different gas discharges. This has given rise to a new field of research in plasma physics, supersonic plasma aerodynamics, which is rapidly progressing today [1, 2]. Specifically, it is conjectured that placement of plasma objects in front of and on the lifting surfaces of the vehicle will improve its aerodynamic characteristics and use of a nonequilibrium gas-discharge plasma will cut the fuel ignition time in a hypersonic ramjet engine. However, although the discharge in the gas flow has been studied for many years, the physics of discharge in the supersonic flow is still in its infancy. Many problems remain to be solved, among which gas breakdown, optimization of the discharge conditions in a supersonic air flow, maintenance of plasma objects in the gas flow, influence of the flow on the plasma parameters, and influence of the discharge on the supersonic flow characteristics are the most significant. Research groups worldwide are now concentrating on studying dc electrode discharges, as well as on pulsed periodic and rf discharges in a supersonic air flow. Such discharges strongly erode the electrodes and the surface of the model and cannot be reliably reproduced in experiments. It is therefore necessary to optimize the conditions for nonequilibrium plasma generation in a supersonic air flow. Our research group has pioneered work in initiating rf discharge of a new type, a microwave discharge generated by a wave on the surface of an insulator over which a supersonic air flows [3].

It is known [4–9] that, when a microwave discharge is initiated inside a gas-filled dielectric-wall tube, the electromagnetic energy applied to the system is converted into a surface wave. The resulting system is self-consistent: for the surface wave to exist, the plasma medium produced by the wave itself is necessary. The wave propagates in space as long as its energy suffices to produce a plasma with an electron concentration no lower than critical concentration $n_{e,\,cr} = m(\omega^2 + \nu^2)/(4\pi e^2)$, where e is the electron charge, m is the electron mass, ω is the circular frequency of the field, and ν is the frequency of electron–neutral collisions. The surface wave does not penetrate into the region where the electron concentration is below $n_{e,\,cr}$, so that the surface discharge is there absent. Such a way of plasma generation has been implemented in a device referred to as the surfatron. This technique has been studied in sufficient detail and is being widely used, for example, in plasma chemistry. Here, we are dealing with a plasma–insulator–free space system (Fig. 1a): a gas-filled low-pressure discharge tube contains a plasma produced by a surface wave, and this plasma is separated from the environment by the dielectric walls.

1063-7842/05/5004-0455$26.00 © 2005 Pleiades Publishing, Inc.

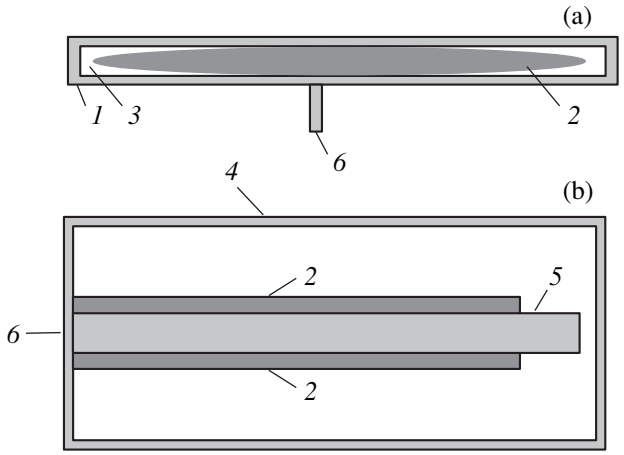

Fig. 1. Generation of the surface microwave discharge (a) inside a dielectric tube and (b) on the surface of a dielectric antenna. (*1*) Dielectric tube, (*2*) plasma of the surface microwave discharge, (*3*) low-pressure gas, (*4*) discharge chamber, (*5*) dielectric antenna, and (*6*) input of the microwave energy.

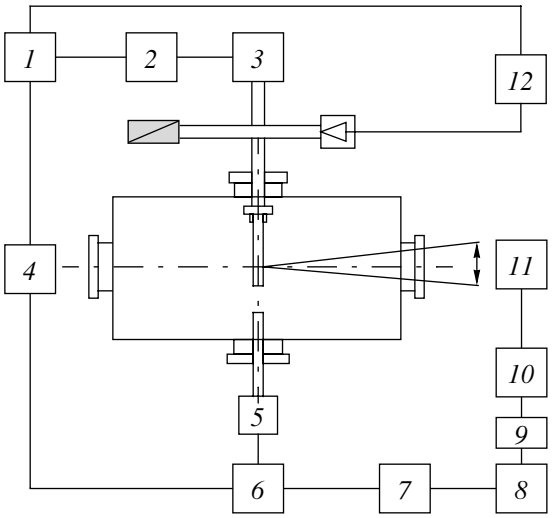

Fig. 2. Schematic of the experimental setup. (*1*, *6*) Synchronizers, (*2*) modulator, (*3*) magnetron, (*4*) driving generator, (*5*) supersonic air flow generator, (*7*) computer, (*8*) power supply unit, (*9*) CCD array, (*10*) photomultiplier, (*11*) monochromator, and (*12*) digital oscilloscope.

In this paper, we turn the system considered above inside out: the plasma covers an insulator on the surface of which a plasma-sustaining microwave electromagnetic wave is generated (Fig. 1b).

EXPERIMENTAL SETUP

The experimental setup used in the experiment consists of a vacuum chamber, magnetron generator, system delivering the microwave energy to the chamber, supersonic flow generator, and diagnostic system (Fig. 2).

As a microwave source, the setup employs a cm-wave pulse magnetron generator described in [10]. This generator can produce both individual pulses and high-rate pulse trains. The magnetron has the following performance parameters: wavelength $\lambda = 2.4$ cm, peak microwave power output $W < 300$ kW, pulse duration $\tau = 1$–200 μs, pulse repetition rate $f = 1$–100 Hz, and duty ratio $Q = 1000$. The average output is no higher than 300 W. The magnetron is fed by a specially designed pulse modulator built around a partially discharging storage capacitor. The pulse modulator accumulates energy for the relatively long time between the pulses and then gives up a small portion of the energy to the microwave generator for the short pulse duration. The microwave power is directed to the discharge chamber through a 9.5×19-mm rectangular guiding channel equipped with control and measuring devices. The channel was hermetically sealed, and the waveguide was filled with SF_6 gas under a pressure of 4 atm to prevent electric breakdown. A specially designed device was used to couple the waveguide end inserted into the discharge chamber to a dielectric (quartz or Teflon) antenna on which a surface microwave discharge in a supersonic air flow was initiated. The envelope of the microwave pulse that was picked up from the detector was displayed on an oscilloscope. The waveform of the envelope was near-rectangular. This signal was also applied to the input of a peak-reading digital voltmeter intended for determination of the microwave pulse amplitude. For this purpose, the voltmeter was precalibrated using a calorimetric power meter, which was connected to the major arm of a directional coupler during the calibration process.

The discharge was initiated in a cylindrical metallic pressure chamber. Its inner diameter and length are 1 and 3 m, respectively. The vacuum system of the chamber allows us to vary the pressure over a wide range from 10^{-3} to 10^3 Torr. The vacuum chamber consists of two, large and small, sections. The large section mounted on a truck can be disconnected from the small one with the help of a locking device and rolled away by rails. This makes it easily accessible for arrangement of test objects and other technological chores. The lateral surface of the chamber accommodates several diagnostic windows of diameter $d = 10$–50 cm and a number of sealed feedthroughs. Thus, we could observe the processes inside the chamber and apply the voltage, as well as control and auxiliary signals, to the chamber without breaking its tightness.

A supersonic air flow with a given Mach number was generated with an electromechanical valve with a tailored Laval nozzle on its outlet pipe. For the nozzle not to affect the propagation of the microwave energy, it is made of an insulating material. The nozzles used in these experiments had a cylindrical or rectangular shape and provided $M = 2$, where M is the Mach num-

ber of the flow. The electromechanical valve was mounted on the flange of the side window so that the supersonic air flow was directed along the horizontal diameter of the chamber. To synchronize the opening of the electromechanical valve with the microwave discharge initiation, the setup is configured with a delay circuit. In the experiments, the electromechanical valve was opened for 2 s, and the surface microwave discharge was initiated for this time. The supersonic flow was directed oppositely to the direction of the surface wave, i.e., to the direction of the surface discharge.

DIAGNOSTIC TECHNIQUES

To measure the threshold characteristics of the surface microwave discharge, we recorded the minimal applied power at which the discharge is initiated on the surface of the insulator versus air pressure p in the chamber at various pulse durations τ. The microwave energy applied was gradually increased with τ and p fixed and the power at which the plasma started to form on the surface was recorded. Such measurements were performed several times with subsequent averaging of the data. Then, the pressure in the chamber was varied with pulse duration fixed and the threshold power at a new pressure was recorded. The time of discharge initiation was either observed visually or taken to be the time when the signal picked up from the collimated photomultiplier facing the antenna region near the edge of the waveguide appeared on the screen of the digital oscilloscope. The second beam of the oscilloscope displayed the signal from the microwave detector. The amplitude of this signal was proportional to the peak microwave pulse power applied.

The general view of the surface microwave discharge was photographed in two projections (side view and top view). The microphotometry of the film allowed us to determine the longitudinal size of the surface discharge at different air pressures, microwave pulse durations, and peak pulse powers. Also, the discharge was recorded by a video camera. Record playback made it possible to measure the dimensions of the discharge at different pulse durations and find its longitudinal velocity.

The gas temperature was determined spectroscopically by taking the line intensity distribution for the rotational structure of the (0; 2) band of the second positive system of nitrogen (photon wavelength λ = 380.5 nm). The vibrational temperature was found from the relative band intensities of the second positive system of molecular nitrogen and from the band intensities of a cyan molecule. To measure the gas and vibrational temperatures, the radiation spectrum of the microwave discharge plasma was recorded with an STÉ-1 spectrograph (with a variable reciprocal linear dispersion of 0.3–1.0 nm/mm), as well as with DFS-12 and MDR-23 monochromators (with reciprocal linear dispersions of 0.5 and 1.3 nm/mm, respectively). The plasma radiation from a particular cross section of the discharge was projected onto the entrance slits of the spectral instruments by a system of lenses and mirrors. The focal lengths of the lenses were chosen in such a way as to demagnify the image of the discharge at the entrance slit. A photomultiplier or a linear CCD array (a diode-type assembly consisting of many light-sensitive elements) placed behind the exit slit served as a radiation detector. The spatial resolution of the recording system was specified by the number of light-sensitive elements and their size. In our system, the number of the elements was 3650, and the size of each of the elements was 8×8 μm. Accordingly, the spatial resolution of the optics used was no worse than 0.4 mm. The video signals from the receiver, which were directly proportional to the intensity of radiation with wavelength λ varying in the range 300–900 nm, were digitized by a software-controlled matching device (an ADC placed on the interface card), arrived at a PC, and were memorized in the form of a database. The discharge spectrum could be either displayed on the monitor or printed out using special software.

EXPERIMENTAL RESULTS

We suggest a new method of initiating a microwave surface discharge with the aim of exerting an optimal effect on the near-surface boundary layer, which arises when a gas (air) flows about the body with a supersonic velocity. To this end, a tailored dielectric antenna was designed and fabricated. In the experiments, the surface microwave discharge was initiated on a 5-cm-long rectangular (9.5 × 19 mm) antenna. The antenna also served as a seal separating the interior of the waveguide filled with SF_6 to a pressure of 4 atm from the interior

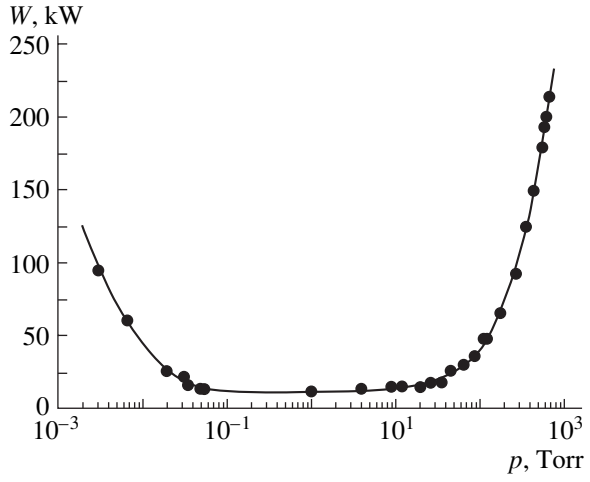

Fig. 3. Minimum microwave pulse power necessary for initiating the surface microwave discharge vs. pressure. The pulse duration is τ = 1.5 μs, and the pulse repetition rate is f = 40 Hz.

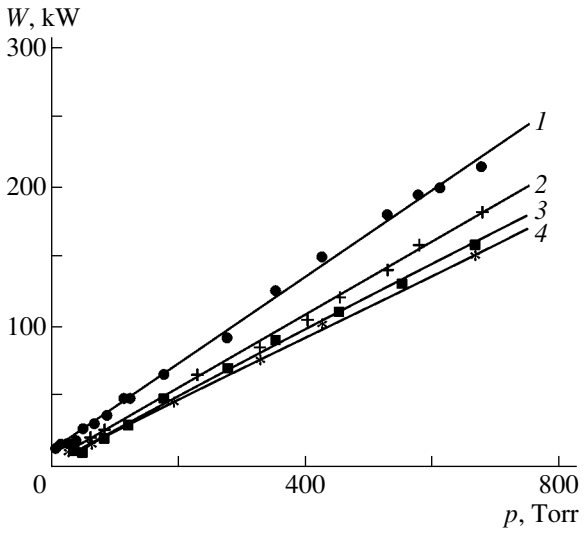

Fig. 4. Threshold characteristics of the surface microwave discharge initiated at pulse durations τ = (*1*) 1.5, (*2*) 5, (*3*) 10, and (*4*) 50–100 μs.

of the pressure chamber, where the air pressure was varied from 10^{-3} to 10^3 Torr.

First, we studied the conditions under which the discharge is initiated and the effect of the supersonic flow on the general form of the discharge. Figure 3 shows the air pressure dependence of the minimum microwave breakdown power at which the discharge is initiated on the surface of the insulator for pulse duration τ = 1.5 μs and pulse repetition rate f = 40 Hz. It can be seen that the power of the generator initiates the surface microwave discharge in a wide range of air pressures (from 10^{-3} to 10^3 Torr). With increasing air pressure, the minimum discharge-initiating power first decreases and then increases. Such a dependence is similar to the Paschen curve and is explained by the fact that diffusion electron losses decline and inelastic electron losses increase when the pressure grows. It is known that, when the air pressure is p < 1 Torr, the main electron loss mechanism at discharge gap breakdown is diffusion and at p = 1–10 Torr, attachment. To compensate for electron losses, a high ionization frequency is necessary. Ionization frequency $\nu_i = f(T_e)$ grows with electron temperature, i.e., with reduced electric field E/n (E is the electric field intensity and n is the molecular concentration) or microwave power W. In air, diffusion loss rate $\nu_d = 10^5/(\Lambda^2 p)[s^{-1}]$ (Λ is the characteristic dimension of the plasma region) is inversely proportional to pressure, while electron attachment rate $\nu_a = 6 \times 10^4 p[s^{-1}]$ linearly grows with pressure. One can therefore expect that, at low (p < 0.1 Torr) and high (p > 10 Torr) air pressures, a higher discharge-initiating power must be delivered to the antenna, which is the case (Fig. 3).

Figure 4 plots the threshold characteristics of the surface discharge vs. pressure for different pulse durations. At a constant air pressure, the discharge-initiating power for τ = 1.5–10 μs drastically drops, while for τ > 50 μs, the breakdown threshold is almost independent of the pulse duration.

Assume that the external field is switched on much faster than the charged particles are generated and remains constant during the avalanching time. Under this assumption, we can suppose that, after the field has been switched on at zero time t = 0, the rates of ionization (ν_i), attachment (ν_a), and diffusion (ν_d) are time-independent; i.e., $\nu_i(t)$, $\nu_a(t)$, and $\nu_d(t)$ = const. Then, from the balance equation for the electron concentration, it follows that the following relationship is valid at impulse breakdown:

$$\nu_i = \frac{1}{\tau}\ln\frac{n_e}{n_{e0}} + \nu_a + \nu_d. \quad (1)$$

Here, the first term on the right of the equation takes into account the effect of pulse duration finiteness on the breakdown characteristics, n_e is the electron concentration, and n_{e0} is the concentration of seed electrons.

At low gas pressures (p < 1 Torr), diffusion coefficient $D \sim 1/p$ is large and electron losses due to diffusion ν_d/ν_a are high. To compensate for the losses, a very high ionization rate, i.e., a very strong field, is necessary. Note that the threshold field is directly proportional to the microwave radiation frequency and inversely proportional to the gas density (pressure) and discharge space size [11].

At high pressures, diffusion electron losses are insignificant, so even a not too high field (low ionization rate) might seem to be sufficient for breakdown. However, in this case, electron losses due to attachment become a key factor. The fact is that these losses limit the ionization rate. Let us evaluate the ionization rate for p > 10 Torr, τ = 50 μs, $n_{e0} = 10^2$ cm^{-3}, and $n_e = 10^{12}$ cm^{-3}. In this case, the attachment rate is higher than the diffusion rate. The first and second terms on the right of expression (1) are roughly equal to 4×10^5 and 6×10^5 s^{-1}, respectively; i.e., their sum equals 10^6 s^{-1}. Therefore, the ionization rate at p = 10 Torr must be equal to, or greater than, 10^6 s^{-1}; at p = 760 Torr, greater than $\approx 5 \times 10^7$ s^{-1}. Thus, calculation of the breakdown threshold at $\tau \le 50$ μs must take into account the microwave pulse duration, which also follows from Fig. 4.

In the plasma space, a number of processes occur, such as gas heating, excitation of the vibrational degrees of freedom of the molecules, increase in the density of long-lived metastable electron-excited states, accumulation of charged particles (electrons and also positive and negative ions), variation in the chemical composition of the gas, and others. Basically, they may change the conditions for gas secondary breakdown

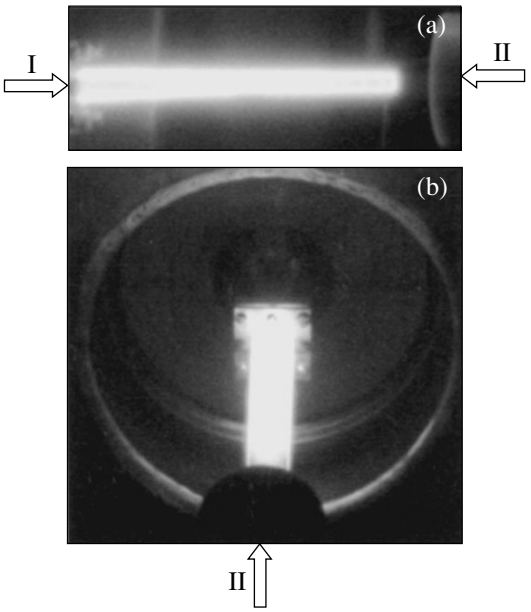

Fig. 5. (a) Side view and (b) top view (at an angle of 45° to the vertical) of the surface microwave discharge on the rectangular dielectric antenna at $M = 2$, $p = 40$ Torr, $\tau = 50$ μs, and $f = 40$ Hz. The arrows show the propagation directions of the (I) microwave energy and (II) supersonic air flow.

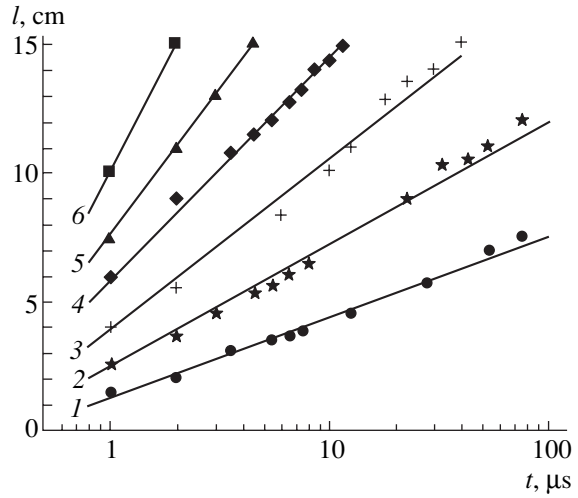

Fig. 6. Length of the surface discharge vs. microwave pulse duration at $p = 10$ Torr; $f = 20$ Hz; and applied microwave power W = (*1*) 25, (*2*) 35, (*3*) 55, (*4*) 75, (*5*) 100, and (*6*) 175 kW.

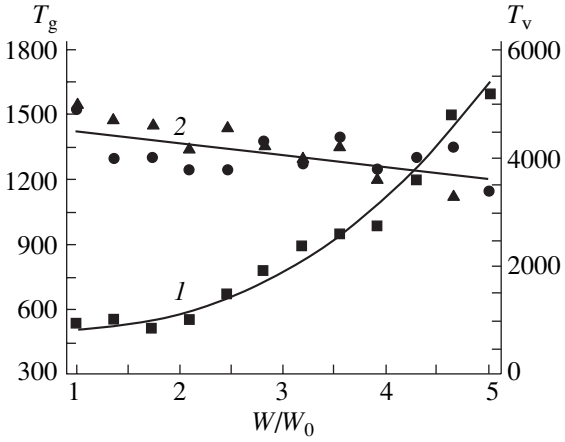

Fig. 7. (*1*) Gas and (*2*) vibrational temperatures vs. reduced power at $p = 40$ Torr, $\tau = 50$ μs, $f = 40$ Hz, and $z = 2.5$ cm. The vibrational temperature was determined from the molecular bands of the second positive system of nitrogen (circles) and molecular bands of cyan (triangles).

[10]. In particular, when the discharge is initiated in air by a train of pulses, the air heats up for the pulse time to a significant temperature depending on the pulse power and duration. If the pulse repetition period is shorter than the characteristic cooling time of the air, the air has no time to cool down to the ambient temperature before the next pulse arrives. The discharge space is a region with a lower air density, $n < n_0$ (where n_0 is the density of the ambient air). In this case, a smaller external field (microwave power) should be applied to reach the breakdown intensity of reduced electric field $(E/n)_b$.

Consider the surface microwave discharge in generated in a supersonic air flow. Time t taken to completely change the environment near the body depends on longitudinal dimension l of the body and on flow velocity, $t = l/v_f$. In our case, $l = 15$ cm and the velocity of the undisturbed flow (at $M = 2$) is $v_f = 550$ m/s. Then, $t \approx 300$ μs. The pulse repetition period in our experiment was $T = 25$–50 ms. This means that the disturbances caused by the previous pulse will fade away by the time of arrival of the next pulse and that the power causing the breakdown does not depend on the pulse repetition rate (which is the experimental case).

Figure 5 presents the general view of a surface microwave discharge excited on a blunted dielectric antenna around which air flows with a supersonic velocity ($M = 2$). It is seen that the discharge is a uniformly glowing plasma, which completely covers the surface of the insulator, and the supersonic air flow does not break the discharge.

The time dependence of the discharge length was studied for air pressures in the chamber $p = 1$–100 Torr and microwave pulse powers $W = 10$–300 kW. As an example, Fig. 6 shows the semilog plots of the discharge length versus the microwave pulse duration at $p = 10$ Torr. The microwave pulse power delivered to the antenna here is taken as a parameter. With the pulse duration fixed, the length of the discharge increases with the power. At the initial stage of the discharge, its propagation velocity may be as high as 10^7 cm/s, i.e., several orders of magnitude greater than the velocity of

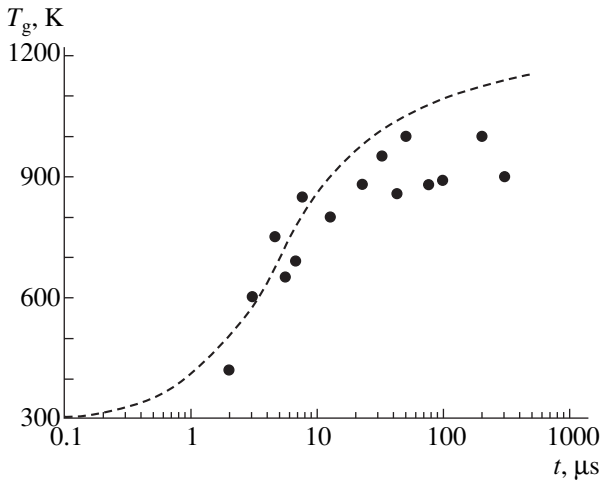

Fig. 8. Time dependence of the gas temperature in the microwave discharge plasma in the cross section $z = 2.5$ cm. The circles are the data points taken at $p = 10$ Torr and $W = 80$ kW; the dashed line is calculation at $E/n = 1.5 \times 10^{-15}$ V cm^2.

sound in air. Similar results were obtained at other pressures.

The gas and vibrational temperatures in different cross sections of the discharge were measured versus the microwave power applied to the antenna. The related curves are shown in Fig. 7. As ratio $\chi = W/W_0$ (W is the microwave pulse power applied to the antenna, and W_0 is the discharge-initiating breakdown power under given conditions) grows, the gas temperature in the cross section with longitudinal coordinate $z = 2.5$ cm increases from ≈500 K at $\chi = 1$ to ≈1600 K at $\chi = 5$. The vibrational temperature, however, remains almost unchanged under these conditions, decreasing insignificantly with increasing the power. From the longitudinal gas temperature distribution, it follows that the temperature is maximal at the site of discharge initiation and drops toward the end of the antenna.

Figure 8 demonstrates the time variation of the gas temperature in the cross section $z = 2.5$ cm. Early in the discharge, gas temperature dT_g/dt grows rapidly at a rate of ≈50 K/μs. The dashed line in Fig. 8 shows the results of mathematical simulation of gas heating. When simulating, we used a nonstationary kinetic model that was developed in [10, 12–14] for studying the energy distribution between different components and the degrees of freedom of the molecular plasma of a freely localized microwave discharge initiated in air by a focused electromagnetic radiation. This model relies upon the Boltzmann equation for the electron energy distribution function, a set of gasdynamic balance equations for the populations of the vibrational levels of the ground and electron-excited states of nitrogen and oxygen and for the concentrations of reactive and charged plasma particles, and a nonstationary heat conduction equation for the gas temperature. The model allows for various processes influencing heating of the gas, such as heat transfer to the translational degrees of freedom via elastic electron–molecule collisions, rotational–translational and vibrational–translational relaxations, vibrational–vibrational exchange, and quenching of electron-excited molecular states. Our calculation shows that the mechanism responsible for rapid heating of the gas is efficient generation of electron-excited states in nitrogen molecules at high values of the reduced electric field ($E/n \geq 10^{-15}$ V cm^2) followed by quenching of these states. Part of the energy of these excited states is converted to heat causing the rapid growth of the gas temperature observed in the experiment.

CONCLUSIONS

A new technique for exciting a discharge in a gas flow is devised and implemented. Initiating a surface microwave discharge of the type considered in this paper is a reliable and easy-to-implement way of generating a low-temperature plasma in a supersonic air flow. The microwave energy is concentrated within a thin surface layer and, therefore, is efficiently delivered to the gas. As follows from the results of mathematical simulation, the basic mechanism responsible for the observed rapid heating of the air is quenching of electron-excited states of nitrogen molecules, which are readily excited at high values of the reduced electric field. The propagation velocity of the surface microwave discharge, reaching 10–100 km/s, is much higher than the velocity of sound in air. Thus, such a discharge-initiating technique is promising for future-generation hypersonic aircraft, which will fly with supersonic velocities at $M = 10$–20.

ACKNOWLEDGMENTS

This work was supported in part by the Russian Foundation for Basic Research (project no. 02-02-17116) and the European Office of Aerospace Research and Development (project no. 2248p of the International Science and Technology Center).

REFERENCES

1. *Proceedings of the AIAA International Space Planes and Hypersonic Systems and Technologies Conferences and of the Workshops on Weakly Ionized Gases: Colorado, 1997; Norfolk, 1998, 1999; Anaheim, 2001; and Reno, 2002, 2003, 2004.*
2. *Proceedings of the International Workshops on Magnetic and Plasma Aerodynamics for Aerospace Applications, Moscow, IVTAN, 1999–2003.*
3. V. M. Shibkov, D. A. Vinogradov, A. V. Voskanyan, *et al.*, Vestn. Mosk. Univ., Ser. 3: Fiz., Astron. **41** (6), 64 (2000).

4. M. Moisan, C. M. Ferreira, Y. Hajlaoui, *et al.*, Rev. Phys. Appl. **17**, 707 (1982).
5. S. A. Dvinin, V. A. Dovzhenko, and G. S. Solntsev, Fiz. Plazmy **8**, 1228 (1982) [Sov. J. Plasma Phys. **8**, 698 (1982)].
6. S. Daviaud, C. Boisse-Laporte, P. Leprince, *et al.*, J. Phys. D **22**, 770 (1989).
7. A. Granier, C. Boisse-Laporte, P. Leprince, *et al.*, Appl. Phys. **20**, 204 (1989).
8. J. Marec and P. Leprince, J. Phys. IV (France) **8**, 7-21 (1998).
9. M. Moisan and C. M. Ferreira, Phys. Scr. **38**, 382 (1998).
10. A. S. Zarin, A. A. Kuzovnikov, and V. M. Shibkov, *Freely Localized Microwave Discharge in Air* (Neft' i Gaz, Moscow, 1996) [in Russian].
11. Yu. P. Raizer, *Gas Discharge Physics* (Nauka, Moscow, 1992; Springer-Verlag, Berlin, 1991).
12. A. M. Devyatov, A. A. Kuzovnikov, V. V. Lodinev, and V. M. Shibkov, Vestn. Mosk. Univ., Ser. 3: Fiz., Astron. **32** (2), 29 (1991).
13. V. M. Shibkov, Teplofiz. Vys. Temp. **35**, 693 (1997).
14. V. M. Shibkov, Teplofiz. Vys. Temp. **35**, 871 (1997).

Translated by A. Khzmalyan

Technical Physics, Vol. 50, No. 4, 2005, pp. 462–467. Translated from Zhurnal Tekhnicheskoĭ Fiziki, Vol. 75, No. 4, 2005, pp. 74–79.

GAS DISCHARGES, PLASMA

Mechanisms of Microwave Surface Discharge Propagation

V. M. Shibkov, S. A. Dvinin, A. P. Ershov, and L. V. Shibkova

Moscow State University, Vorob'evy Gory, Moscow, 119992 Russia

e-mail: shibkov@ph-elec.phys.msu.ru

Received June 22, 2004

Abstract—A microwave discharge propagating over the surface of a dielectric antenna is studied. It is experimentally shown that the velocity of discharge propagation over the surface is maximal early in microwave pulse application and grows with the applied power. The breakdown wave defines the velocity of the discharge at its early stages (t = 1–3 μs). Ambipolar diffusion governs the discharge propagation at the stage of its evolution (t = 3–100 μs), and, finally, slow surface combustion is possible only at the stationary stage of the discharge (t > 100 μs). The electric field is localized in a thin (~1 mm) surface layer. High values of the reduced electric field, E/n = 100–500 Td, provide efficient energy deposition to the plasma, i.e., favor the rapid heating of the gas and the efficient generation of charged particles. This makes the discharge promising for hypersonic aerodynamics. © *2005 Pleiades Publishing, Inc.*

INTRODUCTION

A new type of microwave discharge initiated on insulators by a surface wave has been considered in [1–3]. Essentially, the discharge represents a self-consistent plasma waveguide where the surface wave initiating this discharge propagates; in other words, for the surface wave to exist, a plasma medium produced by the surface wave itself is necessary. The plasma region may be made extended and variously shaped in a wide range of electromagnetic radiation energies and frequencies. Another feature of this discharge is that the concentration of charged particles in the extended plasma region is basically high, because the discharge may exist only at electron concentrations n_e higher than critical concentration n_{cr}. It has been proposed [4, 5] that this discharge be used to generate a plasma in a supersonic air flow. However, before applying this type of discharge in plasma aerodynamics, it is necessary to find the range of external parameters (gas pressure, energy applied to the discharge, and duration of the electromagnetic pulse) in which the discharge may exist. It has been shown [6] that the propagation velocity of the surface discharge exceeds the velocity of sound in air over a wide range of conditions. However, the mechanism of discharge propagation along the antenna is yet to be understood. A variety of mechanisms are known [7–10] to be responsible for microwave discharge propagation. Depending on the discharge initiation and existence conditions, the basic mechanisms may be that associated with a "breakdown wave," ambipolar diffusion, photoionization, heat conduction (slow combustion), electronic heat conduction, etc. The aim of this work is to find the pressure and power dependences of the velocity of surface microwave discharge front propagation along the antenna and reveal the mechanisms that are responsible for discharge propagation.

EXPERIMENTAL RESULTS

The experimental setup used to study the surface discharge and diagnostics methods applied are described elsewhere [6]. A cm-wave pulse magnetron generator was used as a microwave power source. This generator can produce individual pulses or high-rate trains of pulses. It has the following characteristics: wavelength λ = 2.4 cm, the microwave pulse power delivered to the transmission line W < 300 kW, the pulse length (which can be smoothly varied) τ = 1 to 200 μs, and the duty ratio in the train Q = 1000. The average power is no higher than 300 W. The vacuum system allowed us to vary the air pressure in a wide range (from 10^{-3} to 10^3 Torr). The discharge was initiated on a dielectric antenna placed in a cylindrical pressure chamber 1 m in diameter and 3 m long. The microwave power was delivered to the discharge chamber through a 9.5 × 19-mm rectangular waveguide. We assume that the positive direction of the $0Z$ axis is aligned with the direction of microwave surface wave propagation along the antenna. The origin z = 0 is at the end of the waveguide, through which the electromagnetic energy initiating the surface discharge is applied to the antenna. The direction of supersonic flow propagation is opposite to that of the surface electromagnetic wave, i.e., to the direction of discharge propagation.

Figure 1 shows the general view of the surface microwave discharge initiated on the wedge-nose dielectric antenna in still air for different pulse durations. It is seen that the discharge is localized in a thin surface layer and the area covered by the wave-initiated plasma increases with the pulse duration. When the

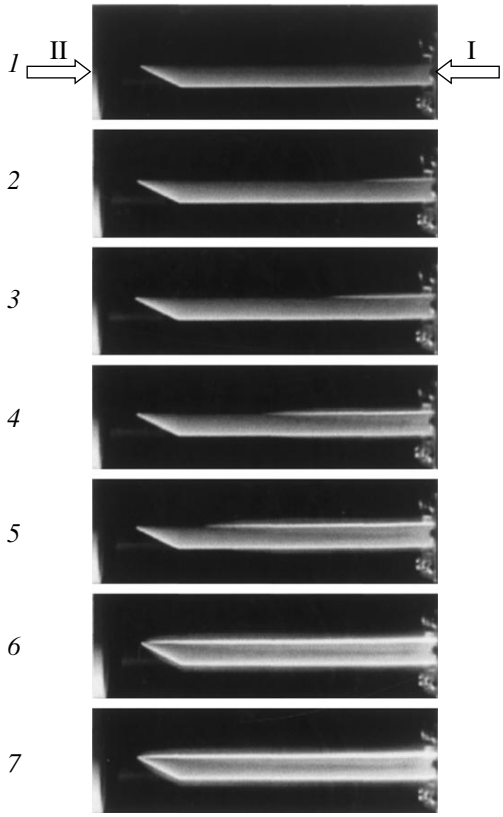

Fig. 1. Surface microwave discharge evolution on the wedge-shaped dielectric antenna in air at p = 40 Torr, W = 40 kW, and microwave pulse length τ = (*1*) 0, (*2*) 2, (*3*) 7, (*4*) 25, (*5*) 50, (*6*) 100, and (*7*) 200 μs. I, microwave pulse; II, supersonic flow.

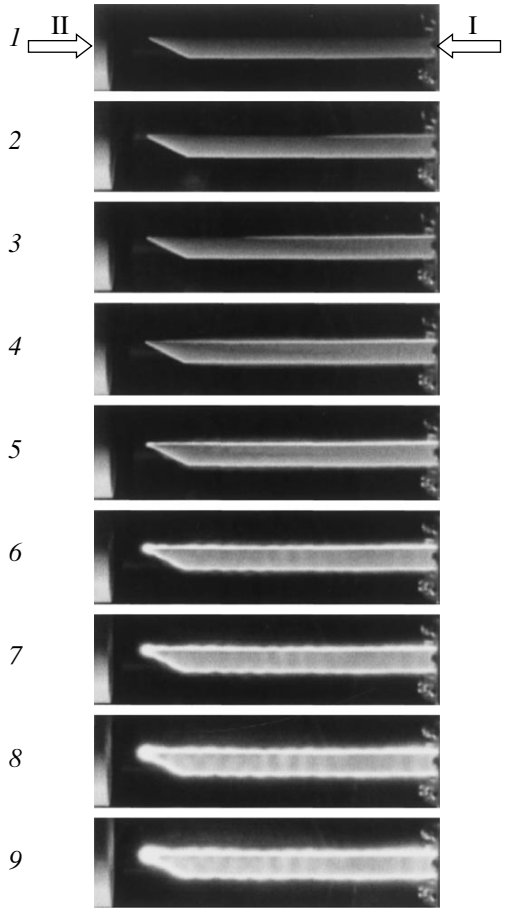

Fig. 2. Combined microwave discharge evolution on the wedge-shaped dielectric antenna in air at p = 40 Torr, W = 60 kW, and microwave pulse length τ = (*1*) 0, (*2*) 2, (*3*) 10, (*4*) 30, (*5*) 50, (*6*) 75, (*7*) 100, (*8*) 150, and (*9*) 200 μs. I, microwave pulse; II, supersonic flow.

microwave power or pulse duration were increased above the value necessary for the surface of the wedge-like antenna to be fully covered by the plasma, a new type of microwave discharge, namely, combined microwave discharge, emerged. This phenomenon is a combination of a microwave discharge initiated on the surface of the wedgelike antenna and a space microwave discharge produced at its front edge (Fig. 2). From Fig. 2, it follows that the area covered by the plasma grows in time with the power fixed. At microwave pulse duration τ = 50 μs, a volume plasma object starts forming at the edge of the antenna. The size of this object increases with pulse duration.

Our calculations show that, when the antenna is covered by the plasma incompletely, the coefficient of energy reflection from its front end is no higher than 0.15. If the discharge occupies the entire surface, the coefficient of reflection from the front end of the antenna may reach 0.85. In this case, a standing wave arises on the antenna surface with the typical spatial modulation of the plasma glow (Fig. 2). From the discharge pattern observed, one can estimate the electron concentration in the plasma.

Studying the evolution of the surface microwave discharge, we found that, in the entire pressure range (p = 1–100 Torr), the longitudinal dimension (length) of the discharge increases with the microwave pulse duration and power delivered to the antenna. As an example, Fig. 3 shows the log–log plot of the longitudinal velocity of surface discharge propagation versus time at p = 10 Torr. The surface discharge propagation velocity is seen to increase with the applied power. Initially, this velocity is high, reaching $v = 10^7$ cm/s at a microwave pulse power of 175 kW. Subsequently, the discharge propagation velocity drops to $v = 10^4$ cm/s at W = 25 kW. It also follows from Fig. 3 that all the straight lines have the same slope. Similar results were obtained at 40, 60, and 100 Torr. It turned out that the experimental time dependence of the longitudinal velocity of the surface discharge is fitted well by the law

$$v = At^{-(0.875 \pm 0.035)}, \quad (1)$$

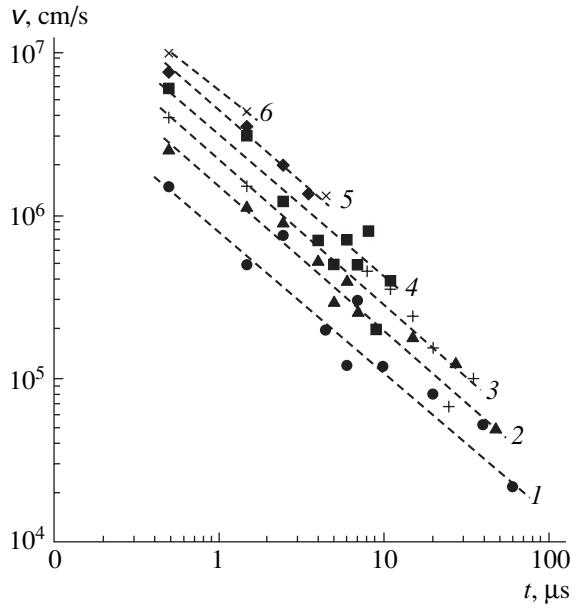

Fig. 3. Longitudinal propagation velocity of the surface microwave discharge versus time at air pressure p = 10 Torr and microwave pulse power W = (*1*) 25, (*2*) 35, (*3*) 55, (*4*) 75, (*5*) 100, and (*6*) 175 kW.

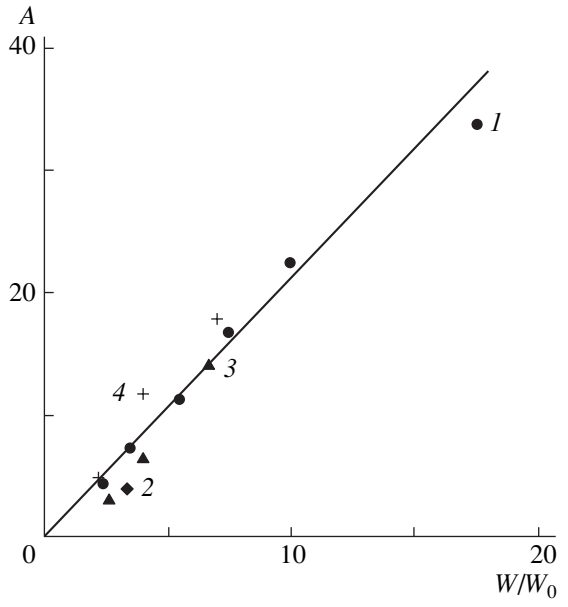

Fig. 4. Coefficient A versus microwave pulse power at air pressure p = (*1*) 10, (*2*) 40, (*3*) 60, and (*4*) 100 Torr.

where A is a power-dependent coefficient and t is the time.

At air pressures p = 10–100 Torr, coefficient A is directly proportional to W/W_0, where W_0 is the threshold power necessary for initiating a surface discharge at a given gas pressure (Fig. 4). Using the relationship $A = f(W)$, one can derive the length of the surface discharge as a function of the microwave power,

$$L = 17\frac{W}{W_0}t^{(0.125 \pm 0.035)}, \qquad (2)$$

where L is the length of the discharge in centimeters and t is the time in seconds.

This formula implies that our experimental setup can initiate a surface microwave discharge of length up to 1 m. In a supersonic (M = 2) air flow, the shape of the discharge on the surface of a rectangular dielectric antenna and the microwave power necessary for supporting this discharge remain almost unchanged [6], because the discharge velocity is much higher than the velocity of sound in air.

It is known [1] that energy delivery to the boundary layer or local heating of the surface of a plate near the turbulent boundary layer noticeably decreases the local coefficient of turbulent friction, since the transverse gradient of the longitudinal velocity decreases and the displacement thickness grows. In the case of a surface microwave discharge, the field is localized in a thin surface layer [2, 3], which favors energy deposition to the plasma and rapid heating of the gas [6]. As a result, the conditions under which the supersonic gas flows over the surface change [4, 5].

The experimental results show that the velocity of discharge propagation over the surface of the dielectric antenna exceeds the velocity of sound in air but is much lower than the electromagnetic wave velocity in free space. To explain such a value of the discharge propagation velocity, it is appropriate to compare it with the ionization rate for gas molecules, i.e., with the critical concentration of electrons at the front of the discharge. To answer the question of whether discharge propagation mechanisms at the stages of discharge formation and evolution are different, let us see how the velocity of the front of the discharge varies with the surface discharge length. To this end, we construct a log–log plot of the discharge propagation velocity along the dielectric antenna versus longitudinal coordinate z. The associated curves $v = f(z)$ are shown in Fig. 5. These curves exhibit a characteristic kink, which indicates that different mechanisms are responsible for the propagation of the discharge at its initial and final stages.

Initially (t = 1–3 μs), the velocity of surface microwave discharge propagation in the discharge initiation region of the antenna (this region is bounded by coordinates z = 1 cm and z = 2 cm, i.e., is adjacent to the waveguide, which delivers the microwave energy to the antenna) exceeds 10^6 cm/s. Such a high discharge velocity in the region of electromagnetic energy delivery can only be provided by a mechanism associated with the breakdown wave. The motion of the surface discharge by the slow combustion mechanism is only possible late (t > 100 μs) in the discharge, when its propagation velocity becomes smaller than the velocity of sound. The most plausible mechanism of discharge

propagation at a low gas pressure is ambipolar diffusion, whereas the photoionization and/or electronic heat conduction can control the discharge propagation only at a high pressure.

Suppose that the basic discharge propagation mechanism is ambipolar diffusion. It is known that the temperature of electrons at the front of the surface microwave discharge varies insignificantly as the discharge propagates; therefore, electron temperature T_e may be set constant within the experimental error. Also, let T_e = 2 eV and $T_i = T_g$ = 300 K. If ambipolar diffusion is the basic mechanism responsible for the loss of charged particles in the plasma, the dependence of discharge propagation velocity v on ionization rate ν_i is given by

$$v = 2\sqrt{D_a \nu_i}, \tag{3}$$

where

$$D_a = \frac{b_i k T_e}{e} \tag{4}$$

is the ambipolar diffusion coefficient, k is the Boltzmann constant, and b_i is the ion mobility. In air, the ion mobility is expressed as [12]

$$b_i p = \frac{2.7\sqrt{1 + M_g/M_i}}{\sqrt{(\alpha/a_0^3)29 \times 10^{-3}}}. \tag{5}$$

Here, p is the gas pressure in Torr and $\alpha/a_0^3 = 11.54$. For the microwave breakdown of air, Mayhan [13] derived the following dependence of the ionization frequency on the reduced electric field:

$$\frac{\nu_i}{p} = 8.35 \times 10^{-4}\left(\frac{E_{eff}}{p}\right)^{5.34}, \tag{6}$$

where E_{eff} is the effective field, which is related to amplitude E_0 of the electric field intensity as

$$E_{eff} = \frac{E_0}{\sqrt{2}}\frac{\nu_{col}}{\sqrt{\nu_{col}^2 + \omega^2}}. \tag{7}$$

Here, $\omega = 2\pi c/\lambda$ is the circular frequency of the microwave field, λ = 2.4 cm, and $\nu_{col} = 5.3 \times 10^9 p$ is the frequency of electron–neutral collisions.

Using Eqs. (3)–(7), we find that, at air pressure p = 10 Torr, the amplitude of the electric field intensity and the velocity of surface microwave discharge propagation are related as

$$E_0 = 45.3 v^{0.375}, \tag{8}$$

where the electric field intensity is expressed in units of V/cm and the velocity, in m/s.

Figure 6 demonstrates the semilog z-dependences of the electric field peak intensity at the front of the propagating surface discharge. The curves were constructed for an air pressure of 10 Torr using the measured velocity of discharge propagation along the antenna. Here, the applied microwave power serves as a parameter. Extrapolating these functions to z = 0, we find that, under the conditions of our experiment, the amplitude of the electric field intensity at the front of the surface microwave discharge near the waveguide edge changes from 2 kV/cm at pulse power W = 25 kW to ~5 kW/cm at W = 175 kW. It should be noted that the results obtained are in good agreement (rather than in conflict) with the field in the waveguide calculated by the

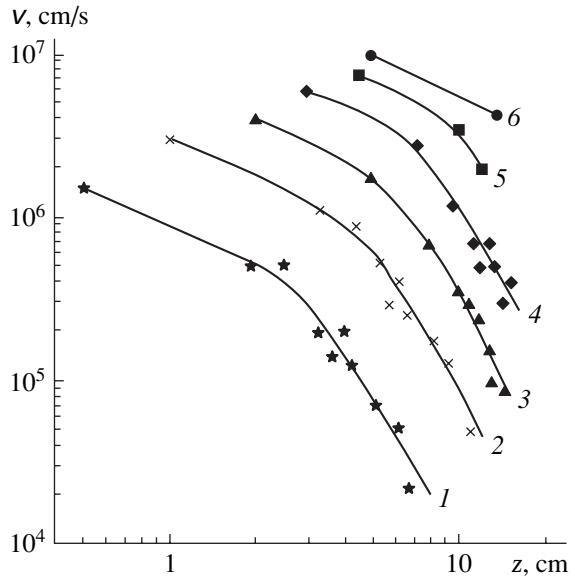

Fig. 5. Propagation velocity of the discharge versus the longitudinal coordinate at p = 10 Torr and microwave pulse power W = (*1*) 25, (*2*) 35, (*3*) 55, (*4*) 75, (*5*) 100, and (*6*) 175 kW.

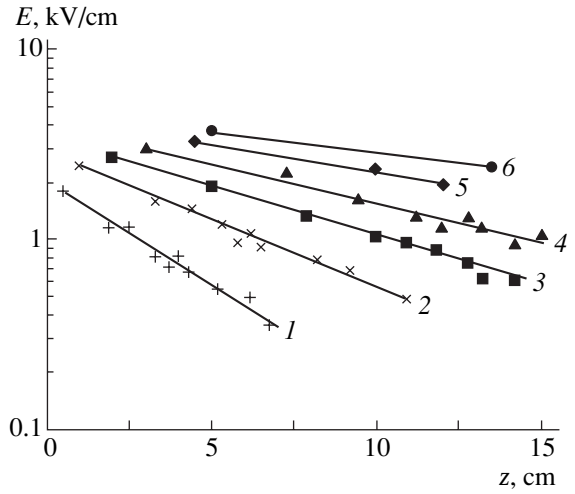

Fig. 6. Electric field amplitude at the front of the surface wave versus the longitudinal coordinate at air pressure p = 10 Torr and applied power W = (*1*) 25, (*2*) 35, (*3*) 55, (*4*) 75, (*5*) 100, and (*6*) 175 kW.

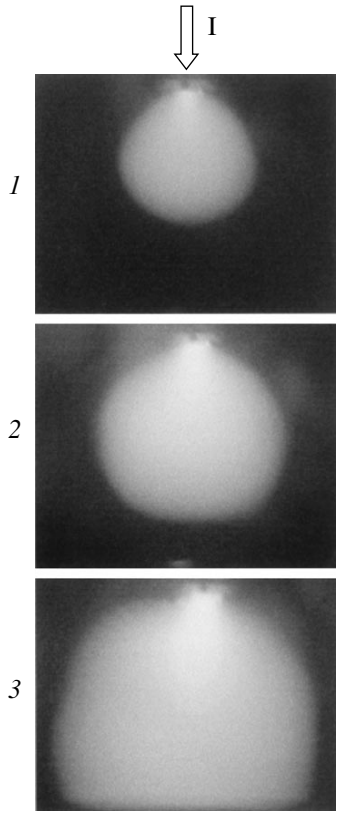

Fig. 7. Top view of the surface microwave discharge on the dielectric plate at p = 40 Torr, τ = 50 μs, and applied microwave power W = (*1*) 50, (*2*) 100, and (*3*) 150 kW. I, application of microwave power.

formula

$$E_0 = 28\sqrt{S}, \quad (9)$$

where power flux density S is expressed in W/cm^2 and amplitude E_0 of the electric field intensity, in V/cm.

For example, at applied pulse power W = 175 kW, the electric field amplitude in the waveguide is $E_0 \approx$ 8 kW/cm; at W = 25 kW, the field amplitude is ≈3k V/cm.

The analytical results obtained for high pressures distinctly contradict the experimental data. Particularly, at a pressure of 100 Torr, the electric field amplitude in the surface discharge calculated in the ambipolar diffusion approximation, $E_0 = 259v^{0.375}$, reaches 15 kV/cm. This value is obviously different from the waveguide field found experimentally.

Next, suppose that the discharge propagation is governed by electronic heat conduction. In this case, the discharge velocity depends on the electric field intensity as

$$v = \frac{\sqrt{\chi_e \sigma T_e}}{\frac{3}{2}kT_e n_e}E_0, \quad (10)$$

where $\chi_2 = 2.56 \times 10^{-3} T_e^{5/2}/\ln\Lambda$ is the electron thermal conductivity in W/(cm K), σ is the electron conductivity, and T_e is the electron temperature in eV.

In air, χ_e = 1.93 W/(m K) and $\sigma p/n_e = 7.2 \times 10^{-18}$ Torr m$^2/\Omega$ [12]. Finally, we obtain

$$E_0 = 1.46 \times 10^{-5}\sqrt{p}\,v, \quad (11)$$

where the velocity is expressed in m/s; the pressure, in Torr; and the electric field intensity, in V/cm.

At pressure p = 100 Torr and discharge propagation velocity $v = 10^5$ m/s, the maximal field amplitude calculated under the assumption that the discharge propagates by the mechanism of electronic heat conduction equals 14.6 V/cm. Such a value of the field amplitude disagrees with the experimental data, and, hence, the mechanism of electronic heat conduction cannot maintain the discharge throughout the pressure range studied.

We also performed experiments aimed at exciting a surface microwave discharge on a plane–parallel Teflon plate measuring 14 × 20 × 1 cm (Fig. 7). At the place where the plasma arises, the applied microwave energy gives rise to an omnidirectional surface wave, which creates a thin (≈1 mm) uniformly glowing plasma layer on the surface of the insulator. The plasma-coated area of the plate expands with increasing the power. The velocity of discharge propagation over the plate, as well as over the antenna, depends on the duration and power of the microwave pulse. For instance, qt W = 350 kW, the discharge entirely covers the plate of surface area 14 × 20 cm for 1 μs.

CONCLUSIONS

The dynamics of a microwave discharge initiated on the surface of insulators by a surface wave is studied. It is shown that ambipolar diffusion specifies the propagation velocity of the surface discharge front at air pressures below 40 Torr. The propagation velocity of the discharge far exceeds the velocity of sound in air. This is the controlling consideration in applying this type of discharge in new-generation aerodynamics technologies to improve the performance parameters of hypersonic aircrafts.

ACKNOWLEDGMENTS

This work was partially supported by the Russian Foundation for Basic Research (project no. 02-02-17116) and the European Office of Aerospace Research and Development (project no. 2248p of the International Science and Technology Center).

REFERENCES

1. V. M. Shibkov, D. A. Vinogradov, A. V. Voskanyan, *et al.*, Vestn. Mosk. Univ., Ser. 3: Fiz., Astron. **41** (6), 64 (2000).
2. V. M. Shibkov, A. V. Chernikov, V. A. Chernikov, *et al.*, in *Proceedings of the 4th International Workshop "Microwave Discharges: Fundamentals and Application," Zvenigorod, 2000* (Yanus-K, Moscow, 2001), pp. 145–153.
3. V. M. Shibkov, A. V. Chernikov, S. A. Dvinin, *et al.*, in *Proceedings of the 15th International Symposium on Plasma Chemistry, Orleans, 2001*, Vol. 1, pp. 179–184.
4. V. M. Shibkov, A. V. Chernikov, A. P. Ershov, *et al.*, AIAA Pap., No. 01-3087, 1 (2001).
5. V. M. Shibkov, A. F. Alexandrov, A. V. Chernikov, *et al.*, AIAA Pap., No. 03-1193, 1 (2003).
6. V. M. Shibkov, A. P. Ershov, V. A. Chernikov, and L. V. Shibkova, Zh. Tekh. Fiz. **75** (4), 67 (2005) [Tech. Phys. **50**, 455 (2005)].
7. Yu. P. Raizer, *Laser Spark and Charge Propagation* (Nauka, Moscow, 1974) [in Russian].
8. S. A. Dvinin and V. A. Dovzhenko, Fiz. Plazmy **14**, 66 (1988) [Sov. J. Plasma Phys. **14**, 41 (1988)].
9. V. B. Gil'denburg, I. S. Gushchin, S. A. Dvinin, and F. V. Kim, Zh. Éksp. Teor. Fiz. **97**, 1151 (1990) [Sov. Phys. JETP **70**, 645 (1990)].
10. A. S. Zarin, A. A. Kuzovnikov, and V. M. Shibkov, *Freely Localized Microwave Discharge in Air* (Neft' i Gaz, Moscow, 1996) [in Russian].
11. A. V. Kazakov, M. N. Kogan, and A. P. Kuryachiĭ, Teplofiz. Vys. Temp. **33**, 888 (1995).
12. Yu. P. Raizer, *Gas Discharge Physics* (Nauka, Moscow, 1992; Springer-Verlag, Berlin, 1991) [in Russian].
13. J. T. Mayhan, J. Appl. Phys. **42**, 5362 (1971).

Translated by A. Khzmalyan

Technical Physics, Vol. 50, No. 4, 2005, pp. 468–472. Translated from Zhurnal Tekhnicheskoĭ Fiziki, Vol. 75, No. 4, 2005, pp. 80–84.

GAS DISCHARGES, PLASMA

Three-Chamber Low-Output-Pressure Glow-Discharge-Based Plasma Generator as a Negatively Charged Ion Source

P. A. Litvinov, V. A. Baturin, A. Yu. Karpenko, S. A. Pustovoĭtov, and S. A. Eremin

Institute of Applied Physics, National Academy of Sciences of Ukraine, Sumy, 40030 Ukraine

e-mail: baturin@ipflab.sumy.ua

Received August 10, 2004

Abstract—A stationary glow discharge initiated in a two-chamber inverted gas magnetron is studied. In the third (emission) chamber, such a discharge system generates a plasma that can be subdivided into two, circumferential and near-axis, regions with considerably differing parameters and also provides a pressure difference in desired areas. It is concluded that the device suggested could be used as an efficient continuous-mode plasma generator making it possible to produce negatively charged gas ions. The results obtained may serve as a basis for negative ion source design optimization. © *2005 Pleiades Publishing, Inc.*

INTRODUCTION

Most electrode systems generating a gas-discharge low-pressure plasma operate using either an incandescent cathode or an rf discharge. The significant disadvantage of a thermionic cathode is its short lifetime, especially in an aggressive environment (for example, in oxygen atmosphere). On the other hand, in the case of an rf discharge, the plasma impedance is unstable, which necessitates careful matching between the parameters of the discharge and an rf antenna, and if the antenna is placed inside the plasma, its insulation becomes a challenge.

Direct-current glow discharges, especially in crossed $E \times H$ fields, are promising for low-temperature plasma generation, because they are stable and easy to initiate. Also, the gas-discharge cell reliably operates at cathode current densities of up to several tens of A/cm^2 and a discharge voltage of several hundreds of volts. The operating pressure varies in the interval 10–10^{-1} Pa. The primary problem associated with glow-discharge-based plasma sources operating in the steady regime is usually the need for reducing the amount of the gas delivered to the chamber, i.e., for expanding the operating pressure range toward lower pressures. This becomes of particular importance when the glow discharge is used in sources of negatively charged ions, where the ions are collected, as a rule, from the entire space of their generation and, accordingly, the free path of a negative ion must be large. The ion loss minimization condition implies a reduction of the pressure before and immediately after the emission orifice, where the ions are still slow and the cross section of their disintegration through collisions with gas molecules is the highest.

As the pressure in a cold-cathode discharge system decreases, the voltages of glow discharge initiation and maintenance rise rapidly. Among the glow-discharge-based low-pressure gas-discharge systems currently available, the inverted gas magnetron merits special attention. Application of a pulsed inverted gas magnetron with pulsed gas delivery [1] in negative ion sources allows for a reduction of the pressure to the point where negative ion stripping becomes insignificant. This is provided owing to the specially tailored gasdynamics of the gas flow in the gas-discharge chamber with constrictions and various velocities of neutral and charged particles. There also exists the possibility of reducing the initiation voltage and pressure of the low-pressure stationary discharge, as well as of expanding the operating pressure range toward lower pressures. This may be achieved by using an auxiliary high-pressure discharge injecting a plasma that penetrates into the low-pressure gas and acts as a plasma cathode supplying primary electrons for maintaining the main discharge.

In this work, we describe experiments on creating a three-chamber cold-cathode plasma generator that produces a stationary cold plasma at a low gas-flow rate and low pressure in its output (emission) chamber.

DESIGN OF THE PLASMA GENERATOR AND PHYSICAL PROCESSES IN ITS GAS-DISCHARGE CHAMBER

The plasma generator (Fig. 1) represents an axisymmetric construction consisting of three chambers with controllable gas flow between them. The copper anode (*1*, *2*) and copper cathode (*3*, *4*) are made of two parts. Part *3* of the cathode and part *1* of the anode constitute first (high-pressure) gas-discharge chamber *5*, while part *4* of the anode and part *2* of the cathode form second (low-pressure) chamber *6*. Chambers *5* and *6* are connected to each other via contracting ring-shaped channel *7*, and chamber *6* is connected to third (emission) chamber *8* via another contracting ring-shaped channel *9*. Because of the flow resistance in the con-

1063-7842/05/5004-0468$26.00 © 2005 Pleiades Publishing, Inc.

tracting channels, the pressure in the chambers is successively reduced. Moreover, in emission chamber *8*, the working gas pressure is reduced further, since the gas expands into a large volume and, in addition, is differentially pumped out in the radial direction. Samarium–cobalt magnets *14* and *15* are mounted above emission electrode *11* and below pole *12*. Case *13* of the plasma generator, which is a major part of the magnetic system, has the form of a hexahedral prism. Gaps of width ≈35 mm are provided between the lateral faces of the prism (not shown in Fig. 1) for radial gas evacuation from the plasma generator. The working gas (oxygen) is delivered to the high-pressure chamber through hole (*18*) on its bottom.

The electrode system constituting discharge chambers *5* and *6* is, in essence, a two-chamber inverted gas magnetron that operates using a glow discharge in cross $E \times H$ fields. Both gas-discharge chambers are connected parallel to one power supply (Fig. 1). The potential difference between the electrodes of the generator is specified by automatically applying a bias to the resistors.

At low pressures, the discharge efficiency depends largely on the electron lifetime. In an inverted magnetron of the given design, both magnetic and electrostatic confinement of the electrons can be accomplished. The application of a longitudinal magnetic field produced by magnets *14* and *15* extends the lifetime of fast electrons starting from the cylindrical surface of the cathode to the central anode, and the end faces of the magnetron, which are under the cathode potential, align the electron flow with the magnetic field. As a result, the fast electrons stay in the chambers for a long time, experience multiple collisions with gas atoms, and participate in ionization events the number of which is sufficient to favor a self-sustained discharge before they reach the anode surface.

The theory of discharge initiation in a set of coaxial electrodes subjected to a uniform magnetic field has been developed [2] for infinite cylinders. In that model, the electric field is assumed to be radial (i.e., $E \perp H$) and its nonuniformity at the edges are ignored. In our version, where the outer electrode is negatively biased, the electric field varies in the radial direction only slightly and the electrons leaving the cathode enter the space where the field strength is moderate. They will describe a hypocycloid, gradually gaining energy. Those experiencing no collisions over one hypocycle will return to the cathode. In the case of elastic and inelastic collisions, the electrons will follow a cycloid path. After each inelastic collision, the radius of the circle of the hypocycloid will decrease. If the maximal radial travel of the electron describing a cycloid exceeds the distance over which it gains an energy equal to the ionization potential, the gas will be ionized. Elastic collisions of the electrons do not diminish the ionization, since almost all of them, after being scattered, gain the energy necessary for ionization in subsequent motion.

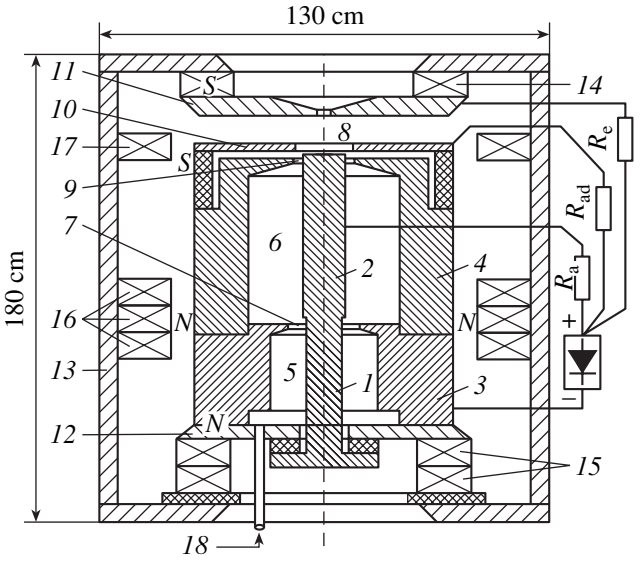

Fig. 1. Design of a three-chamber plasma generator. R_a = 680 Ω, R_{ad} = 630 Ω, and R_e = 13 Ω.

In such a system, a self-sustained discharge can be initiated if [2]

$$\gamma^*\left\{\exp\left[\int_{r_0}^{r_a}\alpha(r)dr\right]-1\right\} = 1, \qquad (1)$$

where γ^* is the effective Townsend coefficient, which characterizes the complex process of secondary emission from the cathode as a whole; r_a is the anode radius; r_0 is the radius starting from which the electron is capable of ionizing the gas; and α is the Townsend first ionization coefficient.

From condition (1), subject to certain assumptions, one can find the discharge initiation voltage and the critical value of the magnetic field above which the self-sustained discharge may exist.

Physical processes taking place in a two-chamber magnetron discharge with plasma-contracting constrictions are very complicated and depend on many parameters; accordingly, a mathematical model for design analysis is difficult to work out. Moreover, the discharge becomes unstable under certain conditions [3], and the instability considerably influences the discharge parameters both qualitatively and quantitatively.

Computer simulation of the equipotential pattern in the discharge chamber as a function of the electrode shape and electrode potentials allowed us to select, in a first approximation, the geometry of the electrode system in the plasma generator, which was then optimized in the course of experiments.

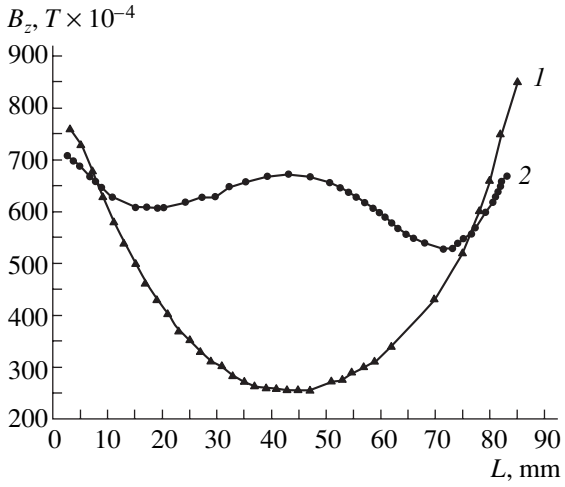

Fig. 2. Axial distribution of the magnetic field in the pole gap of the plasma generator (*1*) without and (*2*) with correcting magnets. The value $L = 0$ (mm) is at the upper pole.

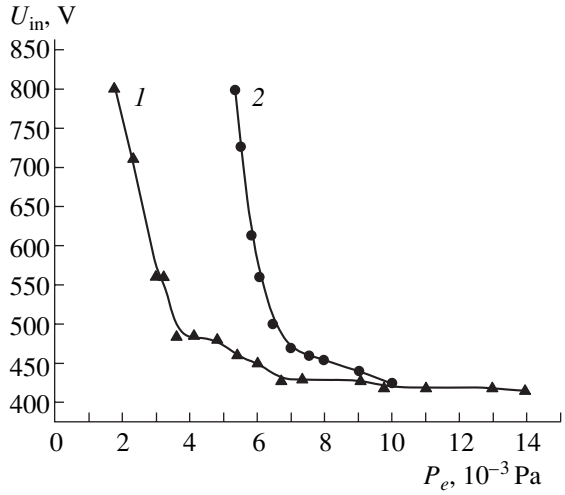

Fig. 3. Discharge initiation voltage vs. the pressure in the emission chamber in a (*1*) two-chamber and (*2*) single-chamber gas magnetron.

RESULTS AND DISCUSSION

In a real ion source, it is usually difficult to produce a uniform magnetic field whose lines of force are perpendicular to those of the electric field throughout the length of the discharge chamber. In our design of the plasma generator, main permanent magnets *14* and *15* creating a magnetic field are mounted at the lower and upper (emission electrode) poles. In the pole gap, these magnets produce the magnetic field strength distribution shown by curve *1* in Fig. 2. It is seen that the magnetic field at the center of the gap drops roughly threefold. To smooth out this nonuniformity, correcting magnets *16* and *17* (Fig. 1) were placed on each of the six faces of magnetic circuit *13*. The location of these magnets on the magnetic circuit faces was optimized, and eventually we arrived at the magnetic field distribution shown by curve *2* in Fig. 2. The experimental results discussed below were obtained with such a magnetic field distribution.

Curve *1* in Fig. 3 shows discharge initiation voltage U_{in} in the magnetron versus pressure P_e in the emission chamber (the pressure is directly proportional to the working gas flow rate). The maximal voltage that could be applied to the discharge gap from the available power supply was 800 V. At such a voltage, the discharge was initiated at gas flow rate Q providing pressure $P_e \approx 1.7 \times 10^{-3}$ Pa in the emission chamber. The initiation voltage decreases with increasing gas flow rate. The experiments showed that, in the pressure interval $P_e \approx (1.7–3.0) \times 10^{-3}$ Pa, the discharge is initiated in the first chamber alone; at $P_e \geq 3 \times 10^{-3}$ Pa, in the second chamber as well. In the latter case, the initiation voltage $U_{in} = 560$ V. Such a conclusion was first drawn from the fact that, as the gas flow rate rose and pressure P_e became equal to $\geq 3 \times 10^{-3}$ Pa, a faint glow in the emission chamber could be observed through the gap between the faces of the magnetic circuit. This conclusion was then confirmed in an additional experiment when cathodes *3* and *4* (Fig. 1) were isolated from each other. With such a modification of the cathode assembly, the gas magnetron, however, could operate for a short time, because cathode *4* was severely overheated. Therefore, subsequent experiments were performed with the initial design.

For comparison, Fig. 3 (curve *2*) shows the U_{in} versus P_e dependence for a single-chamber gas magnetron (chamber *5* was filled with a copper insert). The outer surface of the insert intimately mated the inner surface of cathode *3*, while a ~0.8-mm-wide ring-shaped channel was provided between anode *1* and the inner surface of the insert for working gas delivery to chamber *6*.

It follows from the curves in Fig. 3 that, when the voltage across the discharge gap is 560 V, the discharge is initiated at pressure $P_e \approx 6 \times 10^{-3}$ Pa, which is twice that of the plasma pregenerated in the auxiliary chamber.

Our next goal was to extend the contracted discharge to the emission electrode. The onset of electrical breakdown between the diaphragm-separated plasma and positive electrode apparently depends on the properties of the plasma and parameters of the discharge gap, such as width Δr of the circular slit, gas pressure, and length.

Let us estimate qualitatively the influence of these parameters on the extension of the discharge (to the emission electrode) and on the performance of the plasma generator as a whole.

To maintain a significant pressure difference between the second and third discharge chambers and also to minimize the escape of sputtered cathode particles from the gas magnetron, it is necessary to narrow width Δr of the circular slit. Its minimal value equals

the width of the near-cathode space-charge layer, which prevents the penetration of the plasma into the emission chamber [4]. The thickness of the layer, d, can be estimated from Child's law,

$$d = 2/3\left(\frac{\varepsilon_0\left(\frac{2q}{M}\right)^{1/2}U^{3/2}}{j_i}\right)^{1/2}, \quad (2)$$

where j_i is the density of the ion current toward the cathode, q is the ion charge, M is the ion mass, U is the voltage across the layer, and ε_0 is the dielectric constant.

In view of the fact that the ions in the discharge are not magnetized, the density of the ion current toward the cathode can be estimated from Bohm's law,

$$j_i = 0.4en\left(\frac{2kT_e}{M}\right)^{1/2}. \quad (3)$$

At $n = 10^{12}$ cm^{-3} and electron temperature $T_e = 5$ eV, we have the ion current density ~49.5 mA/cm^2.

Substituting this value of the ion current density into (2) and assuming that voltage drop $U = 350$ V occurs almost exclusively in the near-cathode space-charge layer, we estimate thickness d of the space-charge layer as $d = 1.3$ mm. With regard to the fact that the space-charge layer borders a disturbed quasi-neutral zone (presheath) [5], where some voltage drop also takes place, the minimal width of the circular slit may be taken to be equal to ~1.5 mm.

The upper bound of Δr is specified by the allowable working pressure in the emission chamber. At a given gas flow rate, the pressure in the emission chamber can be controlled by varying the aperture of circular slit *9* and the capacity of the radial evacuation. The pressure should be adjusted so as to minimize the losses of negative ions due to stripping when they drift from the place of birth to the emission orifice.

The smallness condition for negative ion losses due to stripping may be written as $n\sigma_{-0}l \approx 10^{-2}$. At ion energies of several tens of electron volts, the stripping cross section is $\sigma_{-0} \approx 5 \times 10^{-16}$ cm^{-2}; then, for emission chamber length $l_e = 1$ cm, the pressure must be $P_e \le 8 \times 10^{-2}$ Pa. As follows from experiments, this condition is met (at $l_e = 1$ cm) throughout the gas flow rate range if $\Delta r \le 2$ mm.

Physically, it is clear that an electron avalanche in the emission chamber starts when the strength of the electric field between the plasma and emission electrode exceeds a critical value, $E > E_c$. The value of E_c depends on the initial density of electrons penetrating the contracting hole. In addition, for the discharge to be extended to the emission electrode, the gas density in the chamber must exceed some minimal value. To reduce this boundary pressure, it is necessary to raise the gas density inside the emission chamber near its entrance, where the plasma penetrating from the gas magnetron under certain conditions triggers an electron avalanche.

Initially, the experiments on extending the contracted discharge to the emission electrode were carried out at $\Delta r \le 1.5$ mm, $P_e = 5 \times 10^{-3}$–8×10^{-2} Pa, and $l_e = 1$ cm. Discharge current I_d was varied from 0.1 to 3.0 A. It turned out that the extension of the discharge was extremely unstable and that the spontaneous extension was observed only at maximal values of P_e and I_d. Obviously, for the given value of the gap, the discharge could be extended only by increasing the field strength between the plasma, the potential of which is close to the anode potential of the magnetron, and the emission electrode. This could be done either by applying a higher voltage from an extra power supply to the gap or by placing extra electrode *10* (Fig. 1) in the emission chamber near the end face of the magnetron, this electrode being charged positively relative to anode *2*.

Initially, the extra electrode was placed at distance $\Delta l = 1$ mm from the end face of cathode *4* and was connected to the "pole" of the power supply unit through additional resistor $R_{ad} = 630\ \Omega$. The other parameters of the gap remained unchanged. Under these conditions, the extension of the discharge was stable at the discharge current in the magnetron $I_d = 0.5$–0.7 A. As Δl decreased, so did the limiting current of the maintaining discharge at which the current passage to the emission electrode was stable. At $\Delta l = 0.4$ mm, the limiting current was ~0.25 A. A further decrease in Δl was found to be difficult, since the extra electrode shorts out the cathode because of electrode heating during the discharge.

Figure 4 shows the I–V characteristics of the discharges in the gas magnetron (curve *1*) and in the emission chamber (curve *2*) for $\Delta r = 1.5$ mm, $P_e = 1.5 \times 10^{-2}$ Pa, $\Delta l = 0.4$ mm, and $l_e = 0.7$ mm. Once the dis-

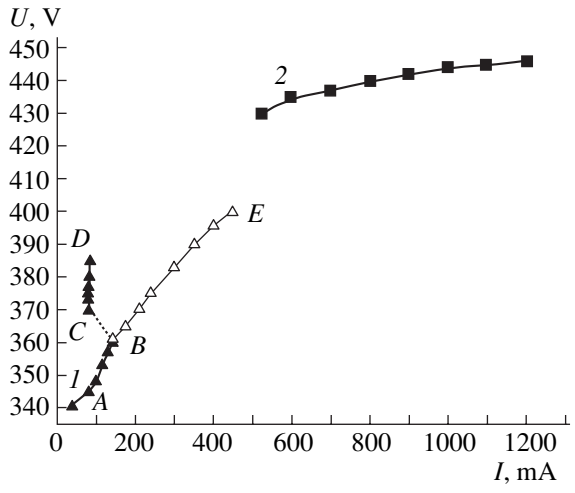

Fig. 4. I–V characteristic of the discharge in (*1*) the gas magnetron and (*2*) emission chamber at $P_e = 1.5 \times 10^{-2}$ Pa.

charge has been initiated, the voltage across the anode–cathode gap drops from U_{in} to the value marked by letter *A* in curve *1*. Then, the *I–V* characteristic follows portion *AB* of curve *1*. At a certain value of the current (point *B*), the discharge is initiated in the emission chamber and the voltage dependence of the anode current follows portion *CD*. With the emission electrode switched off, the *I–V* characteristic will follow curve *ABE*. A decrease (increase) in the pressure in the emission chamber shifts point *B* toward higher (lower) currents. The voltage dependence of the current in the emission electrode circuit (after the gap has been broken down) is presented by curve *2*.

The experiments also showed that, once the gap has been broken down, pressure P_e may be decreased to $\sim 8 \times 10^{-3}$ Pa with the discharge current being the same. In this case, the discharge remains stable.

CONCLUSIONS

Thus, the operation of a three-chamber plasma generator can be represented as follows. Application of a voltage to the electrodes in high-pressure discharge chamber *5* excites a discharge. If ring-shaped slit *7* is sufficiently wide, the resulting plasma penetrates into chamber *6* along the magnetic field. In chamber *6*, the plasma initiates a discharge and, hence, favors plasma generation at a pressure lower than in chamber *5*. If the thickness of the near-cathode space-charge layer is smaller than width Δr of contracting ring-shaped slit *9* and the electric field between the plasma and emission electrode, as well as the gas density in the emission chamber, exceeds a critical value, the plasma from the gas magnetron penetrates into the emission chamber through the slit and initiates an electron avalanche. Thus, a tubular plasma is generated in the emission chamber, which a distinct ring-shaped trace around the emission orifice on the emission electrode indicates.

Because of the double electrical layer, which forms before narrow ring-shaped slit *9* and supplies fast electrons to the area of increased pressure of the working gas effusing from the gas magnetron, favorable conditions for molecule vibrational excitation are provided in this circumferential plasma.

As a result of the diffuse expansion of the circumferential plasma across the magnetic field, an axial plasma is generated. The axial plasma thus generated contains vibrationally excited molecules and also an elevated concentration of slow electrons, since fast electrons cannot penetrate into this area because of the action of the "magnetic filter" [6].

Thus, there appears a high probability that slow electrons in the internal plasma will be attached to vibrationally excited molecules via dissociation with the formation of negatively charged ions [7].

REFERENCES

1. P. A. Litvinov, Vopr. At. Nauki Tekh., Ser.: Yad. Fiz. Issled., No. 4–5, 48 (1997).
2. R. A. Redhead, Can. J. Phys. **36**, 225 (1958).
3. N. A. Kervalishvili, Fiz. Plazmy **15**, 174 (1989) [Sov. J. Plasma Phys. **15**, 98 (1989)].
4. V. A. Kagadeĭ, A. V. Kozyrev, I. V. Osipov, and D. I. Proskurovskiĭ, Zh. Tekh. Fiz. **71** (3), 22 (2001) [Tech. Phys. **46**, 292 (2001)].
5. B. V. Alekseev and V. A. Kotel'nikov, *The Probe Method in Plasma Diagnostics* (Énergoatomizdat, Moscow, 1988) [in Russian].
6. A. J. T. Holmes, Rev. Sci. Instrum. **53**, 1517 (1982).
7. Y. Lee, R. A. Gough, K. N. Leung, *et al.*, J. Vac. Sci. Technol. B **16**, 3369 (1998).

Translated by V. Isaakyan

Technical Physics, Vol. 50, No. 4, 2005, pp. 473–478. Translated from Zhurnal Tekhnicheskoĭ Fiziki, Vol. 75, No. 4, 2005, pp. 85–90.

SOLIDS

Investigation of the Cation Distribution in Perovskite-Like Oxides with Mössbauer Spectroscopy

L. D. Zaripova*, N. V. Boltakova*, A. A. Valiullin, and Sh. Sh. Bashkirov***

** Ul'yanov-Lenin State University, ul. Lenina 18, Kazan, 420008 Tatarstan, Russia*

e-mail: public.mail@ksu.ru

*** Proton Research Innovative Center, Kazan, 420111 Tatarstan, Russia*

e-mail: proton@tbit.ru

Received July 7, 2004

Abstract—Complex perovskite-like oxides, such as $Ln Fe_{2/3}Mo_{1/3}O_3$ orthoferrites, $Ln_{8-y}Sr_yCu_{8-x}Fe_xO_{20}$ (8–8–20), $Pr_4BaCu_4FeO_{13-\delta}$ (4–1–5), $YBa_{2-y}La_yCu_{3-x}Fe_xO_{7-\delta}$, and $Y_{1-y}Ca_yBa_{2-y}La_yCu_{3-x}Fe_xO_{7-\delta}$ (1–2–3), are studied by means of Mössbauer spectroscopy. At room temperature, the spectra of the orthoferrites contain only magnetic components. The spectra of the 1–2–3 compounds contain only magnetically disordered components: iron atoms substitute for copper at Cu(1) sites, taking various configurations: planar squares, quadratic pyramids, and octahedra. Cuprates 8–8–20 and 4–1–5 have a wide diversity of spectra. In the 8–8–20 oxides, a phase related to the pyramidal environment of the iron cations is present at any iron concentration. In all the perovskites, iron cations become magnetically ordered only at octahedral sites of the structure. © *2005 Pleiades Publishing, Inc.*

INTRODUCTION

The name *perovskite-like crystals* usually refers to compounds the structure of which is made up of vertex-to-vertex octahedra or their fragments, pyramids and squares. Perovskite-like structures, being typical of many high-temperature superconductors, are today being used as model compounds for studying the structure–property interplay. Since the properties of these compounds are directly related to the positions of certain cations in the lattice, it is of interest to refine the crystal structure and phase composition of perovskite-like compounds and gain evidence for the stabilizing role of some elements. Chief among the techniques capable of tackling the questions posed is Mössbauer spectroscopy. Using this technique, one can determine the crystallographic position (from the quadrupole split (QS)) and valence (from the isomer shift (IS)) of a cation, as well as the relative concentration of the cations (from the area under curve).

This work generalizes the data obtained in previous studies of complex oxides with different types of perovskite-like structure.

OBJECTS AND METHODS OF INVESTIGATION

The objects of investigation were complex oxides with the $Ln Fe_{2/3}Mo_{1/3}O_3$ cubic perovskite structure (orthoferrites, where Ln = La, Ce, Pr, or Nd) and with the imperfect perovskite structure: $Ln_{8-y}Sr_yCu_{8-x}Fe_xO_{20}$ (Ln = La, Nd, or Pr; y = 1.6–4.0; x = 1.6–3.0; 8–8–20 structure), $Pr_4BaCu_4FeO_{13-\delta}$ (δ = 0, 0.5, 4–1–5 structure), as well as $YBa_{2-y}La_yCu_{3-x}Fe_xO_{7-\delta}$ and $Y_{1-y}Ca_yBa_{2-y}La_yCu_{3-x}Fe_xO_{7-\delta}$ (y = 0.25 and 0.50; x = 0.06 and 0.12; $\delta \approx 0.05$; and 1–2–3 structure).

The samples were synthesized in a laboratory headed by Bazuev at the Institute of Solid-State Chemistry (Ural Division, Russian Academy of Sciences, Yekaterinburg) (for details, see [1–4]).

A series of compounds with a successively varying degree of substitution in one element is impossible to synthesize. We cannot change the concentration of one element while keeping the concentrations of the remaining ones unchanged, since the amounts of the metals in these phases obey strict relationships. If these relationships are violated, the desired phases either do not form or grow inhomogeneous (non-one-phase).

Mössbauer spectra were recorded in gamma absorption geometry with an MS1101E constant-acceleration spectrometer using ^{57}Co embedded in a Cr matrix as a gamma source. The spectra were processed by conventional iteration methods, and a model adopted was verified with the Pearson criterion.

INVESTIGATION OF $Ln Fe_{2/3}Mo_{1/3}O_3$ (Ln = La, Ce, Pr, OR Nd) ORTHOFERRITES

The structure of $Ln FeO_3$ orthoferrite may be viewed as a three-dimensional framework made up of vertex-to-vertex FeO_6 octahedra with cubic–octahedral voids occupied by large Ln cations.

1063-7842/05/5004-0473$26.00

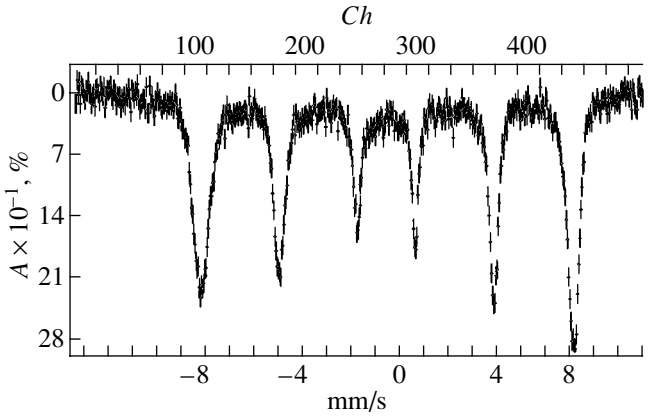

Fig. 1. Mössbauer spectrum for $LaFe_{2/3}Mo_{1/3}O_3$ (calibration against α-Fe). Hereafter, *A* is the absorption; *Ch*, channel number.

A typical room-temperature spectrum for these compounds is shown in Fig. 1. The spectrum is seen to contain only magnetically ordered components (sextets). Such spectra are characteristic of all the orthoferrites considered [5–8].

Table 1. Mössbauer parameters for $LnFe_{2/3}Mo_{1/3}O_3$ orthoferrites at room temperature

Spectral component	*Ln*	*H*, 10^6 A/m	*QS*, mm/s	*IS*, mm/s	*S*, %	*SC*, %
*S*0	La	39.2	−0.03	0.42	12.4	8.8
	Ce	39.2	−0.12	0.43	10.8	
	Pr	38.8	−0.13	0.41	12.8	
	Nd	38.8	−0.18	0.40	10.5	
*S*1	La	38.5	0.00	0.46	24.8	26.3
	Ce	38.5	−0.07	0.48	26.2	
	Pr	38.0	−0.10	0.45	24.0	
	Nd	38.1	−0.08	0.44	25.8	
*S*2	La	37.7	0.03	0.49	28.3	32.9
	Ce	37.7	−0.06	0.51	28.6	
	Pr	37.3	−0.05	0.50	30.0	
	Nd	37.3	−0.07	0.47	34.6	
*S*3	La	37.0	0.03	0.52	23.7	21.9
	Ce	37.0	−0.03	0.55	24.2	
	Pr	36.3	−0.05	0.52	25.0	
	Nd	36.4	−0.06	0.52	20.4	
*S*4	La	35.8	0.04	0.56	10.8	8.2
	Ce	35.8	−0.04	0.57	10.2	
	Pr	34.7	−0.06	0.54	8.1	
	Nd	34.9	−0.01	0.57	8.8	

Notes: The relative error in measuring *H* (local magnetic field) is 0.1×10^6 A/m; *QS*, 0.04 mm/s; *IS* (hereafter isomer shift relative to α-Fe), 0.02 mm/s; and *S* (relative intensity of a given component), 3%. The calculation accuracy for *SC* (calculated relative intensity of a given spectral component) is 0.05%.

To identify the spectra, we used a model that involves a set of spectral components, each being assigned to a probable cation environment from the second coordination sphere of a given iron atom [7, 8]. Estimates based on the binomial distribution yielded the five most probable environments. The results of optimization of this model for the orthoferrites are given in Table 1. The first column lists spectral components, the figure indicating the number of molybdenum ions in the nearest-neighbor environment of a given Fe ion.

The QS values for all the sextets confirm the assumption of the octahedral coordination of iron cations [1]. The IS values of the sextets suggest that the samples contain Fe^{3+} ions alone [9], which contradicts the earlier data for iron ion valent states obtained by indirect methods [1] (it was argued that Fe^{2+} ions are also present in the crystals). The data listed in the two last columns of Table 1 show that the distribution of Fe and Mo ions in the orthoferrites is close to the statistical (calculated) distribution.

To determine the oxidation state of Fe ions in these compounds, we made Mössbauer measurements on the sample with *Ln* = Ce at the boiling point of liquid nitrogen (80 K) (Table 2). As follows from Table 2, sextet *S*4 disappears but another sextet, *SX*, and doublet, *DX*, arise. The ISs of the spectral components in these low-temperature spectra, as well as in the room-temperature spectra, correspond to Fe^{3+} ions [9].

The fact that a distinct paramagnetic doublet is absent in the room-temperature spectra but appears (along with the extra sextet) in the spectra taken at 80 K may indicate the occurrence of a radically new low-temperature magnetic microstructure containing regions where exchange interaction is suppressed by specific structure distortions. There may be other reasons for such an anomalous change in magnetic ordering at reduced temperatures.

INVESTIGATION OF 4–1–5 $Pr_4BaCu_4FeO_{13-\delta}$ AND 8–8–20 $Ln_{8-y}Sr_yCu_{8-x}Fe_xO_{20}$ OXIDES (*Ln* = La, Nd, OR Pr; *y* = 1.6–4.0; *x* = 1.6–3.0)

Crystal structures of type 4–1–5 and 8–8–20 represent a set of connected chains of CuO_6 octahedra and quadratic CuO_5 pyramids aligned with the *c* axis. The structures differ in the way the structural polyhedra are connected, as well as in the presence of chains of planar square groups in the 8–8–20 structure. The rare-earth and alkali metals occupy the voids between the polyhedra, the metal distribution being statistical in the 8–8–20 structure and ordered in the 4–1–5 structure. In addition, the ratio La/Ba in the latter is fixed.

Figure 2 shows the Mössbauer spectra for the 4–1–5 structures that were taken at room temperature. The IS value, (0.19–0.37) ± 0.02 mm/s, implies that all the

iron is in the state Fe^{3+} [9] and occupies primarily (61–69%) the octahedra of the 4–1–5 structure. The rest of the iron occupies the pyramidal sites [6].

The spectra of the $Ln_{8-y}Sr_yCu_{8-x}Fe_xO_{20}$ (*Ln* = La, Pr, or Nd) cuprates studied in this work depend on *x*: they may consist of only doublets or contain magnetic components along with paramagnetic ones [6, 7]. At room temperature, the spectra of all the samples contain three doublets and several sextets [6].

The spectra of $La_4Sr_4Cu_5Fe_3O_{20}$ and $La_{4.5}Sr_{3.5}Cu_6Fe_2O_{20}$ oxygen-deficient perovskite-like oxides contain three paramagnetic doublets, D_1 (8–9%), D_2 (69–73%), and D_3 (19–22%) (Fig. 3), which correspond to three nonequivalent positions of iron ions. According to the isomer shifts, doublets D_1 and D_2 are assigned to Fe^{3+} ions (0.21 ± 0.04 mm/s) and doublet D_3, to Fe^{4+} ions (–0.02 ± 0.04 mm/s). From the QSs of these doublets, the first doublet, (1.40–1.50) ± 0.12 mm/s, can be referred to Fe ions in the pyramidal sites; the rest, to Fe ions in the octahedra, (0.42–0.51) ± 0.07 mm/s, owing to the symmetry of these positions.

The Mössbauer spectrum taken from the $La_{6.4}Sr_{1.6}Cu_{6.4}Fe_{1.6}O_{20}$ sample is a superposition of six sextets (≈81%) and three doublets (≈9%) [7]. These doublets are similar to those observed for the $La_4Sr_4Cu_5Fe_3O_{20}$ and $La_{4.5}Sr_{3.5}Cu_6Fe_2O_{20}$ samples. All the sextets are typical of the octahedral environment of Fe^{3+} (QS = (0.02–0.16) ± 0.07 mm/s, IS = (0.40–0.43) ± 0.04 mm/s, H = (14.5–38.0) ± 0.2 × 10^6 A/m). The parameters of one sextet (QS = –0.06 ± 0.07 mm/s, IS = 0.43 ± 0.04 mm/s, H = 41.6 ± 0.2) × 10^6 A/m) are characteristic of γ-Fe_2O_3 [10] (which possibly did not enter into the synthesis reaction). The other sextets correspond to Fe ions with a different number of similar neighbors.

Low-temperature Mössbauer measurements were also made on the $La_{4.5}Sr_{3.5}Cu_6Fe_2O_{20}$ compound. The spectrum taken at the boiling point of liquid nitrogen (≈80 K) exhibits a faint magnetic structure, with doublets still remaining to be dominant spectral components. Magnetic components cannot be reliably identified. Note only that the arrangement of possible sextets corresponds to Fe^{3+} ions in the octahedral oxygen environment. The percentage of doublets D_1 and D_3 remains virtually the same (7 and 21%, respectively). Only the area of doublet D_2, which corresponds to Fe^{3+} ions in the octahedral environment, changes (diminishes roughly by one-third); that is, magnetic ordering takes place just at some of these sites.

The spectrum of $Pr_{4.4}Sr_{3.6}Cu_{5.6}Fe_{2.4}O_{20}$ consists of three doublets, which persist in all the spectra for the praseodymium series (just as for the lanthanum series). Since the amount of iron in this oxide is the highest and it is certain to be homogeneous (one-phase), we may say with assurance that the limiting value of degree of substitution *x* in the Pr series is larger than in the La series. The doublets distinguished in the spectrum for the $Pr_{4.4}Sr_{3.6}Cu_{5.6}Fe_{2.4}O_{20}$ sample are similar to those in the spectrum for the La-containing cuprates (Table 3).

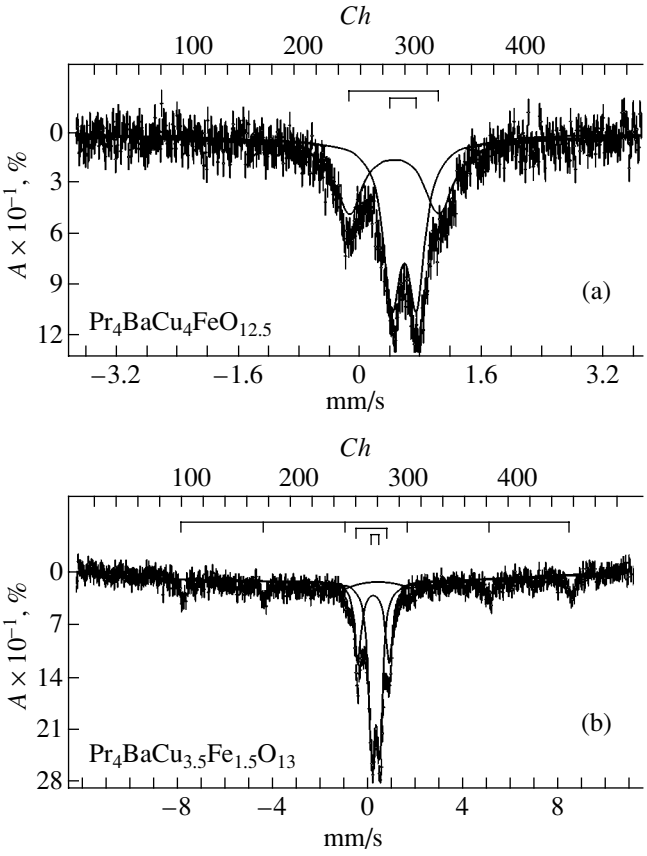

Fig. 2. Mössbauer spectra for the 4–1–5 oxides. Scale calibration against (a) sodium nitroprusside and (b) α-Fe.

The spectra for the $Pr_{4.8}Sr_{3.2}Cu_6Fe_2O_{20}$ and $Pr_{5.2}Sr_{2.8}Cu_{6.4}Fe_{1.6}O_{20}$ samples [8] contain sextets with parameters typical of Fe^{3+} cations in the octahedral environment together with the doublets mentioned above (Table 3).

The Mössbauer spectrum of the $Nd_{4.8}Sr_{3.2}Cu_6Fe_2O_{20}$ sample [8] has several sextets (QS = (–0.36–0.24) ±

Table 2. Mössbauer parameters for $CeFe_{2/3}Mo_{1/3}O_3$ at 80 K

Spectral component	*H*, 10^6 A/m	*QS*, mm/s	*IS*, mm/s	*S*, %
*S*0	43.7	–0.23	0.60	11
*S*1	42.0	0.13	0.54	32
*S*2	41.5	0.05	0.65	25
*S*3	40.2	–0.17	0.76	13
SX	24.6	–0.00	0.33	11
DX	–	0.27	0.45	8

Note: The errors are the same as in Table 1.

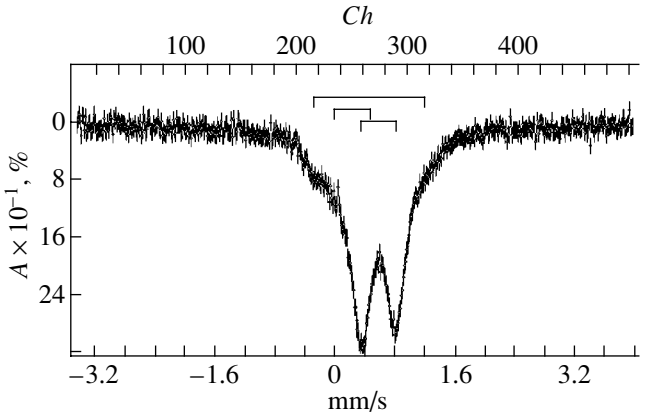

Fig. 3. Mössbauer spectrum for 8–8–20 $La_{4.5}Sr_{3.5}Cu_6Fe_2O_{20}$ perovskite (scale calibration against sodium nitroprusside).

0.10 mm/s, IS = (0.29–0.32) ± 0.05 mm/s, H = (17.9–34.3) ± 0.2 × 10^6 A/m) and three doublets typical of (except for D_3) Fe^{3+} ions. The parameters of the spectrum suggest that a minor part (5%) of the iron is in the pyramidal environment (doublet D_1), while the rest of the ions occupy the octahedral sites [7]. The spectrum for $Nd_{5.2}Sr_{2.8}Cu_{6.4}Fe_{1.6}O_{20}$ also indicates the presence of magnetic components.

Thus, one can distinguish the substitution-related features common to the spectra (cation distributions) taken from all three series. As follows from the IS values, all the spectral components correspond to Fe^{3+} ions, except for doublet D_3, which is assigned to Fe^{4+} [9]. From the QS values and the relative areas of the components, one can assume that most of the iron (corresponding to all the sextets and doublets D_2 and D_3) occupies the tetrahedral sites, while the remaining part (doublet D_1) corresponds to iron cations in the quadratic-pyramid environment. The presence of Fe^{4+} ions seems quite plausible because of the mixed valence of copper in these compounds.

The presence of the sextets may be explained by the fact that the samples contain areas with an increased iron content. The QSs of the sextets differ, because octahedra with a different number of copper ions in the second coordination sphere experience different amount of distortion.

The fact that iron cations occupy mostly octahedral sites in the perovskite structures of both types is quite explainable: iron substitutes for copper in the Cu^{3+} state, which occupies the octahedra [3]. From the data obtained, it follows that the component corresponding to iron cations in the pyramidal environment is present (3–16%) in the spectra of the samples from all the series irrespective of the percentage of the substituent, i.e., even in those compounds where all the iron could occupy the octahedral sites.

Small amounts of iron ions present at the pyramidal sites may be explained either by partial disorder in the iron atom arrangement, which could cause the iron to occupy the pyramidal sites, or by an oxygen deficiency in the CuO_6 octahedra [11]. Studies of $(La,Sr)_8Cu_{8-x}Fe_xO_{20}$ oxygen-deficient cuprates by neutron diffraction indicate a high stability of the oxygen substructure, which is not affected by the iron substituent (the oxygen concentration, O_{20}, remains unchanged). This means that the pyramidal coordinations revealed by Mössbauer spectroscopy are not related to oxygen deficiency but are due to the redistribution of the iron among the octahedral and pyramidal sites [12].

It was found that a decrease in the iron atom concentration results in magnetic ordering. As iron concentration x diminishes, the sextets in the Mössbauer spectra taken from the 8–8–20 compounds appear in all the series (lanthanum, praseodymium, and neodymium) of samples. Remarkably, the magnetic structure is formed by those iron atoms occupying the octahedra.

Thus, when the concentration of iron is low, its atoms form uniformly distributed clusters; that is, the structure contains areas where iron substitutes for copper in greater amounts. In these areas, the magnetic ordering of iron atoms takes place, as demonstrated by the presence of the magnetic components in the spectra. As the magnetic atom concentration rises, the iron distribution over the sample smoothes out.

Thus, our investigation of the perovskite-like compounds indicates that iron atoms in them are not only mere indicators of the state of the structure but are also responsible for structural and magnetic ordering.

Table 3. Characteristic values of the Mössbauer parameters for the 8–8–20 praseodymium-based perovskites

Spectral component	*IS*, mm/s	*QS*, mm/s	H, 10^6 A/m	Line half-width at half maximum, mm/s
D_1	(0.24–0.26) ± 0.08	(1.34–1.56) ± 0.17	–	(0.43–0.52) ± 0.23
D_2	(0.28–0.31) ± 0.05	(0.45–0.49) ± 0.08	–	(0.20–0.31) ± 0.03
D_3	(0.11–0.13) ± 0.06	(0.48–0.49) ± 0.09	–	(0.32–0.50) ± 0.18
S_1–S_5	(0.30–0.38) ± 0.03	(–0.37–0.25) ± 0.07	15.1–35.0 ± 0.3	(0.20–0.52) ± 0.11

INVESTIGATION OF 1–2–3 $YBa_{2-y}La_yCu_{3-x}Fe_xO_{7-\delta}$ AND $Y_{1-y}Ca_yBa_{2-y}La_yCu_{3-x}Fe_xO_{7-\delta}$ OXIDES (y = 0.25 AND 0.5, x = 0.06 AND 0.12, $\delta \approx 0.05$)

In the as-synthesized state, the $YBa_2Cu_3O_7$ compound has a copper framework consisting of two layers of $Cu(2)O_5$ pyramids sharing vertices with $Cu(1)O_4$ planar squares. The unit cell initially has an orthorhombic structure but becomes tetragonal when the sites O(1) and O(5) are half-filled. Both structures correspond to the oxidation state Cu^{2+} in the CuO_5 pyramids and Cu^{3+} in the CuO_4 squares.

The Mössbauer spectra taken from some of the 1–2–3 oxides at room temperature are shown in Fig. 4. Table 4 lists the parameters of the Mössbauer spectra [7] for $YBa_{2-y}La_yCu_{3-x}Fe_xO_{7-\delta}$ and $Y_{1-y}Ca_yBa_{2-y}La_yCu_{3-x}Fe_xO_{7-\delta}$ (y = 0.25 and 0.5, x = 0.06 and 0.12, $\delta \approx 0.05$) solid solutions. In all the spectra, hyperfine magnetic splitting of the resonance lines is absent. The spectra are a superposition of at least four paramagnetic doublets D_1–D_4 of various intensities, which are assigned to four nonequivalent positions of iron atoms. It is assumed that iron substitutes for copper only at Cu(1) sites, being surrounded by planar squares, quadratic pyramids, or octahedra.

Judging from the QS values, these doublets are related to the crystallographic positions as follows. Components D_1 and D_2 are referred to iron atoms at sites Cu(1), which form a planar square (the coordination number is four) and a quadratic pyramid (coordination number is five) [13, 14]. Doublet D_3 may be assigned either to Fe ions at sites Cu(1), which are coordinated into an octahedron [15], or to Fe ions lying near domain walls [15, 16].

All the above components seem to belong to Fe^{4+} ions [9, 17]. Component D_4 exhibits a much larger isomer shift; therefore, we assume that it is related to Fe^{3+} ions. The QS value suggests octahedral coordination of these atoms at Cu(1) sites.

The samples with a larger lanthanum content have a larger fraction of highly coordinated sites (the coordination number exceeds four). This is because O(5) oxygen sites are additionally filled to retain electroneutrality when La^{3+} cations substitute for Ba^{2+} ones [18].

In the Ca-containing samples, the total area of doublets D_3 and D_4 (i.e., the fraction of the iron with the octahedral environment) is constant (32–33%), increasing in the Ca-free samples (owing to component D_3). Also, the pyramidal component increases markedly in the Ca-containing samples. Thus, in the Ca-containing samples, the occurrence of structural octahedra at sites Cu(1) is limited. A reason for such a restriction may be a limited number of oxygen atoms that can leave their positions near Cu sites for Fe-occupied sites. The geometry of the structure may also be a factor: it may so happen that the structure is physically unfeasible at a large number of structural octahedra.

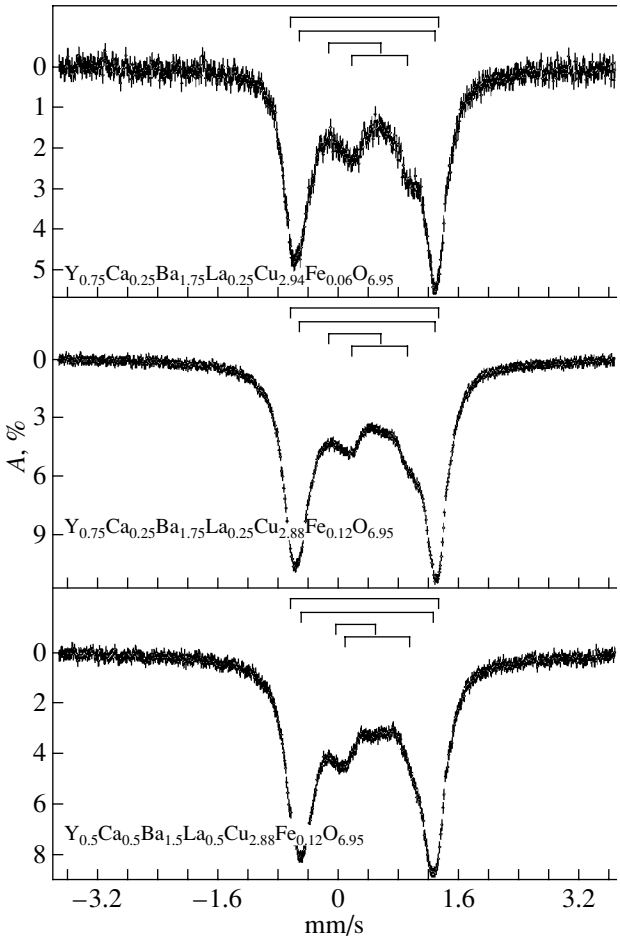

Fig. 4. Mössbauer spectra for the 1–2–3 Ca-containing oxides (scale calibration against sodium nitroprusside).

Thus, our investigation showed that all the iron occupies sites Cu(1) in the crystal lattice of the 1–2–3

Table 4. Mössbauer parameters for the 1–2–3 compounds

Spectral component	*IS*, mm/s	*QS*, mm/s	Half-width at half maximum, mm/s
D_1	(0.06–0.08) ± 0.03	(1.94–2.01) ± 0.04	(0.20–0.27) ± 0.07
D_2	(0.09–0.13) ± 0.03	(1.66–1.82) ± 0.04	(0.35–0.40) ± 0.07
D_3	(–0.06–0.03) ± 0.03	(0.55–0.77) ± 0.04	(0.48–0.52) ± 0.07
D_4	(0.27–0.38) ± 0.03	(0.48–0.85) ± 0.04	(0.20–0.35) ± 0.07

compound (primarily because of its low concentration) and is surrounded by variously configured oxygen atoms. In such complicated substitutions (covering all cation positions), the iron has a coordination number of six even if its concentration is low (0.06 and 0.12), with the percentage of given sites in the Ca-containing samples remaining constant. Substitution of any of the cations reduces the amount of Fe ions with a coordination number greater than four, and calcium limits the increase in the number of octahedral sites. The data obtained may also be viewed as evidence in favor of the earlier supposition [18, 19] that the La^{3+} and Ca^{2+} ions are simultaneously distributed among the Y and Ba sites. Since Ca, unlike La, occupies the Ba sites and has the same oxidation state as Ba, it will not contribute to the inflow of extra oxygen to sites Cu(1), thereby retarding the growth of the number of highly coordinated impurity sites.

CONCLUSIONS

The conclusions that follow from our investigation are as follows.

(1) In all the perovskite-like oxides studied, iron cations become magnetically ordered only in octahedral sites.

(2) In the 8–8–20 oxides, a decrease in the iron content enhances magnetic order.

(3) In the orthoferrites and 4–1–5 oxides, iron is in the oxidation state Fe^{3+} alone; in the oxygen-deficient 8–8–20 and 1–2–3 compounds, it exhibits a mixed valence, being in the Fe^{3+} and Fe^{4+} states.

(4) In the orthoferrites, Fe and Mo cations are statistically distributed over the octahedral sites; in the 4–1–5 and 8–8–20 compounds, iron (irrespective of its concentration) occupies both the octahedral and pyramidal sites; and in the 1–2–3 oxides, iron substitutes for copper only at sites Cu(1), being surrounded by variously coordinated oxygen atoms (from a planar square to an octahedron).

ACKNOWLEDGMENTS

This work was supported by the Research Program of Tatarstan (grant no. 06-6.1-142), CRDF (grant no. REC-007), and the Program in Support of Leading Scientific Schools (grant no. NSh-1708.2003.2).

REFERENCES

1. G. V. Bazuev, V. G. Zubkov, and G. P. Shveikin, Zh. Neorg. Khim. **41**, 2000 (1996).
2. G. V. Bazuev, N. V. Lukin, N. V. Krasil'nikov, *et al.*, Zh. Neorg. Khim. **44**, 341 (1999).
3. G. V. Bazuev, N. V. Lukin, N. A. Kirsanov, *et al.*, Sverkhprovodimost: Fiz. Khim. Tekh. **6**, 1663 (1993).
4. G. P. Shveĭkin, V. A. Gubanov, A. A. Fotiev, *et al*., *Electronic Structure and Physicochemical Properties of High-Temperature Superconductors* (Nauka, Moscow, 1990) [in Russian].
5. Sh. Sh. Bashkirov, L. D. Zaripova, T. I. Chupakhina, *et al.*, in *Proceedings of the 5th All-Russia Scientific Conference "Physical and Chemical Properties of Oxides," Yekaterinburg, 2000*, pp. 82–85.
6. Sh. Sh. Bashkirov, A. A. Valiullin, L. D. Zaripova, *et al.*, Izv. Ross. Akad. Nauk, Ser. Fiz. **65**, 962 (2001).
7. Sh. Sh. Bashkirov, A. A. Valiullin, L. D. Zaripova, *et al.*, http://zhurnal.ape.relarn.ru/articles/2004/025.pdf.
8. Sh. Sh. Bashkirov, A. A. Valiullin, L. D. Zaripova, *et al.*, in *Selected Works of Members of the Academy of Sciences of Tatarstan* (Foliant, Kazan', 2002), pp. 51–59.
9. F. Menil, J. Phys. Chem. Solids **46**, 763 (1985).
10. *Mössbauer Effect and Its Applications to Chemistry*, Ed. by V. I. Goldanskii (Mir, Moscow, 1970; Consultants Bureau, New York, 1964).
11. R. Genouel, C. Michel, N. Nguyen, *et al.*, J. Solid State Chem. **115**, 469 (1995).
12. R. Genouel, C. Michel, and B. Raveau, Chem. Mater. **7**, 2181 (1995).
13. I. S. Lyubutin, V. G. Terziev, S. V. Luchko, *et al.*, Sverkhprovodimost: Fiz. Khim. Tekh. **5**, 1842 (1992).
14. I. S. Lyubutin, V. G. Terziev, and O. N. Morozov, Pis'ma Zh. Éksp. Teor. Fiz. **52**, 1146 (1990) [JETP Lett. **52**, 550 (1990)].
15. I. A. Evstyukhina, I. V. Boĭdachenko, O. V. Tymchuk, *et al.*, Sverkhprovodimost: Fiz. Khim. Tekh. **5**, 2280 (1992).
16. V. A. Shabashov, V. V. Sagaradze, A. G. Golikov, *et al.*, Sverkhprovodimost: Fiz. Khim. Tekh. **5**, 1043 (1993).
17. R. A. Stukan, V. E. Prusakov, A. G. Knizhnik, *et al.*, Sverkhprovodimost: Fiz. Khim. Tekh. **4**, 2368 (1991).
18. G. V. Bazuev, N. A. Kirsanov, D. G. Kellerman, Sverkhprovodimost: Fiz. Khim. Tekh. **4**, 1187 (1991).
19. G. V. Bazuev, G. P. Shveikin, N. A. Kirsanov, Sverkhprovodimost: Fiz. Khim. Tekh. **3**, 131 (1990).

Translated by V. Isaakyan

Technical Physics, Vol. 50, No. 4, 2005, pp. 479–483. Translated from Zhurnal Tekhnicheskoĭ Fiziki, Vol. 75, No. 4, 2005, pp. 91–95.

SOLIDS

Effect of the Conditions of Dynamic Nanoindentation on the Strain-Rate Sensitivity of Hardness for Solids with Different Structures

Yu. I. Golovin, A. I. Tyurin, and V. V. Khlebnikov

Tambov State University, Internatsional'naya ul. 33, Tambov, 392622 Russia

e-mail: golovin@tsu.tmb.ru

Received May 7, 2004

Abstract—A technique for the determination of the strain-rate sensitivity of hardness during dynamic nanoindentation is proposed. The strain-rate sensitivities of the dynamic hardnesses of a wide class of materials (fcc metals, carbon steels, bulk amorphous metallic alloys, ionic and covalent crystals, polymers, and ceramics) are determined. The variation of these strain-rate sensitivities with the relative-strain rate (in the $\dot{\varepsilon}$ range from 3×10^{-3} to 5×10^{3} s^{-1}) and the indentation depth (in the range from 30 nm to 2 μm) is studied. © *2005 Pleiades Publishing, Inc.*

INTRODUCTION

The creation of integrated microelectromechanical systems and intelligent microrobots [1, 2]; the development of systems for recording, storing, and reading of information that are based on mechanical media using touches with atomic-scale tips [3, 4]; atomic force microscopy; and other needs of nanotechnology have generated studies of the mechanical properties of materials on the scale of elementary acts occurring in one micro- or nanocontact. In the future, these works will fill gaps between the descriptions of various phenomena that occur in nanocontacts at the microscopic and atomic scales.

Moreover, many practical methods for the preparation and mechanical treatment of materials, the manufacture of various products from them, and their operation imply significant local elastoplastic surface deformation [5, 6]. Dynamic micro- and nanocontact interactions during dry friction, mechanical grinding and polishing, abrasive and erosion wear, collisions of micro- and nanoparticles with each other and with solid surfaces, contact atomic force microscopy, nanolithography by imprinting and scribing, fine milling, etc. [7], take place in submicron regions under conditions of high strain rates ($\dot{\varepsilon} \gg 10^{2}$ s^{-1}).

The mechanical properties of plastic materials in macrovolumes have been studied over an extremely wide $\dot{\varepsilon}$ range (from 10^{-8} to 10^{6} s^{-1}) (e.g., see [8]). However, fracture in many brittle materials (such as single crystals with covalent bonds, ceramics, glass, etc.) begins earlier than a noticeable plastic deformation develops. Therefore, the plastic properties of such materials are usually studied by microindentation [9–11] and, currently, nanoindentation [12–17]. Such studies produced a number of new and radically important results, including information on substantial changes in the mechanical properties of materials when the indentation depth h decreases to several or several tens of nanometers [12–15]. However, equipment produced by different foreign companies (MTS, Micromaterials, CSEM, EVECO, Hysitron, etc.) for the nanotesting of mechanical properties makes it possible to perform nanoindentation tests only at low values of $\dot{\varepsilon} \sim (10^{-3}$–$10^{-1}$ $s^{-1})$.

Some researchers (e.g., see [18]) tried to determine the rate dependences of the dynamic hardness, fracture toughness, and coefficient of indentation recovery for certain ionic crystals (NaCl, LiF, MgO), glasses, and ceramics in the range $\dot{\varepsilon} \sim 10^{4}$–$10^{5}$ s^{-1}. Since a freely flying striker was used as an indenter, only a rather narrow range of $\dot{\varepsilon}$ values (about one order of magnitude) was covered. Actually, one of the two parameters that are required to determine the hardness (the force and the indentation sizes) could only be estimated from indirect data (along with the duration and real shape of a loading pulse, which are required for estimating v) rather than measured. In the strain-rate range $10^{-3} < \dot{\varepsilon} < 10^{4}$ s^{-1}, which is more important for practice, data are scarce (e.g., see [19]). It should be noted that, for different ranges of $\dot{\varepsilon}$ and deformation-zone sizes (indentation depth h), the strain-rate dependences of the mechanical properties of the same material can have different characters. Therefore, it is fruitful to study the strain-rate sensitivity of the elastoplastic characteristics not only over a wide range of $\dot{\varepsilon}$ but also at different values of h (especially at $h \leq 1$ μm). Apart from their practical importance, such data can contain valuable information on the types and dynamics of elementary plas-

1063-7842/05/5004-0479$26.00

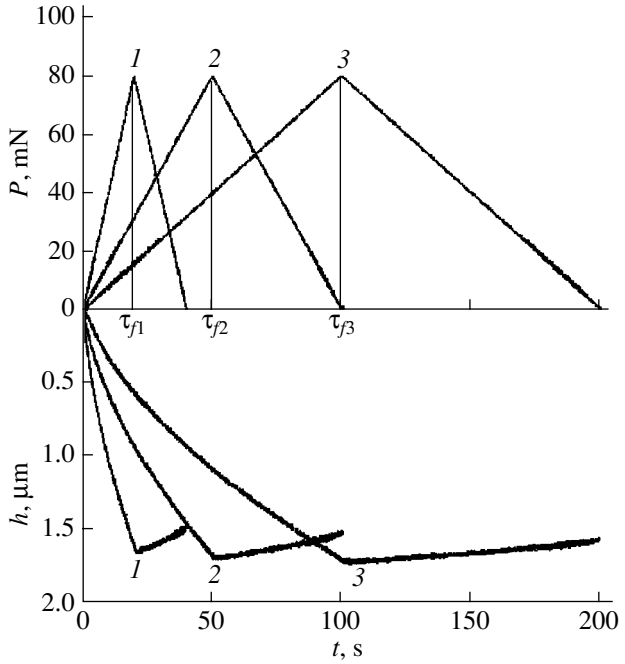

Fig. 1. Typical kinetic dependences of the force ($P(t)$) and the indentation depth ($h(t)$) for various loading pulse front times τ_f upon indenting of LiF crystals: τ_f = (*1*) 20, (*2*) 50, and (*3*) 100 s.

tic-deformation carriers and the nature of mechanical properties on the nanoscale.

The purpose of this work is to determine the strain-rate sensitivity of dynamic hardness and to analyze the variation of the sensitivity with $\dot{\varepsilon}$ (in the $\dot{\varepsilon}$ range from 3×10^{-3} to 5×10^3 s^{-1}, which covers about six orders of magnitude) and with h (in the range from 30 nm to 2 μm) for materials with different mechanical properties.

EXPERIMENTAL

We studied typical representatives of various material classes: ionic and covalent crystals (KCl, LiF, γ-LiF, ZnS, Ge, GaAs, MgO, Si), fcc metals (Al), carbon steels (steel 10), bulk amorphous metallic alloys ($Zr_{46.8}Ti_8Cu_{7.5}Ni_{10}Be_{27.5}$), polymers (polymethyl methacrylate (PMMA)), and ceramics (ZrO_2-based ceramics). For investigation, we used a specially designed computer-assisted dynamic nanoindentation meter [20]. Indentations were made with a diamond Berkovich pyramid loaded by a symmetric triangle force pulse with varied amplitude P_{max} and front duration τ_f (Fig. 1).

The force pulse was formed with an electrodynamic computer-assisted drive. The pulse form $P(t)$ and the time dependence of the indentation depth ($h(t)$) were recorded on a computer at a time resolution of ~50 μs. Typical $P(t)$ and $h(t)$ dependences for LiF are shown in Fig. 1. Then, these data were used to plot complete loading–unloading cycles in the P–h coordinates (Fig. 2). This procedure provided fully controlled testing conditions for various loading rates and allowed us to determine the instantaneous values of the operating force $P(t)$, the indentation depth $h(t)$, the relative-strain rate $\dot{\varepsilon} = (dh/dt)/h(t)$, and the dynamic hardness $H_d(t) = P(t)/A_c(t)$ at a time instant t. Here, $A_c(t)$ is the current contact area in a plastic indentation with allowance for the finite curvature of the real indenter and t is the time.

The $A_c(h_c)$ dependence is usually interpolated by a polynomial function of the form $A_c = C_0h_c^2 - C_1h_c + C_2h_c^{1/2} - C_3h_c^{1/4} + C_4h_c^{1/8} - C_5h_c^{1/16} + \ldots$ [16, 17], where h_c is the plastic indentation depth. The coefficients in the expression for A_c and h_c were determined by the Oliver–Pharr technique [16, 17], which is conventionally applied for quantitative processing of nanoindentation results. Using the numerical values of the coefficients C_n that were determined experimentally for the indenter used in experiment in the indentation-depth range from 30 nm to 2 μm, we can rewrite the equation for A_c in the form

$$A_c(t) = 24.5h_c^2(t) - 1000h_c(t) + 14\,000h_c^{1/2}(t) - 20\,000h_c^{1/4}(t) + 100\,000h_c^{1/8}(t).$$

RESULTS AND DISCUSSION

The dynamic hardness as a function of the instantaneous value of h_c is shown in Fig. 3 for a number of materials. Materials with a high ratio of the static hardness to Young's modulus, $H_{st}/E > 0.04$ (fused silica, Si, Ge, MgO), exhibit weak dependences of H_d on $\dot{\varepsilon}$ and h_c, and materials with $H_{st}/E < 0.04$ (LiF, PMMA, grade 10 steel, ZnS, Al) demonstrate a significant increase in H_d with increasing $\dot{\varepsilon}$ and decreasing h_c (Fig. 3).

Knowing the real kinetics of indenting, we can reconstruct the dynamic $H_d(t)$ and $\dot{\varepsilon}(t)$ curves in the coordinates $\log H_d(h_c) = f(\log \dot{\varepsilon}(h_c))$ by fixing the values of h_c at a given point of the range under study (from 30 nm to 2 μm). Figure 4 shows the variation of H_d normalized to H_{st} with $\dot{\varepsilon}$ for fused silica and LiF crystals. In the $\dot{\varepsilon}$ and h_c ranges under study, the dependences are seen to be almost linear for all the materials, which allows us to determine the strain-rate sensitivity of hardness $\alpha = \log(H_d/H_{st})/\log\dot{\varepsilon}$ at a given h_c (Fig. 4). The values of α for all the materials under study are shown in Fig. 5.

LiF and ZnS demonstrate an interesting specific feature in their $H_d(\dot{\varepsilon})$ dependences (Figs. 4, 5). At low $\dot{\varepsilon}$, the slope is a few times lower than that at high $\dot{\varepsilon}$. For example, for LiF the strain-rate sensitivity in the $\dot{\varepsilon}$

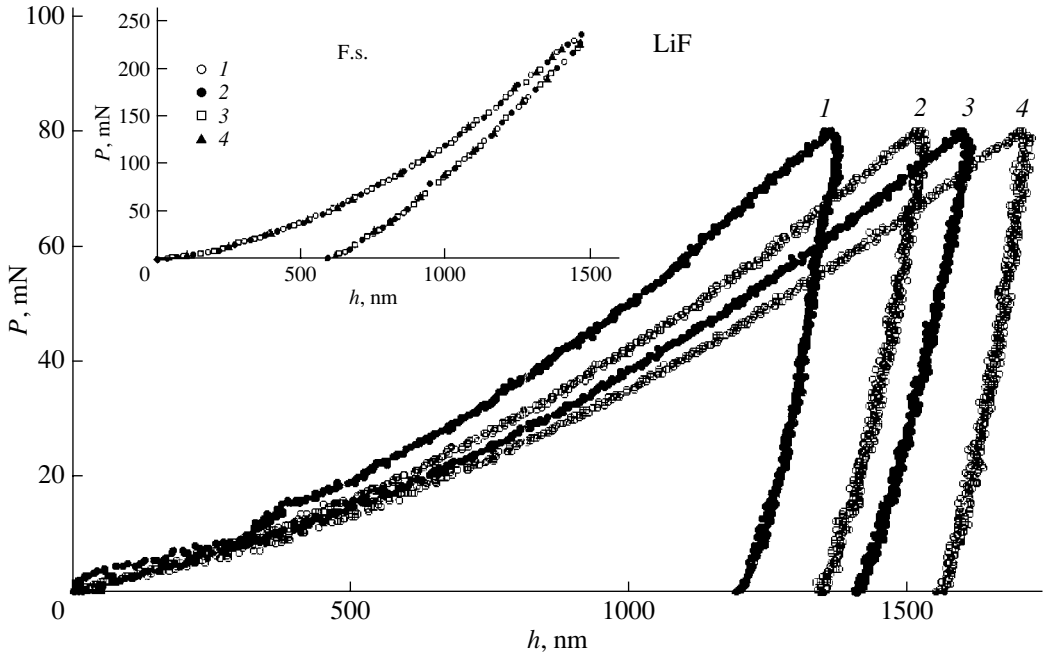

Fig. 2. Typical *P–h* diagrams recorded during identation of LiF crystals and (inset) fused silica: τ_f = (*1*) 0.05, (*2*) 1, (*3*) 10, and (*4*) 100 s.

range from 10^{-2} to 10^{-1} s^{-1} is lower than that in the $\dot{\varepsilon}$ range from 10^{-1} to 10^{2} s^{-1} by a factor of 2.5. For ZnS, α in the $\dot{\varepsilon}$ range from 0.5 to 10^{2} s^{-1} is higher than that in the $\dot{\varepsilon}$ range from 10^{-2} to 0.5 s^{-1} by a factor of 2.2.

When h_c exceeds a certain critical value h_c', α remains virtually unchanged, and it begins to increase with decreasing h_c only at small depths. Such a dependence is observed for all the materials (Fig. 6). For relatively soft materials (Al, ZnS, grade 10 steel, PMMA, KCl, γ-LiF), this increase varies from 50 to 188%. Hard materials (Si, ZrO_2, Ge) (Fig. 6) have smaller values of h_c' at which α begins to increase. For fused silica, α remains constant and equal to zero down to h_c = 30 nm.

Let us discuss the results obtained. In the framework of a simple phenomenological model, indentation can be considered as a relaxation process in which applied forces (stresses) cause the formation and motion of structural defects (dislocations, interstitials, twins, nucleation centers, etc.) [9, 21–24] that tend to decrease the contact stresses. Under static conditions, the material hardness H_{st} is specified by the equilibrium of the applied forces and the drag forces on defects, which are plastic-deformation carriers. Under conditions of a

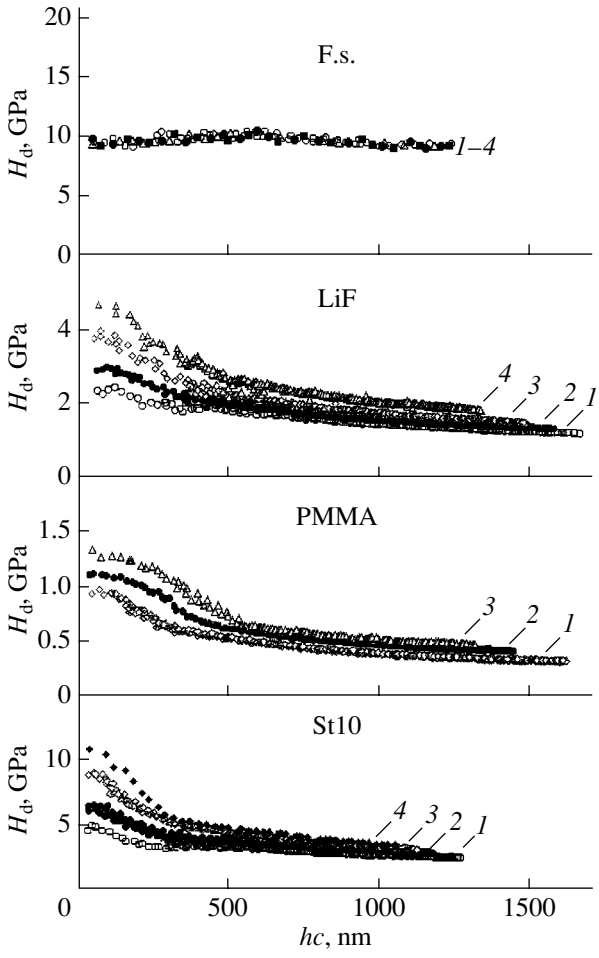

Fig. 3. Effect of the indentation depth h_c on the dynamic hardness H_d of some materials (fused silica (F.s.), LiF, PMMA, steel 10 (St10)): τ_f = (*1*) 100, (*2*) 10, (*3*) 1, and (*4*) 0.05 s.

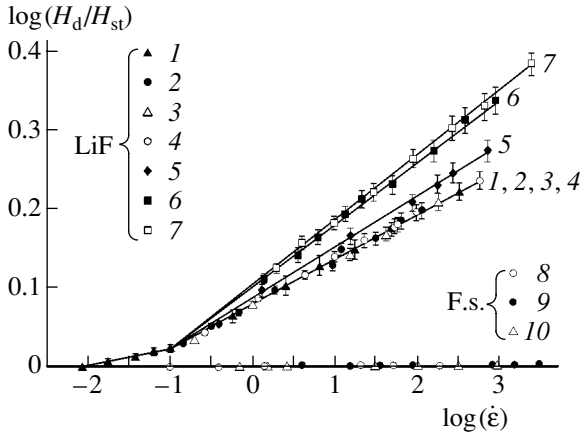

Fig. 4. Dependences of the normalized change in the dynamic hardness H_d/H_{st} of LiF and fused silica (F.s.) on the relative-strain rate $\dot{\varepsilon}$ under an indenter at different values of the indentation depth h_c. For LiF, h_c = (*1*) 1200, (*2*) 1000, (*3*) 750, (*4*) 500, (*5*) 350, (*6*) 200, and (*7*) 50 nm. For fused silica, h_c = (*8*) 900, (*9*) 450, and (*10*) 50 nm. H_{st} is the static hardness.

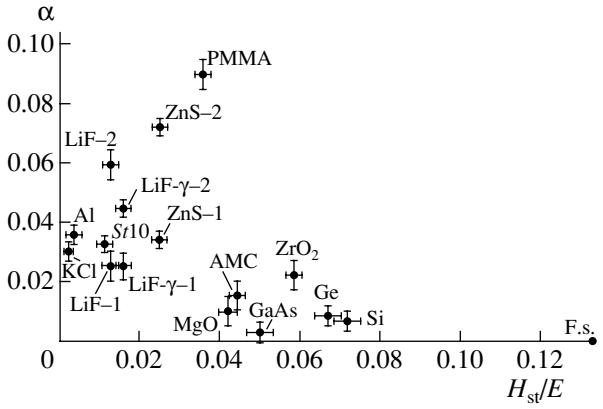

Fig. 5. Strain-rate sensitivity $\alpha = \log(H_d/H_{st})/\log(\dot{\varepsilon})$ for KCl, LiF, γ-LiF, GaAs, Ge, MgO, Si, ZrO_2, ZnS, grade 10 steel, PMMA, $Zr_{46.8}Ti_8Cu_{7.5}Ni_{10}Be_{27.5}$, Al, and fused silica. H_{st} is the static hardness, and E is Young's modulus.

short applied-force pulse and a small indentation depth, the finite rate of defect generation and motion can limit the depth of relaxation of the contact stresses; then, the dynamic hardness H_d is higher than H_{st}. In the general case, in the presence of several competing deformation mechanisms, the $H_d = f(\dot{\varepsilon})$ dependence can have the form schematically shown in Fig. 7. Its horizontal segments correspond to the situation where the rate of stress relaxation by a mechanism dominating in a certain $\dot{\varepsilon}$ range is higher than the loading rate. The inclined segments appear when the characteristic times of relaxation processes are comparable with the loading time, which is equivalent to the appearance of internal-friction peaks under these conditions.

The appearance of inclined segments (an increase in H_d with h_c) in the $H_d = f(h_c)$ dependence can indicate changes in not only the material properties in the surface layer but also changes in the geometrical conditions of operating a certain stress-relaxation mechanism (e.g., the required size of a deformation zone to form a sufficient number of stable dislocation loops in the case of plastic deformation realized via dislocation mechanisms). These conditions can obviously be different for different materials and loading rates.

We believe that the presence of a significant plastic deformation under an indenter in the absence of (for fused silica) or at a low strain-rate sensitivity of H_d (for Si, Ge, GaAs, $Zr_{46.8}Ti_8Cu_{7.5}Ni_{10}Be_{27.5}$, and ZrO_2) and at a very small number or the absence of forming dislocations (which have very low mobility at room temperature), as well as the absence of a relation between H_d and h_c, means that plastic relaxation in these materials occurs via nondislocation processes. These processes

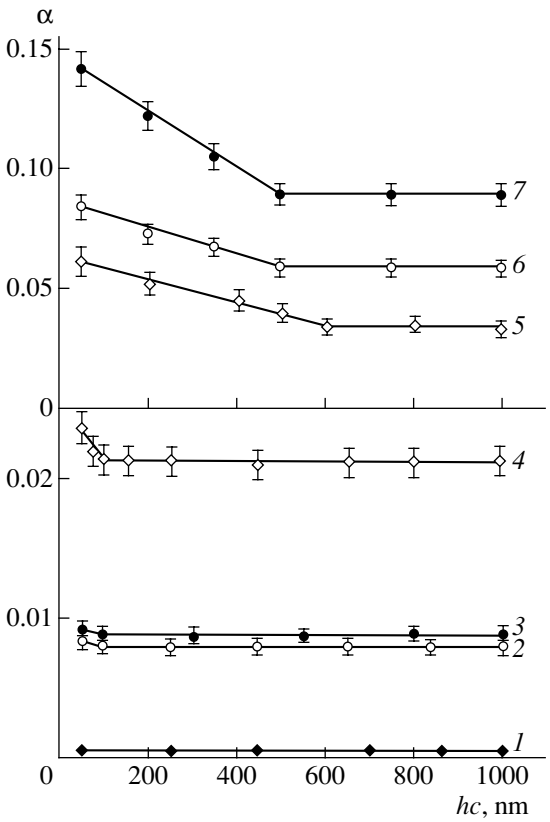

Fig. 6. Dependences of the strain-rate sensitivity of hardness α on the indentation depth h_c for (*1*) fused silica, (*2*) Si, (*3*) Ge, (*4*) ZrO_2, (*5*) grade 10 steel, (*6*) LiF, and (*7*) PMMA.

are the generation and motion (from the indenter) of nonequilibrium point defects, nucleation centers, or localized-shear bands, which are induced by high contact pressures.

The increase in the dynamic hardness and in its strain-rate sensitivity with decreasing h_c for all the

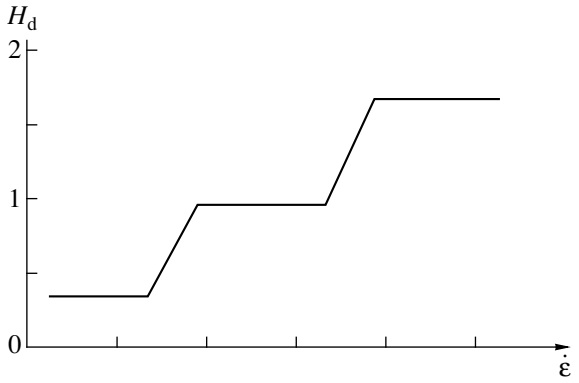

Fig. 7. Schematic diagram for the $H_d = f(\dot{\varepsilon})$ dependence in the presence of several competing deformation mechanisms. The horizontal segments correspond to the situation where the rate of stress relaxation by a mechanism dominating in a certain $\dot{\varepsilon}$ range is higher than the loading rate. The inclined segments appear when the characteristic times of relaxation processes are comparable with the loading time.

materials under study (except for fused silica) also supports this standpoint. Indeed, as the sizes of a locally deformed zone decrease, the probability of nucleation of dislocation loops should decrease and the time it takes for the required number of deformation carriers to form should increase, since point defects have higher nucleation activation energy.

Apparently, thermal-activation analysis of the strain-rate dependences of H_d obtained at various test temperatures will refine the mechanisms that are responsible for certain types of stress relaxation under an indenter.

CONCLUSIONS

We have determined the strain-rate sensitivities of the nanohardnesses of a number of ionic and covalent crystals, metals, metallic alloys, bulk amorphous metallic alloys, ceramics, and polymers. The effects of the scale and rate factors on the strain-rate sensitivities of the hardnesses of the materials have been separated. The critical indentation depths and relative-strain rates at which the strain-rate sensitivity of nanohardness begins to change have been found.

ACKNOWLEDGMENTS

This work was supported by the Russian Foundation for Basic Research (project no. 04-02-17198) and the Ministry of Education of the Russian Federation (project no. E02-3.4-263).

REFERENCES

1. S. M. Spearing, Acta Mater. **48**, 179 (2000).
2. Ch. Poole and F. Owens, *Introduction to Nanotechnology* (Wiley, Indianapolis, 2003).
3. G. Binning and H. Roher, Rev. Mod. Phys. **71**, 324 (1999).
4. G. Marsh, Materials Today **6** (2), 38 (2003).
5. K. Johnson, *Contact Mechanics* (Cambridge Univ. Press, Cambridge, 1987; Mir, Moscow, 1989).
6. E. N. Morozov and M. V. Zenin, *Contact Problems of the Fracture Mechanics* (Mashinostroenie, Moscow, 1999) [in Russian].
7. G. V. Dedkov, Usp. Fiz. Nauk **170**, 585 (2000) [Phys. Usp. **43**, 541 (2000)].
8. M. A. Shtremel', *Strength of Alloys* (MISIS, Moscow, 1997) [in Russian].
9. Yu. S. Boyarskaya, D. Z. Grabko, and M. S. Kats, *Physics of Microindentation* (Shtiintsa, Kishinev, 1986) [in Russian].
10. S. I. Bulychev and V. P. Alekhin, *Materials Testing by Continuous Indentation* (Mashinostroenie, Moscow, 1990) [in Russian].
11. N. A. Stelmashenko, M. G. Walls, L. M. Brown, and Yu. V. Milman, Acta Metall. Mater. **41**, 2855 (1993).
12. Q. Ma and D. R. Clarke, J. Mater. Res. **10**, 853 (1995).
13. K. W. McElhaney, J. J. Vlassak, and W. D. Nix, J. Mater. Res. **13**, 1300 (1998).
14. W. D. Nix and H. Gao, J. Mech. Phys. Solids. **46**, 411 (1998).
15. M. Atkinson, J. Mater. Sci. **30**, 1728 (1995).
16. W. C. Oliver and G. M. Pharr, J. Mater. Res. **7**, 1564 (1992).
17. W. C. Oliver and G. M. Pharr, J. Mater. Res. **19**, 3 (2004).
18. M. M. Chaudhri, J. K. Wells, and A. Stephens, Philos. Mag. A **43**, 643 (1981).
19. Yu. I. Golovin, Yu. L. Iunin, and A. I. Tyurin, Dokl. Akad. Nauk **392** (3), 1 (2003) [Dokl. Phys. **48**, 505 (2003)].
20. Yu. I. Golovin, V. I. Ivolgin, V. V. Korenkov, and A. I. Tyurin, Zh. Tekh. Fiz. **70** (5), 82 (2000) [Tech. Phys. **45**, 605 (2000)].
21. Yu. I. Golovin, *Introduction to Nanotechnology* (Mashinostroenie, Moscow, 2003) [in Russian].
22. Yu. I. Golovin, A. I. Tyurin, and B. Ya. Farber, Philos. Mag. A **82**, 1857 (2002).
23. Yu. I. Golovin, A. I. Tyurin, and B. Ya. Farber, J. Mater. Sci. **37**, 895 (2002).
24. Yu. I. Golovin and A. I. Tyurin, Materialovedenie, No. 1, 14 (2001); No. 2, 10 (2001).

Translated by K. Shakhlevich

Technical Physics, Vol. 50, No. 4, 2005, pp. 484–490. Translated from Zhurnal Tekhnicheskoĭ Fiziki, Vol. 75, No. 4, 2005, pp. 96–102.

RADIOPHYSICS

Interaction of Electromagnetic Waves with Iron–Chromium Multilayer Nanostructures

V. V. Ustinov, A. B. Rinkevich, and L. N. Romashev

Institute of Metal Physics, Siberian Division, Russian Academy of Sciences, ul. S. Kovalevskoĭ 18, Yekaterinburg, 620219 Russia

e-mail: rin@imp.uran.ru

Received June 22, 2004

Abstract—Interaction of traveling electromagnetic waves with MBE-grown Fe/Cr multilayer nanostructures is studied. Measurements are made in the frequency range 5.7–12.5 GHz at magnetic fields of up to 32 kOe. It is found that the dependence of the microwave transmission coefficient on the external magnetic field intensity is similar to the field dependence of the dc giant magnetoresistive effect. As a result of the interaction, the wavenumber varies in proportion to the electrical resistance of the structure. A simulation of the magnetic fields shows that the microwave currents flow largely across the multilayer nanostructure (normally to the layers). © *2005 Pleiades Publishing, Inc.*

INTRODUCTION

Investigation into the properties of metallic multilayer nanostructures is a topical problem of the physics of condensed matter. Interest in these materials is due to their unique spin-dependent transport properties, primarily, the giant magnetoresistive (GMR) effect. Owing to this effect, metallic nanoheterostructures seem promising for nanoelectronics and spintronics. Among the variety of methods used in studying materials of this class, rf electromagnetic techniques are viewed as the most important ones, since they make it possible to evaluate the dynamic and relaxation parameters of nanostructures.

Two basic mechanisms of interaction between electromagnetic waves and magnetic metallic nanostructures can be distinguished. One is related to magnetic moment precession, which acts on the waves. In this case, the interaction results in magnetic resonances, the energy losses being dependent on relaxation in the magnetic subsystem. The other mechanism is associated with eddy currents arising in the metallic nanostructure. Here, the GMP effect shows up explicitly, since Joule losses depend on the conductivity. This mechanism was discovered in [1, 2], where its physics and temperature dependence were studied. Via this mechanism, an external uniform magnetic field influences rf characteristics, giving rise to the microwave GMR (MGMR) effect.

Microwave studies of multilayer metallic nanostructures were pioneered by Krebs *et al.* [1], who performed experiments with Fe/Cr/Fe three-layer structures. The MGMR effect in $[Fe/Cr]_n$ metallic superlattices was first explored in [3] using an original technique of measuring the coefficient of microwave transmission through the nanostructure. For a thin metal plate, the transmission coefficient is inversely proportional to the effective conductivity. Consequently, a correlation between the relative magnetoresistance and transmission coefficient is bound to exist far away from ferromagnetic resonance frequencies and fields. In fact, such a single-valued correspondence was found in the centimeter [3, 4] and millimeter [5] ranges.

High-frequency methods of investigating nanostructures are of great value, since they allow for various orientations of the rf electric field relative to the sample surface plane. Accordingly, one can easily accomplish the configurations where the current passes both over and across the layers. The latter case is of special interest. Here, the electrons moving in a layered nanostructure (e.g., in a magnetic superlattice) repeatedly cross the interfaces, so that spin-dependent scattering by the interfaces is highlighted. In such a configuration of the current, the MGMR effect can be measured, e.g., by arranging the multilayer structure in a resonant cavity so that the variable electric field vector is normal to the surface plane of the structure [6]. The MGMR effect was found to define the dependence of the cavity losses on the external magnetic field [4, 7]. In [8], the microwave magnetoresistance of $[Fe/Cr]_n$ superlattices was measured for the case when the rf current passed in the plane of the layers.

The object of investigation in this work is a traveling electromagnetic wave, which interacts with Fe/Cr magnetic superlattices exhibiting the GMR effect. Experiments were designed in such a way that the current passed normally to the layers. It is shown that changes in the microwave transmission coefficient in absolute value may exceed the dc GMR effect. The influence of giant magnetoresistance on the traveling electromagnetic wave is simulated.

1063-7842/05/5004-0484$26.00 © 2005 Pleiades Publishing, Inc.

EXPERIMENTAL

The samples used were two $[Fe/Cr]_n$ superlattices and a Cr-coated thin Fe film all MBE-grown on 0.5-mm-thick (100)MgO single-crystal substrates in Katun'-S high-vacuum equipment. The growth rate was about 1.5 Å/min. The thickness of the Fe and Cr layers (including that of the Cr buffer layer), as well as the number of pairs of layers in the superlattices, are given in the table. Therein also shown are the values of saturation field H_s and relative dc magnetoresistance measured at H = 30 kOe. The microwave data were obtained from samples of length l = 22.5 mm and width 11.5 mm.

To take microwave measurements, the nanostructure was placed into a rectangular waveguide (Fig. 1) in such a way that the metallic side (film) of the sample was at the center of the waveguide and the longer side of the sample was parallel to the axis of the waveguide. External magnetic field **H** was applied either normally to wavevector Γ of the wave, parallel to the surface plane of the sample (as shown in Fig. 1), or perpendicularly to its surface plane. The measurements were taken at the H_{10} mode of the waveguide, with electric field vector $\mathbf{e}_0$ in the waveguide normal to the plane of the layers. The external field (30 kOe) was generated by an electromagnet. The experiments were carried out at room temperature.

EXPERIMENTAL RESULTS

In the microwave experiments, we determined the relative change in the magnitude of the microwave transmission coefficient, $r_m = [|D(H)| - |D(0)|]/|D(0)|$, where $|D(H)|$ is the magnitude of the transmission coefficient in magnetic field H. Typical field dependences $r_m(H)$ for the Fe/Cr superlattices are illustrated in Fig. 2a. The measurements were taken from superlattice 1 at frequencies f = 7.3, 7.5, and 7.7 GHz. The curves are seen to saturate at fields higher than 13 kOe. For this sample, the relative variation of the transmission coefficient may be appreciable, up to 10–30% according to the frequency. To confirm the fact that the transmission changes observed in the microwave experiments on the magnetic superlattices are due to the GMR effect, we measured $r_m(H)$ on samples where this effect is absent. Figure 2b shows the frequency dependence of the maximal change in the transmission coefficient measured on sample 3 (Cr-coated Fe film) in

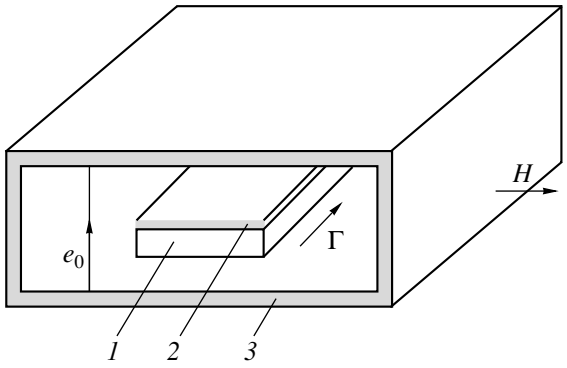

Fig. 1. Geometry of the experiment: (*1*) substrate, (*2*) superlattice, and (*3*) waveguide.

field H = 18 kOe. It is seen that the microwave variation of this parameter is insignificant, no more than 0.5%.

Figure 3 demonstrates the field dependences of dc relative magnetoresistance r/r_{max} and the microwave ratio $r_m/r_{m,\,max}$ measured at f = 11.87 GHz. The coincidence of these curves strongly intimates that the parameter variations at microwaves in the superlattices are associated with the field dependence of their magnetoresistance. For the Fe/Cr superlattices, these variations and the dc magnetoresistance are even functions of the magnetic field (Fig. 4). In addition, these field dependences taken for two configurations of external magnetic field **H** (the field vector is normal or parallel to the plane of the superlattice) are similar to each other. Figure 5 shows the field dependences of the dc magnetoresistance (Fig. 5a) and relative transmission coefficient measured at two frequencies (Fig. 5b). The curves demonstrate that both variations are related to the magnetic field in the material, the intensity of which differs from the external field intensity, since the sample exerts the demagnetizing action.

The experimental data mentioned above suggest that the variation of the microwave transmission coefficient can be attributed to the GMR effect. It should be noted that the relative variations at microwaves may exceed the relative dc magnetoresistance by a factor of two or more. Moreover, the microwave variations may be of different signs at different frequencies of the electromagnetic wave (Fig. 5b). This fact, earlier noticed in [9], was considered as the alternating-sign GMR effect. A property of spin-dependent magnetotransport is that a change in the conductivity in an applied field is always positive. Experimenting with a finite-length

Characterization of the samples

Sample no.	Sample type	Thickness of layers	H_s, kOe	r (30 kOe), %
1	Superlattice	$[Cr(13\ Å)/Fe(24\ Å)]_8/Cr(82\ Å)/MgO$	12.0	–12.4
2	"	$[Cr(12\ Å)/Fe(23\ Å)]_{16}/Cr(77\ Å)/MgO$	12.6	–16.0
3	Cr-coated Fe film	$Cr(10\ Å)/Fe(573\ Å)/Al_2O_3$	≈0.03	–

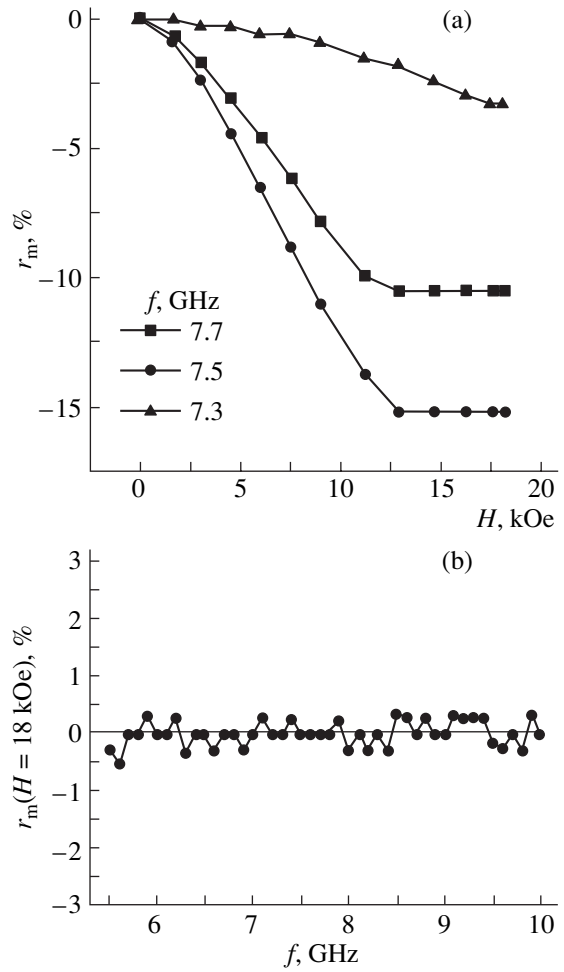

Fig. 2. (a) Relative change in the transmission coefficient in the magnetic field for superlattice 1 at various frequencies and (b) frequency dependence of the microwave changes at $H = 18$ kOe for sample 3.

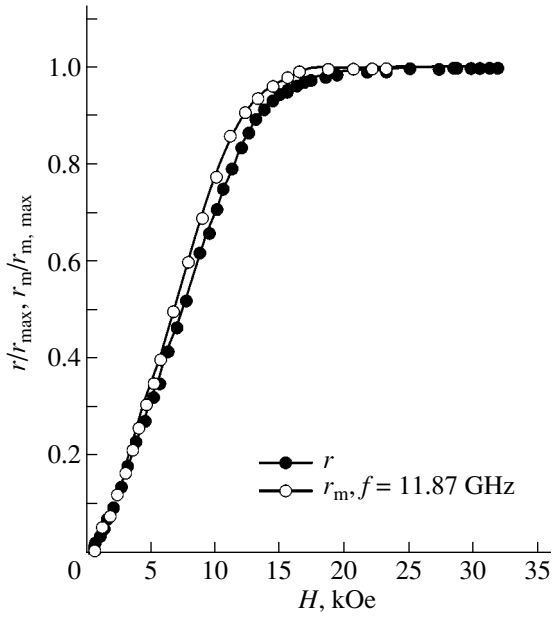

Fig. 3. Variation of the change in microwave transmission coefficient r_m in comparison with the variation of relative magnetoresistance *r* (superlattice 2).

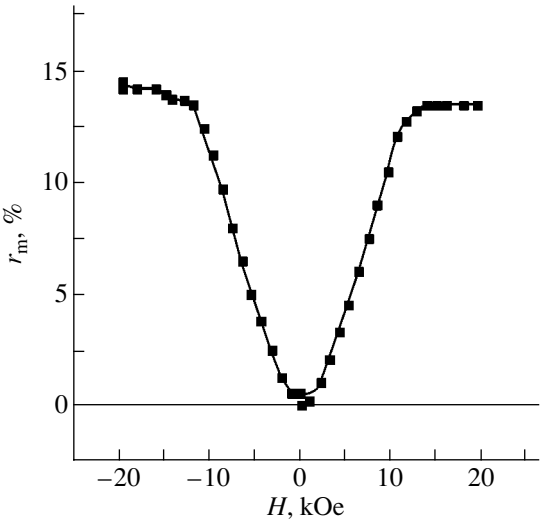

Fig. 4. Relative variation of the transmission coefficient with alternating-sign external magnetic field (sample 1, $f =$ 8.9 GHz).

sample and varying the frequency of the wave, we merely set up conditions under which microwave changes may be either positive or negative.

Figure 6 demonstrates the frequency dependences of r_m that were measured in field $H = 18$ kOe on superlattices of type 2 with different lengths. The filled triangles refer to the 22.5-mm-long sample. It is seen that the microwave variations are of alternating sign and exhibit a distinct minimum near $f = 7.9$ GHz. This minimum corresponds to half-wave resonance (see below), when the sample length accommodates half the wavelength. The sample was shortened twice in such a way that its length equaled first 18.3 mm (empty circles in Fig. 6) and then 13.8 mm (filled circles). With decreasing the length, the minimum in the curve $r_m(f)$ shifted toward higher frequencies. The vertical bars in Fig. 6 show the predicted positions of the resonance for mode H_{10} in the sample of a given length. From the coincidence of the resonance frequencies predicted theoretically with those of the minima in the experimental curves $r_m(f)$, we can conclude that the well-defined dips in Fig. 6 do correspond to half-wave resonance.

After making the microwave measurements on the shortened sample, the three pieces were added together to recover the initial length (22.5 mm) of the sample. Importantly, no care was taken to provide electrical contact between the pieces. The results of microwave measurements on this "composite" sample are shown in Fig. 6 by empty squares. It turned out that the minimum in the curve $r_m(f)$ again (as for the intact sample) lies at

$f \approx 7.9$ GHz. If the sample-containing part of the waveguide is viewed as a resonance system with a minimum in the curve $r_m(f)$, the width of the curve (resonance peak) gives the "Q factor" $Q_0 = 17$ for the initial (intact) sample and $Q_1 = 21$ for the composite sample.

SIMULATION OF THE INFLUENCE OF THE GMR EFFECT ON TRAVELING ELECTROMAGNETIC WAVES

The basic goal of simulation was to reveal interplay between the parameters of the multilayer nanostructures exhibiting the GMR effect and the variation of the wave transmission coefficient. For centimeter electromagnetic waves, skin depth δ in the nanostructures studied is much smaller than the total thickness of metal in the film. Then, the multilayer structure may be characterized by an effective conductivity. In other words, the nanostructure may be considered as a homogeneous metallic plate with conductivity σ [4]. We will restrict our analysis to the range of off-resonance frequencies and magnetic fields and consider the contribution from the GMR effect alone.

In the simulation that follows, we will assume that the width of the sample on which the transmission coefficient magnitude is measured in a magnetic field is equal to width a of the wider wall of the waveguide (the narrower wall of the waveguide is b wide) and its length is l. The process of simulation is subdivided into three stages. First, from a solution to the Helmholtz equation subject to boundary conditions, we find the structure of the rf electric, **e**, and magnetic, **h**, fields and determine a correction to the wavenumber in terms of the perturbation theory. Then, the effective wave impedance of the waveguide with the sample is found. Finally, the effective transmission coefficient and its dependence on the applied magnetic field are calculated.

The structures of fields **e** and **h** in the waveguide with the sample are found by parting the waveguide into three domains. Let us calculate corrections to the fields and to the wavenumber of mode H_{10}, at which measurements are made. The empty domains above and below the sample will be referred to as domains I and III; the central domain (occupied by the sample), as domain II. The distributions of the fields in domains I and III are given by the well-known expressions [10]

$$\begin{aligned} \mathbf{e} &= y_0 e_0 \sin\frac{\pi x}{a} e^{-i\Gamma z}, \\ \mathbf{h} &= \frac{e_0}{W}\left(-x_0 \sin\frac{\pi x}{a} + z_0 \frac{i}{\Gamma}\frac{\pi}{a}\cos\frac{\pi x}{a}\right)e^{-i\Gamma z}, \end{aligned} \tag{1}$$

where x_0, y_0, and z_0 are the unit vectors of the coordinate system. The x, y, and z axes are directed along the wider wall, narrower wall, and waveguide axis, respectively.

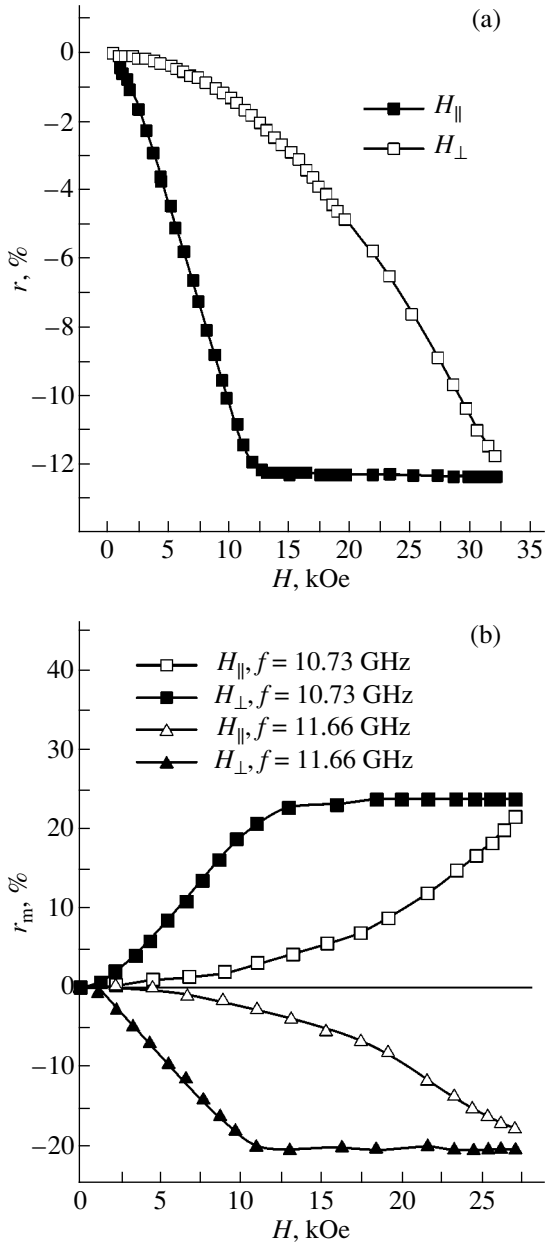

Fig. 5. Field dependences of (a) the relative magnetoresistance and (b) microwave transmission coefficient that were taken in the external field oriented parallel to the sample surface plane (filled symbols) and normally to the sample plane (empty symbols).

In Eqs. (1), e_0 is the amplitude factor and W is the equivalent impedance of the waveguide. The wavenumbers in the absence and presence of the sample are denoted by Γ_0 and Γ_1, respectively, where

$$\Gamma_0 = \frac{\omega}{c}\left[1 - \left(\frac{c}{2af}\right)^2\right]^{1/2}. \tag{2}$$

Electric field **e** in domain II (inside the metal of the nanostructure) is described by the expression that fol-

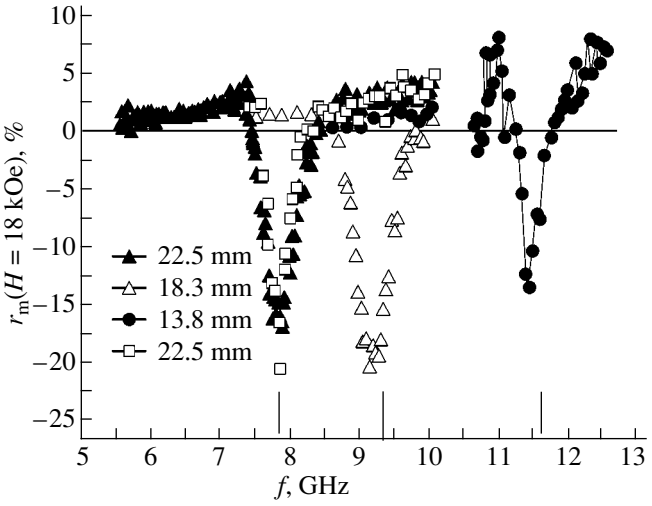

Fig. 6. Frequency dependence of the change in the microwave transmission coefficient for the $[Cr(12\ Å)/Fe(23\ Å)]_{16}/Cr(77\ Å)/MgO$ superlattices of different length.

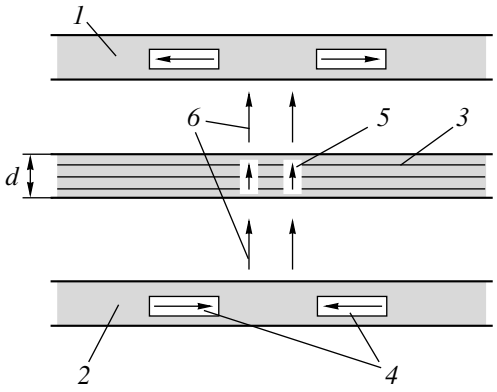

Fig. 7. Passage of the microwave currents. (*1*) Upper wall of the waveguide, (*2*) lower wall of the waveguide, (*3*) superlattice, (*4*) conduction currents in the walls, (*5*) conduction currents in the sample, and (*6*) displacement currents.

lows from the results obtained in [4, 7],

$$\mathbf{e} = y_0 e_0 \sin\frac{\pi x}{a} e^{-i\Gamma z} \times\left\{q\left[e^{\frac{-y-0.5(b-d)}{z_D}} + e^{\frac{y-0.5(b-d)}{z_D}}\right] + 2(1-q)\right\}, \quad (3)$$

where $q = (\omega_0 z_D/v_F)^2$, z_D is the complex screening parameter, ω_0 is the plasma frequency, and v_F is the Fermi velocity.

Equation (3) takes into account the fact that the conventional skin effect makes room for a dynamic analogue of electrostatic screening if thickness d of the metal far exceeds skin depth δ and the electric field vector runs normally to the boundary. Along with the bracketed components, which decay in the metal, expression (3) involves the y-independent term, the penetrating component of the field. Unlike the formulas derived in [4, 7], Eq. (3) contains the fields at two boundaries of the film in explicit form and joins together solutions for the three domains.

To calculate a correction to the wavenumber, we apply the perturbation theory to a waveguide with a magnetically polarized sample [11]. If cross-sectional area S_1 of the sample is much smaller than cross-sectional area S_0 of the waveguide, the change in the wavenumber is given by

$$\Delta\Gamma = \frac{\omega W}{2N_0}\int_{S_1} \mathbf{e}_{0m}\cdot\overleftrightarrow{\Delta\varepsilon}\mathbf{e}_m dS, \qquad N_0 = \int_{S_0}|\mathbf{e}_{0m\perp}|^2 dS. \quad (4)$$

Here, $\omega = 2\pi f$ and $\mathbf{e}_{0m}$ and $\mathbf{e}_m$ are the complex amplitudes of the electric field in the unperturbed and sample-perturbed waveguide, respectively. Change $\overleftrightarrow{\Delta\varepsilon}$ in the permittivity tensor is explained as follows. In the absence of the sample, this tensor is diagonal with nonzero components equal to ε_0. In the presence of the sample without the external magnetic field, the nonzero components are $\varepsilon_{11} = \varepsilon_{22} = \varepsilon_{33} = -i\sigma/\omega$. In the presence of the magnetic field, along with diagonal components $-i\sigma(H)/\omega$, there appear off-diagonal components $\varepsilon_{12} = -\varepsilon_{21} = i\sigma_a(H)/\omega$. In (4), only the interaction due to the change in the conductivity is taken into account. Such a simplification works if the changes in the permittivity tensor are insignificant.

We will perform calculations using formula (4) for frequencies much lower than the plasma frequency, $\omega \ll \omega_0$. Then [4],

$$z_D \approx r_D\left(1 - \frac{\omega^2}{\omega_0^2} + i\frac{\omega\nu}{\omega_0^2}\right), \quad r_D = v_F/\omega_0, \qquad q \approx 1 - 2\frac{\omega^2}{\omega_0^2} + 2i\frac{\omega\nu}{\omega_0^2}, \quad (5)$$

where r_D is the Debye screening length and ν is the electron relaxation frequency.

When the sample is placed in a waveguide without a magnetic field, both the real and imaginary parts of the wavenumber change,

$$\mathrm{Re}(\Gamma_1 - \Gamma_0) = -\varepsilon_0\omega W\left[\frac{r_D}{b} - 2\frac{d}{b}\left(\frac{\omega^2}{\omega_0^2} - \frac{\sigma\nu}{\varepsilon_0\omega_0^2}\right)\right], \quad (6a)$$

$$\mathrm{Im}(\Gamma_1 - \Gamma_0) = -\varepsilon_0 \omega W\left[\frac{\sigma}{\omega\varepsilon_0}\frac{r_D}{b} + 2\frac{d}{b}\left(\frac{\omega\nu}{\omega_0} - \frac{\sigma\omega}{\varepsilon_0\omega_0^2}\right)\right]. \quad (6b)$$

In a magnetic field, the wavenumber is given by

$$\Gamma_1(H) - \Gamma_1 = -iW\frac{2d}{b}\left[1 - 3\frac{\omega^2}{\omega_0^2} + i(\nu_H - \nu)\frac{\omega}{\omega_0^2}\right][\sigma(H) - \sigma], \quad (7)$$

where ν_H is the electron relaxation frequency in magnetic field H.

Formula (7) is valid for the tangential and normal magnetization of the film by the applied field if H is taken to mean the field strength in the film. It follows from this formula that the imaginary part of the change in the wavenumber, which is responsible for energy dissipation, is proportional to the change in the conductivity of the film in a magnetic field.

The reflections of the wave from the ends of the sample with finite length l depend on the ratio between the equivalent impedances of the waveguide with (Z) and without (Z_0) the sample. According to [10, 12], the equivalent impedances are expressed as

$$Z = \frac{\pi}{2}\frac{b}{a}W, \quad Z_0 = \frac{\pi}{2}\frac{b}{a}W_0.$$

Here, W and W_0 are the characteristic impedances introduced for mode H_{10},

$$W_0 = \frac{120\pi}{\sqrt{1 - \left(\frac{c}{2af}\right)^2}}, \quad W = W_0\left[1 - \frac{\Gamma(H) - \Gamma_0}{\Gamma_0}\right].$$

Let ξ designate the relative change in the impedance,

$$\frac{Z - Z_0}{Z_0} = -\frac{\Gamma_1(H) - \Gamma_0}{\Gamma_0} = \xi. \quad (8)$$

Complex transmission coefficient D can be calculated by the formula [13]

$$D = \frac{2ZZ_0}{2ZZ_0\cos\varphi - i(Z^2 - Z_0^2)\sin\varphi}, \quad (9)$$

where φ is the sample-induced phase shift ($\varphi = \Gamma_1 l$).

Magnitude $|D|$ of the transmission coefficient is determined from experimental data. It is calculated by formula (9) in view of (8) for a small variation of the wave impedance, $|\xi| \ll 1$. Separating out the real and imaginary parts, i.e., representing ξ as $\xi = \xi' + i\xi''$, we get

$$|D| = 1 - (\xi'^2 + \xi''^2)\sin\varphi - \xi'\xi''\sin 2\varphi. \quad (10)$$

Thus, having performed the simulation, we established a relationship between the microwave magnetoresistance of the structure and the transmission coefficient.

DISCUSSION

The experimental data presented in Figs. 3–5 strongly suggest that a change in the microwave transmission coefficient in a magnetic field is due to the GMR effect. Indeed, magnetoresistance r and microwave transmission coefficient r_m vary identically with the field. Both variations are even functions of **H** and similar functions of the magnetic field strength in the multilayer nanostructure (the field strength in the sample may differ from the applied field strength because of the presence of demagnetizing fields). The calculation shows that the change in the wavenumber is proportional to the change in the conductivity due to the GMR effect. As follows from formula (7), the off-diagonal components of the conductivity tensor, which are responsible for the Hall effect, make no contribution to the microwave changes in the given arrangement of the sample (Fig. 1). With formulas (7), (8), and (10), it is easy to check that, when the relative change in the wave impedance is small ($|\xi| \ll 1$), the relative change in the transmission coefficient is also proportional to the GMR-induced change in the conductivity, provided that the effective microwave conductivity varies with the magnetic field in the same way as the dc conductivity. The experimental data shown in Figs. 3–5, as well as earlier data [3–6], suggest that what has been said for the effective conductivity of the Fe/Cr nanostructures is valid for the millimeter and centimeter ranges. Note that the calculation of microwave changes by formula (10) requires that the sample be the only essential inhomogeneity in the microwave channel.

The frequency dependence of the microwave changes to a great extent depends on the amount of half-wave resonance in the sample. The measurements of the resonance frequency in samples of different lengths (Fig. 6) showed that operating mode H_{10} persists when the nanostructure is placed in the waveguide. This circumstance is of importance for finding the direction of microwave currents in the structure. In fact, electric field vector **e** of mode H_{10} is normal to the surface plane of the sample and, hence, to the layers. The total thickness of the metal in the nanostructure is much smaller than skin depth δ but exceeds Debye screening length r_D. Under these conditions, the electric field in the metal is of form (3) [4] and contains both the damped and penetrating components. The microwave currents flow normally to the layers of the nanostructure. The measurements shown in Fig. 6 corroborate such a statement. The values of the Q factors ($Q_0 = 17$ for the intact 22.5-mm-long sample placed in the waveguide and $Q_1 = 21$ for the sample of the same length composed of three electrically disconnected

pieces) are noteworthy. In the composite sample, each of the pieces is much shorter than half the wavelength and the currents can hardly pass over the plane of the sample, i.e., along the layers of the nanostructure. In the intact sample, in-plane currents exist. From the values of the Q factors, one can estimate the powers released by variously oriented microwave currents. The current passing normally to the layers is responsible for about 88% the total power released. The scheme of microwave current passage is illustrated in Fig. 7. Shown is only the current component that is normal to the layers. Displacement currents existing in the empty domains of the waveguide transform into conductivity currents in the nanostructure.

CONCLUSIONS

Interaction between a traveling electromagnetic wave and a metallic multilayer nanostructure was investigated. It was found that the GMR effect makes the microwave transmission coefficient dependent on the applied magnetic field strength. The interaction of centimeter-range traveling electromagnetic waves with MBE-grown $[Fe/Cr]_n$ superlattices was studied in greater detail. It was shown the microwave currents pass largely normally to the layers. The frequency dependence of the microwave changes demonstrates that the changes may exceed the relative dc giant magnetoresistance.

The variation of the wavenumber due to the GMR effect was simulated. The imaginary part of the change in the wavenumber varies in proportion to the change in the conductivity of the metallic structure in a magnetic field. It was shown that the off-diagonal components give no contribution to the microwave changes at the field configuration studied in the article. The coefficient of transmission of electromagnetic waves through the multilayer structure was calculated.

ACKNOWLEDGMENTS

This work was partially supported by the Russian Foundation for Basic Research (grant no. 04-02-16464), the Program in Support of Leading Scientific Schools (grant NSh-1380.2003.2), and the program the "Quantum Macrophysics" (Russian Academy of Sciences).

REFERENCES

1. J. J. Krebs, P. Lubitz, A. Chaiken, and G. A. Prinz, J. Appl. Phys. **69**, 4795 (1991).
2. B. K. Kuanr, A. V. Kuanr, P. Grunberg, and G. Nimtz, Phys. Lett. A **221**, 245 (1996).
3. V. V. Ustinov, A. B. Rinkevich, L. N. Romashev, and V. I. Minin, J. Magn. Magn. Mater. **177–181**, 1205 (1998).
4. A. B. Rinkevich, L. N. Romashev, and V. V. Ustinov, Zh. Éksp. Teor. Fiz. **117**, 960 (2000) [JETP **90**, 834 (2000)].
5. Z. Frait, P. Sturc, K. Temst, *et al.*, Solid State Commun. **11**, 569 (1999).
6. V. V. Ustinov, A. B. Rinkevich, and L. N. Romashev, J. Magn. Magn. Mater. **198–199**, 82 (1999).
7. V. V. Ustinov, A. B. Rinkevich, L. N. Romashev, *et al.*, Fiz. Met. Metalloved. **93** (5), 31 (2002).
8. V. V. Ustinov, A. B. Rinkevich, L. N. Romashev, and D. V. Perov, Zh. Tekh. Fiz. **74** (5), 94 (2004) [Tech. Phys. **49**, 613 (2004)].
9. A. B. Rinkevich, L. N. Romashev, V. V. Ustinov, and E. A. Kuznetsov, in *Proceedings of the 9th International Workshop "Challenging Problems of Nanocrystalline Materials: Science and Fabrication," Yekaterinburg, 2002*, p. 169.
10. V. V. Nikol'skiĭ and T. I. Nikol'skaya, *Electrodynamics and RF Wave Propagation* (Nauka, Moscow, 1989) [in Russian].
11. A. G. Gurevich, *Magnetic Resonance in Ferrites and Antiferromagnets* (Nauka, Moscow, 1973) [in Russian].
12. I. V. Lebedev, *Microwave Technology and Devices* (Vysshaya Shkola, Moscow, 1970), Vol. 1 [in Russian].
13. L. M. Brekhovskikh and O. A. Godin, *Acoustics of Layered Media* (Nauka, Moscow, 1989; Springer-Verlag, New York, 1990).

Translated by V. Isaakyan

Technical Physics, Vol. 50, No. 4, 2005, pp. 491–497. Translated from Zhurnal Tekhnicheskoĭ Fiziki, Vol. 75, No. 4, 2005, pp. 103–108.

ELECTRON AND ION BEAMS, ACCELERATORS

Kinetic Approach to the Envelope Equation for a Relativistic Electron Beam Propagating through a Scattering Gas–Plasma Medium in the Presence of the Reverse Plasma Current with an Arbitrary Radial Profile

A. S. Manuĭlov

Smirnov Institute of Mathematics and Mechanics, St. Petersburg State University, St. Petersburg, 198504 Russia

e-mail: Kolesnikov_evg@mail.ru

Received April 29, 2004

Abstract—A kinetic approach is applied to derive the transport equations, the virial equation, the dynamic-equilibrium equation, and the envelope equation for an axially symmetric paraxial relativistic electron beam propagating through a scattering gas–plasma medium in the presence of a reverse plasma current with a radial density profile that is generally different from the beam density profile. The equations obtained include additional terms that account for this difference. © *2005 Pleiades Publishing, Inc.*

INTRODUCTION

In recent years, the problem of the transportation of relativistic electron beams (REBs) through dense gas–plasma media has attracted considerable interest [1–27]. An important aspect of this problem is the transverse evolution of the beam in the scattering background gas.

Since the process of REB propagation in a gas–plasma medium is highly nonequilibrium and is strongly affected by the collective electromagnetic field induced by the charges and currents of the plasma and beam, it is reasonable to construct the REB transportation model on the basis of the kinetic Vlasov–Boltzmann equation with a self-consistent field and the equations for the moments of the distribution functions for the beam particles and phase averages. In the general case, these models should account not only for the self-consistent field, but also for the action of external electromagnetic fields on the beam particles and for the scattering of these particles by the particles of the background gas.

In this paper (in contrast to the previous studies [6–12, 20–25]), the basic equations describing the transverse dynamics of a paraxial monoenergetic REB are derived for the case where the radial profile of the reverse plasma current, $J_{pz}(\mathbf{r}_\perp)$, differs from the radial profile of the beam current density, $J_{bz}(\mathbf{r}_\perp)$. This assumption substantially complicates the derivation of the equations describing the REB transverse dynamics (including the derivation of the envelope equation with the use of the kinetic equation).

It should be noted that the generation of the reverse plasma current after the injection of an REB into a high-density gas, as well as the radial structure of this current, has been studied both experimentally and theoretically [13–19]. It was shown that, in many cases, the radial profile of the reverse plasma current differs from that of the beam current (i.e., the above assumption is well justified).

In contrast to [6, 22–25], we will also assume that complete charge neutralization takes place. In dense gas–plasma media, this is true at sufficiently high values of scalar conductivity σ, when the following condition is satisfied:

$$\tau_c \ll \tau_m, \tag{1}$$

where $\tau_c = (4\pi\sigma)^{-1}$ is the time of charge neutralization and $\tau_m = 4\pi\sigma R_b^2/c^2$ is the skin time (the decay time of the equilibrium reverse plasma current). Here, R_b is the characteristic beam radius and c is the speed of light.

It is known (see [6, 23, 24]) that, in the paraxial approximation, the longitudinal motion of the REB particles is deterministic, whereas their distribution over transverse momenta and coordinates is stochastic and is described by the proper kinetic equation.

In what follows, we restrict ourselves to the practically interesting case of an azimuthally symmetric paraxial beam whose axis is directed along the beam propagation direction and coincides with the z axis of a cylindrical coordinate system.

By analogy to [6–8], we represent the beam as a set of thin transverse segments S^τ, each of which contains a fixed number of particles. The upper index indicates the instant $t = \tau$ at which the segment is injected.

1063-7842/05/5004-0491$26.00

We assume that all the particles within a given segment have the same relativistic masses $m\gamma$ and the same longitudinal velocities $v_z = \beta c$ (the spread in γ within the segment is ignored); i.e., the injected beam is monoenergetic. It is also assumed that the medium through which the beam propagates is uniform. Under these assumptions, all the particles within a segment S^τ evolve in a similar manner along the z coordinate and, at an arbitrary instant, have the same energies $E(t)$ and the same relativistic masses $m_r = m\gamma = E(t)/c^2$. Note that segments S^τ do not intersect one another during the beam propagation [6, 24, 25].

We introduce the distribution function $f^\tau(\mathbf{r}_\perp, \mathbf{p}_\perp, t)$, which describes the distribution of particles over transverse coordinates $\mathbf{r}_\perp$ and momenta $\mathbf{p}_\perp$ within a segment S^τ. The time evolution of this function is described by the kinetic equation

$$\frac{\partial f^\tau}{\partial t} + \frac{\mathbf{p}_\perp}{\gamma m} \cdot \nabla_{\mathbf{r}_\perp} f^\tau + \mathbf{F}_\perp \cdot \nabla_{\mathbf{p}_\perp} f^\tau = I_{sc}, \qquad (2)$$

where $\mathbf{F}_\perp$ is the transverse component of the force exerted on a particle by the collective self-consistent electromagnetic field of the plasma–beam system and I_{sc} is the collision integral.

Under the conditions of complete charge neutralization, we have

$$\mathbf{F}_\perp = q\beta\nabla_{\mathbf{r}_\perp} A_z(t, \mathbf{r}_\perp), \qquad (3)$$

where q is the charge of a beam particle, $\beta = v_z/c$, and $A_z(t, \mathbf{r}_\perp)$ is the solution to equation

$$\nabla_{\mathbf{r}_\perp} A_z = -\frac{4\pi}{c}(J_{bz}(t, \mathbf{r}_\perp) + J_{pz}(t, \mathbf{r}_\perp)). \qquad (4)$$

This solution has the form

$$A_z(t, \mathbf{r}_\perp) = A_z^{(b)}(t, \mathbf{r}_\perp) + A_z^{(p)}(t, \mathbf{r}_\perp), \qquad (5)$$

where

$$A_z^{(b)}(t, \mathbf{r}_\perp) = -\frac{2}{c}\int J_{bz}(t, \mathbf{r}'_\perp)\ln\left|\frac{\mathbf{r}_\perp - \mathbf{r}'_\perp}{R_c}\right| d\mathbf{r}'_\perp, \qquad (6)$$

$$A_z^{(p)}(t, \mathbf{r}_\perp) = -\frac{2}{c}\int J_{pz}(t, \mathbf{r}'_\perp)\ln\left|\frac{\mathbf{r}_\perp - \mathbf{r}'_\perp}{R_c}\right| d\mathbf{r}'_\perp \qquad (7)$$

are the axial components of the vector potential resulting from the beam current and the reverse plasma current, respectively. Here, R_c is the radius of the screening of the collective electromagnetic field by the background plasma (i.e., it is assumed that the condition $A_z|_{r_\perp \geq R_c} = 0$ is satisfied).

When multiple small-angle Coulomb scattering dominates, the collision integral in Eq. (2) can be written in the form [6, 26]

$$I_{sc} = \frac{m\gamma S}{2}\Delta_{\mathbf{p}_\perp} f^\tau. \qquad (8)$$

Here, the quantity S characterizes the average rate of change in the transverse kinetic energy of a beam particle, $E_\perp = p_\perp^2/(2m\gamma)$, due to multiple Coulomb scattering. For a given scattering medium, this quantity is a known function of the total particle energy $E = m\gamma c^2$. Note that collision integral (8) is a particular case of the Fokker–Planck collision integral [6, 26] in which transport over the transverse momentum $\mathbf{p}_\perp$ is zero in view of the scattering isotropy and the tensor of the generalized diffusion coefficient is diagonal and independent of them transverse momentum $\mathbf{p}_\perp$ in view of the isotropy and elastic nature of scattering.

To close the set of Eqs. (2)–(8) requires an additional equation that relates the plasma current density $J_{pz}(\mathbf{r}_\perp)$ to the beam current density $J_{bz}(\mathbf{r}_\perp)$.

In contrast to [6, 24, 25], we cannot represent the density of the reverse plasma current in the form

$$J_{pz}(\mathbf{r}_\perp) = -\alpha_m J_{bz}(\mathbf{r}_\perp),$$

where α_m is the coefficient of the current (magnetic) neutralization, which was considered to be independent of $\mathbf{r}_\perp$ in the studies cited above (i.e., J_{pz} and J_{bz} had the same radial profiles with the same characteristic transverse radii).

For a distribution function f^τ normalized to unity ($f^\tau(\int f^\tau d\mathbf{r}_\perp d\mathbf{p}_\perp = 1)$), the current density is defined by the expression

$$J_{nz}(\mathbf{r}_\perp, t) = I_b(t)\chi_b(\mathbf{r}_\perp, t), \qquad (9)$$

where $I_b(t)$ is the total beam current and

$$\chi_b(\mathbf{r}_\perp, t) = \int f^\tau(\mathbf{r}_\perp, \mathbf{p}_\perp, t) d\mathbf{p}_\perp \qquad (10)$$

is the spatial density of the beam particles normalized to the number of particles N_0 within a segment S^τ.

The density of the reverse plasma current $J_{pz}(\mathbf{r}_\perp, t)$ can be determined from the equation [27]

$$\frac{\partial J_{pz}}{\partial t} + \frac{J_{pz}}{\tau_m} = \frac{\partial J_{bz}}{\partial t}, \qquad (11)$$

where τ_m is the monopole skin time.

For the sake of convenience, J_{pz} can be represented in a form similar to Eq. (9):

$$J_{pz}(\mathbf{r}_\perp, t) = I_p(t)\chi_p(\mathbf{r}_\perp, t), \qquad (12)$$

where $I_p(t)$ is the total reverse plasma current and $\chi_p(\mathbf{r}_\perp, t)$ is the density of plasma particles normalized to the number of plasma particles within a beam segment S^τ.

It can readily be seen that the solution to Eq. (11) has the form

$$J_{pz}(\mathbf{r}_\perp, t) = I_p(t)\chi_p(\mathbf{r}_\perp, t) = -\int_{-\infty}^{t} \frac{\partial(\chi_b I_b)}{\partial t'} \exp\left[\int_t^{t'} \frac{dt''}{\tau_m(t'')}\right]. \quad (13)$$

With allowance for expressions (3), (5), and (8), kinetic equation (2) can be written as

$$\frac{\partial f^\tau}{\partial t} + \frac{\mathbf{p}_\perp}{m\gamma}\cdot\nabla_{\mathbf{r}_\perp} f^\tau + [q\beta\nabla_{\mathbf{r}_\perp}(A_z^{(b)} + A_z^{(p)})]\cdot\nabla_{\mathbf{r}_\perp} f^\tau = \frac{\gamma m S}{2}\nabla_{\mathbf{p}_\perp} f^\tau, \quad (14)$$

where the potentials $A_z^{(b)}$ and $A_z^{(p)}$ are defined by Eqs. (6) and (7).

TRANSPORT EQUATIONS

From Eq. (14), one can obtain the equations for the first moments of the distribution function f^τ, which define the main macroscopic characteristics of the beam.

Integrating Eq. (14) over transverse momenta yields the equation

$$\frac{\partial \chi_b}{\partial t} + \nabla_\perp\cdot\left(\chi_b\frac{\tilde{\mathbf{p}}}{\gamma m}\right) = 0, \quad (15)$$

where $\chi_b(\mathbf{r}_\perp, t)$ is the particle density in a segment S^τ (see Eq. (10)), $\nabla_\perp \equiv \nabla_{\mathbf{r}_\perp}$, and

$$\tilde{\mathbf{p}}_\perp(\mathbf{r}_\perp, t) = \frac{1}{\chi_b}\int \mathbf{p}_\perp f^\tau d\mathbf{p}_\perp \quad (16)$$

is the average transverse momentum.

In view of the fact that $\tilde{\mathbf{p}}_\perp/m\gamma = \tilde{\mathbf{v}}_\perp$ (where $\tilde{\mathbf{v}}_\perp$ is the average transverse velocity of the beam particles), Eq. (15) is nothing more than a conventional continuity equation, which describes the conservation of the number of particles within a given segment.

Multiplying Eq. (14) by $\mathbf{p}_\perp$ and integrating over transverse momenta, we obtain the transport equation for the transverse momentum,

$$\frac{\partial}{\partial t}(\chi_b\tilde{\mathbf{p}}_\perp) + \nabla_\perp\cdot\left(\chi_b\frac{\widetilde{\mathbf{p}_\perp\mathbf{p}_\perp}}{\gamma m}\right) - \chi_b q\beta\nabla_\perp(A_z^{(b)} + A_z^{(p)}) = 0, \quad (17)$$

where

$$\chi_b\widetilde{\mathbf{p}_\perp\mathbf{p}_\perp} = \int f^\tau(\mathbf{r}_\perp, \mathbf{p}_\perp, t)\mathbf{p}_\perp\mathbf{p}_\perp d\mathbf{p}_\perp. \quad (18)$$

With allowance for Eq. (15), Eq. (17) takes the form

$$\left(\frac{\partial}{\partial t} + \tilde{\mathbf{v}}_\perp\cdot\nabla_\perp\right)\mathbf{p}_\perp = -\frac{\nabla_\perp\cdot\tilde{\tilde{\mathbf{p}}}_\perp}{\chi_b} - q\mathbf{E}_\perp^{\text{eff}}, \quad (19)$$

where $\mathbf{E}_\perp^{\text{eff}} = \nabla_\perp(\beta A_z^{(b)} + \beta A_z^{(p)})$ is the transverse component of the effective electric field and

$$\tilde{\tilde{\mathbf{p}}}_\perp = \int(\mathbf{p}_\perp - \tilde{\mathbf{p}}_\perp)(\mathbf{v}_\perp - \tilde{\mathbf{v}}_\perp) f^\tau d\mathbf{p}_\perp \quad (20)$$

is the stress tensor.

Finally, multiplying Eq. (14) by $p_\perp^2/2m\gamma$ and integrating over transverse momenta, we obtain the energy transfer equation

$$\frac{\partial}{\partial t}\left(\chi_b\frac{\tilde{p}_\perp^2}{2m\gamma}\right) + \frac{1}{\gamma}\frac{d\gamma}{dt}\frac{\chi_b p_\perp^2}{2m\gamma} + \nabla_\perp\cdot\left(\chi_b\frac{\widetilde{\mathbf{p}_\perp p_\perp^2}}{2m^2\gamma^2}\right) - q\beta\nabla_\perp(A_z^{(b)} + A_z^{(p)})\cdot\frac{\chi_b\tilde{\mathbf{p}}_\perp}{m\gamma} = \chi_b S, \quad (21)$$

where

$$\chi_b\tilde{p}_\perp^2 = \int f^\tau p_\perp^2 d\mathbf{p}_\perp, \quad (22)$$

$$\chi_b\widetilde{\mathbf{p}_\perp p_\perp^2} = \int f^\tau \mathbf{p}_\perp p_\perp^2 d\mathbf{p}_\perp. \quad (23)$$

The third term on the left-hand side of Eq. (21) characterizes the rate of change in the average energy of the transverse motion of particles in a segment S^τ in the presence of an energy flow with a density

$$\Re_0 = \frac{\chi_b\widetilde{\mathbf{p}_\perp p_\perp^2}}{2m^2\gamma^2} = \frac{\chi_b\widetilde{\mathbf{v}_\perp p_\perp^2}}{2m\gamma}. \quad (24)$$

The fourth term on the left-hand side of Eq. (21) can be represented in the form

$$-\frac{q\beta\chi_b\tilde{\mathbf{p}}_\perp}{m\gamma}\cdot\nabla_\perp(A_z^{(b)} + A_z^{(p)}) = \mathbf{J}_\perp\cdot\mathbf{E}_\perp^{\text{eff}}, \quad (25)$$

where $\mathbf{J}_\perp = -q\chi_b\tilde{\mathbf{p}}_\perp/m\gamma = -q\chi_b\tilde{\mathbf{v}}_\perp$ and $\mathbf{E}_\perp^{\text{eff}}$ is the transverse component of the effective electric field (Eq. 19).

It follows from Eq. (21) that this term characterizes the rate of change in the energy of transverse motion due to the work done by the forces exerted on the beam particles by the self-consistent collective electromagnetic field.

Finally, the second term on the left-hand side of Eq. (21) and $\chi_b S$ describe the rates of change in the energy of transverse motion due to inelastic and elastic collisions of the beam particles with the gas–plasma particles, respectively.

VIRIAL EQUATION. THE DYNAMIC EQUILIBRIUM CONDITION

We take the scalar product of momentum transport equation (17) and $\mathbf{r}_\perp$ and integrate the expression obtained over transverse coordinates. As a result, we obtain

$$\frac{d}{dt}\left(\frac{\gamma m}{4}\frac{d\Re^2}{dt}\right) = 2(E_\perp - T_B) - 4\left(\frac{I_p}{I_b}\right)T_B\int\chi_b\mathbf{r}_\perp\cdot\nabla_\perp\int\chi_p'\ln\left|\frac{\mathbf{r}_\perp-\mathbf{r}_\perp'}{R_c}\right|d\mathbf{r}_\perp'd\mathbf{r}_\perp, \quad (26)$$

where

$$E_\perp = \int\chi_b\frac{\tilde{p}_\perp^2}{2m\gamma}d\mathbf{r}_\perp \quad (27)$$

is the average kinetic energy of the transverse motion of particles in a beam segment,

$$\Re^2 = 2\int\chi_b r_\perp^2 d\mathbf{r}_\perp \quad (28)$$

is the doubled mean-square radius of the beam segment, and

$$T_B = I_b\frac{q\beta}{2c} = \frac{m\gamma v_z^2}{2}\left(\frac{I_b}{I_A}\right) \quad (29)$$

is the so-called effective Bennett temperature (here, I_b is the total beam current, $I_A = \beta\gamma mc^3/q$ is the limiting Alfvén current, and v_z is the axial component of the beam particle velocity). Note also that, in Eq. (26), I_p is the total reverse plasma current and $\chi_p' = \chi_p(\mathbf{r}_\perp', t)$.

Simplifying the last term on the right-hand side of Eq. (26), we obtain

$$\frac{d}{dt}\left(\frac{\gamma m}{4}\frac{d\Re^2}{dt}\right) = 2\left\{E_\perp - T_B\left[1 + \frac{I_p}{I_b}(2 - C_p)\right]\right\}, \quad (30)$$

where

$$C_p = 2\int\chi_p\chi_b'\frac{\mathbf{r}_\perp\cdot(\mathbf{r}_\perp-\mathbf{r}_\perp')}{|\mathbf{r}_\perp-\mathbf{r}_\perp'|^2}d\mathbf{r}_\perp d\mathbf{r}_\perp'. \quad (31)$$

Equation (30) generalizes the well-known equation [6, 23–25] to the case $\chi_p \neq \chi_b$. For the sake of simplicity, we introduce the following notation for the form factor:

$$\Gamma = 1 + (2 - C_p)\frac{I_p}{I_b}. \quad (32)$$

It can easily be shown that, if $\chi_p = \chi_b$, then $C_p = 1$. In this case, we have $\Gamma = 1 + I_p/I_b = 1 - \alpha_m$, where $\alpha_m = -I_p/I_b$ is the coefficient of current neutralization for $\chi_b = \chi_p$.

Let us introduce the average virial,

$$V = -\frac{q\beta}{2}\int\chi_b\mathbf{r}_\perp\cdot\nabla_\perp(A_z^{(b)} + A_z^{(p)})d\mathbf{r}_\perp. \quad (33)$$

Performing integration in Eq. (33), we obtain

$$V = T_B\Gamma. \quad (34)$$

From Eq. (30), we find the virial equation

$$E_\perp - \frac{d}{dt}\left(\frac{m\gamma}{8}\frac{d\Re^2}{dt}\right) = V. \quad (35)$$

Setting $d\Re^2/dt = 0$ in Eq. (35), we arrive at the necessary condition for the dynamic equilibrium of a beam segment:

$$E_\perp = \Gamma T_B = \left[1 + \frac{I_p}{I_b}(2 - C_p)\right]T_B. \quad (36)$$

Equality (36) generalizes the well-known Bennett equilibrium condition [6, 22] to the case of different radial profiles of the beam current and the reverse plasma current ($\chi_b(\mathbf{r}_\perp, t) \neq \chi_p(\mathbf{r}_\perp, t)$).

EQUATION FOR THE AVERAGE TOTAL TRANSVERSE ENERGY OF THE BEAM PARTICLES

Let us consider the total energy Ψ of the beam particles within a segment. This energy is the sum of the average kinetic energy of the transverse motion $E_\perp$ and the average potential energy of the particles in the effective collective electric field $\mathbf{E}_\perp^{\text{eff}} = -\nabla_\perp(-\beta A_z^{(b)} - \beta A_z^{(p)})$:

$$\Psi = E_\perp + \Lambda_\beta, \quad (37)$$

where

$$\Lambda_\beta = -\frac{1}{2}\int\chi_b q\beta(A_z^{(b)} + A_z^{(p)})d\mathbf{r}_\perp. \quad (38)$$

In order to find the equation for the average transverse energy of the beam particles, we differentiate Eq. (37) over time. After some manipulations, we obtain

$$\frac{d\Psi}{dt} = \frac{dE_\perp}{dt} + \frac{d\Lambda_\beta}{dt} = -\frac{E_\perp}{\gamma}\frac{d\gamma}{dt} + \frac{\Lambda_\beta}{q\beta I_n}\frac{d}{dt}(q\beta I_n) + \int\chi_b S d\mathbf{r}_\perp + q\beta I_n\int\left\{\nabla_\perp\left(\frac{A_z^{(b)} + A_z^{(p)}}{I_n}\right)\cdot\left(\frac{\chi_b\mathbf{p}_\perp}{\gamma m}\right) - \frac{\partial}{\partial t}\left(\frac{\chi_b(A_z^{(b)} + A_z^{(p)})}{2I_n}\right)\right\}d\mathbf{r}_\perp, \quad (39)$$

where $I_n = I_b + I_p$ is the total current in the plasma–beam system.

By a little algebra, we arrive at the equation

$$\frac{dE_\perp}{dt} = \int \chi_b S d\mathbf{r}_\perp - \frac{E_\perp}{\gamma}\frac{d\gamma}{dt} - \Lambda_\beta \frac{d}{dt}\ln\left(\frac{\Lambda_\beta}{T_B}\right) + q\beta I_0 L, \quad (40)$$

where

$$L = -\frac{1}{c}\iint\left\{\frac{I_p}{I_b}\chi_p' \frac{\partial \chi_b}{\partial t} - \chi_b \frac{\partial}{\partial t}\left(\frac{I_p}{I_b}\chi_p'\right)\right\}\ln\left|\frac{\mathbf{r}_\perp - \mathbf{r}_\perp'}{R_c}\right| d\mathbf{r}_\perp' d\mathbf{r}. \quad (41)$$

Equation (40) can be rewritten in the form

$$\frac{dE_\perp}{dt} = \left(\frac{dE}{dt}\right)_{\text{enc}} + \left(\frac{dE}{dt}\right)_{\text{los}} + \left(\frac{dE}{dt}\right)_\beta + \left(\frac{dE}{dt}\right)_{\chi_b \neq \chi_p}, \quad (42)$$

where

$$\left(\frac{dE}{dt}\right)_{\text{enc}} = \int \chi_b S d\mathbf{r}_\perp, \quad (43)$$

$$\left(\frac{dE}{dt}\right)_{\text{los}} = -\frac{E_\perp}{\gamma}\frac{d\gamma}{dt}, \quad (44)$$

$$\left(\frac{dE}{dt}\right)_\beta = -\Lambda_\beta \frac{d}{dt}\ln\left(\frac{\Lambda_\beta}{T_B}\right), \quad (45)$$

$$\left(\frac{dE}{dt}\right)_{\chi_p \neq \chi_b} = q\beta I_b L. \quad (46)$$

Here, formulas (43) and (44) describe the rates of change in the average transverse kinetic energy of the beam particles within a segment due to elastic and inelastic collisions of the beam particles with the particles of the background gas–plasma medium, respectively; formula (45) describes the corresponding rate of change caused by the work done by the forces exerted on the beam particles by the self-consistent effective transverse electric field; and formula (46) describes the rate of change of $E_\perp$ due to the work done by the forces exerted on the beam particles in the case $\chi_b(\mathbf{r}_\perp, t) \neq \chi_p(\mathbf{r}_\perp, t)$.

EQUATION FOR THE MEAN-SQUARE RADIUS OF A BEAM SEGMENT (EQUATION FOR THE BEAM ENVELOPE)

In this section, we will derive the equation for mean-square beam radius (or the so-called envelope equation) for an axially symmetric paraxial relativistic beam with allowance for multiple elastic scattering and the nonlaminar character of the beam in the presence of the reverse plasma current with a radial profile differing from that of the beam current (i.e., $\chi_p(\mathbf{r}_\perp, t) \neq \chi_b(\mathbf{r}_\perp, t)$). To this end, both parts of Eq. (40) for the average total transverse energy of the beam particles are multiplied by Lorentz factor γ. As a result, we obtain

$$\frac{d(\gamma E_\perp)}{dt} = \gamma\Lambda_\beta \frac{d}{dt}\left[\ln\left(\frac{T_B}{\Lambda_\beta}\right)\right] + \gamma\int \chi_b S d\mathbf{r}_\perp - 2\gamma T_B L^*, \quad (47)$$

where $L^* = -cL$, c is the speed of light, and L is defined by formula (41).

We now turn to the virial equation in form (30). Multiplying Eq. (3) by $\gamma/2$ and differentiating the result obtained over t yield

$$\frac{d}{dt}(\gamma E_\perp) = \frac{1}{2}\frac{d}{dt}\left\{\gamma\frac{d}{dt}\left[\frac{\gamma m}{4}\frac{d}{dt}\Re^2\right]\right\} + \frac{d}{dt}(\gamma\Gamma T_B), \quad (48)$$

where Γ is defined by expressions (31) and (32).

Equating the right-hand sides of Eqs. (47) and (48), we obtain the equation

$$\frac{1}{2}\frac{d}{dt}\left\{\gamma\frac{d}{dt}\left[\frac{\gamma m}{4}\frac{d\Re^2}{dt}\right]\right\} = \gamma\Lambda_\beta\frac{d}{dt}\left[\ln\left(\frac{T_B}{\Lambda_\beta}\right)\right] + \gamma\int\chi_b S d\mathbf{r}_\perp - 2\gamma T_B L^* - \frac{d}{dt}(\gamma\Gamma T_B). \quad (49)$$

After multiplying Eq. (49) by $2\Re^2$ and performing some manipulations, we arrive at the equation

$$\frac{d}{dt}\left(\gamma^2\Re^3\frac{d^2\Re}{dt^2} + \gamma\frac{d\gamma}{dt}\Re^3\frac{d\Re}{dt}\right) = \frac{4\Re^2\gamma}{m}\left\{\Lambda_\beta\frac{d}{dt}\left[\ln\left(\frac{T_B}{\Lambda\beta}\right)\right] - \frac{1}{\gamma}\frac{d}{dt}(\gamma\Gamma T_B) + \int\chi_b S d\mathbf{r}_\perp - 2T_B L^*\right\}. \quad (50)$$

After integration, Eq. (50) becomes

$$\gamma^2\Re^3\frac{d^2\Re}{dt^2} + \gamma^2\Re^3\frac{d\gamma}{dt}\frac{1}{\gamma}\frac{d\Re}{dt} = \int_\tau^t\left[\frac{\Re^2\gamma}{m}\left\{\Lambda_\beta\frac{d}{dt'}\left[\ln\left(\frac{T_B}{\Lambda_\beta}\right)\right] - \frac{1}{\gamma}\frac{d}{dt'}(\gamma\Gamma T_B) + \int\chi_b S d\mathbf{r}_\perp - 2T_B L^*\right\}\right]dt'. \quad (51)$$

Finally, we arrive at the desired envelope equation,

$$\frac{d^2\Re}{dt^2} + \frac{1}{\gamma}\frac{d\gamma}{dt}\frac{d\Re}{dt} + \frac{4\Gamma T_B}{m\gamma\Re} = \frac{1}{\gamma^2\Re^3} \times \int_\tau^t \frac{4\Re^2\gamma}{m}\left\{\int\chi_b S d\mathbf{r}_\perp - 2T_B L^* - \Gamma T_B\frac{d\tilde{\Gamma}}{dt'}\right. \quad (52)$$

$$-\Lambda_\beta \frac{d\ln\Gamma}{dt'}\Big\}dt' + \frac{K_0}{\gamma^2\Re^3},$$

where

$$\tilde{\Gamma} = \frac{\Lambda_\beta}{\Gamma T_B} - \ln\left(\frac{\Re^2}{2R_c^2}\right), \quad (53)$$

K_0 is the integration constant, and τ is the injection time of the beam segment.

GENERALIZED EQUATION FOR THE MEAN-SQUARE RADIUS OF A QUASI-STEADY BEAM

We assume that, at any instant, the beam state in an arbitrary segment S^τ is close to dynamic equilibrium; i.e., condition (36) is approximately satisfied:

$$E_\perp \approx \Gamma T_B = \left[1 + \frac{I_p}{I_b}(2 - C_p)\right]T_B, \quad (54)$$

where T_B is the effective Bennett temperature (see formula (29)) and C_p is the coefficient defined by expression (31).

Let us consider the time evolution of the mean-square radius of a quasi-equilibrium beam. We combine Eq. (40) with dynamic equilibrium condition (54) to obtain

$$\frac{d(\Gamma T_B)}{dt} + \frac{d\Lambda_\beta}{dt} = -\frac{\Gamma T_B}{\gamma}\frac{d\gamma}{dt} + \Lambda_\beta\frac{d}{dt}(\ln T_B) + \int \chi_b S d\mathbf{r}_\perp - 2T_B L^*, \quad (55)$$

where $L^* = -cL$.

We add and subtract $\Lambda_\beta d/dt(\ln\Gamma)$ on the right-hand side of Eq. (55). As a result, we have

$$\frac{d(\Gamma T_b)}{dt} + \frac{d\Lambda_\beta}{dt} = -\frac{\Gamma T_B}{\gamma}\frac{d\gamma}{dt} + \Lambda_\beta\frac{d}{dt}\ln(\Gamma T_B) - \Lambda_\beta\frac{d}{dt}\ln\Gamma + \int \chi_b S d\mathbf{r}_\perp - 2T_B L^*. \quad (56)$$

Differentiating Eq. (53) over time, we obtain

$$\frac{1}{\Re^2}\frac{d\Re^2}{dt} + \frac{d\tilde{\Gamma}}{dt} = \frac{1}{\Gamma T_B}\left(\frac{d\Lambda_\beta}{dt} - \frac{\Lambda_\beta}{\Gamma T_B}\frac{d(\Gamma T_B)}{dt}\right). \quad (57)$$

Using Eq. (57), we find the quantity $d\Lambda_\beta/dt - \Lambda_\beta d/dt\ln(\Gamma T_B)$ and substitute it into Eq. (56) to obtain

$$\frac{d(\Gamma T_B)}{dt} + \Gamma T_B\left(\frac{1}{\Re^2}\frac{d\Re^2}{dt} + \frac{d\tilde{\Gamma}}{dt}\right) = -\frac{\Gamma T_B}{\gamma}\frac{d\gamma}{dt} - \Lambda_\beta\frac{d}{dt}\ln\Gamma + \int \chi_b S dr_\perp - 2T_B L^*. \quad (58)$$

After dividing both parts of Eq. (58) by ΓT_B and performing some manipulations, we finally arrive at the equation

$$\frac{d}{dt}[\ln(\gamma\Re^2\Gamma T_B)] = \frac{1}{\Gamma T_B}\int \chi_b S d\mathbf{r}_\perp - \frac{d\tilde{\Gamma}}{dt} - \frac{1}{\Gamma T_B}\left(\Lambda_\beta\frac{d}{dt}\ln\Gamma + 2T_B L^*\right). \quad (59)$$

Equation (59) generalizes the well-known Nordsick equation [6] to the case of the reverse plasma current with an arbitrary radial profile. This equation also takes into account the phase mixing of the particle trajectories in the anharmonic collective field of the plasma–beam system.

REFERENCES

1. A. A. Rukhadze, L. S. Bogdankevich, S. E. Rosinskiĭ, and V. G. Rukhlin, *Physics of High-Current Relativistic Electron Beams* (Atomizdat, Moscow, 1980) [in Russian].
2. A. N. Didenko, V. P. Grigor'ev, and Yu. P. Usov, *High-Power Electron Beams and Their Application* (Atomizdat, Moscow, 1977) [in Russian].
3. R. B. Miller, *Introduction to the Physics of Intense Charged Particle Beams* (Plenum, New York, 1982; Mir, Moscow, 1984).
4. J. D. Lawson, *The Physics of Charged-Particle Beams* (Clarendon Press, Oxford, 1977; Mir, Moscow, 1980).
5. R. C. Davidson, *Theory of Nonneutral Plasmas* (Benjamin, Reading, 1974; Mir, Moscow, 1978).
6. E. P. Lee, Phys. Fluids **19**, 60 (1976).
7. E. P. Lee, Livermore Lab. Rep. UCID-16490, 14 (1974).
8. E. P. Lee and R. K. Cooper, Part. Accel. **7**, 83 (1976).
9. E. R. Nadezhdin, Pis'ma Zh. Tekh. Fiz. **16** (21), 73 (1990) [Sov. Tech. Phys. Lett. **16**, 838 (1990)].
10. E. R. Nadezhdin, Fiz. Plazmy **17**, 327 (1991) [Sov. J. Plasma Phys. **17**, 194 (1991)].
11. E. R. Nadezhdin and G. A. Sorokin, Fiz. Plazmy **14**, 619 (1988) [Sov. J. Plasma Phys. **14**, 365 (1988)].
12. R. F. Fernsler, R. F. Hubbard, and M. Lampe, J. Appl. Phys. **75**, 3278 (1994).
13. G. P. Mkheidze and G. A. Mesyats, in *Encyclopedia of Low-Temperature Plasma*, Vol. 4: *Gas and Plasma Lasers*, Ed. by V. E. Fortov (Nauka, Moscow, 2000), pp. 108–126 [in Russian].
14. Yu. F. Bondar', A. A. Goman'ko, A. A. Korolev, *et al.*, Pis'ma Zh. Tekh. Fiz. **14**, 1116 (1988) [Sov. Tech. Phys. Lett. **14**, 490 (1988)].
15. Yu. F. Bondar', A. A. Goman'ko, A. A. Ermakov, *et al.*, Prib. Tekh. Éksp., No. 6, 139 (1987).
16. Yu. F. Bondar', S. N. Kabanov, A. A. Korolev, *et al.*, Preprint No. 57, IOFAN (Institute of General Physics, Russian Academy of Sciences, 1986).
17. Yu. F. Bondar', G. P. Mkheidkhe, and A. A. Savin, Kratk. Soobshch. Fiz., No. 10, 17 (1986).

18. S. V. Arlantsev, G. P. Mkheidze, A. A. Savin, *et al.*, Preprint No. 184, IOFAN (Institute of General Physics, USSR Academy of Sciences, 1987).
19. V. P. Grigor'ev and A. G. Potashev, Izv. Vyssh. Uchebn. Zaved. Fiz. **33** (12), 59 (1990).
20. M. A. Vlasov, I. P. Denisova, and S. V. Nikonov, Radiotekh. Élektron. (Moscow) **29**, 1595 (1984).
21. E. K. Kolesnikov and A. S. Manuilov, Radiotekh. Élektron. (Moscow) **35**, 218 (1990).
22. E. K. Kolesnikov and A. S. Manuilov, Zh. Tekh. Fiz. **67** (7), 108 (1997) [Tech. Phys. **42**, 648 (1997)].
23. A. S. Manuilov, Available from VINITI, No. 6028-85 (Leningrad, 1985).
24. E. K. Kolesnikov and A. S. Manuilov, Zh. Tekh. Fiz. **67** (11), 62 (1977) [Sov. Phys. Tech. Phys. **42**, 1297 (1977)].
25. A. S. Manuilov, Zh. Tekh. Fiz. **70** (1), 76 (2000) [Tech. Phys. **45**, 74 (2000)].
26. R. L. Liboff, *Introduction to the Theory of Kinetic Equations* (Wiley, New York, 1969; Mir, Moscow, 1974).
27. E. P. Lee, Livermore Lab. Rep. UCID-18940, 33 (1981).

Translated by A. Sidorova

Technical Physics, Vol. 50, No. 4, 2005, pp. 498–502. Translated from Zhurnal Tekhnicheskoĭ Fiziki, Vol. 75, No. 4, 2005, pp. 109–113.

SURFACE, ELECTRON AND ION EMISSION

Thermally Stimulated Desorption of Na^+ and Cs^+ Ions from a NaAu Alloy Film Grown on Au

M. V. Knat'ko, M. N. Lapushkin, and V. I. Paleev

Ioffe Physicotechnical Institute, Russian Academy of Sciences, Politekhnicheskaya ul. 26, St. Petersburg, 194021 Russia

e-mail: Lapushkin@ms.ioffe.rssi.ru

Received September 8, 2004

Abstract—The formation of Na^+ and Cs^+ ions on and their thermal desorption from the surface of a NaAu alloy film grown on metallic gold are studied. It is shown that thermionic emission from insulator-coated metallic substrates is governed by a sequence of processes, such as diffusion of Na and Cs adatoms into the film, ionization of these atoms at the insulator–metal interface, diffusion of the resulting ions toward the surface, and desorption of the ions. The effect of weak electric fields on ion diffusion and desorption is investigated. © *2005 Pleiades Publishing, Inc.*

INTRODUCTION

Electron exchange between a solid surface and atoms leaving the surface proceeds through electron tunneling and plays a decisive role in the ionization of particles being desorbed. The stochastic nature of electron transitions between particles and a solid was taken into account in the development of a statistical approach to describing surface ionization of atoms thermally evaporating from the emitter surface [1, 2].

Let us consider surface ionization of alkali metal atoms on metallic emitters in a weak electric field. In an adatom–substrate system, the times to charge and thermal equilibria are, respectively, on the order of $\tau_{ch} \sim 10^{-14}$ s and $\tau_t \sim 10^{-11}$ s. The lifetime of alkali atoms on the metal surface (the time to desorption) is $\tau_d \geq 10^{-6}$ s even if the adsorbent temperature is as high as T = 3000 K. Under these conditions, the particle–emitter adsorption system is in thermodynamic equilibrium and the ion-to-atom ratio in the flux of thermally desorbed particles is given by the well-known Saha–Langmuir formula [2].

Thermodynamic equilibrium in the system can be disturbed by the absence of charge equilibrium between adatoms and the substrate. During absorption of the atoms on nonmetallic adsorbents, this may happen if the level of the valence electron of an adatom falls into the band gap of the solid, so that adatom–substrate electron exchange becomes difficult. In this case, we may face the situation when $\tau_d < \tau_{ch}$. In such a nonequilibrium system, the basic dependences describing thermionic emission may differ from those obtained for surface ionization, as was analytically shown by Morgulis as early as in 1948 [3]. In practice, adsorption systems of this kind can be formed by using wide-gap semiconductors (insulators) as adsorbents, which can withstand heating to temperatures high enough to evaporate particles at such low adsorbate densities that do not alter the thermionic properties of the emitter. In the adsorption systems used in our study, adsorbate–adsorbent electron exchange was made difficult owing to the fact that gold substrates covered by a film of a gold–alkali metal M (M = Cs, K, Na) alloy were used as ion emitters. MAu alloys have the electronic properties of wide-gap semiconductors. The band gap of these materials varies between 2.6 and 2.8 eV [4, 5].

Films of these alloys grown on a gold substrate withstand long-term annealing at T = 1250 K [6]. Specifically, NaAu films keep their physicochemical properties at this temperature for several tens of hours. At temperatures above 600 K, these film systems can emit M^+ ions when M atoms come from external sources, as well as alkali metal ions via intrinsic thermionic emission [6–9]. The thermal desorption current depends on the temperature of the emitter and is also affected by external actions on the emitter. For example, irradiation of the emitter by photons with an energy $h\nu$ exceeding 2.4 eV considerably changes the ion yield and thermal desorption characteristics [5, 7, 10].

Below are the results of an investigation into the thermally stimulated desorption of Na^+ and Cs^+ ions in the case when alkali metal atoms come to a gold substrate that is covered by a thin layer of NaAu alloy. The effect of weak electric fields on such an ionization process is also considered.

EXPERIMENTAL

Experiments were performed in a magnetic sector mass spectrometer intended for studying thermally stimulated desorption of atoms and positive ions from

1063-7842/05/5004-0498$26.00

the surface [6–10]. The mass spectra could be swept by varying the magnetic field.

The flux of alkali metal atoms (flux density ν is $\leq 10^{13}$ cm^{-2} s^{-1}) was directed from evaporators onto the central part of an emitter, a gold strip (Au 99.99%) covered by a film of the alloy. The formation of the alloy film on the gold surface is described elsewhere [6]. The strip was biased up to $\Delta U = \pm 1800$ V relative to the input electrode of the focusing system of the ion source. Such a potential generated an electric field of up to $E \cong \pm 1.2 \times 10^3$ V/cm near the emitter surface. The surface of the substrate was cleaned by heating in an oxygen atmosphere ($P = 2 \times 10^{-6}$ Torr) for 2 h. The windows in the ion source chamber were used for determination of the ion emitter temperature with an optical pyrometer, as well as for introduction of light beams in studying thermally stimulated processes at the surface. In the range below 700°C, the emitter temperature was estimated by extrapolating the experimentally found dependence $T_e = a + b\ln R$ (where R is the resistance of the strip, which depends on the filament current, and a and b are coefficients).

Below, we report a number of characteristics and specific features of the ionization process that were found when studying the thermally stimulated desorption of Na^+ and Cs^+ ions from the NaAu/Au surface in the mass spectrometer.

The mass spectrum lines for Na^+ ions at different thicknesses of the alloy film on the surface is shown in Fig. 1. The linewidth increases considerably as the NaAu layer gets thicker. A similar dependence was obtained for Cs^+ ions when Cs atoms were ionized on this emitter. The introduction of O_2 into the ion source chamber (the O_2 pressure was varied from $5 \times 10^{-7} < P(O_2) < 5 \times 10^{-6}$ Torr), which affects the composition of the layer and the potential distribution on its surface, also broadens the mass spectrum lines of Na^+ and Cs^+ ions.

The change in the thermally stimulated desorption current of Na^+ and Cs^+ ions lags behind the change in ion flux density ν of alkali metal atoms arriving at the strip from the atomic source. When the Na flux is shut off, the ion current decreases gradually. For instance, if the flux of Na atoms is shut off for a time $\Delta t = 600$ s at temperatures $T = 1130$–1150 K, the Na^+ current drops roughly 100-fold, i.e., to values one order of magnitude exceeding the noise level of the ion detector of the mass spectrometer. The average lifetime of Na adatoms on the surface is $\tau_d \approx 0.1$ s at such temperatures. If the atoms were ionized on the uncovered Au emitter surface, the time it takes for the ion current to drop down to the detectability of the detector would be much shorter. Thus, the findings of this work substantiate our earlier conclusions [6] that the diffusion of alkali metal atoms and ions plays an important role in the formation and degradation of the alloy film, as well as in the thermal desorption of these particles from the surface. In

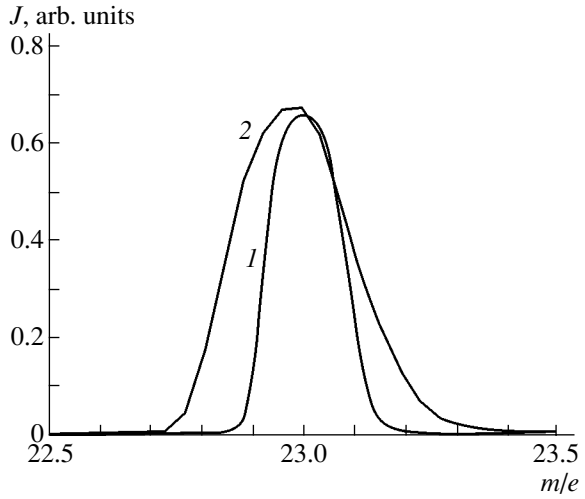

Fig. 1. Sodium ion lines in the mass spectrum of thermally stimulated desorption from the NaAu/Au surface: (*1*) thin film and (*2*) thick film.

[6], we also determined the activation energy of sodium atom diffusion in the NaAu alloy, ≈3.20 eV. This value is well below the value of 5.1 eV for the activation energy of Na diffusion in metallic gold.

The data presented indicate that ionization of alkali metal atoms on the surface of heated metallic emitters differs from thermal desorption of alkali ions from metals covered by nonmetallic film coatings. Therefore, a number of experiments were performed aimed at elucidating an atom ionization mechanism and at understanding how the emitter temperature and applied electric field affect the ionization process and transport of the particles.

We obtained the dependences of the thermal desorption current of Na^+ ions on time t_d of action of ion-extracting electric field $E(d)$ and on time Δt_r of action of ion-blocking electric field $E(r)$. In addition, we kept track of the ion emission with the voltage applied to the emitter switched off for a time Δt_0, $E = 0$.

Figure 2 shows a family of curves $I(t_d)$ for Na^+ ions thermally desorbed from the gold strip covered by a thin (two to three monolayers) film of the NaAu alloy when a Na atom flux was directed to the emitter. All the curves were taken after the strip had been kept at $E = 0$ for $\Delta t = 400$ s. The features of the ion desorption process are the following: (i) the general form of the $I(t_d)$ dependence varies with T; (ii) at the time the ion-accelerating voltage is switched on, initial current $I(0)$ takes a minimal value when emitter temperature T is maximal and then increases, passing through a maximum, as T declines; (iii) throughout the emitter temperature range, the time it takes for $I(t_d)$ to reach the saturation emission current is rather long, the saturation current being the lowest when T is the highest; and (iv) the form of the initial portions of the $I(t_d)$ curves depends on T,

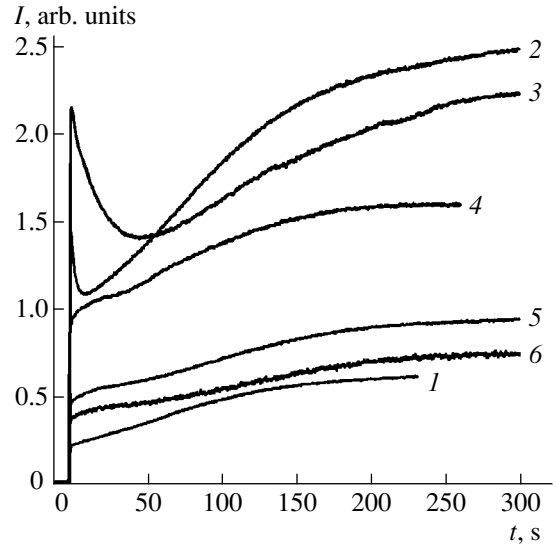

Fig. 2. Time dependences $I(t_d)$ of the thermal desorption current for sodium ions at NaAu/Au emitter temperatures of (*1*) 1070, (*2*) 1020, (*3*) 970, (*4*) 900, (*5*) 860, and (*6*) 800 K.

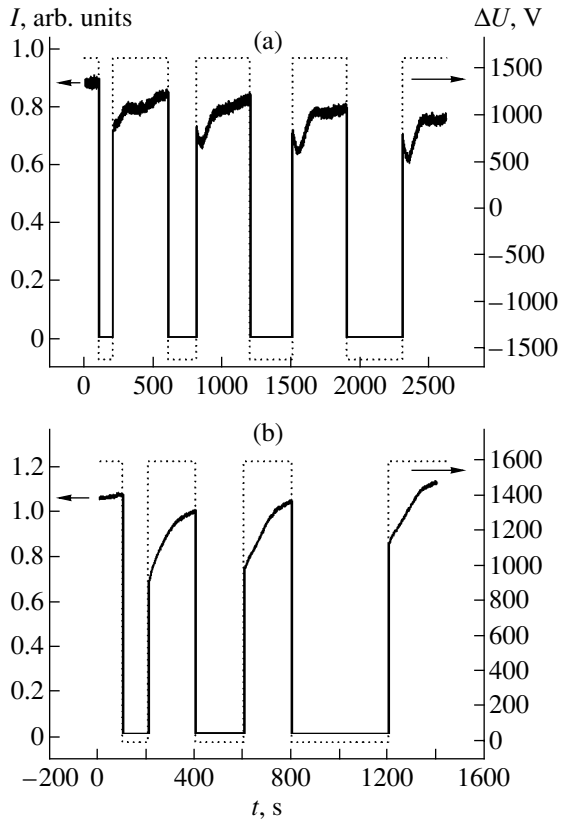

Fig. 3. (a) Time dependences $I(t_d)$ for sodium ions upon switching off the ion-extracting voltage for Δt_0 = 100, 200, 400 s. (b) Time variations $I(t_d)$ for sodium ions upon applying the blocking voltage for Δt_r = 100, 200, 400 s. The dotted line shows the waveform of the applied voltage.

the $I(t_d)$ curves peaking just in these portions when T varies between 900 and 1020 K.

Let us now see how an electric field changes the form of the $I(t_d)$ curves. To this end, the current was cut off by switching off the ion-extracting voltage for a certain time period Δt. As a result, the ions were blocked on the surface and the desorption flux consisted of only Na atoms; accordingly, the concentration of the alkali metal on the emitter rose. Two methods of ion blocking were used (see Fig. 3): (i) the ion-extracting voltage was switched off for a time Δt_0, so that only those ions could leave the surface whose energy was high enough to overcome the desorption barrier, and (ii) an ion-blocking field, $E(r) \approx 1.2 \times 10^3$ V/cm, was applied to the emitter for time intervals Δt_r. From the results presented, it follows that even a weak electric field influences the concentration of the ions in the near-surface region of the alloy film, since the form of the $I(t_d)$ curve considerably depends on the strength of field E applied to the emitter.

The dependences $I(t_d)$ presented in Fig. 4 also suggest that the magnitude and direction of the electric field vector at the surface are of significance. In the case shown in Fig. 4a, the ion current was picked up by switching on the ion-extracting voltage, which was increased in ΔU = 200 V steps after $I(t_d)$ had saturated. In the other case (Fig. 4b), the current of Na^+ ions was picked up first with voltage ΔU_1 = 800 V. Then, the extracting voltage was increased to ΔU_2 = 1800 V and subsequently, after the system had been kept at the saturation current for t_d = 400 s, was decreased again to ΔU_1 = 800 V. It is clear from Fig. 4a that, as ΔU increases, the current of thermally stimulated desorption of Na^+ ions gradually tends to the saturation value corresponding to a given ΔU. On the other hand (Fig. 4b), a decrease in the voltage by 1000 V ($\Delta U_2 \longrightarrow \Delta U_1$) causes the current to peak with the subsequent decline to the initial value of the saturation current for ΔU_1.

The method proposed was also used to study the effect of weak electric fields on the thermal ionization of Cs atoms on this emitter. Basically, the results for Cs atom ionization are consistent with those for Na atom ionization.

RESULTS AND DISCUSSION

The line broadening in the mass spectrum of thermal desorption of Na^+ and Cs^+ ions with an increase in the NaAu layer thickness (Fig. 1) was observed earlier for the thermal desorption of K^+ ions at the initial stages of KAu alloy formation on the gold substrate surface [9]. The fact that the broadening is appreciable indicates that the ions subjected to applied voltage difference ΔU have different energies at the entrance to the focusing system of the mass spectrometer. For thermally stimulated desorption, the spread in particle initial velocities

is rather small [2]. One can assume that the broadening of the mass spectrum lines stems from a spread in the potential over the operating (ion-emitting) area of the emitter. Note that, like KAu alloy [9], the film of NaAu alloy exhibits insulating properties [6] throughout the operating emitter temperature range.

The absence of electron tunneling between the metal substrate and adsorbed alkali metal atoms is corroborated by the experimental data shown in Fig. 2. The ion current density is the lowest when the emitter temperature is the highest (curve *1*). For surface ionization of atoms on metallic gold, which has the electron work function $\varphi = 4.7 \pm 0.1$ eV [7], the Na^+ emission intensity grows with emitter temperature in the range 1000–1200 K [11] in agreement with the theory of this process. The experimental data presented in Fig. 2 suggest that, in the temperature range being studied, lifetime τ_d of Na atoms adsorbed on the alloy film is shorter than time τ_{ch} of electron tunneling; therefore, the atoms are desorbed in the nonionized state. Because of short τ_d, the concentration of Na adatoms on the surface is low and the diffusion flux of the atoms into the film is depleted. Only those particles may ionize in the system studied that penetrate into the interior of the film. The concentration of such particles increases with decreasing temperature, as indicated by the increase in the ion emission intensity (curves *2* and *3*). The fact that the maximal (saturation) ion current passes through a maximum with decreasing strip temperature indicates that the emission is a complex process involving (i) diffusion of atoms embedded in the layer to the centers of ionization, (ii) ionization of the atoms, and (iii) diffusion of the ions toward the surface with subsequent desorption.

The processes that may be responsible for electron loss by an alkali metal atom are as follows: (i) the transition of an electron to a free gold atom (not incorporated into the structure of the alloy), $M + Au \longrightarrow M^+ + Au^-$; (ii) ionization of impurity atoms with the transition of the electrons to the conduction band of *M*Au insulating crystals; or (iii) ionization of *M* atoms that reached the alloy–substrate interface via electron tunneling into the metal (a process similar to surface ionization with the subsequent drift of the electrons from the interface into the insulator). The last-mentioned process seems to be the most plausible, as follows from the experimental $I(t_d)$ dependences.

The experiments showed that a thin insulating film present on the metal surface allows a weak electric field to penetrate into the alloy and have a noticeable influence on the thermal ionization characteristics. The depth profile of Na^+ ions in the alloy film depends on the magnitude and direction of the electric field vector. For example, if $E = 0$, the Na^+ ion distribution in the alloy is distinct from that when fields $E(d)$ and $E(r)$ are applied to the strip. As follows from the experimental data shown in Figs. 3 and 4, the run of the $I(t_d)$ curve

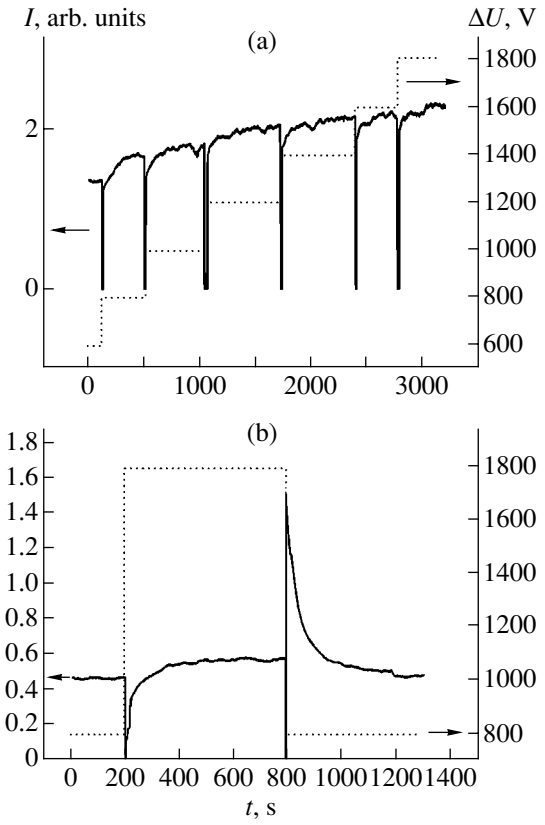

Fig. 4. Sodium ion current vs. ion-extracting voltage ΔU. The dotted line shows the time variation of the applied voltage. (a) ΔU is increased in 200 V steps and (b) ΔU is increased by 1000 V for $\Delta t = 600$ s.

can be controlled by varying the magnitude and direction of *E*.

At emission-blocking fields in the range $E(r) \le 1 \times 10^3$ V/cm, the concentration of the ions localized on the surface can be considerably reduced by appropriately selecting the interval Δt_r (which depends on the temperature as well). In this case (Fig. 3b), the electric field changes the distribution of Na^+ ions across the alloy film. At the instant the ion-extracting voltage is switched on, the emission current is lower than the saturation current for the steady-state desorption of the ions and the time taken to recover the diffusion flux of the ions to the surface is rather long ($t \approx 100$–200 s).

The dependence $I(t_d)$ takes another form when ΔU is switched off and the emitter heated to $900 < T < 1020$ K is kept for a certain time Δt_0 at $E = 0$ (see Fig. 2, curves *2–4*, and Fig. 3a). It is seen that the $I(t_d)$ curves exhibit a clear-cut peak of Na^+ emission at the instant the extracting voltage is switched off and the height of the peak depends on the temperature and Δt_0 (these parameters specify the gradient of the concentration of alkali metal atoms and ions over the thickness of the alloy film, as well as the rate of diffusion particle exchange between the surface and near-surface layers).

For instance, when ΔU was switched off for a time Δt_0 not exceeding 100 s, the peak did not appear in the $I(t_d)$ dependence (Fig. 3a). On the other hand, if Δt_0 exceeds 100 s, the peak intensity increases with Δt_0. The height of the peak may be assumed to be dependent on the concentration of the ionic component in the sodium adlayer on the emitter surface (the ions cannot be thermally desorbed in the absence of the ion-extracting field). Application of the field for a while reduces the ion concentration on the surface of the film, since the rate of ion diffusion from deep-seating layers is lower than the rate of ion desorption. Moreover, the ion-extracting voltage causes polarization of the insulating film on the metallic substrate with the formation of a positively charged layer at the insulator/vacuum interface. This may enhance the desorbed Na^+ ion flux at the instant the electric field changes from $E = 0$ to $E(d)$, because Coulomb repulsion between the ions and positively charged layer loosens bonds between the emitter and the ions in the adlayer. The curve $I(t_d)$ saturates when the field produced by the ions in the adlayer, charges distributed over the thickness of the film, and the polarization of the film become steady.

It seems likely that the polarization of the insulating film in an electric field is of importance in the emission dynamics shown in Fig. 4. As field $E(d)$ increases (Fig. 4a), so does the positive charge density in the upper layer of the alloy, which for a while suppresses the emergence of Na^+ ions. As the mobile ion concentration in the film varies and the electric field affects the rate of ion diffusion, current $I(t_d)$ gradually grows. The abrupt decrease in $E(d)$ leads to an excess positive charge at the film–vacuum interface and is responsible for the peak in the emission intensity of the ions localized in the adlayer near the interface (Fig. 4b).

CONCLUSIONS

Thus, the thermodynamically equilibrium process of surface ionization of atoms on metals, which is related to electron tunneling between the solid and particles during their desorption, differs considerably from the thermal desorption of ions from metallic substrates covered by an insulating film. In the latter case, the ion emission comprises the sequence of processes, such as adatom diffusion into the interior of the coating, ionization of diffused atoms accompanied by electron transition to the metal, ion diffusion to the surface, and thermal desorption of the ions.

Note that, in an *M*/NaAu/Au adsorption system, one can control the surface concentration of alkali metal atoms with the help of weak electric fields, as is shown in this study, or by irradiation by light, as was shown in [5, 7, 10]. Alkali metal particles adsorbed on the surface serve as active centers in thermally stimulated heterogeneous reactions involving organic molecules [12]. The possibility of controlling the concentration of the active centers may be useful in controlling heterogeneous chemical reactions.

ACKNOWLEDGMENTS

This study was supported by the Russian State Program "Surface Atomic Structures," project GK no. 1152.

REFERENCES

1. L. N. Dobretsov and M. V. Gomoyunova, *Emission Electronics* (Nauka, Moscow, 1966) [in Russian].
2. É. Ya. Zandberg and N. I. Ionov, *Surface Ionization* (Nauka, Moscow, 1971) [in Russian].
3. N. D. Morgulis, Zh. Tekh. Fiz. **18**, 567 (1948).
4. W. E. Spicer, A. H. Sommer, and J. C. White, Phys. Rev. **115**, 57 (1959).
5. M. V. Knat'ko, M. N. Lapushkin, and V. I. Paleev, Zh. Tekh. Fiz. **68** (10), 108 (1998) [Tech. Phys. **43**, 1235 (1998)].
6. M. V. Knat'ko, V. I. Paleev, and M. N. Lapushkin, Phys. Low-Dimens. Semicond. Struct. **5/6**, 85 (1998).
7. É. Ya. Zandberg, M. V. Knat'ko, V. I. Paleev, *et al.*, Pis'ma Zh. Tekh. Fiz. **21** (19), 15 (1995) [Tech. Phys. Lett. **21**, 774 (1995)].
8. M. V. Knat'ko, V. I. Paleev, and É. Ya. Zandberg, Phys. Low-Dimens. Semicond. Struct. **7/8**, 27 (1996).
9. M. V. Knat'ko, M. N. Lapushkin, and V. I. Paleev, Phys. Low-Dimens. Semicond. Struct. **9/10**, 85 (1999).
10. M. V. Knat'ko, V. I. Paleev, and M. N. Lapushkin, Zh. Tekh. Fiz. **68** (10), 104 (1998) [Tech. Phys. **43**, 1231 (1998)].
11. É. Ya. Zandberg, M. V. Knat'ko, V. I. Paleev, and M. M. Sushchikh, Phys. Low-Dimens. Semicond. Struct. **7**, 79 (1994).
12. M. V. Knat'ko, M. N. Lapushkin, and V. I. Paleev, Zh. Tekh. Fiz. **74** (7), 99 (2004) [Tech. Phys. **49**, 905 (2004)].

Translated by M. Lebedev

Technical Physics, Vol. 50, No. 4, 2005, pp. 503–507. Translated from Zhurnal Tekhnicheskoĭ Fiziki, Vol. 75, No. 4, 2005, pp. 114–117.

EXPERIMENTAL INSTRUMENTS AND TECHNIQUES

Setup Parameters Controlling the Growth Rate of Silicon Carbide Epitaxial Layers in a Vacuum

S. Yu. Davydov, A. A. Lebedev, N. S. Savkina, and A. A. Volkova

Ioffe Physicotechnical Institute, Russian Academy of Sciences, Politekhnicheskaya ul. 26, St. Petersburg, 194021 Russia

e-mail: Sergei.Davydov@mail.ioffe.ru

Received April 29, 2004

Abstract—An extension of the model suggested in [5] allows us to consider the influence of the growth cell geometry, as well as temperature and pressure gradients, on the growth rate of SiC epitaxial layers in a vacuum. The experimental dependences of the substrate temperature on the current in an induction coil that are taken for different positions of the cell relative to the inductor are discussed. © *2005 Pleiades Publishing, Inc.*

INTRODUCTION

A variety of computational schemes have been developed to describe gas-phase epitaxial growth of semiconductor films. However, all these schemes bear on transfer of film-forming atoms and molecules through an inert gas filling the working space of the reactor [1–3]. Only the last section of review [4] is devoted to film growth in a rarefied atmosphere (vacuum). The scarcity of relevant publications is not a great surprise. In an inert atmosphere, particle free path λ is much shorter than typical geometric dimensions r and l of a growth cell (r is the inner radius of the cell, l is the distance between a vapor source and a substrate). This fact allows using the hydrodynamics equations to describe transfer processes. In a rarefied atmosphere, conversely, $\lambda \gg r, l$ and stochastic processes taking place in the cell are described, as a rule, by the Monte Carlo method.

In [5], we suggested a simple model of the epitaxial growth of SiC layers. The model is based on the Hertz–Knudsen equation, which assumes the molecular flux of silicon carbide, J, to be expressed by

$$J = Xp, \quad X = (2\pi MRT)^{-1/2}, \tag{1}$$

where M is the SiC molecular weight, R is the universal gas constant, T is the temperature, and $p = B\exp(-Q/RT)$ is the equilibrium SiC vapor pressure (Q is the heat of sublimation of SiC, B is a coefficient).

We also introduced an empiric coefficient of sticking of silicon carbide molecules to the substrate, $\alpha = A\exp(-E_a/RT)$, where E_a is the potential (activation) barrier that must be overcome by a molecule so that it will adhere to the substrate and A is a preexponential. Then, growth rate G has the form

$$G = \frac{M}{\rho} Xp\alpha, \tag{2}$$

where ρ is the density of the growing SiC film.

The experimental results were compared with reduced growth rate $g \equiv G/G_0$, where rate G corresponds to some temperature T and G_0, to maximal temperature T_0 used in a given experiment. Such a model gives a good fit to the experimental data, as was shown in [5].

As follows from Eqs. (1) and (2), we ignored in [5] the fact that particle sticking to the cell walls and a temperature gradient may affect the particle flux. In the framework of our model, we will consider how these factors influence the growth rate.

EXPERIMENTAL SETUP

The setup for sublimation growth of epitaxial layers in a vacuum was detailed elsewhere [6]. The inductively heated growth (graphite) cell contains a source of SiC vapor (synthesized SiC powder) and a single-crystalline SiC substrate on which the epitaxial layer grows. The schematic of the growing cell and its arrangement inside a cylindrical inductor connected to an rf oscillator (oscillating tube) are shown in Fig. 1. A specially tailored mechanical device moves the cell inside the inductor. The current of the inductor and, hence, the substrate temperature are controlled by applying a high voltage to the anode of the tube. In practice, the anode current of the oscillating tube, I_a, is the basic controlling parameter.

INFLUENCE OF THE REACTION SPACE GEOMETRY

Let the reaction space of the growing cell be a cylinder (Fig. 1) with inner radius r and length l. The molecules move randomly, being scattered mainly on the cell walls (see, for example, Fig. 24 in [4]). Let the coefficient of molecule sticking to the walls be

1063-7842/05/5004-0503$26.00

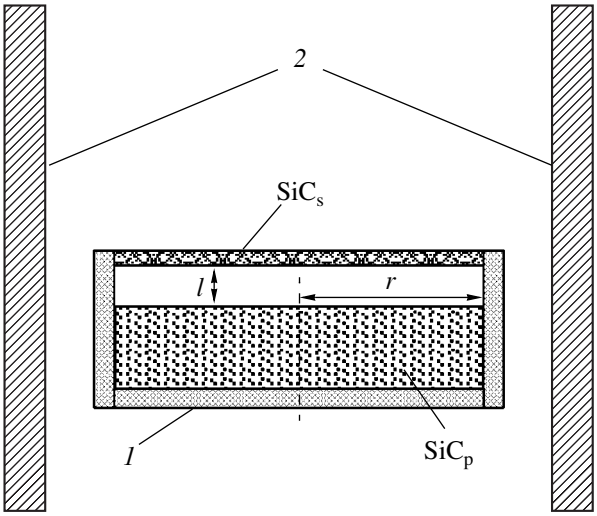

Fig. 1. Schematic of the cell for growing SiC epitaxial layers in a vacuum and its arrangement inside the cylindrical inductor. *1*, growth cell; *2*, inductor; SiC_p, silicon carbide powder; and SiC_s, substrate.

expressed as $\bar{\alpha} = \bar{A}\exp(-\bar{E}_a/RT)$, where $\bar{E}_a$ is the energy barrier that must be overcome by a SiC molecule so that it will adhere to the graphite wall. Then, a decrease in the particle flux due to wall scattering is $dJ = -(J/r)dz$, where axis z coincides with the axis of the cylinder. The flux arriving at the wall is $\bar{J}(l) = J(0)[1 - \exp(-l/r)]$, where $J(0)$ is the initial flux (the flux from the source, see (1)). The number of particles sticking to a unit wall area per unit time is $\bar{\alpha}\bar{J}$, and $(1 - \bar{\alpha})\bar{J}$ particles return to the mainstream. The flux arriving at the substrate is $J(0)[1 - \bar{\alpha}(1 - \exp(-l/r))]$. The number of particles sticking to a unit substrate area per unit time equals

$$\tilde{J} = J(0)F(l/r), \quad F(l/r) = \alpha f(l/r), \qquad (3)$$

where

$$f(l/r) = 1 - \bar{\alpha}[1 - \exp(-l/r)].$$

Thus, the growth rate can be expressed as

$$\tilde{G} = Gf(l/r), \qquad (4)$$

where G is given by (2).

For $\bar{\alpha} = 0$ and $l = 0$, we have $\tilde{G} = G$. For $l = \infty$, $\tilde{G} = G(1 - \bar{\alpha})$; i.e., the growth rate decreases because of SiC molecule sticking to the walls. For $\bar{\alpha} = 1$, we have $\tilde{G} = G\exp(-l/r)$. Finally, when $(l/r) \gg 1$, the growth ceases, since all the SiC molecules stick to the walls.

It is easy to show that, for $(l/r) \ll 1$, $F \approx \alpha[1 - \bar{\alpha}(l/r)]$; i.e., a decrease in the SiC molecular flux due to sticking is vanishingly small. Consider now the limit $(l/r) \gg 1$. For simplicity, we put $\bar{\alpha} = \alpha$, thereby assuming that the molecules equiprobably stick to the graphite walls of the reactor and to the substrate. By varying sticking coefficient α, it is easy to check that function F has a maximum, $F_{max} \approx 0.25$, at $\alpha^* \approx 0.25$. For $l \approx r$, $F \approx \alpha[1 - \bar{\alpha}(1 - e^{-1})]$. Assuming again that $\bar{\alpha} = \alpha$, we get $F_{max} \approx 0.395$ at $\alpha^* \approx 0.79$.

Thus, a source of silicon carbide molecules in the growing cell should be placed at a distance $l \le r$ from the substrate. It is such a geometry that is implemented in our setup: $l = 7$mm and $r = 18$ mm. Of course, the above consideration greatly simplifies the real physical pattern in the reactor (for example, processes, such as multiple reflections of particles from the walls, scattering by the substrate with subsequent transfer of the molecules to the walls, etc., are omitted). However, it may provide a proper insight into the influence of the reaction space geometry on the growth rate of epitaxial layers. Note that taking into account the SiC molecular flux toward the walls leads to straightforward renormalization of the growth rate (the appearance of additional factor $f(l/r)$; see Eq. (4)). When the value of $\tilde{G}$ is fitted to the experimental data according to the model described in [5], considering $f(l/r)$ will change mainly the value of dimensionless factor A. The temperature dependence also becomes more complicated, becoming

$$\tilde{G} \propto G\{1 - \bar{A}\exp(-\bar{\omega}_a)[1 - \exp(-l/r)]\},$$

(where $\bar{\omega} \equiv \bar{E}_a/RT_0$) instead of

$$G \propto T^{-1/2}\exp(-\omega),$$

where $\omega \equiv (Q + E_a)/RT_0$).

In this case, to determine additional model parameters $\bar{E}_a$ and $\bar{A}$, extra data points or any simplification like $\bar{\alpha} = \alpha$ are needed.

INFLUENCE OF TEMPERATURE AND PRESSURE GRADIENTS

Now let us discuss the effect of a SiC vapor pressure gradient and a temperature gradient, $\Delta T = T(0) - T(l)$, in the cell on the growth rate ($T(0)$ is the source temperature; $T(l)$ is the substrate temperature; and l is, as above, the source–substrate distance). To this end, we will consider the problem of gas flow through a tube of length l and radius r [7]. Unlike work [7], where it was assumed that $l/r \gg 1$, we take this ratio to be arbitrary ($\lambda \gg r, l$, as before). Then, the flux can be approximated as

$$J = (16/3)\frac{I}{\sqrt{2\pi MR}}\Omega, \quad \Omega \equiv \left(\frac{p(l)}{\sqrt{T(l)}} - \frac{p(0)}{\sqrt{T(0)}}\right),$$
$$I \approx r/l\left[\arctan\frac{l}{2r} + \frac{l}{2r}\left(\frac{l}{2r}\arctan\frac{2r}{l} - 1\right)\right]. \qquad (5)$$

Here, $p(0)$ and $p(l)$ are the SiC vapor pressures above the source and substrate, respectively. For $l/r \gg 1$, Eq. (5) transforms into the corresponding formula in

Table 1. Dependence of substrate temperature T_l on anode current I_a of the oscillating tube and on position z of the growth cell relative to the inductor

z, mm	I_a, A									
	1.00	1.25	1.50	1.75	2.00	2.25	2.50	2.75	3.00	3.25
0	900	1029	1109	1200	1294	1375	1470	1494	1594	1720
5	905	1032	1121	1208	1294	1396	1476	1501	1616	1750
10	909	1043	1127	1221	1306	1414	1482	1513	1627	1760
15	914	1064	1139	1234	1313	1402	1489	1537	1643	1765
20	914	1070	1142	1228	1319	1426	1494	1542	1643	1760
25	919	1093	1150	1228	1324	1426	1489	1548	1648	1755
30	924	1090	1153	1236	1326	1426	1494	1542	1643	1750
35	924	1093	1156	1234	1326	1426	1482	1537	1638	1735
37.5	924	1083	1156	1231	1324	1420	1470	1531	1632	1725

[7] and $I \approx \pi(r/2l)$.[1] In the opposite limit, $l/r \ll 1$, we have $I \approx \pi(l/8r)$.

If the SiC vapor pressure were constant, i.e., the condition $p(0) \approx p(l) \approx p$ were satisfied, we would have

$$\Omega \approx (1/2)(\Delta T/T(0))(p/\sqrt{T(0)}); \quad (6)$$

in other words, the temperature gradient would be the only driving force of the process. Equation (5) implies, however, that, in the general case, the film grows if $\Omega > 0$, because the flux of SiC molecules will be directed from the source to the substrate just under this condition. We then obtain from (5)

$$\sqrt{T(0)/T(l)} > (p(0)/p(l)). \quad (7)$$

Putting $p(0)/p(l) = \alpha J(0)/\tilde{J}$ (see (3) and (4)), we obtain

$$\sqrt{T(0)/T(l)} > (f(l/r))^{-1}. \quad (8)$$

The right of inequality (8) exceeds unity by definition (see (4)). Thus, the condition $T(0)/T(l) > 1$ is a necessary but not sufficient condition for the growth. In fact, the condition $T(0)/T(l) > 1$ may be met even if inequality (8) has a reverse sign. In this case, Ω is negative and the gas flows from the substrate to the source, i.e., the substrate is etched.

Inequality (8) can be recast in the form

$$\frac{\Delta T}{T(l)} > \tau \equiv 2\bar{\alpha}\frac{1-\exp(-l/r)}{f(l/r)}. \quad (9)$$

It follows from (9) that, for $\bar{\alpha} = 0$, the layer grows at any positive temperature gradient ΔT, while at $\bar{\alpha} \neq 0$, ΔT must be finite and increase with l/r. For example, at $(l/r) \ll 1$, we have $\tau \approx 2\bar{\alpha}(l/r)$; at $l/r \gg 1$, $\tau \approx 2\bar{\alpha}/(1-\bar{\alpha})$; and at $l/r = 1$, $\tau \approx 1.26\bar{\alpha}/(1-0.63\bar{\alpha})$.

[1] To derive an expression for flux J, the formula for gas amount Q derived in [7] should be divided by $\pi r^2 M$.

Thus, the growth cell geometry meeting the weak inequality $l/r \leq 1$ is also preferable for producing a temperature gradient. Clearly, sticking coefficient $\bar{\alpha}$ must be low in this case.

SUBSTRATE TEMPERATURE VERSUS SUBSTRATE POSITION RELATIVE TO THE INDUCTION COIL

Table 1 demonstrates the experimental dependence of substrate temperature $T_l(r)$ on current I_a. The coordinate $z = 0$ corresponds to the lowest position of the substrate relative to the bottom of the inductor. The substrate is raised along axis z in 5-mm steps. Our aim is to deduce an analytical dependence for which purpose the results of [8] are invoked. The temperature is assumed to be invariable, so that the time derivatives in the equations are neglected. In addition, parameter κ_{gas}, which is the thermal conductivity of argon in [8], is formally set equal to zero, since the growth proceeds in a vacuum and not in argon. Then, system of equations (1.1) in [8] is replaced by

$$\mathrm{div}(\kappa \mathrm{grad} T) = -\mu, \quad (10)$$

where κ is the thermal conductivity of crystalline SiC and μ is the specific (per unit volume) thermal power generated by the inductor. Later on, subscript l is omitted. We are interested in temperature variation along the z direction, which is aligned with the setup axis. Then, assuming that κ is z-independent, we obtain

$$\frac{d^2T(z)}{dz^2} = -\mu/\kappa \equiv -a. \quad (11)$$

Let us introduce position parameter z^* that is defined by the relationship $(dT/dz)_{z^*} = 0$. At this position of the growth cell, the substrate temperature reaches a maximum, T_{max}, for given current I_a. Let the temperature corresponding to $z = 0$ be denoted as Θ

Table 2. Substrate temperature T_l (°C) calculated as a function of position z (mm) of the substrate relative to the inductor for different values of current I_a(A)

z	0	5	10	15	20	25	30	35	37.5
I_a = 1 A, z^* = 35 mm, Θ = 900°C, T_{max} = 924°C									
T_l^{theor}	900	906	912	916	920	922	924	924	924
T_l^{exp}	900	905	909	914	914	919	924	924	924
I_a = 2 A, z^* = 32.5 mm, Θ = 1294°C, T_{max} = 1326°C									
T_l^{theor}	1294	1303	1311	1317	1322	1324	1326	1326	1325
T_l^{exp}	1294	1294	1306	1313	1319	1324	1326	1326	1324
I_a = 3 A, z^* = 25 mm, Θ = 1594°C, T_{max} = 1648°C									
T_l^{theor}	1594	1613	1629	1639	1646	1648	1646	1639	1635
T_l^{exp}	1594	1616	1627	1643	1643	1648	1643	1638	1632
I_a = 3.25 A, z^* = 15 mm, Θ = 1720°C, T_{max} = 1765°C									
T_l^{theor}	1720	1745	1760	1765	1760	1745	1720	1685	1664
T_l^{exp}	1720	1750	1760	1765	1760	1755	1750	1735	1725

(obviously, Θ is a function of I_a). Then, we finally arrive at

$$T = T_{max} - (T_{max} - \Theta)(1 - z/z^*)^2. \quad (12)$$

Note that

$$a = 2(T_{max} - \Theta)/(z^*)^2. \quad (13)$$

Having determined the values of z^*, T_{max}, and Θ from the experimental dependences of T_l on I_a (omitted), we calculated substrate temperature $T_l(z)$ (Table 1). For I_a = 1, 2, and 3 A, theory and experiment are in excellent agreement, while for I_a = 3.25 A, the calculation underpredicts T_l at $z > z^*$. The asymmetric run of the curve $T_l(z)$ at I_a = 3.25 A is noteworthy.

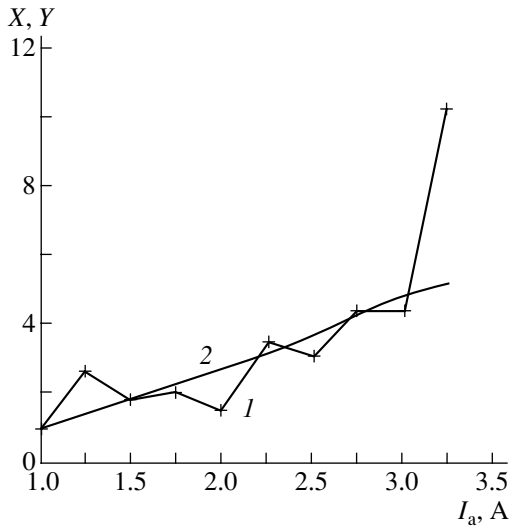

Fig. 2. (*1*) $X = a(I_a)/a(I_a = 1\ A)$ and (*2*) $Y = I_a^2\,\kappa_1/(I_a = 1\ A)^2\kappa$ as a function of I_a.

Figure 2 shows the ratio of coefficients a (see (13)) in the form $X = a(I_a)/a(I_a = 1\ A)$ versus I_a (curve *1*). Since $a \propto \mu$ (see (11)) and specific thermal power μ is proportional to the current squared [8], Fig. 2 also shows the dependence of ratio $Y = I_a^2\,\kappa_1/(I_a = 1\ A)^2\kappa$ on I_a (curve *2*). Here, κ_1 is the thermal conductivity at temperature Θ corresponding to I_a = 1 A and κ corresponds to temperatures Θ for I_a = 1.25, 1.5 A, etc. (Table 2). The temperature dependence of the thermal conductivity for 6H-SiC were taken from [9].

In view of the fact that the approximation is crude, one can conclude that curves *1* and *2* are in fairly good agreement in the range $1 \le I_a \le 3$ A and diverge severely (by a factor of two) at I_a = 3.25 A. The reasons for such a discrepancy still remain unclear.

ACKNOWLEDGMENTS

This work was partially supported by the Russian Foundation for Basic Research (project no. 03-02-16054b); INTAS (project no. 01-0603); and NATO SfP (project no. 978011).

REFERENCES

1. A. I. Zhmakin, Yu. N. Makarov, D. Kh. Ofengeim, and M. S. Ramm, in *Problems of Mathematics Physics and Applied Mathematics* (Ioffe Physicotechnical Institute, Russian Academy of Sciences, St. Petersburg, 2001), pp. 208–234 [in Russian].
2. M. Selder, L. Kadinsky, and F. Durst, in *Problems of Mathematics Physics and Applied Mathematics* (Ioffe Physicotechnical Institute, Russian Academy of Sciences, St. Petersburg, 2001), pp. 235–252 [in Russian].
3. E. Kaldis and M. Piechotka, in *Handbook of Crystal Growth*, Ed. by D. Hurle (Elsevier, Amsterdam, 1994), Vol. 2, pp. 615–656.
4. K. F. Jensen, in *Handbook of Crystal Growth*, Ed. by D. Hurle (Elsevier, Amsterdam, 1994), Vol. 3, pp. 543–599.
5. S. Yu. Davydov, A. A. Lebedev, N. S. Savkina, *et al.*, Fiz. Tekh. Poluprovodn. (St. Petersburg) **38**, 153 (2004) [Semiconductors **38**, 150 (2004)].
6. N. S. Savkina, A. A. Levedev, D. V. Davydov, *et al.*, Mater. Sci. Eng., B **61–62**, 50 (2000).
7. L. D. Landau and E. M. Lifshitz, *Course of Theoretical Physics*, Vol. 10: *Physical Kinetics* (Nauka, Moscow, 1979; Pergamon, New York, 1981).
8. O. Klein and P. Philip, J. Cryst. Growth **247**, 219 (2003).
9. O. Nilsson, H. Mehling, R. Horn, *et al.*, High Temp.–High Press. **29**, 73 (1997).

Translated by M. Astrov

Technical Physics, Vol. 50, No. 4, 2005, pp. 508–512. Translated from Zhurnal Tekhnicheskoĭ Fiziki, Vol. 75, No. 4, 2005, pp. 118–121.

SHORT COMMUNICATIONS

Townsend Coefficient and Runaway of Electrons at Relativistic Velocities

A. N. Tkachev and S. I. Yakovlenko

General Physics Institute, Russian Academy of Sciences, ul. Vavilova 3, Moscow, 119991 Russia

Received March 17, 2004

Abstract—An electron-multiplication regime at large field strengths, in which case an electron can acquire a relativistic kinetic energy over the multiplication length, is considered. It is shown that, even in such superstrong fields, the Townsend electron-multiplication mechanism is valid if the distance between the electrodes is rather large. The Townsend coefficient and the drift velocity in helium are obtained in such fields. The electron-escape curve, which separates the region of efficient electron multiplication from the region where electrons escape from the gap without undergoing multiplication, is obtained. © *2005 Pleiades Publishing, Inc.*

INTRODUCTION

On the basis of a simulation by the method of multiparticle dynamics, it was recently revealed [1–3] that, if the distance between the electrodes is rather large, the Townsend regime of ionization is realized even in high fields, where the ionization friction can be disregarded and where a continuous growth of the mean energy of electrons is expected according the traditional point of view [4–6]. It was also found that the Townsend coefficient depends nonmonotonically on the ratio of the field strength to pressure. A nonmonotonic behavior of the multiplication coefficient leads to the double-valuedness of the curves that separate the region of intense electron multiplication from the region of electron escape without multiplication (analogs of Paschen curves). These results are especially important in connection with obtaining electron beams of subnanosecond duration and record current amplitude (about 70 A in air and about 200 A in helium) at atmospheric pressure [7].

Not very high voltages, at which relativistic effects can be disregarded, were considered previously. Since the creation of generators in which a megavolt voltage is reached within a nanosecond, it would be of interest to assess the degree of applicability of the Townsend coefficient concept at relativistic electron speeds. Below, this issue is considered for the example of helium.

MULTIPLICATION AND STICKING OF ELECTRONS

Description of the model used. The multiplication and runaway of electrons in helium were simulated on the basis of one of the modifications of the particle method [8]. Specifically, we considered the multiplication of electrons and their transfer between two planes that are separated by a distance d and between which a constant voltage U was applied (the field strength is then $E = U/d$) long before the appearance of the electrons in question. The electrons were produced at the cathode, having chaotic directions of the velocities, their initial energies obeying the Poisson distribution at a mean value of $\varepsilon_0 = 0.2$ eV. At small time steps, we solved the equations of motion for all electrons and simulated elastic and inelastic collisions with probabilities determined by cross sections for elementary processes.

The cross sections used in the present study for various elementary events were given in [1]. In contrast to what was done in [1], however, we employ here, for the ionization cross section, an approximation that includes relativistic effects,

$$\sigma_i(\varepsilon) = \frac{f_1(\varepsilon) f_2(\varepsilon)}{f_1(\varepsilon) + f_2(\varepsilon)}\ \text{cm}^2,$$

$$f_1(\varepsilon) = 1.3\times 10^{-18}(\varepsilon - I)\frac{1 + 3\times 10^{-6}(\varepsilon - I)^2}{1 + 0.009(\varepsilon - I)},$$

$$f_2(\varepsilon) = 2.05\times 10^{-15}\left\{\frac{2.36}{\varepsilon} + \frac{2\gamma^2}{\gamma+1}\frac{1}{\varepsilon}\left[\ln\frac{\varepsilon}{I}\sqrt{\frac{\gamma+1}{2}}\right.\right.$$

$$\left.\left. + \left(\frac{1}{\gamma} - \frac{1}{2\gamma^2}\right)\ln 2 + \frac{1}{2\gamma^2} + \frac{(\gamma-1)^2}{16\gamma^2}\right]\right\}.$$

Here, $\varepsilon = m_e c^2(\gamma - 1)$ is the kinetic energy of an incident electron (the rest mass being subtracted) in eV; $I = 24$ eV is the ionization energy of the helium atom; and $\gamma = (1 - \nu^2/c^2)^{-1/2}$, ν being the electron speed. We note

1063-7842/05/5004-0508$26.00 © 2005 Pleiades Publishing, Inc.

that the cross section has a minimum at $\varepsilon \approx 4m_e c^2 \approx 2 \times 10^6$ eV (see Fig. 1).

Electron trajectory. Suppose that the electric field of strength **E** is directed along the *x* axis and that, at the initial instant $t = 0$, the electron being considered has the coordinates $x(0)$, $y(0)$, and $z(0) = 0$ and the momenta $p_x(0)$, $p_y(0)$, and $p_z(0)$.

For the momentum at an arbitrary instant *t*, the solution to the equation of motion $d\mathbf{p}/dt = \mathbf{F} \equiv e\mathbf{E}$ yields

$$p_x(t) - p_x(0) = Ft; \quad p_y(t) - p_y(0) = 0; \quad p_z(t) - p_z(0) = 0. \tag{1}$$

The velocities are expressed in terms of the momenta by using the relation (which is valid at an arbitrary instant *t*) [9, 10]

$$\mathbf{v}(t) = \frac{\mathbf{p}(t)c^2}{W(t)}, \tag{2}$$

where

$$W(t) = c\sqrt{m^2c^2 + p^2(t)} \tag{3}$$

is the particle energy at the instant *t*.

The coordinates are obtained by integrating the velocities with respect to time. For an arbitrary instant *t*, this yields

$$x(t) - x(0) = \frac{1}{F}[W(t) - W(0)], \tag{4a}$$

$$y(t) - y(0) = \frac{p_y(0)c}{F}\ln\frac{W(t) + cp_x(t)}{W(0) + cp_x(0)}, \tag{4b}$$

$$z(t) - z(0) = \frac{p_z(0)c}{F}\ln\frac{W(t) + cp_x(t)}{W(0) + cp_x(0)}. \tag{4c}$$

In [10], this result was obtained by a more cumbersome method.

Formulas convenient for calculations. Formulas (1)–(4) solve the problem at hand completely, but they are not convenient for numerical calculations. The point is that, in the case of low velocities (momenta), the calculation of the coordinates by formulas (4) would lead to errors because of errors in rounding. In view of this, it is better to transform Eqs. (4a)—(4c) identically in order to single out leading terms in the momentum. For this, we make, in Eq. (4a), the identical transformation

$$W(t) - W(0) \longrightarrow \frac{(W(t) - W(0))(W(t) + W(0))}{W(t) + W(0)} = \frac{W^2(t) - W^2(0)}{W(t) + W(0)},$$

express the squares of the energies in terms of the momenta, and collect similar terms. Further, we transform the expression under the logarithm sign in (4b) with the aid of the chain of equalities

$$\frac{W(t) + cp_x(t)}{W(0) + cp_x(0)} = \frac{W(t) - W(0) + W(0) + cp_x(t) - cp_x(0) + cp_x(0)}{W(0) + cp_x(0)} = 1 + \frac{W(t) - W(0) + cFt}{W(0) + cp_x(0)}$$

and express the difference $W(t) - W(0)$ in terms of $x(t) - x(0)$ by formula (4a).

As a result, the expressions for the coordinates assume the form

$$x(t) - x(0) = \frac{c^2}{F}\frac{(p_x(t) - p_x(0))(p_x(t) + p_x(0))}{W(t) + W(0)},$$

$$y(t) - y(0) = \frac{p_y(0)c}{F} \times \ln\left[1 + \frac{F(x(t) - x(0)) + cFt}{W(0) + cp_x(0)}\right], \tag{5}$$

$$z(t) - z(0) = \frac{p_{zy}(0)c}{F} \times \ln\left[1 + \frac{F(x(t) - x(0)) + cFt}{W(0) + cp_x(0)}\right],$$

which is convenient for calculations.

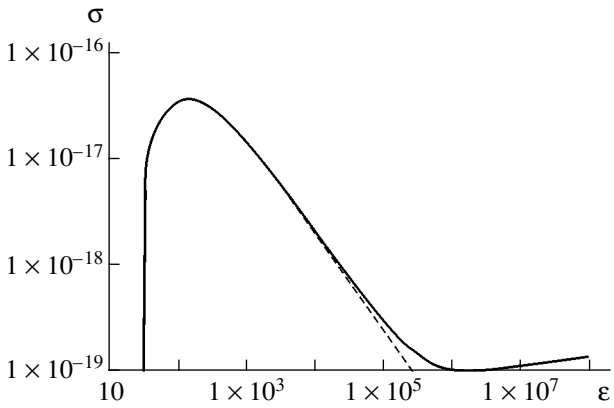

Fig. 1. Cross section for the ionization of a helium atom as a function of the incident-electron energy: (solid line) cross section used in the present study and (dashed line) cross section used in [1].

RESULTS OF THE CALCULATIONS

Townsend regime of ionization. As is well known, the Townsend regime of gas ionization in an external electric field is characterized by two features. First, the number of ionization events grows exponentially with

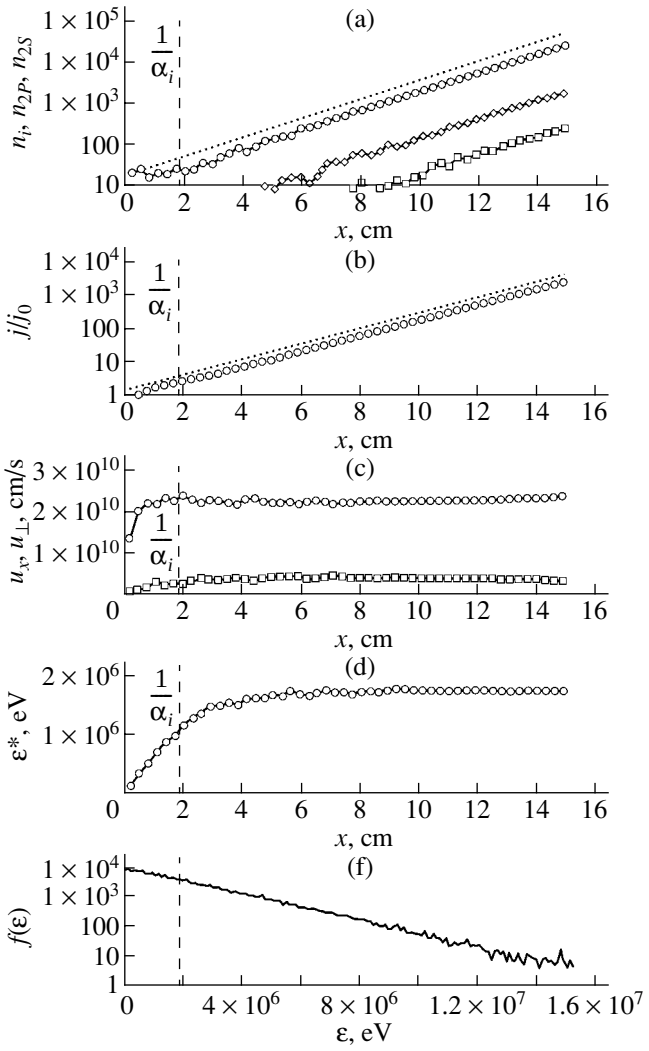

Fig. 2. Properties of electron multiplication in the Townsend regime vs. the distance x from the cathode at $N = 3.2 \times 10^{18}$ cm^{-3} (p = 100 Torr), U = 15 MV, d = 15 cm, and E = 10 MV/cm (E/p = 7.7 MV/(cm atm): (a) number n_i of product ions (circles) and number of atoms excited to the 2^1P (n_{2P}, diamonds) and 2^1S (n_{2S}, boxes) states, along with the dependence 20exp(0.53x/cm) at $\alpha_i = 0.53$ cm^{-1} and $\alpha_i d \approx 8$ (dotted line); (b) ratio of the electron flux at a given point, $j(x)$, to the electron flux from the cathode, j_0, along with the dependence 1.7exp(0.53x/cm) (dotted line); (c) projection u_x of the electron velocity onto the x axis aligned with the electric field (circles) and modulus of the velocity $u_\perp$ in the plane orthogonal to the x axis (boxes); (d) mean electron energy (the steady-state value of the mean energy, ε* ≈ 1.5 MeV ≈ $3m_ec^2$, is much less than eU = 15 MeV); and (f) energy (eV) distribution of electrons that reached the anode (arbitrary units).

increasing distance from the point at which the first electron was produced. Second, the mean speed and the mean energy of the electrons do not depend on this distance. As in [1–3], the Townsend multiplication coefficient was accordingly determined from the slope of the dependence of the logarithm of the electron current on the distance from the cathode (see Fig. 2). The slope takes the same value for the logarithm of the number of ionization, sticking, and excitation events. Of course, the distance between the electrodes must exceed the inverse Townsend coefficient (multiplication length α_i^{-1}).

The calculations reveal that, at rather large distances between the electrodes, $d > \alpha_i^{-1}$, the Townsend ionization regime is realized even in the case where the mean speed and the mean energy of the electrons are relativistic, $\varepsilon^* \sim m_ec^2 \approx 0.5 \times 10^6$ eV. The main features of this regime are qualitatively similar to those in the case of nonrelativistic speeds (Fig. 2). As the distance x from the cathode increases, the number of electron-production events grows exponentially, along with the number of inelastic collisions. Also, the mean energy of the electrons, ε*; the mean projection of the velocity onto the field direction, u_x; and the mean projection of the velocity onto the plane orthogonal to the field, $u_\perp$, take values independent of x. The distribution of electrons that reached the anode peaks in the region of low energies, $\varepsilon^* \ll eU$. The Townsend regime of ionization sets in at some distance from the cathode, $x \sim \alpha_i^{-1}$, this distance corresponding to the characteristic multiplication length.

As might have been expected, the Townsend coefficient α_i as a function of E/p (Fig. 3) decreases sharply after attaining a maximum at $E/p \approx 200$ kV/(atm cm) (this maximum was revealed in [1]), but, because of the boundedness of the mean speed, it then reaches a constant value. This occurs at $E/p \approx 5$ MV/(atm cm) with ε* ≈ 0.5 MeV and $u_x \approx 2.3 \times 10^{10}$ cm/s.

Escape curve. In contrast to the conventional approach advocated in [4–6], it was proposed in [1–3] to assume that runaway electrons appear to be dominant in the case where the distance d between the electrodes becomes commensurate with the characteristic multiplication length—that is, with the inverse Townsend coefficient α_i^{-1}. For $\alpha_i d < 1$, electrons that run away also dominate the spectrum of electrons that reach the anode. Accordingly, the criterion that determines the boundary value of the field strength E_{cr} has the form

$$\alpha_i(E_{cr}, p)d = 1.$$

In the Townsend coefficient, we factor out pressure or the gas density and consider that the remaining factor depends only on the reduced field strength E/p: $\alpha_i(E/p) = p\xi(E/p)$. For flat electrodes, $E = U/d$; also, $E_{cr} = U_{cr}/d$. The criterion for the escape of electrons

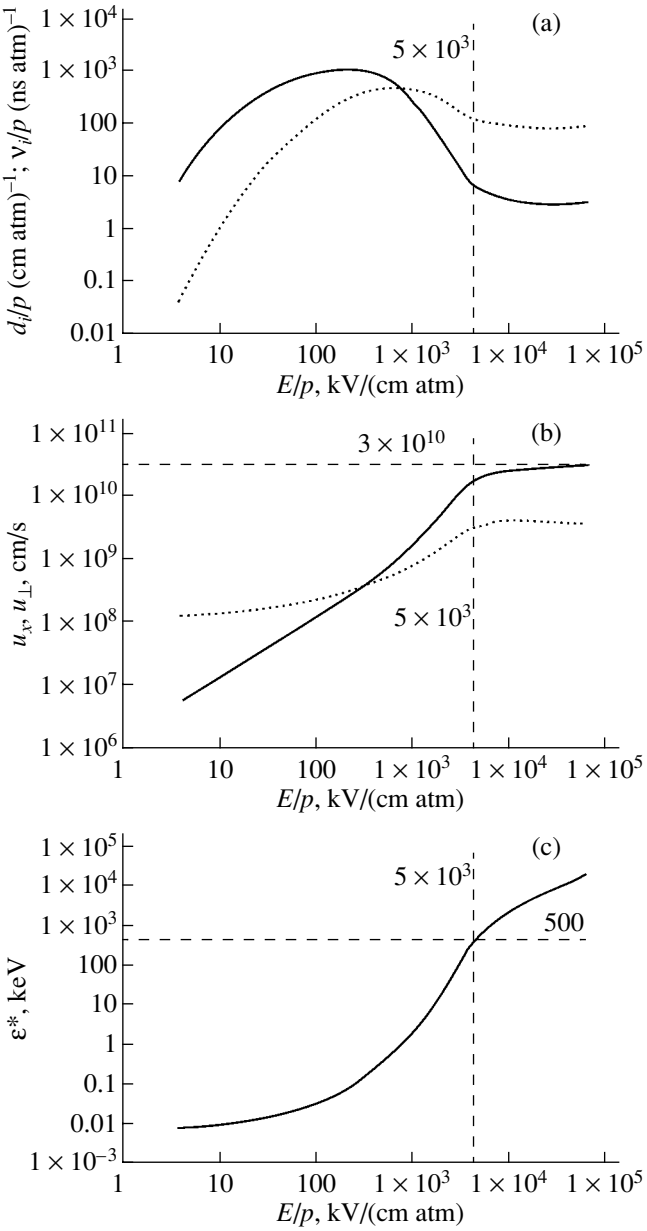

Fig. 3. Ionization and drift features vs. the reduced field strength E/p (points were obtained at various values of the field strength for p = 100 Torr): (a) Townsend coefficient normalized to pressure, α_i/p (solid line), and ionization frequency normalized to pressure, ν_i/p (dotted curve); (b) mean projection u_x of the electron velocity onto the x axis aligned with the electric field (circles) and mean modulus of the velocity $u_\perp$ in the plane orthogonal to the x axis (boxes); and (c) mean electron energy.

from the gap between the electrodes then assumes the form

$$pd\xi(E_{cr}p) = 1, \quad \text{or} \quad pd\xi(U_{cr}pd) = 1. \qquad (6)$$

Equation (6) provides an implicit dependence of the critical voltage $U_{cr}(pd)$ on the product of the distance between the electrodes and pressure, pd. This dependence is illustrated in Fig. 4. The electron-escape curve $U_{cr}(pd)$ separates the region of efficient electron multiplication from the region in which electrons leave the discharge gap without undergoing multiplication. This curve is universal for a given gas.

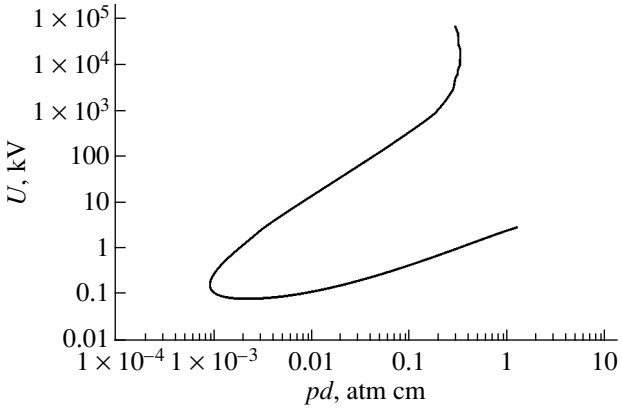

Fig. 4. Universal curve $U_{cr}(pd)$ separating the region of electron escape without significant multiplication (outer region) from the region of intense multiplication (inner region).

One can single out three branches on the electron-escape curve $U_{cr}(pd)$ (see Fig. 4). The lower two branches are similar to the escape-curve branches obtained for the nonrelativistic case in [1]. The fact that there appear the turning point at $pd \sim 0.3$ atm cm on the upper branch of the nonrelativistic escape curve and, accordingly, the third branch, which was absent in the nonrelativistic case, is due to an increase in the ionization cross section at high energies because of relativistic effects. We note that, for $pd > 0.3$ atm cm, the multiplication of electrons occurs, in contrast to what we have in the nonrelativistic case, at any values of the voltage across the discharge gap that exceed the threshold determined by the lower branch of the escape curve.

CONCLUSION

We have considered the regime of electron multiplication at high field strengths, in which case an electron can acquire a relativistic kinetic energy over the multiplication length. It has been shown that, even in such superstrong fields, the Townsend electron-multiplication mechanism is realized if the distance between the electrodes is rather large.

REFERENCES

1. A. N. Tkachev and S. I. Yakovlenko, Pis'ma Zh. Éksp. Teor. Fiz. **77**, 264 (2003) [JETP Lett. **77**, 221 (2003)].
2. A. N. Tkachev and S. I. Yakovlenko, Pis'ma Zh. Tekh. Fiz. **29** (16), 54 (2003) [Tech. Phys. Lett. **29**, 683 (2003)].

3. A. M. Boĭchenko, A. N. Tkachev, and S. I. Yakovlenko, Pis'ma Zh. Éksp. Teor. Fiz. **78**, 1223 (2003) [JETP Lett. **78**, 709 (2003)].

4. L. P. Babich, T. V. Loĭko, and V. A. Tsukerman, Usp. Fiz. Nauk **160** (7), 49 (1990) [Sov. Phys. Usp. **33**, 521 (1990)].

5. Yu. D. Korolev and G. A. Mesyats, *The Physics of Impulse Breakdown in Gases* (Nauka, Moscow, 1991) [in Russian].

6. Yu. P. Raizer, *Gas Discharge Physics* (Nauka, Moscow, 1992; Springer-Verlag, Berlin, 1991).

7. V. F. Tarasenko, S. I. Yakovlenko, V. M. Orlovskiĭ, *et al.*, Pis'ma Zh. Éksp. Teor. Fiz. **77**, 737 (2003) [JETP Lett. **77**, 611 (2003)].

8. A. N. Tkachev and S. I. Yakovlenko, Laser Phys. **12**, 1022 (2002).

9. L. D. Landau and E. M. Lifshitz, *Course of Theoretical Physics*, Vol. 2: *The Classical Theory of Fields* (Nauka, Moscow, 1988; Pergamon, Oxford, 1975).

10. V. V. Batygin and I. N. Toptygin, *Problems in Electrodynamics* (Fizmatgiz, Moscow, 1962; Academic, London, 1964).

Translated by A. Isaakyan

Technical Physics, Vol. 50, No. 4, 2005, pp. 513–516. Translated from Zhurnal Tekhnicheskoĭ Fiziki, Vol. 75, No. 4, 2005, pp. 122–124.

SHORT COMMUNICATIONS

Angular Splitting of the Bragg Diffraction Order in an Acoustooptical Modulator Due to a Frequency-Modulated Acoustic Wave

S. N. Antonov

Institute of Radio Engineering and Electronics, Russian Academy of Sciences (Fryazino Branch), pl. Vvedenskogo 1, Fryazino, Moscow oblast, 141120 Russia

e-mail: olga-ant@yandex.ru

Received April 2, 2004; in final form, September 4, 2004

Abstract—Effects of angular splitting of the Bragg diffraction order arising in light acoustooptical diffraction by a frequency-modulated acoustic wave are considered. These effects occur when the size of the light spot in the acoustooptical interaction zone exceeds the characteristic spatial period of the modulating function. The Bragg diffraction order is found to be split into several beams. The directions of the additional beams, their number, and intensities are determined by the modulation parameters. In particular, there occurs a situation where the diffracted field consists of three beams of equal intensity spaced at a distance approximately equal to the diffraction divergence of the incident beam and the diffraction total efficiency is of the order of 100%. Therein lies the difference between this diffraction regime and the case where several independent acoustic waves are generated in the interaction domain and the diffraction total efficiency is limited to the intermodulation arisen. The effect is used in design of modulators for systems of image plotting with the help of high-power lasers. © *2005 Pleiades Publishing, Inc.*

In a number of engineering problems connected with the use of acoustooptical (AO) Bragg modulators, it is necessary to form a diffracted field consisting of several beams which are close in the angular space. A basic requirement here is that the formation of such a field involves no significant losses in light energy. In other words, if a single Bragg diffraction order is transformed into several beams, the total power should not decrease. In particular, such a requirement arises in thermal imaging systems using a high-power laser, where the distribution of energy over the light spot on the material being processed should be modified directly in the process of image recording [1].

Note that, when solving such a problem by the obvious method of exciting several acoustic waves with close frequencies in an AO medium, the total power of the diffraction orders is basically limited. This limitation is due to the transfer of light power into intermodulation orders. For instance, a well-known fact established in [2] is that, two independent acoustic waves with close frequencies being supplied at the acoustic line of an AO modulator, the maximal efficiency of diffraction of two diffraction orders with close angles does not exceed 68%.

In this paper, some features of AO interaction are presented, which motivate the splitting of Bragg diffraction order without loss in optical power. This solves the engineering problem posed above to a higher degree.

Experiment conditions are given in Fig. 1. Here, optical radiation *3* with spot size *d* is transmitted trough AO modulator *1* with piezoelectric transducer *2* (the plane of the diagram is orthogonal to the plane of diffraction). The acoustic wave is a frequency-modulated signal whose angular frequency $\omega(t)$ at instant t is given

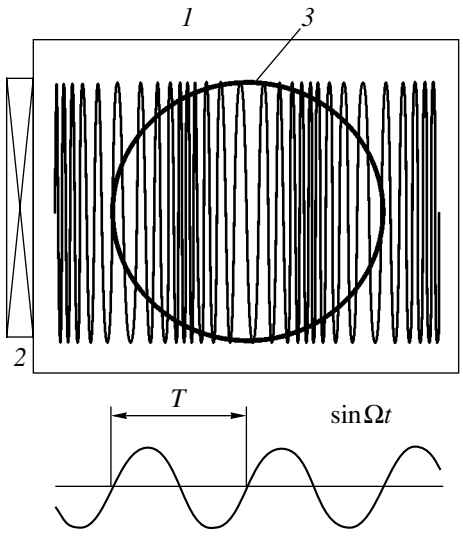

Fig. 1. Relations between the size of the light beam and the variation period of the sound wave frequency.

1063-7842/05/5004-0513$26.00

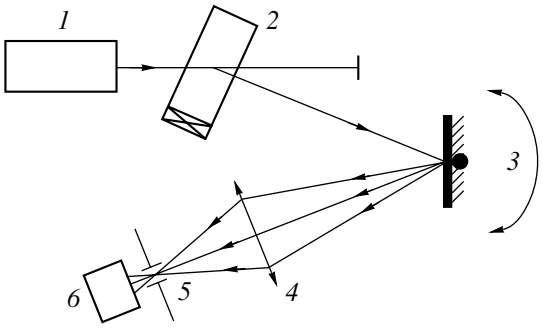

Fig. 2. Experimental setup.

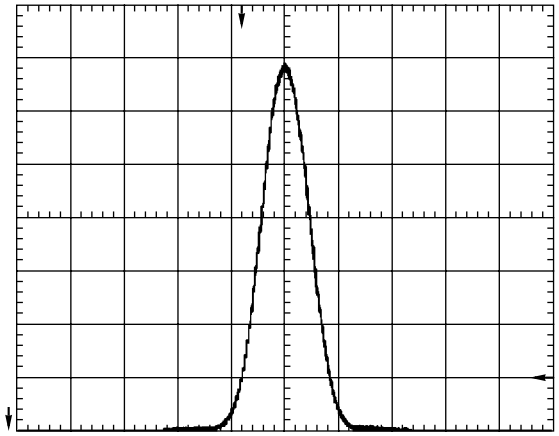

Fig. 3. Angular spectrum of the unmodulated Bragg diffraction order.

by the known expression

$$\omega(t) = \omega_0 + \Delta\omega_m \sin\Omega t, \qquad (1)$$

where ω_0 is the central value of frequency, $\Delta\omega_m$ is the maximal deviation of frequency from the central value, and Ω is the angular frequency of the modulating signal.

Measured in Hz, the frequencies are $\omega_0 = 2\pi f_0$, $\Delta\omega_m = 2\pi\Delta f_m$, and $\Omega = 3\pi F$. The frequency modulation index is then equal to $M = \Delta f_m/F$. The spatial period T of the modulating function can be written as $T = v/F$. The experimental setup is schematized in Fig. 2. Here, laser beam *1* is supplied at Bragg cell *2*. The diffracted beam at the cell output is directed toward angle scanning mirror *3*. Reflected from the mirror, the beam is incident on lens *4* with diaphragm *5* and photodetector *6* mounted in the focal plane. Such a system gives the time-base sweep of the angular spectrum of the diffracted beam. As an AO medium, a TeO_2 single crystal is taken in the regime of anisotropic diffraction by a slow acoustic wave (the velocity of the acoustic wave is $v = 0.617 \times 10^6$ mm/s). A single-mode fiber laser emitting at wavelength $\lambda = 1.06$ μm with linear polarization and light spot aperture $d = 0.6$ mm in the AO interaction zone (the beam divergence is of the order of 2 mrad) is used. The sound central frequency in the AO modulator is equal to $f_0 = 34$ MHz. The frequency F of the modulating function is varied within a range from 0 to 2 MHz and the deviation value, to 3 MHz.

Figure 3 shows an oscillogram of the detected signal in the absence of modulation. From here on, a large horizontal mesh of the screen corresponds to 1.4 mrad. In all experiments, the acoustic wave power remains constant and provides unmodulated diffraction at least 95% efficient.

The modulating function frequency being low, i.e., when $T > d$, the Bragg beam is scanned around the central position at frequency F, which is well known in acoustooptics [3]. The enhancement of F results in decreased scanning amplitude. As soon as the value F_k corresponding to the equality $T = d$ is attained (in our case, $F_k \approx 1$ MHz), the scanning terminates. As frequency F exceeds this value, two side diffraction orders of intensity proportional to the frequency modulation index arise around the central beam. Such a situation is illustrated by Fig. 4, where $F = 1.1$ MHz and modulation index $M = 1.5$. The beam is seen to be split into two additional beams and the interference pattern at frequency F between the maximums of the central and

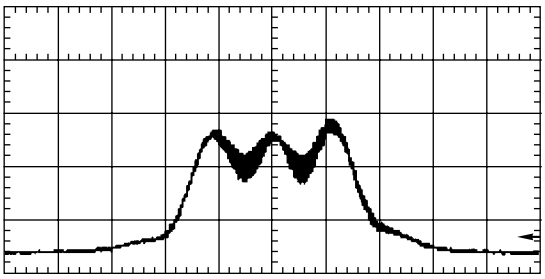

Fig. 4. Diffracted field for $F = 1.1$ MHz, $\Delta f_m = 1.65$ MHz, and $M = 1.5$.

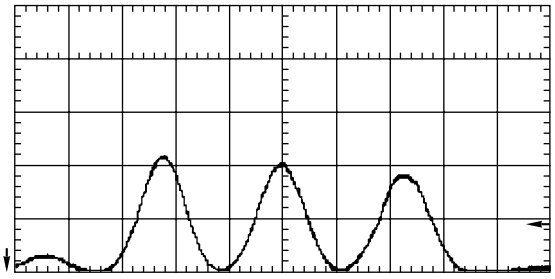

Fig. 5. Diffracted field for $F = 1.1$ MHz, $\Delta f_m = 1.65$ MHz, and $M = 1.5$.

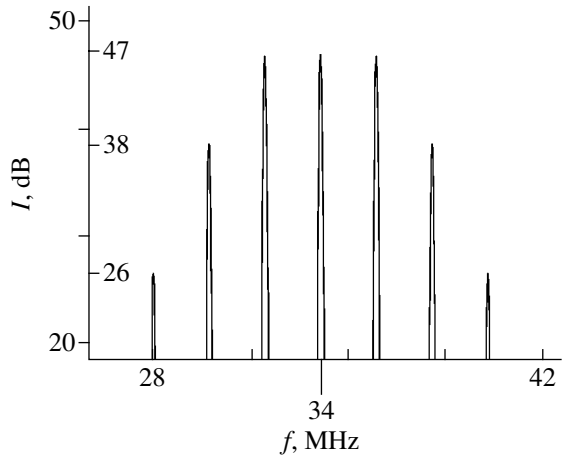

Fig. 6. Calculated spectrum of the electric signal.

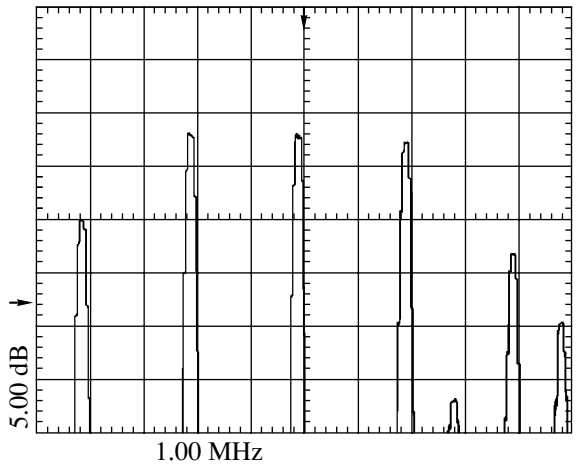

Fig. 7. Spectrum of the signal supplied to the piezoelectric transducer. A large horizontal cell corresponds to 1 MHz, and a vertical one, to 5 dB.

side diffraction orders is observed (due to their intersection).

When the value F_d is attained, the side beams degenerate into individual separated diffraction orders (in the experiment conditions, $F_d \approx 1.4$ MHz) and the interference pattern vanishes. Figure 5 shows the oscillogram of the detected signal at frequency $F = 2$ MHz, which corresponds to $T = d/2 = 0.3$ mm. Here, about two periods of the modulating function fit within the light spot. It is demonstrative that, the intensities of the obtained three beams being summed, the total intensity approximately amounts to 90% of the unmodulated beam intensity. Hence, almost all the light energy is allocated to these three diffraction maximums. A further enhancement of value M results in suppressing the principal diffraction order and generating additional beams.

To interpret the picture observed, consider the frequency spectra of frequency-modulated signal (1). For small modulation indices, the spectrum of such a signal is little different from that of the amplitude-modulated signal and consists of a high-intensity central component and two side components of low intensity. The specific features become apparent for M close to unity and higher. Figure 6 shows the calculated spectrum that corresponds to the signal presented in Fig. 5. Here, I denotes the relative intensity of the spectral components and f is the frequency. The distance between the components is seen to be equal to the modulating function frequency $F = 2$ MHz. Moreover, the first two side components are of the same intensity as the central one (at frequency $f = 34$ MHz), while the next components (at frequencies 30 and 38 MHz) are 9-dB suppressed. Figure 7 demonstrates the signal spectrum for the above experiment measured by means of a spectrum analyzer. The experimental data are seen to be in good agreement with the calculations.

Thus, a rapid and multiple (in light aperture) variation of sound frequency gives rise to diffraction orders corresponding to the spectral components of the sound wave. It is important that these diffraction orders are of a constant amplitude, their total power is approximately equal to the power of the (unmodulated) principal order, and the number of arising beams is determined by the depth of frequency modulation (modulation index).

It should be noted that no essential effects of intermodulation occur. In the experimental conditions corresponding to Fig. 5 (the maximal efficiency of three separate diffraction beams), the intensity of maximums that arise near the zeroth order is within 3–5% of the total intensity of diffraction maximums.

CONCLUSIONS

Summing up, we can say that, in conditions where $T < d$, the diffracted beam is split into several beams with the angular distance $\Delta\alpha$ between them determined by the obvious relation

$$\sin\Delta\alpha = \lambda F/v. \qquad (2)$$

With the use of relation (2) and expression $\Delta\Theta = 4\lambda/\pi d$ for the total divergence of the laser beam, the value of the modulating function at which the arising side beams are completely separated from the original beam can be written (with due regard for the smallness of angles) in the form

$$F_d = 4v/\pi d. \qquad (3)$$

Note that the experimentally obtained value $F_d = 1.4$ MHz is in good agreement with the calculated one.

The discovered effect is undeniably useful in practical applications and might be of interest for theorists both from the viewpoint of deeper investigation and for the purposes of optimization in various applications. However, it should not be overlooked that the explicit analytical expression describing this regime of AO

interaction (with due account taken of the high diffraction efficiency) is very hard to find.

Acoustooptical modulators based on the described interaction are employed in computer-to-plate equipment for flexo plate processes, photo stencil systems, and laser markers ("Al'fa" Research and Production Center, Moscow, http//www.alphalaser.ru).

ACKNOWLEDGMENTS

The author is grateful to V.I. Mirgorodskiĭ for his help in mathematical simulation of signal spectra.

REFERENCES

1. S. N. Antonov and V. I. Mirgorodskiĭ, Zh. Tekh. Fiz. **74** (1), 84 (2004) [Tech. Phys. **49**, 83 (2004)].
2. D. Hecht, IEEE Trans. Sonics Ultrason. **24**, 7 (1977).
3. L. N. Magdich and V. Ya. Molchanov, *Acoustooptic Devices and Their Applications* (Sov. Radio, Moscow, 1978; Gordon and Breach, New York, 1988).

Translated by A. Pankrat'ev

Technical Physics, Vol. 50, No. 4, 2005, pp. 517–519. Translated from Zhurnal Tekhnicheskoĭ Fiziki, Vol. 75, No. 4, 2005, pp. 125–127.

SHORT COMMUNICATIONS

Effect of Discharge Incorporation into a Solid Insulator Immersed in an Insulating Fluid

G. A. Vorob'ev

Tomsk State University of Control Systems and Radio Electronics, Tomsk, 634050 Russia

e-mail: office@tusur.ru

Received May 14, 2004

Abstract—When a solid insulator with electrodes on its surface is immersed in an insulating fluid and a high-voltage pulse with a rise time of several microseconds is applied to the electrodes, which generate a nonuniform electric field, the solid insulator experiences destructive breakdown. © *2005 Pleiades Publishing, Inc.*

The phenomenon being discussed in this article is of great applied significance if a solid insulator involved in the process is void-free and consolidate and has a dielectric strength E on the order of 10^8 V/m. The phenomenon has been formally recognized as a discovery [1].

The history of the effect dates back to the mid-1950s, when A.A. Vorob'ev repeatedly put forward the idea of rock destruction (crushing, cutting, well boring, etc.) by application of high-voltage pulses. For practical implementation of this idea, it is necessary that the electrodes be closely spaced and that the discharge be initiated in a solid insulator rather than in the environment, which is usually a liquid or air. Therefore, below, we will consider two media: a solid insulator and an insulating fluid.

The time variation of the voltage (the so-called voltage–second characteristic [2–4]) was taken as an appropriate breakdown characteristic for these media. Figure 1 [5, Fig. 6.26] shows the voltage–second characteristics for two solid insulators (ice and organic glass) and transformer oil in the case of the tip–plane electrode configuration with the tip charged positively. When the tip is under a positive potential, the breakdown voltage of solid insulators is lower than that at negative polarity of the tip. For transformer oil, polarity has an insignificant effect and the breakdown voltages are nearly the same at any polarity of the tip electrode [5]. The breakdown voltages were recalculated for an electrode gap of 4 cm, since the minimum bores were equal to 8 cm. As is seen from Fig. 1, the voltage–second characteristics for the solid insulators and transformer oil intersect at points *a* and *b*. This means that, for exposure times shorter than those corresponding to points *a* and *b*, the breakdown voltage of transformer oil exceeds the breakdown voltages of the solid insulators.

Chepikov verified this fascinating effect experimentally [3]. A metallic ring-shaped electrode with an inner diameter of 8 cm was applied on the surface of a solid insulator immersed in transformer oil. The ring was grounded. A tip electrode to which a high-voltage positive pulse was applied was brought into contact with the surface of the solid insulator. At a pulse duration of 10^{-5} s or more, the discharge apparently propagated over the solid insulating surface, visualizing carbon filaments due to oil decomposition by a sequence of earlier discharges. However, when the pulse leading edge was several microseconds long, the discharge penetrated into the solid insulator. As a solid insulator, we used Teflon, which offers a high cracking resistance when subjected to the discharge.

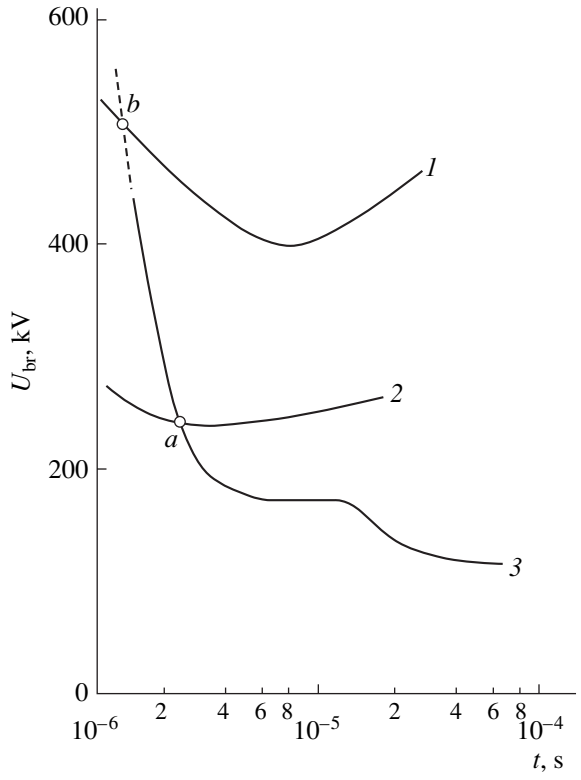

Fig. 1. Voltage–second characteristics of (*1*) organic glass, (*2*) ice, and (*3*) transformer oil.

1063-7842/05/5004-0517$26.00 © 2005 Pleiades Publishing, Inc.

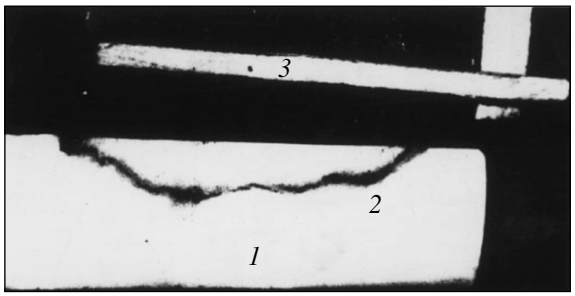

Fig. 2. (*1*) Discharge in (*2*) Teflon with (*3*) a match shown for comparison. The dark space is transformer oil.

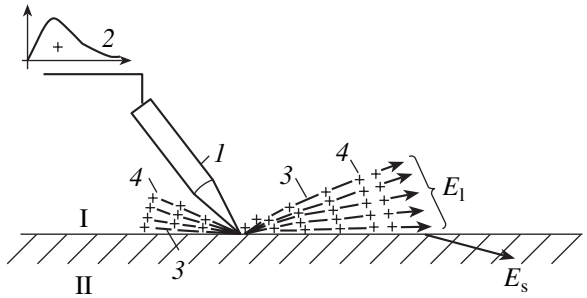

Fig. 3. Discharge processes in (I) transformer oil and (II) solid insulator. *1*, tip electrode; *2*, high-voltage pulse; *3* and *4*, charges in discharge channels in transformer oil; E_l, the field intensity in the liquid (transformer oil); and E_s, the field intensity in the solid insulator.

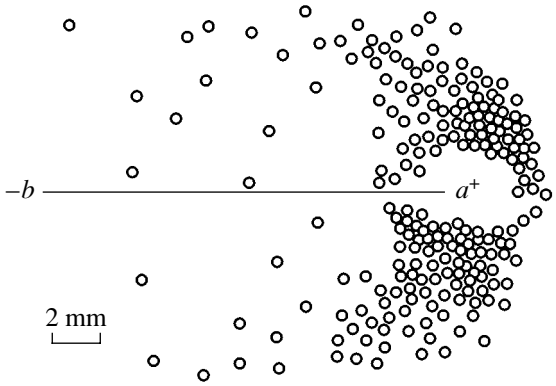

Fig. 4. Distribution of sites of discharge incorporation into the solid insulator (small circles) with two tips used as electrodes. The positively and negatively charged tips touch the surface at points *a* and *b*, respectively.

The discharge channel in Teflon is shown in Fig. 2 (the intact part of the solid insulator is removed). A standard match (*3*) of length 46 mm is shown for comparison.

The horizontal length of the discharge channel was 32 mm. Hence, the discharge first traveled a distance of 14 mm in the oil and only then entered into the solid insulator. The fact of penetration will be discussed below. First, the mechanism behind discharge incorporation will be recalled [2].

A voltage pulse applied to the tip initiates discharges in the liquid, producing a bundle of discharge channels whose ends form a near-spherical surface (Fig. 3). In other words, the electric field in the liquid becomes uniform and the discharge stops. At the same time, on the surface of the solid insulator, the field increases, favoring discharge incorporation into the solid at this place.

The data shown in Fig. 4 also indicate that the incorporation takes place not under the tip [6]. The sites of incorporation are located mainly near the positively charged tip in accordance with the polarity effect mentioned above, which is observed at breakdown of solid insulators.

It was of interest to define a minimum dielectric strength of the liquid at which the discharge can still be incorporated into the solid insulator. While tentative, our calculations turned out to be in satisfactory agreement with recent data for rock destruction.

Let us assume that (i) a bundle of discharges breaks down the liquid near the tip (Fig. 4) in a uniform field and (i) the breakdown voltage of the solid insulator meets the minimum breakdown voltage predicted by Val'ter and Inge as early as in the 1930s [7, Fig. 449].

Our aim is to determine a minimum dielectric strength (breakdown voltage) of the liquid, $E_{br,\,l}$, at which the discharge can still be incorporated into the solid insulator at a given dielectric strength of the solid insulator $E_{br,\,s}$. The latter may be set equal roughly to $(2–3) \times 10^8$ V/m.

Let us introduce coefficients *k*, *m*, and *l*. Coefficient *k* is defined as

$$k = \frac{V_{br,\,s}(d)}{V_{br,\,s\,min}(d)}, \quad (1)$$

where $V_{br,\,s}(d)$ is the breakdown voltage of a solid insulator in a uniform field at electrode gap *d* and $V_{br,\,s\,min}(d)$ is the minimum breakdown voltage of the solid insulator at the same *d*. Coefficient *m* is defined as

$$m = \frac{E_{br,\,s}}{E_{br,\,s}(d)}, \quad (2)$$

where $E_{br,\,s}$ is the dielectric strength of a solid insulator of thickness 0.1–0.3 mm (at which the dielectric strength is usually determined) and $E_{br,\,s}(d)$ is the dielectric strength of the solid insulator for thickness *d* (at which the effect of discharge incorporation is studied). Coefficient *l* is defined as

$$l = \frac{E_{br,\,l}}{E_{br,\,l}(d)}, \quad (3)$$

where $E_{br,\,l}$ is the dielectric strength of the liquid at electrode gap $d = 0.1–0.2$ mm and $E_{br,\,l}(d)$ is the field inten-

sity at which the effect of discharge incorporation into the solid is observed.

From Eqs. (1)–(3), we obtain

$$\frac{E_{\mathrm{br,\,s}}}{E_{\mathrm{br,\,l}}} = \frac{km}{l} \quad \text{or} \quad E_{\mathrm{br,\,l}} = E_{\mathrm{br,\,s}}\frac{l}{km}. \tag{4}$$

Coefficients k, m, and l were determined from the experimental data given in [7]: $k = 25.6$ from Fig. 496, $m = 1.63$ from Fig. 407, and $l = 2.07$ from Fig. 176.

Eventually, we get $E_{\mathrm{br,\,l}} = (0.099–0.148) \times 10^8$ V/m; i.e., $E_{\mathrm{br,\,l}} = 5\%$ of $E_{\mathrm{br,\,s}}$ at an exposure of several microseconds.

We are not aware of materials with such a value of $E_{\mathrm{br,\,s}}$. Yet, rocks more than 20 years old have been destroyed in tap water, which generally validates the calculation performed.

The effect of discharge incorporation into a solid insulator may find application in high-voltage power engineering.

REFERENCES

1. A. A. Vorob'ev, G. A. Vorob'ev, and A. G. Chepikov, *Scientific Discovery, Diploma no. 107, Registration no. 122, December 14, 1961* (Russian Academy of Natural Sciences, Moscow, 1999).
2. G. A. Vorob'ev, Doctoral Dissertation (Tomsk, 1963).
3. A. A. Vorob'ev, *Degradation of Dielectric Strength and Breakdown of Insulators* (Tomsk. Gos. Univ., Tomsk, 1961) [in Russian].
4. A. A. Vorob'ev and G. A. Vorob'ev, *Electrical Breakdown and Damage of Solid Insulators* (Vysshaya Shkola, Moscow, 1966) [in Russian].
5. *High-Voltage Technology*, Ed. by L. I. Sirotinskiĭ (Gosénergoizdat, Moscow, 1953), Vol. 2.
6. B. V. Semkin, Candidate's Dissertation (Tomsk, 1966).
7. G. I. Skanavi, *Physics of Insulators: The High-Field Range* (Fizmatgiz, Moscow, 1958) [in Russian].

Translated by M. Astrov

Technical Physics, Vol. 50, No. 4, 2005, pp. 520–522. Translated from Zhurnal Tekhnicheskoĭ Fiziki, Vol. 75, No. 4, 2005, pp. 128–130.

SHORT COMMUNICATIONS

Ferromagnetic Resonance in Epitaxial Films of Uniaxial Barium Hexaferrites

I. V. Zavislyak, V. I. Kostenko, T. G. Chamor, and L. V. Chevnyuk

Shevchenko National Institute, Kiev, 01033 Ukraine

e-mail: zav@univ.kiev.ua

Received June 22, 2004

Abstract—The magnetic parameters of epitaxial barium hexaferrite films are studied. The hysteresis of the field and frequency dependences of ferromagnetic resonance in the films is investigated in the ranges of the multidomain–monodomain and monodomain–multidomain transitions. The effect of the substrate thickness on film–microwave field interaction is examined. © *2005 Pleiades Publishing, Inc.*

INTRODUCTION

Hexagonal ferrites (in particular, barium ferrite $BaFe_{12}O_{19}$) offer a possibility of raising the operating frequencies of microwave devices to 100 GHz or higher owing to their high uniaxial anisotropy and comparatively narrow ferromagnetic resonance (FMR) linewidth $2\Delta H$ [1]. Use of yttrium iron garnets in this frequency range is infeasible because of the need to apply high magnetic fields.

Epitaxial films have a number of advantages over bulk single crystals [2]. Growth of 2- to 5-μm thick films by the method of liquid phase epitaxy lasts several tens of minutes, so this process is more controllable than growth of bulk single crystals. The quality of single-crystal epitaxial films is expected to be greatly improved in the immediate future. Furthermore, application of epitaxial films makes it possible to design mm-wave integrated devices for spin-wave electronics. For these reasons, investigation of epitaxial films aimed at improving their magnetic performance at microwaves and applying them in mm-wave devices (resonators, filters, time-delay lines, etc.) is a challenging problem.

In this study, we report experimental data concerning FMR in "pure" and aluminum-substituted barium hexaferrite epitaxial films (a total of several tens of films were studied). The films were grown on strontium hexagallate ($SrGa_{12}O_{19}$) substrates under different process conditions and tested on a measuring bench. The traveling-wave ratio (TWR), which is proportional to the imaginary part of the permeability of the film, was measured as a function of a stepwise varying external magnetic field at a fixed frequency. The increment in magnetic field values was chosen arbitrarily and was smaller near the peak of the resonance curve. In addition, a panoramic meter of the voltage standing-wave ratio (VSWR) was used. In this case, the measured TWR values account for the total losses in the waveguide channel, namely, the losses in the unloaded waveguide, those due to FMR in the hexaferrite film, and those due to dielectric resonance in the substrate. It should be noted that the losses in the unloaded waveguide and those in the substrate are independent of external field H_0, whereas the absorption in the hexaferrite film is field-dependent. Therefore, the absorption can be easily found from the total losses by subtraction. Anisotropy field H_a is determined by the formula

$$H_a = \frac{\omega_0}{\gamma} - H_0 + 4\pi M_0,$$

where $4\pi M_0$ is the saturation magnetization, γ is the gyromagnetic ratio, and ω_0 is the resonance frequency.

The values of resonance frequency ω_0 and H_0 were found in our experiments, and M_0 was taken from independent (published) data. In our calculations, we assumed that this value is the same for all the pure barium hexaferrite epitaxial films grown, $M_0 = 0.375$ kG [3].

When external field H_0 is sufficient for saturation, the resonance peak may "wander" over the nonferromagnetic loss spectrum, which adversely affects the accuracy of determining $2\Delta H$. As follows from numerous measurements of $2\Delta H$, the error in measuring $2\Delta H$ with a VSWR panoramic meter does not exceed 10% and is about 5% when this parameter is measured on a measuring bench. Analysis of the experimental data obtained allowed us to reveal some FMR features.

Depending on the film growth method, uniaxial anisotropy field H_a varies from 15.3 to 17.1 kOe. For bulk single crystals, H_a is approximately 17 kOe and $2\Delta H$, 25–30 Oe. In the majority of the films, field H_a is lower than in the bulk single crystals and $2\Delta H$ varies between 40 and 200 Oe. It is known that additional uniaxial anisotropy field H_a' arises in barium hexafer-

1063-7842/05/5004-0520$26.00 © 2005 Pleiades Publishing, Inc.

rite epitaxial films, which is caused by elastic stresses due to film–substrate lattice mismatch [4]. For $BaFe_{12}O_{19}$, $\Delta a/a$ (a is the lattice parameter of the substrate and Δa is the difference between the lattice parameters of the film and substrate) equals 1.65% [5]. Therefore, total uniaxial anisotropy field $H_{a\Sigma}$ will vary from film to film and nonuniform elastic stresses will broaden the FMR line. In addition, thermal diffusion of gallium ions from the substrate to the film may occur during the epitaxial growth of barium hexaferrite, as observed in [6].

The figure shows resonance frequency ω_0 versus external field H_0. For normally magnetized films, two frequency (field) ranges may be distinguished where the curve ($\omega_0(H_0)$) behaves in a radically different manner. Under lower-than-saturation fields, the films exhibit a domain structure, which is responsible for the run of the curve $\omega_0(H_0)$. It was reported that, if initially ($H_0 = 0$) the structure consists of plane–parallel domains, the resonance frequency in more than 50-μm-thick barium hexaferrite films (slabs) is nearly independent of the field [7]. As the film gets thinner, the decline in the FMR frequency with increasing field H_0 becomes noticeable. In films several micrometers thick, this effect is bound to be even more significant [7]. This assumption is confirmed by our measurements (see the figure). As the field approaches the saturation value (the arrows indicate the direction of external field variation), the frequency decreases by about 3 GHz. In our case, saturation field $H_1 = 3.7$ kOe, which is 1 kOe less than $4\pi M_0 = 4.71$ kOe. For the bulk single crystals at $H_0 > H_1$, the resonance frequencies are fitted by straight line $\omega_0 = \gamma(H_a + H_0 - 4\pi M_0)$. The dashed line in the figure depicts the dependence $\omega_0(H_0)$ for the slab. As is seen, the transition to the curve for the monodomain (saturated) slab (point A) occurs at $H_1 = 4\pi M_0$. For the thin films, $H_1 < 4\pi M_0$. After the external field has decreased to $H_0 = H_1$, the dependence $\omega_0(H_0)$ exhibits hysteresis. In field $H_0 = H_1$, the domain structure does not originate. With a further decrease in field H_0 to value H_2 (which we call the separation field), the film remains in the monodomain state. The hysteresis may be explained by the features of magnetic anisotropy in the films and/or by the presence of defects. At $H_0 < 4\pi M_0$, internal magnetic field $H_3 = H_0 - 4\pi M_0 < 0$ tends to demagnetize the film via growth of reverse magnetization nuclei. However, if the concentration of defects in the film is high, it may remain in the monodomain state even in the absence of the field. Otherwise, at $H_2 < H_1$, reverse-magnetization domains rapidly grow and the film turns into the multidomain state in a stepwise manner. However, as follows from the figure, the decline in H_0 is not accompanied by a step at point H_2 and curves *1* and *2* do not coincide at $H_0 < H_2$. It seems likely that the film does not represent a simply connected magnetic domain but consists of individual blocks, in which the domain structure nucleates at different values of H_0 in

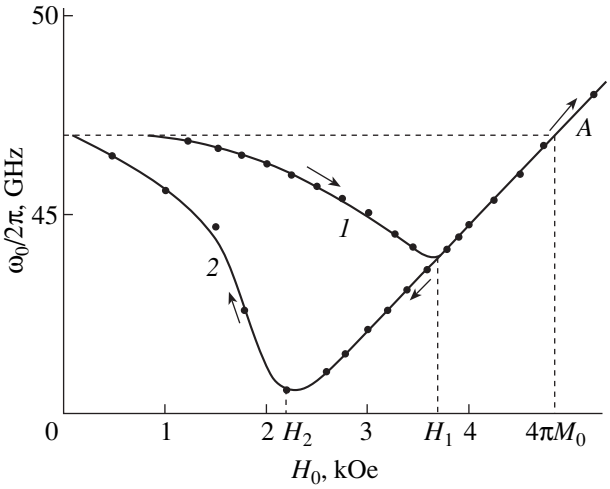

Hysteresis of the resonance frequency vs. field dependence in the epitaxial barium hexaferrite film when H_0 (*1*) rises and (*2*) declines. $H_a = 16.8$ kOe, $2\Delta H = 100$ Oe.

the interval $0 < H_0 < H_2$. The value of H_2 and the run of the curve $\omega_0(H_0)$ in the range $H_0 < H_2$ may indicate the film quality. It would be of great importance to correlate $2\Delta H$ with field H_2 and with the behavior of curve *2*.

The 35- to 45-μm-thick films turned out to be optimal for investigating FMR in the single-crystal slabs, since the absorption drops as the films get thinner. Moreover, when the thickness is less than 25 μm, the waveguide technique cannot provide satisfactory results for all the parameters under study [7]. At the same time, the good 3-μm-thick films ($2\Delta H = 40$ Oe) grown on the 400-μm-thick strontium hexagallate substrate interact with the microwave field as vigorously as the 30- to 35-μm-thick films. Supposedly, the concentration of the field in the substrate has an effect on the absorption of the film (although other reasons should not be ruled out). To validate this assumption, we measured the variation of the absorption and resonance frequencies in the waveguide system with decreasing substrate thickness (the thickness of the hexaferrite film remained unchanged). From the data listed in the table, it follows that, as the substrate becomes thinner, absorption K_m in the resonance curve peak decreases considerably. At the same time, the experimental value of $2\Delta H$ also decreases, whereas the anisotropy field remains virtually unchanged. If the decrease in the absorption can be adequately explained, the reason for the decline in $2\Delta H$ with decreasing the substrate thickness is still unclear. The data presented in the table were obtained by using the panoramic VSWR meter.

Finally, we examined a composite structure made by pressing a 25-μm-thick single-crystal hexaferrite film against a strontium hexagallate substrate. In this case, the absorption intensity of the ferrite film increased insignificantly. These findings, as well as the observed decrease in the FMR linewidth with decreasing the sub-

Dependence of magnetic parameters H_a and $2\Delta H$, as well as of the absorption in the waveguide system, on the substrate thickness for the 5-μm-thick rectangular epitaxial barium hexaferrite film

Substrate thickness, μm	K_m	K_0	f_0, GHz	H_0, kOe	$2\Delta f$, MHz	$2\Delta H$, Oe	H_a, kOe
500	0.91	0.10	44.87	4.00	270	96	16.73
450	0.85	0.10	44.72	4.00	230	82	16.68
400	0.67	0.08	44.60	4.00	200	71	16.63
290	0.24	0.07	44.65	4.00	170	60	16.65
190	0.13	0.05	45.49	4.23	170	60	16.72

Notes: K_m is the absorption in the resonance curve peak; K_0, the absorption in the waveguide system outside the FMR line.

strate thickness, indicate that relaxation mechanisms extrinsic to the bulk single crystals may appear in epitaxial barium hexaferrite films. To clarify these mechanisms needs further investigation.

CONCLUSIONS

(1) In epitaxial barium hexaferrite films, the value of H_a is lower than in bulk hexaferrite single crystals and a correlation between H_a and FMR linewidth is absent.

(2) In normally magnetized epitaxial barium hexaferrite films, hysteresis of the field and frequency dependences of FMR is observed in going from the multidomain state to the monodomain one and vice versa.

(3) In epitaxial barium hexaferrite films, the microwave radiation absorption under FMR increases sharply as compared with the bulk single crystals.

REFERENCES

1. S. V. Lebedev, C. E. Patton, M. A. Wittenauer, *et al.*, J. Appl. Phys. **91**, 4426 (2002).
2. H. L. Glass, J. Appl. Phys. **61**, 4113 (1987).
3. Yu. M. Yakovlev and S. Sh. Gendelev, *Single-Crystal Ferrite in Radio Electronics* (Sov. Radio, Moscow, 1975) [in Russian].
4. S. V. Vonsovskii, *Magnetism* (Nauka, Moscow, 1971; Wiley, New York, 1974).
5. C. Tanasolu, V. Florescu, and M. Rosenberg, Mater. Res. Bull. **6–8**, 1257 (1971).
6. P. Roschmann, M. Lemke, W. Tolksdorf, and F. Welz, Mater. Res. Bull. **19**, 385 (1984).
7. V. I. Kostenko and M. A. Sigal, Phys. Status Solidi B **170**, 569 (1992).

Translated by Yu. Vishnyakov

Technical Physics, Vol. 50, No. 4, 2005, pp. 523–525. Translated from Zhurnal Tekhnicheskoĭ Fiziki, Vol. 75, No. 4, 2005, pp. 131–133.

SHORT COMMUNICATIONS

Linear Frequency-Modulated Pulse Compressor Based on a Three-Mirror Ring Cavity

Yu. Yu. Danilov*, S. V. Kuzikov*, V. G. Pavel'ev, Yu. I. Koshurinov**, and D. Yu. Shchegol'kov****

** Institute of Applied Physics, Russian Academy of Sciences, ul. Ul'yanova 46, Nizhni Novgorod, 603950 Russia*

e-mail: danilov@appl.sci-nnov.ru

*** Lobachevski State University, pr. Gagarina 23, Nizhni Novgorod, 603950 Russia*

Received July 12, 2004

Abstract—A pulse compressor using a three-mirror cavity is tested at a frequency of 34.27 GHz and a low power level. The cavity is fed by a wave beam reflected from the corrugated mirror. The fourfold compression of a rectangular chirp is reached with an efficiency of ≈60%. © *2005 Pleiades Publishing, Inc.*

(1) To cut the cost of electron linacs, the microwave pulse is usually compressed before entering into the accelerating section [1, 2]. For example, in the SLED compressor [3–5], the pulse, when passing through the resonant structure, experiences a 180° phase shift. The same approach is also applied in the compressor based on a quasi-optical three-mirror cavity [6]. However, the band of high-power microwave sources usually shrinks with increasing frequency and the rate of phase modulation of their output signal progressively drops. There arises a need for using pulse compression with a smoother modulation, specifically, linear frequency modulation (chirp) [7, 8].

(2) A lossless compressor based on a reflectionless cavity fed by a chirp can be characterized by three independent parameters: $\alpha = \pi\mu_0 T^2$, which describes the rate of frequency variation; $\beta = 2\pi(f_0' - f_c)T$, which is responsible for an initial offset from resonance; and $\gamma = \pi f_0' T/Q_{ext}$, which is proportional to the ratio between the pulse width and the time of energy accumulation in the cavity. Here, T and μ_0 are the time and rate of variation of the initial pulse frequency, respectively; f_0' is the real part of the eigenfrequency of the cavity; f_c is the initial frequency of the chirp; and Q_{ext} is the external Q factor. Following [1], we take T/s as the duration of the working part of the output pulse ($s > 1$ is a desired compression ratio) and by efficiency mean the ratio of the energy accumulated within interval T/s to the energy of the input pulse. The position of this interval, as well as parameters α, β, and γ, are optimized for a maximal efficiency. In the experiment being described, the compression ratio to be achieved was taken to be four, which is close to the compression ratio obtained in experiments with the SLED [3] and VPM [4] compressors. Using the numerical method described in [8], it was found that, for $s = 4$, the efficiency reaches a maximum (65.9%) at $\alpha = 11.78$, $\beta = 8.61$, and $\gamma = 2.11$.

(3) A pilot compressor (Fig. 1) was designed for a frequency of 34.27 GHz and a duration of the output pulse working part of 22.5 ns. Such a duration results from frequency scaling of the SLED parameters (this compressor is designed for 11.4 GHz) [9].

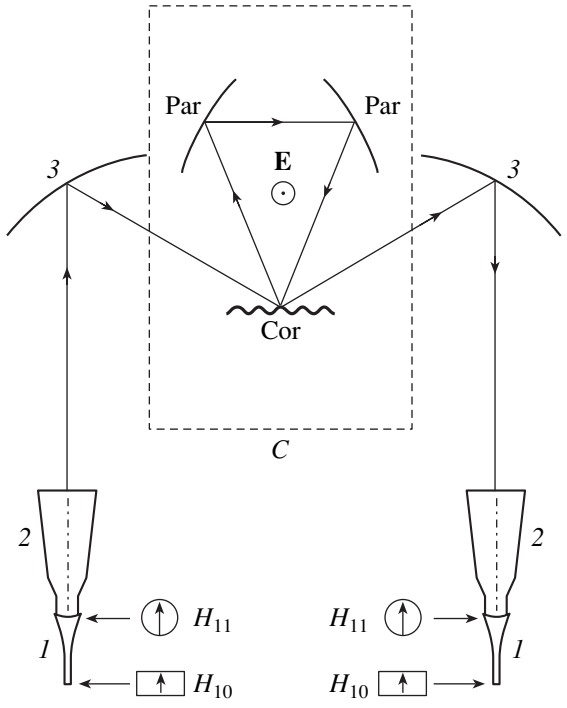

Fig. 1. Diagram of the compressor with the input/output system. *C*, cavity; Cor, plane corrugated mirror; and Par, paraboloid mirror.

1063-7842/05/5004-0523$26.00 © 2005 Pleiades Publishing, Inc.

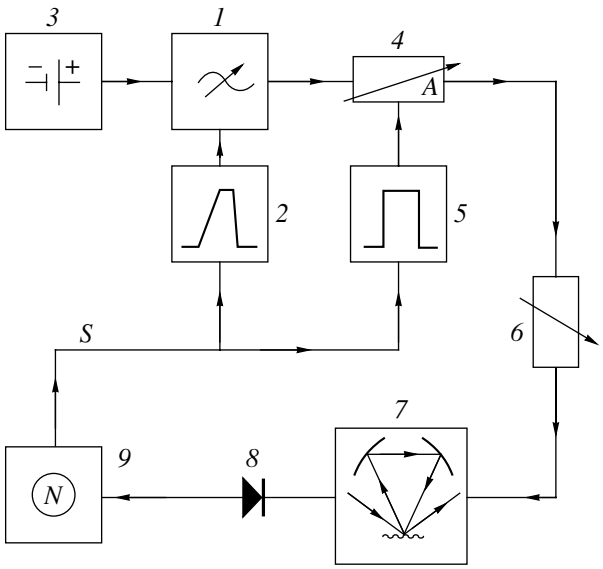

Fig. 2. Experimental setup. *S*, synchronization.

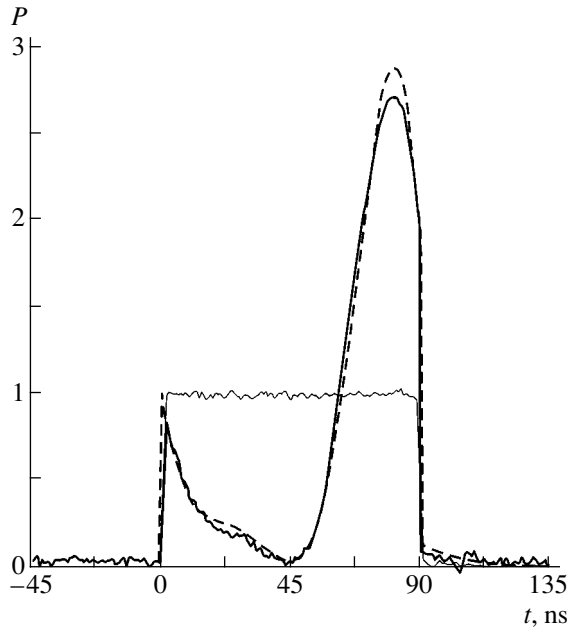

Fig. 3. Envelopes of the input and output pulses. Continuous curves, experiment; dashed curve, theory with allowance for intrinsic losses of the cavity.

As in [6], the cavity of the compressor was made up of three mirrors (Fig. 1). One of them was corrugated in such a way that, with the operating mode freely oscillating, the circulating wave flux was partially scattered to produce the (–1)st diffraction maximum alone and the beam scattered lay in the plane of circulation of the intracavity flux. The reversal of the wave flux provides optimal excitation of the cavity by the flux, according to the reciprocity principle.

The electric field of the cavity's working mode was directed normally to the flux circulation plane (which raises the dielectric strength of the system at high powers). Two mirrors were rectangular, and their working surface had the form of an elliptic paraboloid; the third one, also rectangular, was taken to be planar in a zeroth approximation. The structure of the fields was calculated by the Fox–Li method [10]. Sinusoidal corrugation "applied" on the planar mirror was calculated with the integral equation method [11]. When connected, the centers of the mirrors made up an isosceles triangle. The parameters of the cavity were as follows. The paraboloid mirrors were 227 mm (in the plane of Fig. 1) ×150 mm (in the perpendicular plane), and the radii of curvature of the paraboloids were 5313.7 mm (in the plane of Fig. 1) and 796.5 mm (in the perpendicular plane). The corrugated mirror measured 224 mm (in the plane of Fig. 1) ×110 mm (in the perpendicular plane), the corrugation period was 6.79 mm, and the corrugation amplitude was 0.9 mm. The center distance of the paraboloid mirrors was 270.38 mm, and the distance between the centers of the planar and paraboloid mirrors was 320 mm. The quantities measured in the experiments were the following: the working frequency was 34.27 GHz; the loaded Q factor, 4200; and the unloaded Q factor, 72000.

The system of energy supply to the cavity was designed so as to match the structures of the natural mode of the cavity (TEM_{00n} mode) and the feeding beam on the corrugated mirror. The system (Fig. 1) consisted of (*1*) transition section between a rectangular waveguide with working mode H_{10} and a circular waveguide with mode H_{11}, (*2*) a horn (made up of tapered sections of the circular waveguide [12]) converting mode H_{11} to a Gaussian beam, and (*3*) a specially profiled focusing mirror. The system of energy extraction from the compressor was the same (Fig. 1).

(4) The experimental setup used to measure the compression parameters at a low power level (Fig. 2) included (*1*) a Gunn-effect oscillator with a built-in varicap, (*2*) a controllable-shape video generator for controlling the frequency of oscillator *1* by applying a voltage to the varicap, (*3*) a constant bias driver, (*4*) an electrically controlled driver of microwave pulse envelope, (*5*) a pulser to form envelope *4*, (*6*) a precision attenuator, (*7*) compressor, (*8*) a detector, and (*9*) an oscilloscope.

A desired rate of variation of the initial pulse frequency was provided by setting an appropriate rate of rise of the voltage in the control pulse from generator *2*. An optimal mean frequency of the pulse was sought by varying the constant bias from driver *3*.

(5) Figure 3 shows the envelopes of the initial (rectangular) and compressed power pulses. For an input pulse of width 90 ns, the power gain (compression ratio (4) times efficiency) was found to be ≈2.4 and the efficiency (≈60%), 6% lower than the value predicted.

Note that use of a chain of cavities is one way of improving the efficiency of chirp compression [8].

ACKNOWLEDGMENTS

The authors thank M.I. Petelin for encouragement.

This work was supported by the Russian Foundation for Basic Research, grant no. 03-02-17107.

REFERENCES

1. P. B. Wilson, in *Application of High-Power Microwaves*, Ed. by A. V. Gaponov-Grekhov and V. Granatstein (Artech House, Boston, 1994), pp. 229–317.
2. A. N. Lebedev and E. A. Perel'shtein, in *Relativistic Microwave Electronics*, Ed. by A. V. Gaponov-Grekhov (Inst. Prikl. Fiz. Akad. Nauk SSSR, Gor'kii, 1990), pp. 217–255 [in Russian].
3. Z. D. Farcas, H. A. Hogg, G. A. Loew, and P. B. Wilson, in *Proceedings of the 9th International Conference on High Energy Accelerator, Stanford Linear Accelerator Center* (SLAC, Stanford, 1974), pp. 576–582.
4. V. E. Balakin and I. V. Syrachev, in *Proceedings of the 3rd European Particle Accelerator Conference, Berlin, 1992*, pp. 1173–1175.
5. Yu. Yu. Danilov, S. V. Kuzikov, V. G. Pavel'ev, and S. M. Leshchinsky, Pis'ma Zh. Tekh. Fiz. **27** (6), 59 (2001) [Tech. Phys. Lett. **27**, 245 (2001)].
6. Yu. Yu. Danilov, S. V. Kuzikov, V. G. Pavel'ev, *et al.*, Pis'ma Zh. Tekh. Fiz. **27** (19), 5 (2001) [Tech. Phys. Lett. **27**, 803 (2001)].
7. M. I. Petelin and M. L. Tai, AIP Conf. Proc. **337**, 303 (1995).
8. Yu. Yu. Danilov and M. L. Tai, Zh. Tekh. Fiz. **71** (4), 99 (2001) [Tech. Phys. **46**, 460 (2001)].
9. P. B. Wilson, SLAC–PUB–7449, April 1997.
10. A. Fox and T. Li, *Optical Resonators: A Collection of Articles* (Inostrannaya Literatura, Moscow, 1963), pp. 325–362 [in Russian].
11. G. G. Denisov and S. V. Kuzikov, Int. J. Infrared Millim. Waves **18**, 733 (1997).
12. G. G. Denisov and S. V. Kuzikov, in *Proceedings of the 20th International Conference on Infrared and Millimeter Waves, Orlando, 1995*, pp. 297–298.

Translated by V. Isaakyan

Technical Physics, Vol. 50, No. 4, 2005, pp. 526–527. Translated from Zhurnal Tekhnicheskoĭ Fiziki, Vol. 75, No. 4, 2005, pp. 134–135.

SHORT COMMUNICATIONS

Effect of Surface Properties on the Shear Wave Parameters

V. V. Dudko, A. A. Yushkanov, and Yu. I. Yalamov

Moscow State Regional University, Moscow, 105005 Russia

e-mail: vladimi2000@mail.ru

Received August 3, 2004

Abstract—The interaction of a viscous gas with a vibrating surface is studied in terms of the Maxwell boundary conditions with regard to isothermal slip. © *2005 Pleiades Publishing, Inc.*

Recently, investigation of shear waves in gases has attracted much attention [1]. However, in [1], analysis of the waves in the gas volume was carried out without considering the interaction with the surface. In this paper, we study shear waves generated in a gas by a solid surface executing in-plane vibrations. The influence of isothermal slip [2] on the parameters of the waves generated is taken into account.

Let us consider the following problem: a gas fills up the half-space $x > 0$ above an unbounded planar surface. The surface executes harmonic in-plane vibrations along the Y axis with a frequency ω. The velocity of the surface is much lower than the mean thermal velocity of gas molecules. Our goal is to describe the behavior of the gas and determine a force acting on the surface. The velocity of the surface is given by the expression $u = A\exp(-i\omega t)$. The velocity of the gas near the surface ($x = 0$) must obey the boundary condition

$$V_y = c_m\lambda\frac{\partial v}{\partial x} + A\exp(-i\omega t), \qquad (1)$$

where c_m is the coefficient of isothermal slip [2–4] and

$$\lambda = \sqrt{\frac{\pi m}{2kT}}\frac{\eta}{\rho} \quad [2]$$

is the molecule mean free path. Here, η is the dynamic viscosity of the gas, ρ is the density of the gas, m is the molecular mass of the gas, T is the temperature, and k is the Boltzmann constant. The gas motion is described by the Navier–Stokes equation [5]

$$\frac{\partial \mathbf{v}}{\partial t} + (\mathbf{v}\cdot\nabla)\mathbf{v} = -\frac{1}{\rho}\operatorname{grad} p + \nu\Delta\mathbf{v},$$

where $\nu = \eta/\rho$ is the kinematic viscosity.

Obviously, gas velocity $\mathbf{v}$ is directed along the Y axis and is independent of y; hence, $(\mathbf{v}\cdot\nabla)\mathbf{v} = 0$. Also, since $v_x = 0$, $\partial p/\partial x = 0$ and, accordingly, $p = \text{const}$. The process is isothermal, $T = \text{const}$.

Let us denote $v_y = v$. Then, the Navier–Stokes equation takes the form

$$\frac{\partial v}{\partial t} = \nu\frac{\partial^2 v}{\partial x^2}. \qquad (2)$$

A solution to this equation is sought in the form

$$v = a\exp(-kx - i\omega t). \qquad (3)$$

Substituting (3) into (2) yields

$$k = (1-i)\sqrt{\frac{\omega}{2\nu}}. \qquad (4)$$

Substituting solution (3) into boundary condition (1), we obtain $a = -c_m\lambda k a + u_0$. Then, $a = u_0/(1 + c_m\lambda k)$ or, with regard to (4),

$$a = \frac{u_0}{1 + c_m\lambda(1-i)\sqrt{\dfrac{\omega}{2\nu}}}.$$

Introduce the designation $\delta = \sqrt{2\nu/\omega}$, where δ is the depth over which vibration-induced disturbances penetrate into the gas [5]. The problem is considered in the hydrodynamic approximation with allowance for slip. This implies the fulfillment of the condition $\lambda \ll \delta$. Then, the frequency of surface vibrations must meet the condition $\omega \ll 2\nu/\lambda^2$. Amplitude a can be expressed as

$$a = \frac{u_0}{1 + \dfrac{c_m\lambda}{\delta}(1-i)} = u_0\frac{1 + \dfrac{c_m\lambda}{\delta} + i\dfrac{c_m\lambda}{\delta}}{1 + 2\dfrac{c_m\lambda}{\delta} + 2\left(\dfrac{c_m\lambda}{\delta}\right)^2}.$$

Since ratio λ/δ is small, this expression can be reduced to

$$a \approx u_0\left(1 - \frac{c_m\lambda}{\delta} + i\frac{c_m\lambda}{\delta}\right).$$

From this expression, we can find the difference between the phase of vibrations of the surface and that

of vibrations of the near-surface layer of the gas (see figure),

$$\begin{cases} \sin\varphi = \dfrac{c_m\lambda}{\delta} \\ \cos\varphi = 1 - \dfrac{c_m\lambda}{\delta}, \end{cases} \qquad \varphi \approx \arctan\frac{c_m\lambda}{\delta} \approx \frac{c_m\lambda}{\delta}.$$

Thus, the phase difference is proportional to the Knudsen number of the problem. The gas velocity is given by

$$v(x, t) = u_0\left(1 - \frac{c_m\lambda}{\delta}\right)\exp\left(-\frac{1-i}{\delta}x - i\omega t + i\frac{c_m\lambda}{\delta}\right).$$

The *Y*-directed friction force with which the gas acts on a unit surface area has the form

$$\sigma_{xy} = -\nu\rho\frac{\partial v_y}{\partial x}\bigg|_{x=0}$$

$$= \nu\rho u_0\frac{1-i}{\delta}\left(1 - \frac{c_m\lambda}{\delta}\right)\exp\left(-i\omega t + \frac{ic_m\lambda}{\delta}\right).$$

Coefficient c_m depends on the character of gas molecule scattering by a solid surface; i.e., on kinetic boundary conditions [2, 6]. Accommodation [2] and specular–diffuse kinetic [6] boundary conditions are routinely used. For the former, the problem of isothermal slip has been solved analytically in terms of the BGK model for collision integral [2],

$$c_m = \frac{2 - 0.8534q}{q}. \tag{5}$$

Here, q is the accommodation coefficient of tangential momentum. For the specular–diffuse boundary conditions, no analytical solution has been found. However, this problem has been solved numerically [7] and also by a regularly approximate method [8]. Note that isothermal slip coefficients c_m obtained for the boundary conditions of both types differ only slightly [9]. Hence, expression (5) for the isothermal slip coefficient may be regarded as valid.

The expression for the friction force can be transformed into

$$\sigma_{xy} = \sqrt{2}\frac{\nu\rho}{\delta}u_0\left(1 - \frac{c_m\lambda}{\delta}\right)\exp[-i(\omega t - \varphi)],$$
$$\varphi = \frac{3}{4}\pi + \frac{c_m\lambda}{\delta}. \tag{6}$$

It follows from formula (6) that isothermal slip attenuates the friction force with which the gas acts on the surface. Moreover, the slip makes a contribution to the phase shift between the surface velocity and the force acting on the surface from the gas. In experiments, this effect may be used in determining the isothermal slip coefficients for different combinations of gases and surfaces. From the q dependence of c_m (see (5)), one can find a corresponding value of q. Note in conclusion that, although the accommodation coefficient of tangential momentum is of great practical importance, its experimental determination is a challenging problem [6].

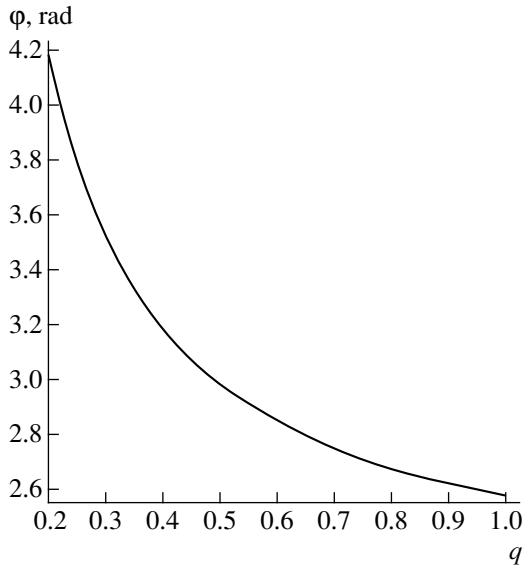

Phase difference φ as a function of the accommodation coefficient of tangential momentum at $\lambda/\delta = 0.2$.

REFERENCES

1. C. Cercignani, Z. Angew. Math. Phys. **36**, 61 (1985).
2. C. Cercignani, *Mathematical Methods in Kinetic Theory* (Plenum, New York, 1969; Mir, Moscow, 1973).
3. I. N. Ivchenko and Yu. I. Yalamov, Izv. Akad. Nauk SSSR, Mekh. Zhidk. Gaza, No. 6, 139 (1968).
4. S. A. Savkov and A. A. Yushkanov, Izv. Akad. Nauk SSSR, Mekh. Zhidk. Gaza, No. 5, 149 (1986).
5. L. D. Landau and E. M. Lifshitz, *Course of Theoretical Physics*, Vol. 6: *Fluid Mechanics* (Nauka, Moscow, 1988; Pergamon, New York, 1987).
6. M. N. Kogan, *Rarefied Gas Dynamics* (Nauka, Moscow, 1967; Plenum, New York, 1969).
7. C. E. Siewert and F. Sharipov, Phys. Fluids **14**, 4123 (2002).
8. A. V. Latyshev and A. A. Yushkanov, Zh. Vychisl. Mat. Mat. Fiz. **44**, 1107 (2004).
9. A. V. Latyshev and A. A. Yushkanov, Izv. Ross. Akad. Nauk, Mekh. Zhidk. Gaza, No. 2, 193 (2004).

Translated by M. Astrov

Technical Physics, Vol. 50, No. 4, 2005, pp. 528–530. Translated from Zhurnal Tekhnicheskoĭ Fiziki, Vol. 75, No. 4, 2005, pp. 136–138.

SHORT COMMUNICATIONS

Radiation Resistance of Advanced GaAs MESFETs

E. V. Kiselyova, M. A. Kitaev, S. V. Obolensky, V. T. Trofimov, and V. A. Kozlov

Lobachevski State University, ul. Ul'yanova 16, Nizhni Novgorod, 603950 Russia

e-mail: obolensk@rf.unn.ru

Received August 17, 2004

Abstract—The radiation resistance of GaAs MESFETs with a channel length of 30–80 nm is studied. It is shown that the resistance is controlled by quasi-ballistic effects in the transistor channel and amounts to 5×10^{14}–5×10^{15} fast neutrons per square centimeter. © *2005 Pleiades Publishing, Inc.*

It is known that linewidth shrinkage in semiconductor devices improves not only their high-frequency performance but also their radiation resistance. GaAs MESFETs can be grouped into three classes [1, 2] according to the channel length: those where the channel length (i) far exceeds the length of energy relaxation (>1 μm), (ii) is comparable to the length of energy relaxation (0.2–1.0 μm), and (iii) is comparable to the length of momentum relaxation (0.05–0.20 μm). The devices from the last-named class are recent advances, and their radiation resistance has not been explored so far.

Neutron irradiation of GaAs generates radiation-induced defect clusters consisting of 5–10 subclusters [3, 4] with characteristic dimensions of 10–15 nm that are 10–40 nm apart. These clusters are completely nontransparent for thermal electrons, and hot electrons (W = 0.3–1.0 eV) are scattered by individual subclusters. Therefore, the transconductance of the current–voltage characteristics of the FETs from the first class decreases in proportion to neutron fluence F_n, whereas for the FETs belonging to the second class, the transconductance drops in proportion to $\sqrt[3]{F_n}$ [3, 5, 6].

In the devices from the third class, the radiation resistance rises further due to the velocity burst effect [7, 8]. In the case of short channels, the cross section of scattering by subclusters decreases considerably: since the energy of carriers reaches 1 eV [2], the space-charge region of subclusters narrows and scattering proceeds virtually on their cores [8]. The electrons undergo mainly elastic small-angle scattering by impurities, as well as by charged point radiation-induced defects and subclusters [8]; i.e., the carriers become almost insensitive to scattering centers.

The radiation resistance of MESFETs depends on a number of parameters, specifically, carrier concentration, gate metal material, etc. [3, 5, 6]. In this paper, we study the effect of neutron irradiation on the performance of ultrashort-channel MESFETs (belonging to the third class). Since the channel length in such transistors is determined as the doubled length of the space-charge region of the gate [9] and, hence, strongly depends on the gate and drain voltages, the parameters of ballistic motion and, accordingly, the radiation resistance of the device depend on the constant supply voltage (bias).

It was shown [8] that the distribution of radiation-induced defects in planar metal–semiconductor structures is nonuniform because of metal atom injection into the semiconductor under irradiation. Therefore, the concentration and size of radiation-induced defect subclusters are nonuniformly distributed over the active layer of the device and the concentration of the subclusters in the channel may be several times higher than in the substrate [8]. In this paper, it is proposed that an Au/light metal/semiconductor composition be used in order to increase the radiation resistance (Fig. 1). Importantly, the metal layer (Ti) adjacent to the semiconductor must have an atomic mass smaller than that of the semiconductor and the thickness of the metal layer must exceed the range of the gold atoms, which gain energy from fast neutrons. In this case, the gold atoms become embedded in the titanium layer under irradiation and do not reach the GaAs layer, while the

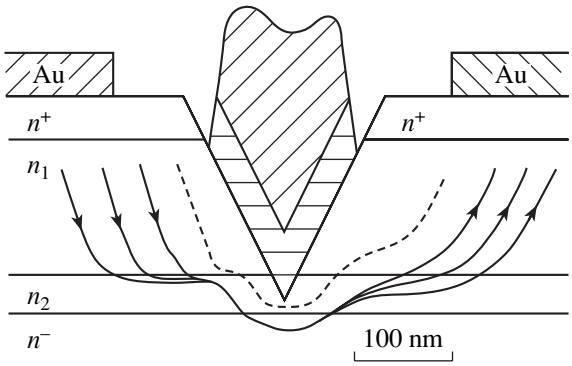

Fig. 1. Charge carrier motion in a V-groove-gate FET. $n^+ = 10^{19}$ cm^{-3}; $n_1 = 2 \times 10^{17}$ cm^{-3}; $n_2 = (7–9) \times 10^{19}$ cm^{-3}; $n^- = 10^{14}$ cm^{-3}. The dashed line is the boundary of the space-charge region of the gate.

1063-7842/05/5004-0528$26.00

Ti atoms injected into the semiconductor generate a smaller number of radiation-induced defects than the atoms of the semiconductor itself.

In this work, we concentrate on devices with a heavily doped active layer, $(7–9) \times 10^{17}$ cm^{-3}, and consider their functioning as an attenuator (the source–drain voltage is V_{12} = 0.1–0.3 eV) or as an amplifier (V_{12} = 2.0–2.5 eV). For gate–source voltages V_{31} = 0.3–0.4 V, drain–source voltages V_{12} = 0.1–0.2 V, and the doping level mentioned above, the channel length (estimated as the doubled size of the space-charge region of the gate) roughly equals 30 nm, which is two to four times smaller than in the devices considered in [8]. With such voltages across the electrodes, intervalley electron transitions are energetically forbidden, since $eV_{12} < W_{\Gamma L}$, where $W_{\Gamma L}$ is the energy gap between the Γ and L valleys.

In the amplification mode, the channel length was 80–100 nm. Owing to the high quality of the Schottky barrier, a positive gate voltage up to 0.6 V increased the gate current insignificantly (to 10–30 μA) with the operating drain currents in the range 3–10 mA. This made it possible to measure the high-frequency parameters of the transistors in this regime.

The static and dynamic characteristics of the devices were measured before and after exposure to neutron radiation with a bell-shaped energy spectrum covering the range 0.01–3.0 MeV (the neutron mean energy was 1.5 MeV). The fluence ranged between 10^{14} and 1.5×10^{16} cm^{-2} (see table). The measurements are presented in Fig. 2 and in the table.

The experimental data were processed using the models described in [4, 7]. The electron energy distributions along the channel for various fluences and transistor's operating modes were analyzed. Comparing the calculated and experimental results leads us to the following conclusions.

(1) When the drain voltage decreases (Fig. 2), i.e., when the amplification mode changes to the attenuation mode, quasi-ballistic carrier motion (the velocity burst effect) takes place throughout the channel of the transistor and the charge carrier energy in the channel varies between 0.10 and 0.25 eV. The frequency of slow-electron scattering by defect clusters is high, while the radiation resistance estimated as the ratio of the drain currents before and after irradiation (Fig. 2) is smaller than in the case of high drain voltages.

(2) A high current density in the channel is related to a high velocity of electrons after the velocity burst. At the same time, the electron density in the channel is low, $(1–5) \times 10^{16}$ cm^{-2}. When radiation-induced defects are generated, the channel is cut off, whereas the resistance of the source and drain regions changes only slightly. This effect allows restoration of both static and dynamic operating conditions of the transistor through a decrease in the gate bias voltage (see the inset to Fig. 1 and table). At a gate voltage of 0.6 V, the transistor continues to efficiently operate up to a fluence of 1.5×10^{16} cm^{-2} in spite of the increase in the leakage current. A self-bias circuit, which serves as a detector of the neutron radiation fluency, may be built around a voltage divider made of semiconductor and metallic resistors incorporated into the transistor chip.

(3) When the gate bias is fixed, the rate of the device's performance degradation is proportional to the

Variation of the quasi-ballistic V-groove-gate MESFET parameters under neutron irradiation

Device no.	Fluence, 10^{15} cm^{-2}	Source–gate voltage, V	Drain current*, mA	Gate–source capacitance, pF	Gain factor at 37 GHz, dB	Noise factor at 37 GHz, dB
1	To 0.7	–0.97	11	0.083	6	3.3
		–0.97	6.5	0.067	6	4.9
		–0.64	10.1	0.078	5.5	3.6
2	To 0.7	–0.21	12.6	0.095	6	3.4
		+0.08	12.6	0.093	6	4.2
		0	11.5	0.087	6	3.5
		–0.21	8.2	0.076	6	5
3	To 4	–0.3	14.2	0.098	6	3.2
		+0.44	9.3	0.085	6	4.1
		0	4.5	0.067	5	3.4
		–0.3	1.8	0.055	1.6	–
4	To 4	–0.96	13.6	0.086	5.5	3.8
		+0.07	13.6	0.103	6	5
		0	12.6	0.095	5.8	4.5
		–0.96	1.6	0.034	1.2	–
5	To 6.5	–0.52	14.0	0.079	6.0	3.4
		+0.6	14.0	0.095	6	5.4
		0	7.3	0.067	5.5	4.8
		–0.52	2.2	0.045	2.1	–
6	To 6.5	–0.95	10.7	0.078	5.5	3.3
		0	11.4	0.082	6	5.4
		–0.07	10.7	0.065	6	5
		–0.95	1.9	0.047	0.9	–
7	To 15	0	10.1	0.078	6	4.2
		0	0.8	0.023	1.1	–
		+0.59	5	0.056	4.2	5.7
8	To 15	–0.21	14.0	0.095	6	3.5
		+0.63	14.0	0.092	6	3.8
		0	5.9	0.067	5	5.5
		–0.21	2.2	0.043	0.5	–

* The drain voltage was taken from the range 2–3 V so as to minimize the noise factor at a gain of 5.5 or 6.0 dB.

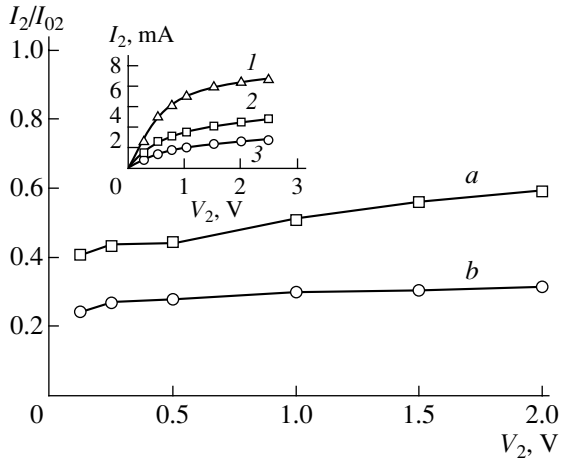

Fig. 2. Relative variation of the drain current vs. the drain voltage after fast-neutron irradiation with fluences of (a) 5×10^{14} and (b) 10^{15} cm^{-2}. I_0 is the drain current before irradiation. The inset shows the dependence of the drain current on the drain voltage (*1*) before and (*2*, *3*) after fast-neutron irradiation with fluences of 10^{15} cm^{-2} at gate voltages of (*1*, *3*) –1.25 and (*2*) –0.9 V.

neutron fluence, as for the case of long-channel devices. However, the threshold fluence at which the MESFET performance starts degrading is 1.5–3 times higher. For fluences of up to 5×10^{15} cm^{-2}, the efficiency of the transistor can be recovered by varying the gate voltage. At higher fluences, positive gate voltages higher than 0.5–0.6 V could remedy the problem; however, the leakage current of the gate increases in this case.

(4) The gain can be completely recovered by varying the gate voltage. At the same time, the minimal noise factor is recovered to a value 10–30% higher than that before irradiation (see table). This can be explained by broadening the bell-shaped electron energy distribution function after neutron irradiation, which is caused by the increase both in the rate of scattering by defects and in the rate of intervalley transitions. The latter is responsible for the enhancement of drain current fluctuations, as well as for noise in the transistor.

ACKNOWLEDGMENTS

The authors are grateful to T.M. Agakhanyan, D.V. Gromov, V.T. Gromov, V.K. Kiselev, A.N. Kachemtsev, and D.I. Tetel'baum for detailed discussion of the results, as well as for valuable comments and suggestions.

REFERENCES

1. M. S. Shur, *GaAs Devices and Circuits* (Plenum, New York, 1987; Mir, Moscow, 1991).
2. Yu. Pozhela, *Physics of High-Speed Transistors* (Mokslas, Vil'nyus, 1989) [in Russian].
3. E. R. Astvatsatur'yan, D. V. Gromov, and V. M. Lomako, *Radiation-Induced Effects in GaAs Devices and Integrated Circuits* (Minsk. Gos Univ., Minsk, 1992) [in Russian].
4. S. V. Obolenskiĭ, Izv. Vyssh. Uchebn. Zaved. Élektronika, No. 6, 67 (2002).
5. R. Zulig, in *VLSI Electronics*, Vol. 11: *GaAs Microelectronics*, Ed. by N. C. Einspruch (Academic, New York, 1985; Mir, Moscow, 1988), pp. 501–547.
6. A. V. Bobyl', R. V. Konakova, V. K. Kononov, *et al.*, Elektron. Tekh., Ser. 8: Upr. Kachl. Stand., Nos. 4–5, 31 (1992).
7. N. V. Demarina and S. V. Obolenskiĭ, Zh. Tekh. Fiz. **72** (1), 66 (2002) [Tech. Phys. **47**, 64 (2002)].
8. S. V. Obolenskiĭ, Mikroélektronika, No. 2, 153 (2004).
9. N. A. Volchkov, K. S. Zhuravlev, M. A. Kitaev, *et al.*, Izv. Ross. Akad. Nauk, Ser. Fiz. **68**, 93 (2004).

Translated by M. Lebedev